| | |
|---|---|
| **Titre:**<br>Title: | Manufacturing and Performance of Long-Length 2G High-Temperature Superconducting Tapes with Current Flow Diverter Architecture for Magnet Applications |
| **Auteur:**<br>Author: | Haifa Ben Saad |
| **Date:** | 2024 |
| **Type:** | Mémoire ou thèse / Dissertation or Thesis |
| **Référence:**<br>Citation: | Ben Saad, H. (2024). Manufacturing and Performance of Long-Length 2G High-Temperature Superconducting Tapes with Current Flow Diverter Architecture for Magnet Applications [Thèse de doctorat, Polytechnique Montréal]. PolyPublie. https://publications.polymtl.ca/59463/ |

| | |
|---|---|
| **URL de PolyPublie:**<br>PolyPublie URL: | https://publications.polymtl.ca/59463/ |
| **Directeurs de recherche:**<br>Advisors: | Frédéric Sirois |
| **Programme:**<br>Program: | Génie des matériaux |

**POLYTECHNIQUE MONTRÉAL**
affiliée à l'Université de Montréal

# Manufacturing and performance of long-length 2G high-temperature superconducting tapes with current flow diverter architecture for magnet applications

**HAIFA BEN SAAD**
Département de génie électrique

Thèse présentée en vue de l'obtention du diplôme de *Philosophiæ Doctor*
Génie des matériaux

Septembre 2024

**POLYTECHNIQUE MONTRÉAL**
affiliée à l'Université de Montréal

Cette thèse intitulée :

# Manufacturing and performance of long-length 2G high-temperature superconducting tapes with current flow diverter architecture for magnet applications

présentée par **Haifa BEN SAAD**
en vue de l'obtention du diplôme de *Philosophiæ Doctor*
a été dûment acceptée par le jury d'examen constitué de :

**Clara SANTATO**, présidente
**Frédéric SIROIS**, membre et directeur de recherche
**Ludvik MARTINU**, membre
**Marco BONURA**, membre externe

# DEDICATION

*To my parents,*
*I wouldn't have been able to accomplish this without your genes*
. . .

# ACKNOWLEDGEMENTS

This thesis owes its existence to the extremely valuable assistance, support along with encouragement, and guidance offered by several individuals. First, I would like to express my sincere gratitude to my thesis supervisor Frédéric Sirois for his continuous guidance and for providing me the resources I needed throughout my PhD. During my PhD journey, he offered me academic advice and efficient feedback on the methodology I chose and my draft chapters, which helped me grow intellectually. He has gone above and beyond to provide me with assistance in my research. He offered exceptional help in assisting me in moving away from my hometown for the first time, settling down in Montreal, and starting working at Polytechnique Montreal during the Covid-19 crisis. Despite the challenges of the pandemic, he performed an important role in ensuring a smooth beginning in this journey. I would also like to show my gratitude to Christian Lacroix for sharing in depth his expertise in measurement setups and numerical simulation tools. During my research, he was always available physically or by phone to assist me during my experiments and to take part in interesting discussions concerning my PhD project in particular, or the broader realm of superconductivity.

I would like to thank Christophe Clément for his availability and his continuous assistance in the clean room. A significant part of this work would not have been possible without his dedication. I also extend my heartfelt gratitude to all my friends/lab-mates Delano Horn-Bourque, Alexandre Arsenault, Jaël Giguère, Thomas Leduc, Simon-Mathieu Bergeron Hartman, Hamza Errabie, Jean-Hughes Fournier-Lupien, Gregory Girard, Marina Gasparini Pinho and Lucile Moret for providing help in the laboratory and for their pleasant friendship.

My sincere thanks also go to Danko van der Laan, Jeremy Weiss, and Kyle Radcliff at Advanced Conductors Technology (ACT) for offering the opportunity to collaborate in fabricating and testing high-current cables. I would also like to thank Mariia Zhuldybina for her sharing her expertise in inkjet printing experiments and for her priceless friendship.

Finally, I would like to give special gratitude to my mother Zina Ben Saâd for believing in me and for the prayers during difficult times and persistent encouragement. Many thanks to my father Chokri Ben Saâd who has been more than just a father but also my mentor in life and my teacher since childhood. I am sincerely indebted for the support of my little sister Sirine Ben Saâd for sharing tears and always being present in my life even being thousands of miles apart.

# RÉSUMÉ

Les rubans supraconducteurs d'oxydes de terres rares (REBCO) sont capables de générer des champs magnétiques intenses qui dépassent 20 T, et de conduire l'électricité sans aucune perte résistive à la température de l'azote liquide. Ces rubans sont caractérisés par une structure en couches minces déposées sur un substrat métallique, ce qui les rend aussi mécaniquement flexibles. Plusieurs recherches sont effectuées pour pouvoir utiliser ces matériaux dans les électro-aimants, les limiteurs de courant de défaut, et l'électrification des transports. Ces rubans sont aussi utilisés pour construire des aimants à forts champs magnétiques pour la fusion nucléaire, les accélérateurs des particules et l'imagerie médicale. Malgré les progrès réalisés au niveau de la fabrication et de la production des rubans REBCO sur des grandes longueurs, la couche supraconductrice possèdent des inhomogénéités au niveau du courant critique ($I_c$) le long des rubans. Les zones qui possèdent un $I_c$ plus faible que la valeur moyenne, générent des points chauds quand le courant appliqué est proche de $I_c$. De plus, ces points chauds se propagent le long du conducteur à une vitesse appelée vitesse de propagation de la zone normale (NZPV). Celle-ci est de l'ordre de quelques centimètres par seconde. La faible NZPV combinée avec les inhomogénéités du courant critique génère un gradient de température local qui peut endommager de façon permanante les dispositifs supraconducteurs.

Ainsi, il est primordial d'avoir une méthode rapide et efficace pour la détection des points chauds. Actuellement, un effort considérable est déployé pour développer des méthodes de détection à la fois fiables, sensibles et rapides pour protéger les aimants à base de rubans REBCO contre l'emballement thermique. L'augmentation de la NZPV des rubans REBCO est une approche prometteuse pour limiter le risque de développement des points chauds et accélérer la détection de ceux-ci. Cette approche est réalisable en utilisant une architecture de ruban particulière qui agit sur la NZPV sans dégrader les propriétés supraconductrices des rubans, et qui est appelée «Current Flow Diverter» (CFD). Celle-ci consiste à intégrer une résistance d'interface non uniforme entre la couche de REBCO et la couche de stabilisateur (argent). Cependant, l'effet CFD a seulement été démontré sur des rubans d'une longueur de quelques centimètres. De plus, la complexité de la réalisation de cette architecture la rend inadéquate pour une production industrielle en grande longueur.

En prenant compte de ce défi, l'objectif principal de cette thèse est de *développer une procédure de fabrication de rubans CFD de grande longueur pour évaluer leur performance dans des dispositifs supraconducteurs.* Pour cette raison, le premier sous-objectif est d'automatiser

la méthode de fabrication de l'architecture CFD. Dans le premier article, des systèmes mécaniques de type bobine à bobine (Reel-to-Reel) ont été développés pour produire des rubans CFD de grande longueur. Ces systèmes utilisent un procédé motorisé de masquage et un système de gravure chimique. Des mesures locales de la NZPV sur un échantillon CFD fabriqué en utilisant ce système ont montré une bonne uniformité sur la longueur du ruban, contrairement aux échantillons fabriqués par la méthode manuelle.

Le deuxième sous-objectif de cette thèse est d'implémenter une approche alternative de fabrication sans avoir recours à des étapes de masquage ou de gravure chimique, afin de réduire le coût de fabrication et d'éviter le gaspillage de métaux précieux. Ce procédé est basé sur l'impression locale d'argent directement sur la surface du REBCO. L'étape d'impression à jet d'encre (IJP) est suivie par un recuit sous oxygène pendant une heure pour diminuer la résistance d'interface entre la couche de REBCO et l'argent imprimé. Une couche d'argent est ensuite déposée par pulvérisation magnétron, recouvrant toute la surface du REBCO. Les résultats présentés dans le deuxième article de cette thèse ont montré que les rubans CFD créées avec la méthode IJP possèdent une NZPV 3 à 6 fois plus élevée que celle des rubans réguliers, d'où la démonstration du succès de cette nouvelle séquence de fabrication pour créer l'architecture CFD qui n'exige pas des étapes de gravure chimique ou de masquage.

Durant ce projet, l'intégration de l'architecture CFD dans des câbles supraconducteurs à fort courant a été testée. Le troisième sous-objectif consistait à fabriquer un câble de type CORC® (Conductor On Round Core) en assemblant six rubans REBCO de type CFD, appelé câble CORC® CFD. Le troisième article présente une étude comparative entre un câble CORC® CFD et un câble CORC® régulier fabriqué avec six rubans réguliers. Les résultats indiquent que le courant critique du câble CORC® CFD augmente de 540 A à 1031 A, lorsque la température d'opération diminue de 77.3 K à 67.2 K. Les mesures de la NZPV ont montré qu'un facteur de gain de 4.5 est obtenu entre la NZPV du câble CORC® CFD et celle du câble CORC® régulier. De plus, la NZPV a été mesurée en fonction de la température d'opération, soit de 67 K à 77 K. Il a été démontré que la NZPV obtenue est indépendante de la température d'opération et varie seulement avec le courant appliqué. Ces résultats sont en accord avec les mesures de NZPV de rubans REBCO individuels rapportées dans la littérature. L'intégration de l'architecture CFD dans des câbles CORC® représente un jalon important qui a le potentiel d'améliorer la vitesse de détection des points chauds au niveau des câbles supraconducteurs.

Comme la détection rapide des points chauds est primordial pour protéger les aimants supraconducteurs à fort champ magnétique, une étude du comportement d'un ruban REBCO CFD bobiné a été réalisée dans cette thèse. Pour ce faire, un ruban CFD et un ruban régulier de 50 cm de longueur ont été enroulés sur un support en bois formant respectivement deux bobines minimalistes, une CFD et une régulière, d'un tour et demi. La NZPV de la bobine CFD était 3 à 4 fois plus élevée que celle de la bobine régulière. La mesure du seuil des tensions développées aux bornes des bobines suite à l'apparition d'un point chaud montre que celui-ci est 3 à 4 fois plus élevé dans le cas de la bobine CFD après la transition supraconductrice/normale, similaire au facteur de gain au niveau de la NZPV. De plus, des simulations numériques ont été réalisées en utilisant un modèle électrothermique basé sur la méthode des éléments finis pour estimer la température maximale du point chaud. Les simulations indiquent que la loi de puissance, généralement utilisée pour décrire la caractéristique $E$-$J$ des rubans REBCO, surestime la réponse électrothermique des rubans quand le courant appliqué est plus faible que le courant critique.

Un nouvel aspect a été exploré dans ce projet dans le cadre de la performance de l'architecture CFD au niveau de l'amélioration de la détection des points chauds. Pour explorer cet aspect, une expérience de détection des points chauds a été réalisée sur un ruban REBCO CFD et parallèlement, sur un ruban REBCO régulier. Cette expérience consiste à déclencher la décharge du courant lorsqu'un seuil de tension ($V_d$), défini au préalable, est détecté. Les résultats de cette expérience montrent que la détection des points chauds est accélérée dans le cas du ruban CFD. Par exemple, la décharge du courant appliqué est déclenchée 7.1 ms plus tôt lorsque $V_d$ est de 20 mV. Cependant, les résultats obtenus numériquement en effectuant des simulations avec la loi de puissance ne concordent pas avec les résultats expérimentaux des rubans CFD et réguliers. Par conséquent, un modèle appelé modèle «piecewise», basé sur une fonction par morceaux représentant les différents régimes de la transition supraconductrice/normale a été développé. Les simulations montrent que le modèle piecewise prédit une réponse électrothermique du ruban régulier beaucoup plus proche de l'éxperience qu'avec la loi de puissance. Cependant, ce modèle ne permet pas la modélisation du comportement des rubans CFD.

En résumé, le concept CFD a été validé sur des échantillons d'une longueur d'un mètre, sur des câbles supraconducteurs et sur des bobines à petite échelle. De plus, une approche alternative de fabrication CFD a été explorée, qui pourrait éventuellement simplifier la production des rubans CFD en grandes longueurs et réduire leur coût. Ceci représente un progrès pour l'industrialisation de cette architecture, qui a le potentiel de résoudre le problème des points chauds dans les dispositifs supraconducteurs.

# ABSTRACT

Rare Earth Barium Copper Oxide (REBCO) High Temperature Superconductors (HTS) provide high current densities, high magnetic fields, and good mechanical flexibility. That's why these conductors make attractive candidates to deliver powerful magnets capable of generating an intense magnetic field that exceeds 20 T. REBCO cables and magnets are currently the hot topics of many research areas such as fault current limitation, energy transmission, clean fusion energy, high energy physics, and high-resolution magnetic resonance imaging. Particularly, strong magnetic fields are needed in fusion magnets, particle accelerator magnets, and medicine (MRI). This requirement can be addressed by building robust REBCO-based high-field magnets. However, the performance of REBCO magnets is limited by the risk of local failures due to the high probability of nucleation of nonsuperconducting resistive zones, called hot spots. These hot spots expand along REBCO tapes at a certain speed called Normal Zone Propagation Velocity (NZPV). Unfortunately, the NZPV of REBCO tapes does not exceed a few centimeters per second (0.1-10 cm/s at 77 K). This low NZPV promotes a concentration of heat in a small region when a hot spot appears, leading to a localized thermal runaway. This localized heating requires a very sensitive and rapid quench detection system, as the local temperature increases rapidly. This makes superconducting devices prone to catastrophic failures, which is costly and represents a threat to all superconducting devices based on REBCO tapes. In addition, REBCO tapes exhibit local millimeter-scale fluctuations in their critical current along their length. When the applied current oversteps the critical current of the defective zones, local superconducting-to-normal transitions, called a quench, occur generating local Joule heating. To overcome this issue, a promising solution is to increase the NZPV of REBCO tapes, and thus increase the quench voltage, which may facilitate quench detection before a thermal runaway occurs. This is now possible thanks to the Current Flow Diverter (CFD) concept, which consists in an innovative architecture of REBCO tapes, developed in Polytechnique Montréal, with a higher NZPV compared to regular (commercial) REBCO tapes. The CFD architecture requires patterning a high interfacial resistance between the stabilizer layer (silver) and the superconducting layer (REBCO). Although the efficiency of this architecture in increasing the NZPV was proved on centimeter-scale REBCO tapes, the complexity of its manufacturing process makes it unattractive for industrial production. Therefore the main objective of this work is to *find a fabrication process for implementing the CFD architecture in long lengths and quantify their performance in quench situations.*

In order to address the main objective, an automatic reel-to-reel setup was developed, capable

of fabricating high-quality meter-scale REBCO tapes. This setup was composed of a motorized masking system and a chemical etching system. In the first article, meter-scale CFD REBCO tapes were fabricated by employing the reel-to-reel method. Their performance was compared with CFD tapes fabricated with the manual fabrication method. NZPV measurements along with visual inspections and numerical simulations revealed that the handmade method engenders geometrical imperfections along the length of REBCO tape, which affects the NZPV uniformity over the length. These imperfections were reduced by adapting the automatic reel-to-reel setup leading to a good NZPV uniformity over the length of the tape.

During this project, a second sub-objective was defined, which was the exploration of a second approach to reduce the fabrication steps of the CFD architecture, making it more straightforward and less costly. In the second article of this thesis, the inkjet printing (IJP) approach was employed to print conductive silver tracks on top of the REBCO layer. The IJP step was followed by annealing in an oxygen atmosphere and silver deposition by sputtering to cover the overall surface of the REBCO layer. NZPV measurements at 77 K and in self-field revealed an increase in the NZPV of the CFD IJP tapes by a factor of 3-6 compared to regular REBCO tapes, which confirms the existence of the CFD effect. There was no need to apply masking or chemical etching during this process, which eliminates the waste of precious metals (silver) and further simplifies the CFD fabrication process into a single silver printing step that can be easily integrated into the industrial manufacturing line of REBCO tapes.

The availability of a fabrication process capable of producing meter-scale CFD REBCO tapes paved the way for a third sub-objective, which was the investigation of the CFD architecture in a high-current superconducting cable geometry. In the third article of this thesis, a Conductor on Round Core (CORC®) cable assembled from six one-meter-long CFD REBCO tapes was manufactured, to test the performance of the CFD architecture in a cable configuration. In parallel, a regular CORC® cable containing six regular REBCO tapes was fabricated. Temperature dependence measurements of the critical current and the NZPV of the CFD and regular CORC® cables were performed at a temperature range of 67 to 77 K. The critical current of the CFD CORC® cable increased from 540 A at 77.3 K, to 1031 A 67.2 K. the NZPV of the CFD CORC® cable was 4.5 higher than that of the regular CORC® cable. It was also shown that the NZPV of the CFD and regular CORC® cables is only determined by the applied current, and is not influenced by the temperature, which is consistent with the NZPV variation of single REBCO tapes. These results demonstrated the successful incorporation of the CFD architecture in a CORC® cable geometry, which has the potential of improving quench detection in high-current cables.

In addition to testing the CFD architecture in high-current cables, the fourth sub-objective of this thesis consisted in the fabrication of a small-scale coil made of 1.5 turns of a CFD REBCO tape. The quench behavior of the CFD coil was compared with that of a regular coil made from a regular tape. NZPV measurements showed that the NZPV of the CFD coil was increased by a factor of 3 to 4 compared to the regular coil. The same gain factor was obtained when comparing the quench voltage in the CFD coil with that in the regular coil. Numerical finite element simulations were carried out to recreate the experimental results and extract the hot spot temperature variation over time. It was demonstrated that the power law model, commonly employed to describe the $E$-$J$ characteristics of REBCO tapes, overestimates the electrothermal response of regular REBCO tapes when the applied current is lower than the critical current.

Another interesting preliminary experiment was conducted in the scope of this work as a fourth sub-objective, which consisted in comparative quench detection experiments applied to both CFD and regular REBCO tapes. Three voltage thresholds were defined in this experiment ($V_d = 5, 10,$ and 20 mV) to trigger the discharge of the applied current once $V_d$ was detected. Results showed that regardless of the voltage thresholds defined in the experiment, the quench was detected faster in the case of the CFD REBCO tape. The detection gain time increased from 3.7 to 7.1 ms, when $V_d$ was increased from 5 mV to 20 mV. The experimental results couldn't be recreated using the power law model, which prompted us to develop a new model, called the piecewise model, to accurately predict the quench behavior of REBCO tapes. This model uses the Bézier curves as a smooth transition between the power law state and the normal state. Results showed that the piecewise model better estimates the developed voltage upon a quench across regular REBCO tapes. However, further calibrations of this model are needed to improve its accuracy and to model the quench behavior of CFD REBCO tapes.

Finally, this thesis opened up several possibilities to explore the performance of the CFD architecture in large-scale superconducting devices. The conventional handmade method was upgraded to produce long-length CFD REBCO tape. The second proposed IJP method has the potential to reduce the waste and cost of the CFD fabrication process and increase the production capacity. The efficiency of the CFD architecture was proved in high-current cables, and shown earlier quench voltage detection in REBCO single tapes. Further investigations of the CFD architecture in large-scale coils at different temperatures and under a magnetic field or in enhancing other forms of quench detection are still required to fully test the potential of this architecture, which is now possible thanks to the availability of long-length CFD REBCO tapes.

# TABLE OF CONTENTS

# LIST OF TABLES

## LIST OF FIGURES

# LIST OF SYMBOLS AND ACRONYMS

## Acronyms

| | |
|---|---|
| 0D | Zero dimension |
| 1D | One dimension |
| 2D | Two dimensions |
| 3D | Three dimensions |
| ACT | Advanced Conductors Technology |
| Ag | Silver |
| $Al_2O_3$ | Aluminum Oxide |
| AMSC | American Superconductor |
| Ba | Barium |
| b-CFD | Buffer layers Current Flow Diverter |
| BSCCO | Bismuth Strontium Calcium Copper Oxide |
| Bi2223 | Bismuth Strontium Calcium Copper Oxide ($(Bi,Pb)_2Sr_2Ca_2Cu_3O_x$) |
| CCs | Coated Conductors |
| CCT | Canted Cosine Theta |
| Ce | Cerium |
| $CeO_2$ | Cerium Oxide |
| CERN | European Organization for Nuclear Research |
| CFD | Current Flow Diverter |
| CFS | Commonwealth Fusion Systems |
| CORC® | Conductor on Round Core |
| CTL | Current Transfer Length |
| Cu | Copper |
| CuO | Copper Oxide (I) |
| $CuO_2$ | Copper Oxide (II) |
| DC | Direct Current |
| EDS | Energy Dispersive Spectroscopy |
| ENEA | Italian National Agency for New Technologies, Energy and Sustainable Economic Development |
| FEM | Finite Element Modeling |
| FeSc | Iron based Superconductor |
| FIB | Focused Ion Beam |

| | |
|---|---|
| $H_2O_2$ | Hydrogen Peroxide |
| HTS | High Temperature Superconductors |
| IBAD | Ion Beam Assisted Deposition |
| IJP | InkJet Printing |
| IRL | Industrial Research Limited |
| ISD | Inclined Substrate Deposition |
| ITER | International Thermonuclear Experimental Reactor |
| KIT | Karlsruher Institut für Technologie |
| LaBaCuO | Lanthanum Barium Copper Oxide |
| $LaMnO_3$ | Lanthanum Manganite |
| LBNL | Lawrence Berkeley National Laboratory |
| LMIS | Liquid Metal Ion Source |
| LSM | Laboratory of Superconductivity and Magnetism |
| LTS | Low Temperature Superconductors |
| $MgB_2$ | Magnesium Diboride |
| MgO | Magnesium Oxide |
| MIT | Massachusetts Institute of Technology |
| MOCVD | Metal-Organic Chemical Vapor Deposition |
| MOD | Metal-Organic Deposition |
| MPZ | Minimum Propagation Zone |
| MQE | Minimum Quench Energy |
| MRI | Magnetic Resonance Imaging |
| Nb-Ti | Niobium–Titanium |
| NdFeB | Neodymium Iron Boron |
| NHMFL | US National High Magnetic Field Laboratory |
| $NH_4OH$ | Ammonium Hydroxide |
| Ni | Nickel |
| NMR | Nuclear Magnetic Resonance |
| NZPV | Normal Zone Propagation Velocity |
| O | Oxygen |
| PCB | Printed Circuit Board |
| PLD | Pulsed Laser Deposition |
| PVD | Physical Vapor Deposition |
| RABiTS | Rolling Assisted Bi-axially Textured Substrates |
| RCE | Reactive Co-Evaporation |
| RE | Rare Earth |

| | |
|---|---|
| REBCO | Rare Earth Barium Copper Oxide |
| ReBaCuO | Rare Earth Barium Copper Oxide |
| RF | Radio Frequency |
| RSD | Relative Standard Deviation |
| SC | Superconductor |
| SD | Standard Deviation |
| SEM | Scanning Electron Microscopy |
| SP | SuperPower Inc. |
| STAR | Symmetric Tape Round |
| STI | Superconductor Technologies Inc |
| TDL | Thermal Diffusion Length |
| TEM | Transmission Electron Microscopy |
| TSTC | Twisted-Stacked Tape Cable |
| USMDP | U.S Magnet Development Program |
| W | Tungsten |
| $Y_2O_3$ | Yttrium Oxide |
| YBCO | Yttrium Barium Copper Oxide |
| YSZ | Yttria-Stabilized Zirconia |

## Symbols

| | |
|---|---|
| $a$ | $a$-axis of the REBCO lattice |
| $A$ | Area |
| $b$ | $b$-axis of the REBCO lattice |
| $\mathbf{B}$ | Magnetic field density |
| $c$ | $c$-axis of the REBCO lattice |
| $C$ | Volumetric specific heat |
| $d$ | Distance |
| $\mathbf{E}$ | Electric field vector |
| $d_{\mathrm{Cu}}$ | Volume density of copper |
| $D$ | Drop spacing |
| $E$ | Electric field |
| $E_c$ | Critical electric field |
| $E_s$ | Electric field in the superconductor |
| $f$ | CFD coverage fraction |
| $F$ | Force |

| | |
|---|---|
| $\mathcal{F}$ | Faraday constant (96 485.3321 sA/mol) |
| $F_L$ | Lorentz force |
| $F_P$ | Pinning force |
| $f_v$ | Volume fraction |
| $h$ | Slope |
| $H$ | Magnetic field |
| $H_c$ | Critical magnetic field |
| $H_{c1}$ | Lower critical magnetic field |
| $H_{c2}$ | Upper critical magnetic field |
| $H^*$ | Irreversibility magnetic field |
| $I$ | Current |
| $I_c$ | Critical Current |
| $I_{c,r}$ | Current transfer fitting parameter |
| $\mathbf{J}$ | Current density vector |
| $J$ | Current density |
| $J_c$ | Critical current density |
| $\ell$ | Displacement of the CFD layer |
| $l_c$ | Contact length |
| $L$ | Length |
| $L_c$ | Critical load |
| $M_{\mathrm{Cu}}$ | Molar mass of copper |
| $n$ | Power law exponent |
| $\mathbf{n}$ | Unit normal vector |
| $n_{FF}$ | Flux flow exponent |
| $n_r$ | Current transfer fitting parameter |
| $p$ | Ratio |
| $P$ | Perimeter |
| $Q$ | Heat |
| $Q_{ini}$ | Initial heat disturbance |
| $q$ | Heat flux |
| $R_i$ | Interfacial resistance |
| $R_c$ | Resistance criterion |
| $t$ | Twist pitch |
| $T$ | Temperature |
| $T_0$ | Operation Temperature |
| $T_c$ | Critical temperature |

| | |
|---|---|
| $T_{cs}$ | Current sharing temperature |
| $t_d$ | Quench detection time |
| $T_m$ | Gallium melting temperature |
| $u$ | Bézier parameter |
| $V$ | Voltage |
| $V_c$ | Critical voltage |
| $V_d$ | Voltage threshold |
| $V_q$ | Quench voltage |
| $w$ | Width |
| $w_f$ | CFD layer width |
| $w_t$ | Total width |
| $\alpha$ | Steckly criterion |
| $\beta$ | Winding angle |
| $\phi_0$ | Magnetic flux through one vortex |
| $\omega$ | Thickness of the copper layer |
| $\rho$ | Electrical resistivity |
| $\rho_{ff}$ | Flux flow state resistivity |
| $\rho_m$ | Mass density |
| $\rho_n$ | Normal state resistivity |
| $\sigma$ | Electrical conductivity |
| $\sigma_n$ | Normal state conductivity |
| $\sigma_{FF}$ | Flux Flow conductivity |
| $\sigma_{PL}$ | Power law conductivity |
| $\delta$ | Oxygen content |
| $\Delta t$ | Time period |
| $\tau$ | Discharge time constant |
| $\kappa$ | Thermal conductivity |
| $\chi_e$ | Ion charge |

# LIST OF APPENDICES

# CHAPTER 1 INTRODUCTION

## 1.1 Basic concepts

The interest in superconductivity is growing year after year thanks to the rapid technological advancement derived from this technology. The ability of superconducting materials to carry electricity without any resistive loss below a certain temperature known as the critical temperature and to generate intense magnetic fields offer new opportunities to develop superconducting devices that can revolutionize medical diagnostics, energy storage and transmission, electric aviation, and science in general. For many years, the potential of superconductivity was limited due to the extremely low temperature required to enable it [1].

The discovery of High Temperature Superconductors (HTS) in 1986 revolutionized the research on superconductivity, with scientists introducing and investigating a wide range of materials and superconducting applications [2]. This class of superconductors has the unique ability to exhibit superconducting properties above the boiling point of liquid nitrogen and to generate the world's most intense magnetic field [3].

Recently, Rare Earth Barium Copper Oxide (REBCO) superconductors demonstrated applications in research and high-field magnets. Powerful magnets based on REBCO superconductors are being designed and studied for nuclear fusion reactors, high-energy physics, and nuclear magnetic resonance. Furthermore, this class of superconductors found applications in a wide range of areas including electric aviation [4], fault current limiters [5], wind turbine generators [6], and power cables [7].

Today, REBCO conductors are commercially available in the form of multi-layered tapes, with a production capacity of a few thousands of kilometers per year. Despite the advancement realized in improving the processing methods of REBCO materials to maximize their performance, thermal, mechanical, or electromagnetic disturbances may still disrupt the stability of REBCO tapes during operation and lead to a transition from the superconducting state to the normal state, named quench.

A challenge with REBCO tapes is that the superconducting layer has zones with a lower critical current than the average value. In addition, the local magnetic field in an HTS magnet is not uniform and decreases unevenly the critical current. Following a disturbance, thermal instabilities, known as hot spots, can cause irreversible damage to the superconductor when the applied current is close to the local critical current. These hot spots expand at a certain speed known as the Normal Zone Propagation Velocity (NZPV). However, the NZPV of REBCO tapes is slow compared to that of low-temperature superconductors. This low NZPV is related to the high specific heat of REBCO tapes. When hot spots appear, their normal zone propagates slowly, causing a local temperature increase that can permanently damage the superconductor before the hot spot is detected [8, 9].

The emerging need for the safe operation of high-field superconducting applications pushed researchers to design several protection systems to detect hot spots and decrease their irreversible and destructive impact on REBCO tapes. However, the low NZPV of REBCO tapes represents a major issue that limits the efficiency and sensitivity of the protection systems.

## 1.2 Research questions

Increasing the NZPV of REBCO tapes has the potential to improve quench protection systems and prevent localized heat dissipation. Previous research at Polytechnique Montréal has shown that modifying the conventional template of REBCO tapes can increase the NZPV. This is expected to enable a faster detection of hot spots. This modification involves creating a non-uniform interfacial resistance between the superconducting layer and the stabilizer and is called the Current Flow Diverter (CFD) concept [10].

Currently, the CFD architecture is an effective strategy that acts on the NZPV without degrading the superconducting properties of REBCO tapes. However, the implementation of the CFD architecture in the template of REBCO tapes requires complex processing steps that are not suitable for an industrial manufacturing line. Thus, it has not yet been integrated into hundreds of meters of REBCO tapes, and its impact has only been demonstrated in short lab-scale samples. Furthermore, the influence of the CFD architecture on the mechanical properties of the conductor has not been explored yet.

A second concern related to the conventional CFD fabrication method is the loss of silver, as this method requires chemical etching of the silver layer on top of the superconducting layer. If this silver is not recycled or recovered elsewhere in the process, a significant cost is required to produce long CFD REBCO tapes and precious material waste occurs along this process. Furthermore, applying recycling processes implies additional costs.

Today, REBCO tapes are assembled and used in the form of coils or high-current cables. Efficient quench detection is crucial for protecting these superconducting coils and cables after the appearance of a hot spot. The geometrical layout of REBCO tapes implies a redistribution of the current between the conductors when a transition to the normal state occurs. The dynamics of the normal zone propagation depend on the current distribution in REBCO coils and high-current cables upon a quench. The effectiveness of the CFD architecture in a coil or cable configuration has not been investigated yet due to the lack of long-length CFD conductors. The development of the CFD concept into an industrially viable design involving hundreds of meters of REBCO tapes is a hurdle to overcome to improve the performance of REBCO tapes under high fields and expand their safety operation margin.

## 1.3 Research objectives

Based on the research questions, the main objective of this project is to find a fabrication process for implementing the CFD architecture in long lengths to quantify their performance in quench situations. The intermediate objectives that stem from the latter are as follows:

1. *Fabrication of long-length REBCO tapes with CFD architecture*
   The available processes are unable to produce hundreds of meters of CFD REBCO tapes. Therefore, the development of an automated reel-to-reel mechanical system capable of handling long REBCO tapes without damaging their superconducting properties is an essential tool for incorporating the CFD architecture in long-length conductors. To achieve this objective, our primary aim is to automate the method that is currently being used to create the CFD architecture for short superconducting lab-scale samples of around 12 cm long. This process involves masking with a Kapton film, chemical etching of silver, and silver deposition.

2. *Development of an alternative low-cost manufacturing process of the CFD architecture*
   To decrease the production cost of hundreds of meters long CFD REBCO tapes, the second objective aims at developing an alternative fabrication approach by direct deposition of conductive patterns on top of the superconducting layer followed by an oxygen annealing. Inkjet printing of conductive patterns will be used to demonstrate the feasibility of a fabrication process without the need to use chemical etching or masking.

3. *Evaluate the performance and the feasibility of the CFD architecture in a cable layout based on CFD REBCO tapes*
   Integrating the CFD architecture concept into the fabrication of REBCO cables for high-field applications is a promising solution for protecting superconducting applications against hot spots. The project's third objective following the development of an automatic approach for the fabrication of long-length CFD REBCO tapes is to design and build a test REBCO cable and a test single-turn REBCO coil assembled from REBCO tapes with the CFD architecture and demonstrate the existence of the CFD effect.

4. *Investigate the potential of the CFD concept in improving quench protection systems of REBCO tapes*
   The CFD architecture has the potential to improve the detection of hot spot nucleation across REBCO tapes. The fourth objective aims at performing voltage detection tests on CFD REBCO tapes to further investigate their voltage temporal profile during the discharge of the applied current. To better simulate the transition from the superconducting state to the normal state, and estimate accurately the temperature of the hot spot during the transition, we aim to develop an original electrothermal model based on a piecewise HTS conductivity model.

## 1.4 Thesis outline

This article-based thesis is organized in ten chapters, which include three articles. The next chapter of this thesis presents a **literature review** synthesizing research work conducted on HTS REBCO tapes. Chapter 3 describes the research **methodology** adopted to achieve the research objectives. Chapter 4 presents **article 1**, which discusses the engineering of meter-scale REBCO tapes with the CFD architecture and the influence of the CFD architecture on certain mechanical properties of REBCO tapes. Chapter 5 contains **article 2**, which presents an alternative manufacturing process of the CFD architecture in REBCO tapes. Chapter 6 presents **article 3**, which concerns the development of high-current cables assembled from REBCO tapes with the CFD architecture. Chapter 7 discusses the physical layout of a single-turn test coil made of CFD REBCO tapes and the simulation model developed to estimate the voltage across REBCO tapes during a transition from the superconducting state to the normal state. Chapter 8 describes the voltage detection experiment performed on CFD REBCO tapes. Finally, chapters 9 and 10 include a general discussion and a conclusion, respectively.

# CHAPTER 2 LITERATURE REVIEW

## 2.1 Fundamentals of high-temperature superconductivity

In 1911, the Dutch physicist Kamerlingh Onnes first investigated mercury's electrical properties at a low temperature. His measurements revealed that the electrical resistance of mercury dropped to zero at a temperature of 4.2 K. This phenomenon is called superconductivity. The temperature below which mercury becomes superconducting, also called critical temperature ($T_c$), was defined as a fundamental parameter separating the superconducting and normal state [11].

In 1986, the breakthrough of Johannes Bednoz and Karl Muller allowed the discovery of High Temperature Superconductors (HTS). The study of the electrical properties of transition metal oxide ceramics led to the discovery of superconductivity in Lanthanum Barium Copper Oxide (LaBaCuO) with a critical temperature of 35 K [2]. Following this breakthrough, superconductivity was discovered in a series of materials with higher transition temperatures. Despite discovering several cuprate superconductors with high $T_c$ at ambient pressure, many of these materials did not meet the industrial requirements because of their toxicity, complex manufacturing process, or poor performance under a magnetic field. Bismuth Strontium Calcium Copper Oxide (BSCCO) and REBCO remained among the few promising HTS materials for industrial use. In the category of superconducting wires, the bismuth-based compounds were known as the first generation (1G) HTS conductors, with a critical temperature ranging from 90 K to 110 K. Their architecture consists of a filamentary structure embedded in a silver matrix. Rare-earth-based compounds were considered as the second generation (2G) HTS conductors, with a critical temperature of up to 93 K. Unlike 1G HTS conductors, 2G HTS conductors have a multilayered structure.

In the 2000s, superconductivity was discovered in i) the intermetallic compound Magnesium Diboride ($MgB_2$), with $T_c = 39$ K [12], and ii) in iron-based superconductors (FeSC), with a $T_c$ up to 55 K [13–15].

Three conditions must be met to maintain a completely lossless superconducting state. The material dissipates when the temperature exceeds the $T_c$ value. The second parameter is the critical current density ($J_c$). $J_c$ is the maximum current density carried by a superconductor. Above this value, the resistivity of the material starts to increase. The final parameter is the critical magnetic field ($H_c$), above which the superconductor becomes resistive. The three parameters are coupled thermodynamically, creating a critical surface limited by $T_c$, $J_c$, and

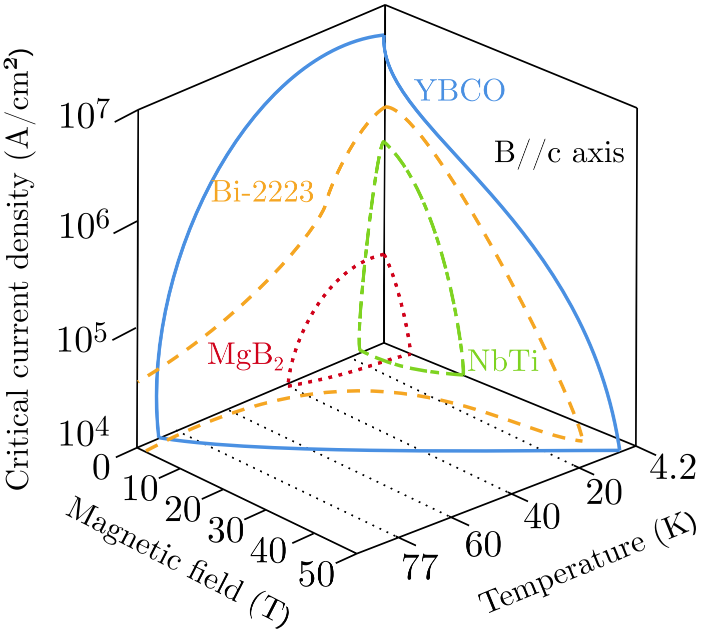

Figure 2.1 Critical current density as a function of the magnetic field and the temperature for yttrium barium copper oxide (YBCO) (blue solid line), bismuth strontium calcium copper oxide (Bi2223) (orange dashed line), magnesium diboride ($MgB_2$) (purple dotted line), and niobium-titanium (Nb-Ti) (green dashed line) superconductors. The magnetic field is parallel to the *c*-axis for YBCO. Adapted from [16].

$H_c$. The critical surfaces of Yttrium Barium Copper Oxide (YBCO), Bismuth Strontium Calcium Copper Oxide ($(Bi,Pb)_2Sr_2Ca_2Cu_3O_x$) (Bi2223), magnesium diboride ($MgB_2$), and Niobium–Titanium (Nb-Ti) are presented in Figure 2.1. The critical current density of the rare-earth-based YBCO compound is relatively high for high values of the magnetic field ($B$) and temperature ($T$) compared to other superconducting materials. Therefore, REBCO materials are more promising for high-field applications [16].

### 2.1.1 Type I vs. type II superconductors

In 1933, Meissner and Ochsenfeld discovered that, below their critical temperature, superconductors are distinguished from perfect conductors by their ability to expel the magnetic flux from their inside volume. Shielding currents flowing on the surface of the superconductor cancel the penetration of the magnetic field, leading to the phenomenon of perfect diamagnetism, also called the Meissner-Ochsenfeld effect. However, the Meissner state is sustained until a limiting value of the critical magnetic field is reached. Type I superconductors are distinguished by having a single critical magnetic field that tends to zero when the temperature increases towards its critical value [17]. Despite the interesting properties of type I superconductors, the superconducting state is lost for a low value of the external magnetic field, which makes this class of materials unsuitable for high-field applications.

On the other hand, type II superconductors have two critical magnetic fields, $H_{c1}$ and $H_{c2}$. The upper critical magnetic field ($H_{c2}$) is very high, and it allows for a gradual transition from the superconducting state to the normal state, which makes type II superconductors great for high-field applications [18, 19].

### 2.1.2 Mechanism of superconductivity in type II superconductors

All HTS superconductors are type II superconductors. Below $H_{c1}$, they are in the Meissner state, completely expelling any external magnetic field from inside the material. Above their lower critical magnetic field, HTS conductors enter in a mixed state called the Shubnikov phase, in which the external magnetic field is only partially expelled. The penetration of the magnetic flux occurs in the form of flux tubes called vortices. In the absence of defects and at low temperatures, vortices are arranged periodically, forming the Abrikosov lattice. Each vortex is surrounded by screening currents, which generate a quantum of a magnetic flux $\phi_0$ inside the vortices with the same direction as the external magnetic field, as shown in Figure 2.2. The remaining area between the vortices remains superconducting until the external magnetic field exceeds $H_{c2}$ [18, 19]. Figure 2.3 illustrates the $H$-$T$ phase diagrams for type I (on the left) and type II superconductors (on the right).

The mixed state can dissipate energy if the vortices move. Indeed, due to Lorentz's forces ($F_L$) generated by the combination of a transport current transverse to the field, the vortices can be set in movement. This displacement induces energy dissipation. This phenomenon is called flux flow.

Vortices must be anchored to impede their displacement. Pinning centers are created inside HTS conductors to oppose the flow of vortices. Structural defects generate pinning force ($F_P$) to keep the vortices anchored in the so-called vortex-glass state. Free motion of vortices is generated if the Lorentz forces exceed the pinning forces ($F_L \geq F_P$), resulting in flux flow.

Vortex pinning centers can be intrinsic defects such as point defects (0D), grain boundaries (2D), and stacking faults (3D). However, to enhance vortex pinning, artificial defects such as nanocolumns (1D) and nanoparticles (3D) are intentionally introduced during the growth of REBCO materials [21]. Figure 2.4 reveals the different defects that act as pinning centers in

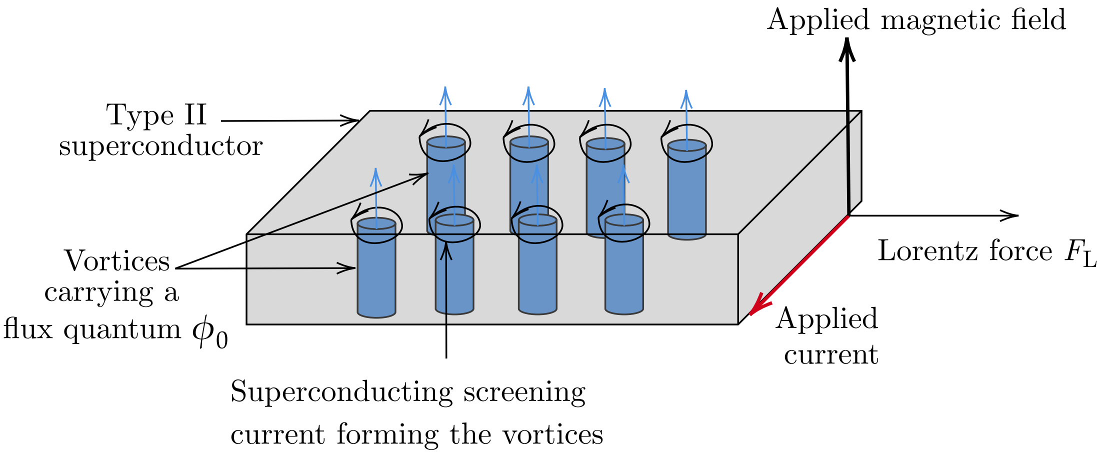

Figure 2.2 The mixed state in a type II superconductor. The penetration of the magnetic flux in the superconductor is in the form of current vortices. Adapted from [20].

REBCO materials.

The vortex-glass state is maintained if the pinning force is strictly positive ($F_P > 0$) and thermal fluctuations are sufficiently low. However, as the operating temperature increases, thermal agitation disrupts the pinning mechanisms, which allows vortices to move from their lattice position. This displacement of the vortices caused by thermal fluctuations leads to a phase change from the vortex-glass state to the vortex-liquid state. The phase change between the vortex-glass state and the vortex-liquid state is separated by the so-called irreversibility line ($H^*(J,T)$) as shown in Figure 2.3. The pinning is ineffective above $H^*(J,T)$, meaning that $F_P = 0$.

Even in the vortex-glass state, when $F_P$ is greater than $F_L$, thermal agitation, along with the non-uniform distribution of the pinning centers, increases the possibility of vortex jumps between pinning centers. This displacement of the pinned vortices is called flux creep.

### 2.1.3 The *E*-*J* characteristic of HTS superconductors

In HTS superconductors, the relation between the electric field ($E$) and the current density ($J$) is non-linear. Mathematically, the dependence of $E$ on $J$ can be modeled by a power law to describe the $E$-$J$ characteristics macroscopically [22]:

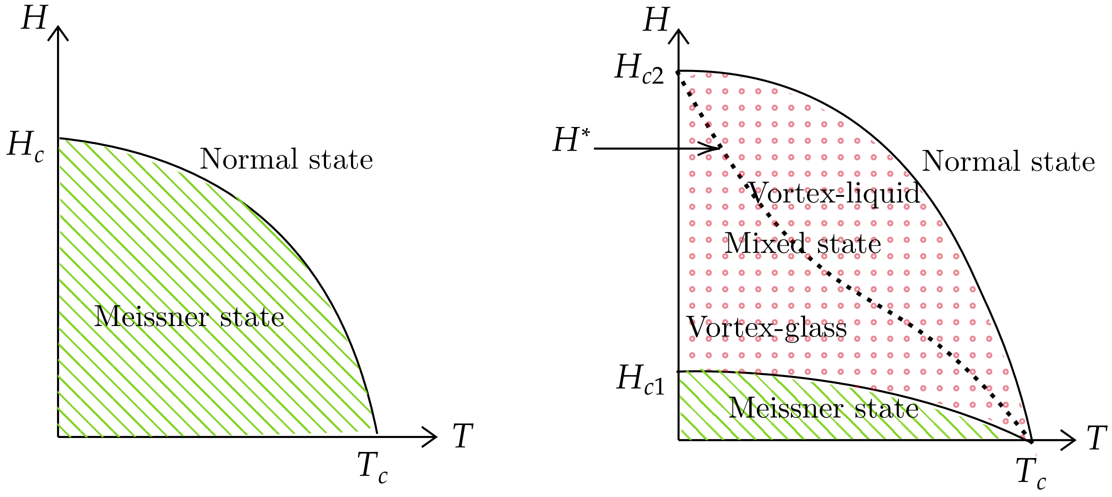

Figure 2.3 Phase diagram of type I (on the left) and type II superconductors (on the right) as a function of the applied magnetic field and temperature. The dotted line represents the irreversibility line $H^*(J,T)$.

$$\mathbf{E} = E_c \left(\frac{|\mathbf{J}|}{J_c}\right)^n , \tag{2.1}$$

where the $J_c$ is usually defined at an electric field threshold $E_c = 1\ \mu\text{V/cm}$. The power exponent $n$ is a non-linear function of the temperature and the magnetic field that indicates the sharpness of the transition from the superconducting state to the normal state. For HTS conductors, the exponent n is typically between 25 and 35 [23].

Figure 2.5 illustrates the $E$-$J$ characteristics of type II superconductors. Vortices are pinned when $J$ is low; no electric field is generated. As $J$ increases towards $J_c$, the vortices jump between pinning sites, generating an electric field, and the resistivity is no longer zero around $J_c$. The $E$-$J$ function is curved around $J_c$ to represent the flux creep. Increasing $J$ above $J_c$ increases the Lorentz force higher than the pinning force, and the flux flow regime occurs, inducing the free motion of vortices, which generates an electric field proportional to $J$.

It has been shown that in the flux flow regime, the $E$-$J$ curve can be represented by a linear variation where the slope is defined by the flux flow resistivity ($\rho_{ff}$) of the HTS conductor [24, 25].

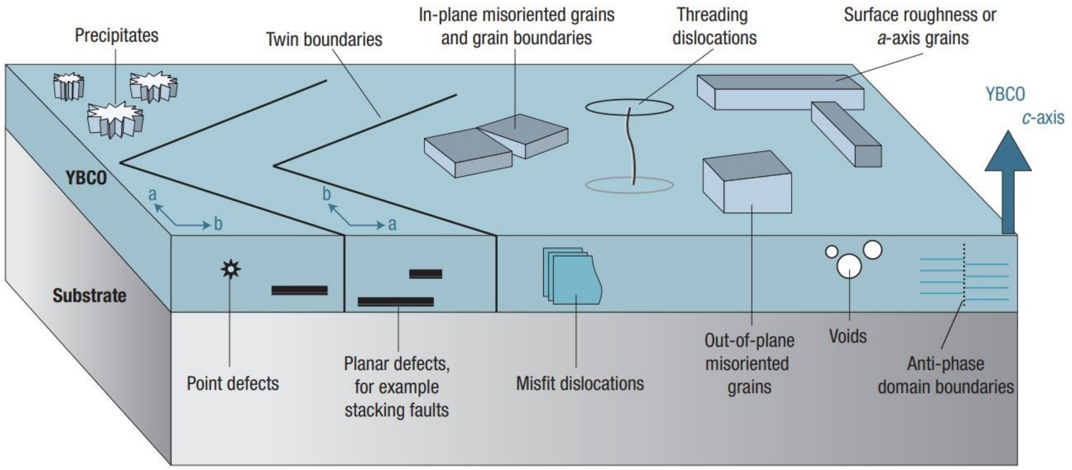

Figure 2.4 Intrinsic and artificial vortex pinning centers in HTS conductors. Image from: [21].

$$E = \rho_{ff}(B,T)(J - Jc)\,. \tag{2.2}$$

However, the power law model is usually used to describe the electro-thermal behavior of HTS conductors in flux creep and flux flow. When the superconductor transits to the normal state, the $E$-$J$ characteristics become ohmic. In this regime, the normal state resistivity ($\rho_n$) of the superconducting material becomes the slope of $E$ vs. $J$.

## 2.2 REBCO coated conductors

Among the HTS group of materials, Rare Earth Copper Oxide (REBCO, also referred to as ReBaCuO) compounds opened up new possible superconducting applications due to their ability to operate at a temperature above the boiling temperature of liquid nitrogen (77 K). The following section is dedicated to describing the structural properties of REBCO Coated Conductors (CCs).

### 2.2.1 Structure of REBCO conductors

REBCO compounds are arranged in a multilayered tape structure grown on flexible, thin metal substrates. Regardless of their flexible structure, REBCO conductors are ceramic compounds, which makes them mechanically brittle. As shown in Figure 2.6, their crystal structure includes $CuO_2$ planes corresponding to the crystallographic $ab$ planes and CuO chains. The $c$-axis is perpendicular to the $CuO_2$ planes. Moreover, the crystallographic struc-

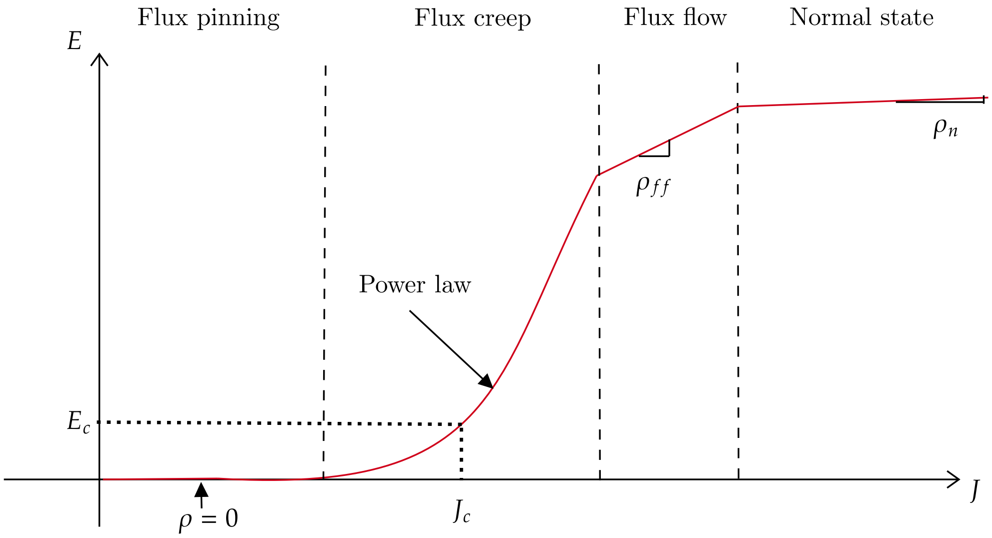

Figure 2.5 Schematic of the non-linear $E$-$J$ characteristic in type II superconductors.

ture of these oxides depends essentially on the oxygen stoichiometry. For example, in yttrium barium copper oxide ($YBa_2Cu_3O_{7-\delta}$), the crystallographic structure is composed of a triplet of oxygen-deficient perovskite units. For $\delta<0.65$, the YBCO structure is orthorhombic, and the lengths of the $a$, $b$, and $c$ axes are unequal. The orthorhombic lattice exhibits superconducting properties associated with the oxygen-filled CuO chains. However, if $0.65<\delta<1$, the crystal lattice becomes a tetragonal insulating system due to the loss of oxygen atoms in the CuO chains required for exhibiting superconductivity. As a result, the oxygenation of REBCO compounds is necessary to confer their superconducting properties [27].

REBCO tapes possess anisotropic transport properties depending on the orientation of the magnetic field. $J_c$ is higher when the field is parallel to the crystalline planes $ab$ than when it is parallel to the $c$-axis. Epitaxial growth along the $c$-axis is favored for this class of superconducting materials to align the $ab$ planes with the direction of the transport current. On the other hand, grain boundaries act as barriers against transporting electrical charges if misaligned in REBCO superconductors. Along with the pinning, $J_c$ depends on the orientation of the grain boundaries. The grains of the REBCO film must be aligned with the $c$-axis, and the angle of the grain boundaries must be low to maximize the value of $J_c$. In practice, the grain boundary misorientation angle is kept lower than $4^\circ$ to maximize $J_c$ [27].

Figure 2.7 presents the typical architecture of commercial REBCO tapes. It is essential

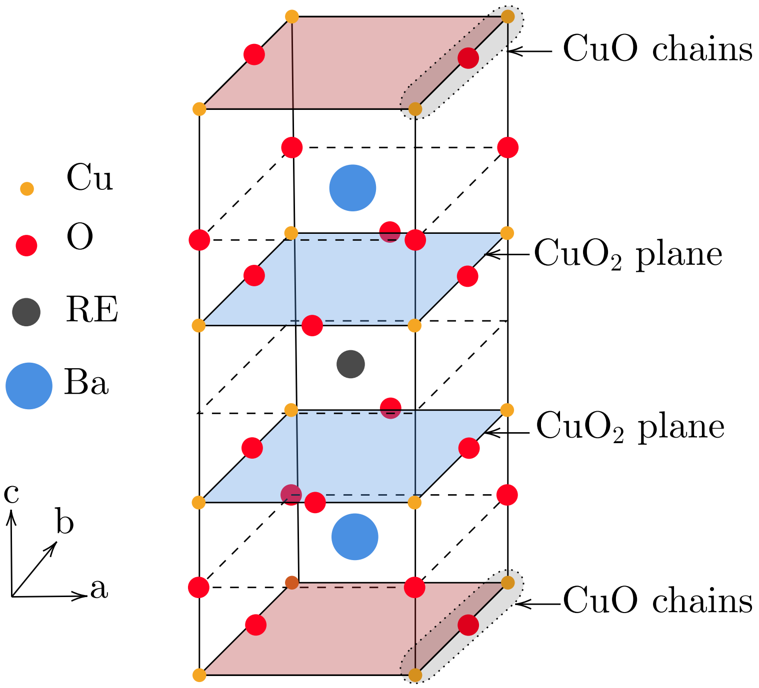

Figure 2.6 The crystal lattice of YBCO compound containing $CuO_2$ planes and $CuO_\delta$ chains ($\delta$ is the oxygen vacancies). Adapted from [26].

to highlight that the layer thicknesses and composition in the REBCO tape are related to the supplier's manufacturing approach. A common commercial architecture includes a silver layer surrounding the whole tape, followed by a copper surrounding layer.

### Substrate

The substrate must sustain mechanical stresses while providing flexibility. Three leading technologies are adapted for growing commercial REBCO tapes depending on their texturing approach. The Rolling Assisted Bi-axially Textured Substrates (RABiTS) architecture commonly uses a metal substrate of nickel-tungsten alloy (Ni-W). Ni-W is used in this approach because its thermal expansion coefficient is similar to that of REBCO and exhibits relatively good mechanical properties. The surface of the substrate is biaxially textured to guarantee grain boundary alignment. Rolling, followed by heat treatment, is applied to ensure the texturing of the substrate. Subsequently, the buffer layers are deposited on the textured substrate. The main advantage of this technique is that it does not require a vacuum environment during texturization [28].

The second architecture is the Ion Beam Assisted Deposition (IBAD). This approach takes place in a vacuum environment. In this method, the substrate consists of a layer of stainless steel or Hastelloy. The IBAD technique relies on generating texture during the deposition of the buffer layers that can be made from Magnesium Oxide (MgO), Yttria-Stabilized Zirconia (YSZ), or Cerium Oxide ($CeO_2$). In the IBAD approach, high energy ion beams are applied for the texturing of the coating [29].

The third technology is the Inclined Substrate Deposition (ISD) developed by the REBCO tape manufacturer THEVA Dünnschichttechnik GmbH [30]. The ISD relies on tilting a non-textured substrate to a certain angle (commonly between 20° and 30°) with respect to the deposition direction so that the *c*-axis would be placed at an angle with the normal direction of the REBCO tape. The biaxial texture is generated in the buffer layers and then transferred to the REBCO layer. The crystal growth in a non-parallel direction to the *c*-axis is faster, which enables faster fabrication of thick REBCO layers [30–32].

### Buffer layers

The buffer layers are a stack of thin films of different compounds. Each thin layer has a specific role in the REBCO structure. In the RABiTS approach, a layer of Yttrium Oxide ($Y_2O_3$) is deposited firstly on the Ni-W substrate to induce structure compatibility within the substrate. Subsequently, a layer of YSZ is deposited on top of the $Y_2O_3$ layer to prevent the diffusion of Ni and W atoms in the REBCO layer. A film of cerium oxide ($CeO_2$) is added as the final buffer layer to avoid the lattice mismatch between the YSZ layer and the REBCO layer since its lattice parameters match those of REBCO.

The buffer layers of the IBAD and ISD techniques differ from those integrated into the RABiTS architecture. Four layers of amorphous Aluminum Oxide ($Al_2O_3$), $Y_2O_3$, Magnesium Oxide (MgO), and Lanthanum Manganite ($LaMnO_3$) are nucleated on top of the substrate one after another. The layer of $Al_2O_3$ acts as a barrier against the diffusion of oxygen and metal atoms. The layer of $Y_2O_3$ ensures the chemical stability of the MgO layer, which is subsequently deposited for biaxial texturing. Finally, a layer of $LaMnO_3$ is deposited on the MgO layer, formed in the perovskite structure compatible with the structure of the REBCO compound [31, 32].

### Superconductor layer

The coating of the superconducting material is deposited following the deposition of the buffer layers. Different thin film deposition techniques are being used for REBCO thin film

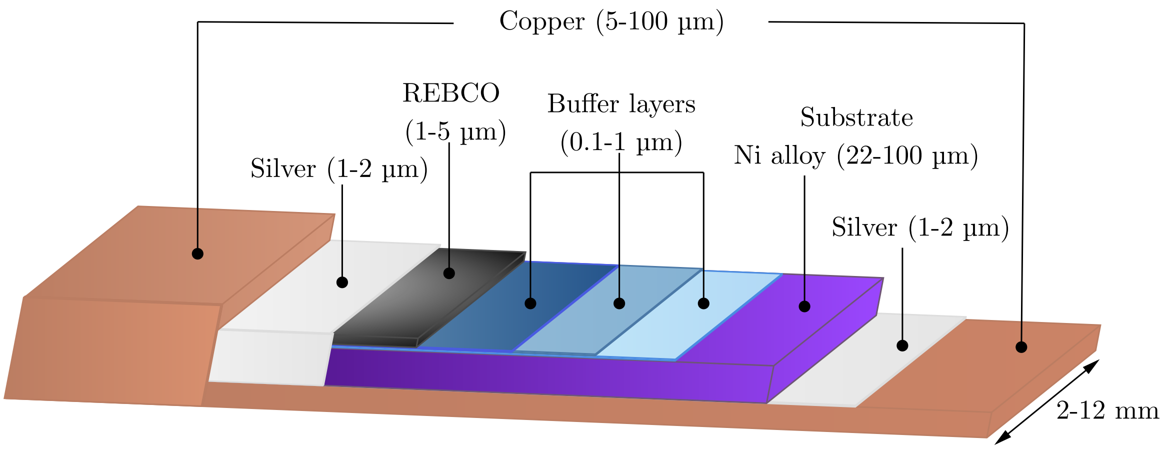

Figure 2.7 Generic architecture of commercial REBCO tape. The represented thickness of the layers is not to scale. Adapted from [33].

deposition. These techniques can be physical, such as Pulsed Laser Deposition (PLD) and Reactive Co-Evaporation (RCE), or chemical, such as Metal-Organic Chemical Vapor Deposition (MOCVD) and Metal-Organic Deposition (MOD). Manufacturers of REBCO-coated conductors are adapting these techniques depending on their cost, difficulty, homogeneity, and production rate to respond to the high demand for long-length REBCO tapes for several high-field applications that we discuss later. Fujikura Ltd., SuperOX Japan LLC., and Shanghai ST Co. manufacturers use the IBAD/PLD approach to produce REBCO tapes. SuperPower Inc. applies the IBAD/MOCVD method, whereas SUNAM uses the IBAD/RCE technique, and American Superconductor (AMSC) is the only manufacturer that used to apply the RABiTS/MOD technique, but they stopped this production a few years ago [34–37].

### Stabilizer

After the deposition of the superconducting film, a metallic layer is deposited around the whole tape. The metallic shunt provides chemical protection against contamination, mechanical protection against scratches, and electrical protection by providing a low-resistance path to the current, to reduce heat dissipation in the superconducting layer during a transition to the normal state. This metallic layer is commonly made of copper, silver, or both and it is called stabilizer. Furthermore, current contacts cannot be installed or soldered directly on the REBCO because they degrade the critical current. Therefore, the current injection occurs on the surface of the metallic shunt. However, the interfacial resistance between the

REBCO layer and the stabilizer must be low enough to prevent heat generation in the current terminals. Silver deposition on the REBCO surface followed by annealing in an oxygen atmosphere promotes the reduction of the interfacial resistance between the REBCO and the stabilizer down to $10^{-9}$ $\Omega$.cm$^2$ [38]. It was also demonstrated that the silver layer possesses good oxygen solubility and permeability and has a catalytic effect during the oxygenation of the REBCO layer [39].

## 2.3 Stability of REBCO conductors

### 2.3.1 Homogenity of the critical current

Despite the existence of several techniques to deposit high-performance REBCO layers and the progress made by the manufacturers to optimize wire properties, the control of the critical current uniformity over long-length REBCO tapes remains a significant challenge. Several deposition parameters require precise control, which is difficult to ensure during the growth of hundreds of meters of REBCO thin layers. The uniformity of the critical current depends on the micro-fluctuations of the tape manufacturing line. Therefore, the critical current is characterized by variations of 10-15% around its average value. Figure 2.8 shows the tape star measurement of the critical current as a function of the length of a THEVA REBCO tape [30]. The results reveal that the critical current varies by 10% around its average value as a function of the length. The zones where the critical current is the lowest are the most likely to generate hot spots. Hot spots are local resistive zones and can propagate along the conductor, generating a transition to the normal state called a quench. A. Zampa et al. [9] have studied the behavior of these zones when the applied current exceeds the reduced critical current of the defective zones. Initially, the defective zone generates heat that spreads horizontally along the width of the tape, forming a dissipation column. This dissipation area extends longitudinally along the tape, leading to the propagation of the resistive zone.

### 2.3.2 Minimum quench energy

During the operation of REBCO-based devices, REBCO tapes can be subjected to several disturbances that can lead to a transition from the superconducting state to the normal state. These disturbances can be i) thermal: caused by poor cooling or heat generated in current contacts; ii) mechanical: caused by Lorentz force or thermal contraction, or structural defects within the conductor; iii) electromagnetic: caused by AC losses; or iv) related to an intrinsic defect in the superconductor, such as inhomogeneous critical current. The disturbance energy can lead to heating and thermal runaway. The nucleation of a normal zone following a

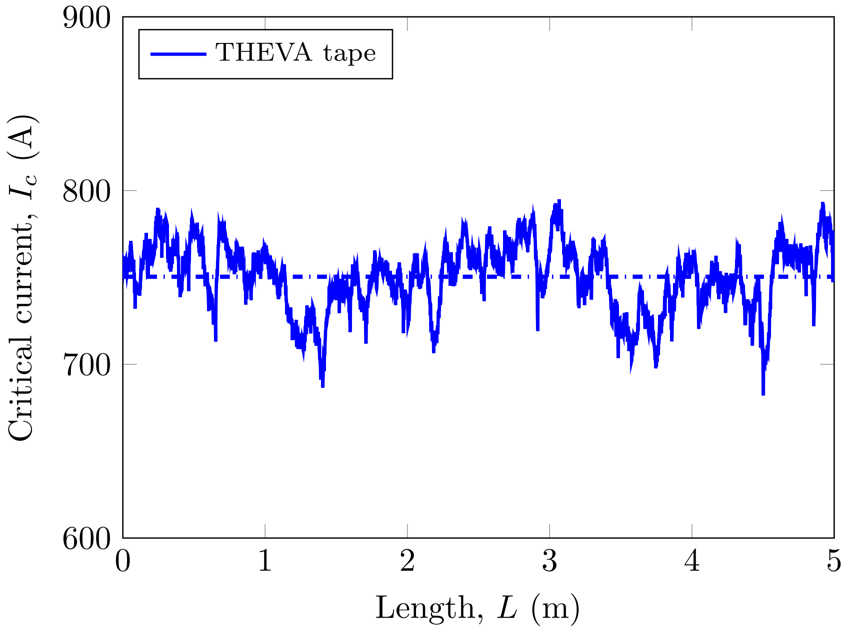

Figure 2.8 Tapestar measurements of the critical current of a commercial THEVA REBCO tape as a function of the length of the tape. The blue dashed line refers to the average critical current value [30].

disturbance depends on the criterion of cryostability. This criterion, defined by Steckly et al. [40], relies on whether the dissipated heat can be conquered by the cooling rate. If the generated heat $Q$ is less than the heat evacuated by the heat flux $q$, thermal stability is achieved, and the superconductor remains in a cryostable state. The superconductor operates safely despite the disturbance under this Steckly condition. This condition can be expressed as follows [41]:

$$Q = \frac{\rho_{\text{Stabilizer}} J^2 A}{f_v P} < q = h(T_c - T_0)\,, \tag{2.3}$$

$$\alpha = \frac{\rho_{\text{Stabilizer}} J^2 A}{f_v P h(T_c - T_0)} < 1\,, \tag{2.4}$$

where $\rho_{\text{Stabilizer}}$ is the resistivity of the stabilizer, $J$ represents the overall current density, $A$ stands for the cross-sectional area, $f_v$ is the volume fraction of the stabilizer, $P$ represents the perimeter that is connected to the coolant, $\alpha$ is the Steckly criterion, and $h$ is the convection coefficient, *i.e.* the slope of the curve representing the variation of $q$ as a function of the temperature difference ($\Delta T$) between the surface of the tape and the coolant temperature.

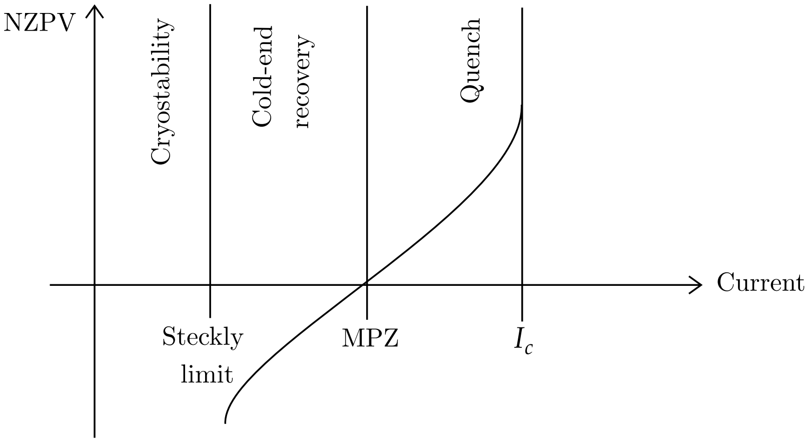

Figure 2.9 Representation of the recovering and non-recovering normal zone regime regimes following a perturbation in HTS conductors. At a certain value of the applied current, the MPZ is nucleated, which leads to quench propagation when the current is increased. Adapted from [41].

Following equation (2.4), the Steckly criterion depends on the volume fraction of the stabilizer. Increasing the thickness of the stabilizer leads to decreasing $\alpha$ and Joule heating. However, it reduces the overall current density of the conductor in parallel, which is not practical in the case of HTS devices.

Beyond the cryostable operation condition, a second condition related to the recovery of the superconducting state is defined and called cold-end recovery. In the work of Maddok et al. [42], a new criterion was defined related to the size of the developed resistive zone upon a perturbation. Two different phenomena can happen following the appearance of a normal zone. The generated heat can be conquered by heat conduction, and the normal zone shrinks and disappears for smaller zones. When the normal zone is large, the heat loss by conduction will not be sufficient to limit its growth, and it will propagate along the conductor, leading to a quench. As a result, the nucleation of a Minimum Propagation Zone (MPZ) must occur for a quench to happen. Following this concept, a minimum energy is required to create the MPZ. The latter is called the Minimum Quench Energy (MQE).

In conclusion, if the perturbation generates a higher energy than the MQE of the HTS conductor, the normal zone propagates at a certain velocity called the Normal Zone Propagation Velocity (NZPV), as shown in Figure 2.9. Otherwise, it is resorbed if the perturbation does not exceed the MQE.

### 2.3.3 Normal zone propagation velocity

As mentioned in the previous section, the NZPV is the velocity of the propagating quench. It is constant over time if the applied field and current are constant. In the non-recovering normal zone regime, the resistance of the REBCO layer increases, and the path of the applied current is distributed between the superconducting layer and the metallic stabilizer when the temperature reaches the current-sharing temperature ($T_{cs}$) as shown in Figure 2.10. The temperature in the quench initiation zone rises because of ohmic heating, and the voltage generated at the terminals is proportional to the NZPV. When $T > T_c$, the applied current flows completely in the metallic stabilizer. The thermal diffusion equation is expressed as follows [41, 43]:

$$C(T)\frac{\partial T}{\partial t} = \nabla(\kappa(T)\nabla T) + \rho(T)J^2 + Q_{ini}\,, \tag{2.5}$$

Where $C(T)$ is the volumetric specific heat, $\kappa(T)$ stands for the thermal conductivity. The term $C(T)\frac{\partial T}{\partial t}$ represents the thermal inertia. The term $\nabla(\kappa(T)\nabla T)$ stands for the heat conduction. The term $\rho(T)J^2$ represents the Joule heating, and the term $Q_{ini}$ is the initial heating perturbation.

The normal zone not only propagates along the conductor, but it also propagates in the transverse direction between REBCO tapes in a stack or a coil configuration, as shown in Figure 2.11. However, the transverse direction propagation is slower than the longitudinal propagation because the longitudinal thermal conductivity is larger than the transverse thermal conductivity. The following expression shows the ratio between the longitudinal and the transverse propagation velocity, namely $\mathrm{NZPV}_{\mathrm{Longitudinal}}$ and $\mathrm{NZPV}_{\mathrm{transverse}}$ respectively [44]:

$$\frac{\mathrm{NZPV}_{\mathrm{Tranverse}}}{\mathrm{NZPV}_{\mathrm{Longitudinal}}} = \sqrt{\frac{\kappa_{\mathrm{Transverse}}}{\kappa_{\mathrm{Longitudinal}}}}\,. \tag{2.6}$$

REBCO coated conductors are known to have a relatively low NZPV. Figure 2.12 shows measurements of the NZPV of three commercial REBCO tapes from SuperPower Inc (SP) [34] (green diamond), Superconductor Technologies Inc (STI) [45] (black x) and THEVA Dünnschichttechnik GmbH [30] (blue triangles), at 77 K and in self-field, as a function of the applied current. The width ($w$) of SP and STI tapes was 4 mm, and it was 12 mm for THEVA tapes. The NZPV is in the order of a few centimeters per second for all SP, STI, and THEVA REBCO tapes. Significant thermal energy can be stored during a quench, causing a localized high peak temperature in the hot spot. A thermal runaway exposes the conductor to irreversible damage if a quench is not detected. The combination of the non-uniform critical

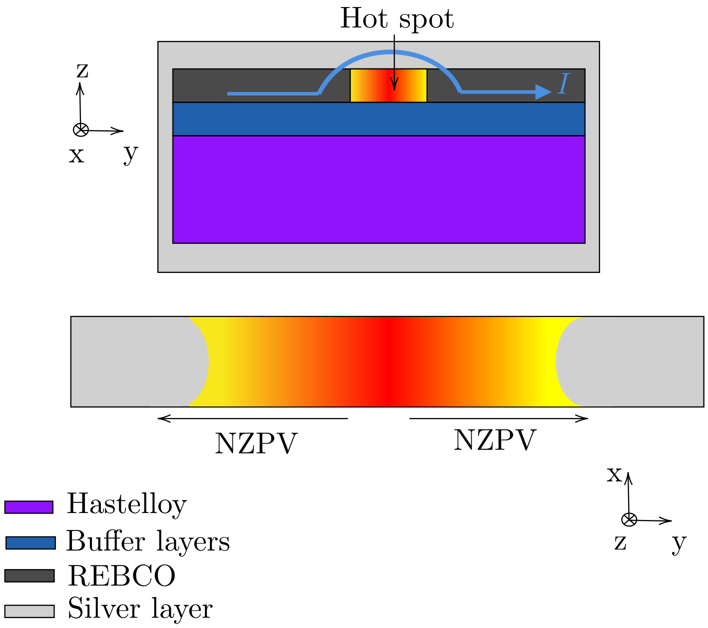

Figure 2.10 Top: a cross-sectional view of a REBCO tape during hot spot nucleation. Bottom: propagation of the NZPV in a longitudinal direction along the length of a REBCO tape.

current and the low NZPV promotes the risk of localized heating degradation of the REBCO tape. It is important to note that the measured REBCO tapes do not include a layer of copper in their architecture. Commercial REBCO tapes are usually surrounded by a copper layer. The NZPV of copper-surrounded REBCO tapes is lower than that of silver-surrounded REBCO tapes presented in Figure 2.12 due to their increased thermal mass.

## 2.4 REBCO cables and applications

### 2.4.1 Main cable geometries made with REBCO tapes

Superconducting cables manufactured by assembling REBCO tapes generate much interest due to their capacity to carry large currents and reduce AC losses when a variable current or magnetic field is applied. Various cabling configurations have been proposed during the last decade [46]. The most common REBCO cables are shown in Figure 2.13. REBCO cables can be classified into two categories based on the geometry of their cross-section.

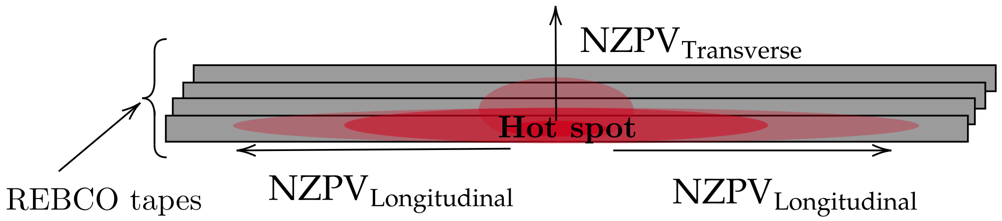

Figure 2.11 In red: propagation of the NZPV in a longitudinal direction along the length of an HTS tape and in a transverse direction along the *c*-axis of a stack of REBCO tapes.

### Rectangular cables

**Roebel cables:** This cable design was invented at the beginning of the 20th century by Ludwig Roebel as a potential candidate to reduce losses in copper cables. This design was later applied to REBCO tapes at the Karlsruher Institut für Technologie (KIT) in 2006. The Roebel cable consists of a stack of meander-shaped tapes. To achieve the Roebel cable geometry shown in Figure 2.13(a), a reel-to-reel pneumatic machine was developed in KIT that removes the unwanted region along the width of REBCO tapes by punching. An assembling device of the punched tapes was developed by Industrial Research Limited (IRL) to manufacture long-length Roebel cables [47]. In this configuration, REBCO tapes are transposed and not twisted, meaning that all the tapes see the same electromagnetic conditions over one twist pitch. The main challenge of this cabling configuration is to avoid damaging the edges of the tapes during the punching.

**Twisted-Stacked Tape cable (TSTC):** The concept of TSTC was first studied at the Massachusetts Institute of Technology (MIT) to simplify the manufacturing process of REBCO cables. The TSTC geometry consists of twisting a stack of flat REBCO tapes longitudinally without modifying the standard geometry of single REBCO tapes. Several institutes like Italian National Agency for New Technologies, Energy and Sustainable Economic Development (ENEA) and KIT adopted different configurations to produce TSTC cables. Three options were explored. The REBCO tapes can be firstly stacked, then twisted along their axis, and finally claded. The second option is to clad the stack of the tapes before applying the twist. The third option involves embedding the prepared stack of tapes in the helical grooves created in a metallic structure [48]. Studies conducted on the TSTC REBCO cables showed that it is a simple cabling method and that it produces compact cable with high current density and partial transposition. An example of a TSTC REBCO cable is shown in

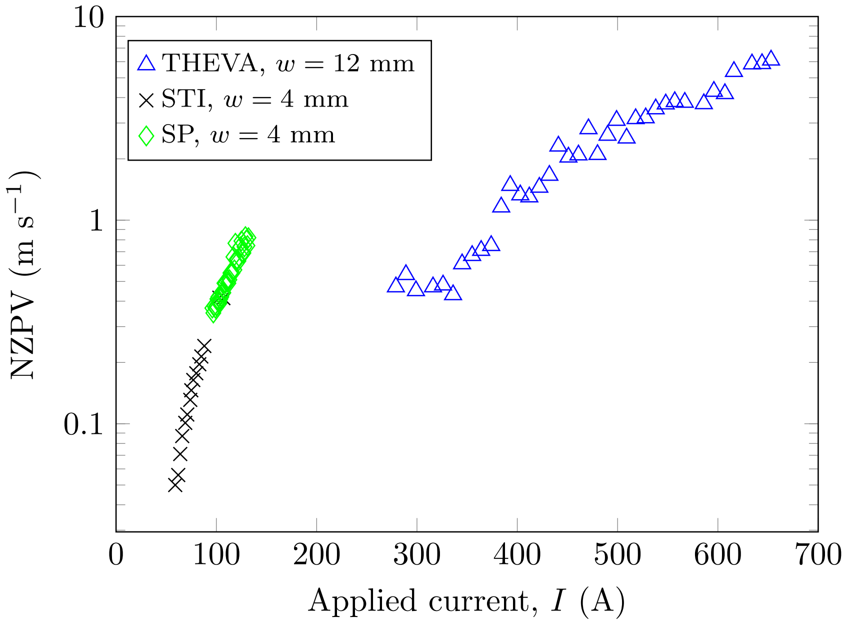

Figure 2.12 Measurements of the NZPV of three commercial REBCO tapes from SuperPower Inc (SP) [34] (green diamond), Superconductor Technologies Inc (STI) [45] (black x) and THEVA Dünnschichttechnik GmbH [30] (blue triangles), at 77 K and in self-field as a function of the applied current. The width ($w$) of SP and STI tapes was 4 mm, and it was 12 mm for THEVA tapes.

Figure 2.13(b).

**Non-twisted-stacked cable:** To further simplify the manufacturing process of stacked tapes present in the TSTC cabling, the non-twisted stack of REBCO tape geometry was proposed. REBCO tapes are stacked along the $c$-axis in this cabling configuration without twisting. The stack of REBCO tapes is inserted in a copper structure and wrapped by a stainless-steel jacket to provide mechanical reinforcement as shown in Figure 2.13(c) [49]. In this case, the tapes are not transposed and the current is not evenly distributed among the tapes.

### Round cables

**Conductor on Round Core (CORC®) cable:** This cabling concept was proposed by DC Vander Laan et al. [54, 55] who is currently the president and CEO of ACT, the leading manufacturer of CORC® cables. The cabling approach involves winding REBCO tapes helically around a conductive former (usually copper) facing inwards. The winding direction is

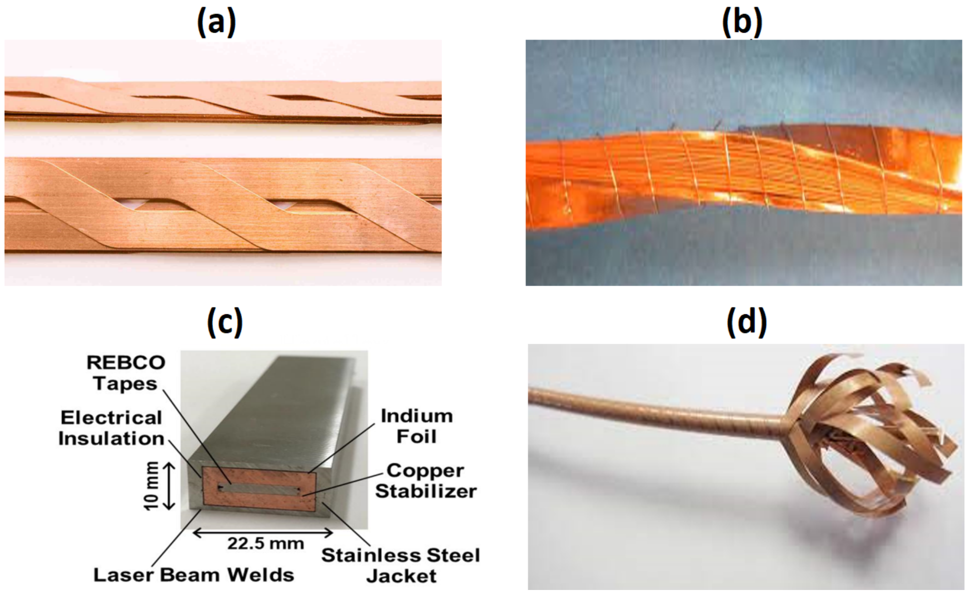

Figure 2.13 Cabling configurations of common REBCO high-current cables. (a) Roebel cable, image from [50], (b) TSTC cable, image from [51], (c) non-twisted stacked cable, image from [52] and (d) CORC® cable, image from [53].

alternated from one layer to another, resulting in high flexibility because the tapes are free to slide when the cable is bent. Along with their flexibility, CORC® cables are characterized by mechanical stability because the REBCO layer faces the former, which means that the superconducting layer is subjected only to compressive strain, which reduces the risk of critical current degradation during the cabling. The diameter of the former depends on the REBCO tape architecture. ACT is manufacturing CORC® cables with a former diameter ranging from 5 to 8 mm and CORC® wires with a former diameter ranging from 2.5 to 4.5 mm, with REBCO tapes with reduced substrate thickness (30 $\mu$m) and reduced width (2 mm). Reducing the former diameter increases the flexibility of the cable. An example of a CORC® cable fabricated by ACT is shown in Figure 2.13(d).

**Symmetric Tape Round (STAR®) wires:** STAR® REBCO wires refer to symmetric tape round wires. In this configuration, REBCO tapes with thin substrate (10-18 $\mu$m of thickness), or the so-called symmetric tapes, are wound helically around a small diameter former. The use of symmetric tapes provides high-bending strain tolerance because the superconducting layer is closer to the neutral axis of the tape. Recently, STAR® wires were fabricated with a copper former diameter of 0.51 mm to 0.81 mm and contained six to twelve REBCO tapes. The critical current of these wires after winding was only reduced to 86.5%

and 95% of $I_c$ after bending at a 15 mm radius, which is promising for high-field applications.

### 2.4.2 High-field applications of REBCO conductors

Among commercial superconductors, REBCO conductors possess higher $J_c$ in an extensive range of magnetic fields and temperatures (see Figure 2.1), which makes them a very attractive candidate for high-field applications. When the temperature is lowered to 4.2 K, the critical magnetic field of REBCO conductors can exceed 100 T. That is why significant progress has been realized in developing and studying HTS magnets based on REBCO single tapes and REBCO cables. The world's highest magnetic field record was achieved by using REBCO tapes. US National High Magnetic Field Laboratory (NHMFL) constructed a magnet with an insert of REBCO coils to generate a 45.5 T steady magnetic field [3]. This achievement has proved the potential of REBCO tapes for high-field devices. In particular, the magnetic confinement nuclear fusion community, the future particle accelerators community, and the Nuclear Magnetic Resonance (NMR) market are all interested in designing and testing REBCO magnets that generate high magnetic fields.

#### Fusion magnets

Fusion energy responds to the emerging need for a carbon-free energy source. To produce fusion energy, high-temperature and high-pressure plasma made of two isotopes of hydrogen (deuterium and tritium) must be confined and prevented from any expansion. An intense magnetic field can trap the plasma in a so-called fusion power reactor. The generation of intense magnetic fields is a feature of superconducting materials. Ongoing projects based on Low Temperature Superconductors (LTS), like the International Thermonuclear Experimental Reactor (ITER) project, are currently working on demonstrating the concept of fusion energy by building a fusion reactor based on low-temperature superconducting magnets. Recently, Commonwealth Fusion Systems (CFS) and MIT have used magnets made from REBCO conductors to design the fusion device SPARC and, more lately, the fusion power plant ARC. These REBCO magnets shown in Figure 2.14 are made from toroidal-shaped coils and are capable of generating a toroidal magnetic field of up to 20 T [57–59]. The main advantage of using HTS conductors in fusion magnets is the ability to generate the same fusion power density as ITER with a much smaller machine size and at higher cryogenic temperatures, especially with the emergence of high current REBCO cables (10 kA at a temperature of 4.2 K and a magnetic field of 20 T [60]). Many conceptual designs have been developed for fusion magnets made from high-current cables such as CORC® REBCO cables and TSTC REBCO cables [61, 62].

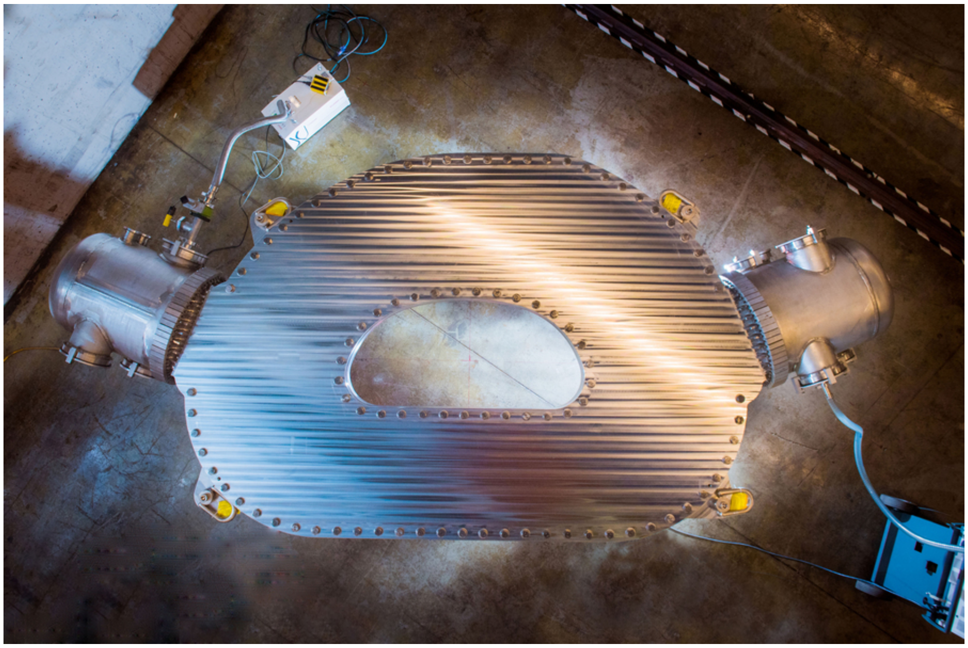

Figure 2.14 CFS REBCO magnet for fusion power. Image from [56, 57].

### Accelerator magnets

In particle accelerators, the Lorentz force of a magnetic field is used to bend the particle beam trajectory to keep it circulating inside the storage ring. The particle accelerator has dipole and quadrupole magnets for beam bending and focusing. The energy of the particle beam is related to the size of the acceleration and the dipole magnetic field. To achieve higher collision energies during particle acceleration, increasing the effective radius of acceleration and the strength of the dipole magnetic field is required (above 20 T). This achievement can only be realized by HTS conductors. For this matter, The European Organization for Nuclear Research (CERN) initiated the EuCARD program to develop REBCO magnets for the particle physics community. First, an insert dipole magnet was built from three racetrack coils made of REBCO cables containing a stack of two tapes. This dipole magnet generated a magnetic field of 5.4 T at a temperature of 4.2 K [64]. The EuCARD2 program focused on the design of accelerator magnets using Roebel REBCO cables. The magnetic field of this dipole magnet was 4.5 T at a temperature of 4.2 K [65].

Other than the European collaboration, the U.S Magnet Development Program (USMDP) is collaborating with Lawrence Berkeley National Laboratory (LBNL) and ACT to develop accelerator magnets using REBCO CORC® cables. These magnets were the so-called Canted Cosine Theta (CCT) magnets, where layers of REBCO conductors were embedded in tilted

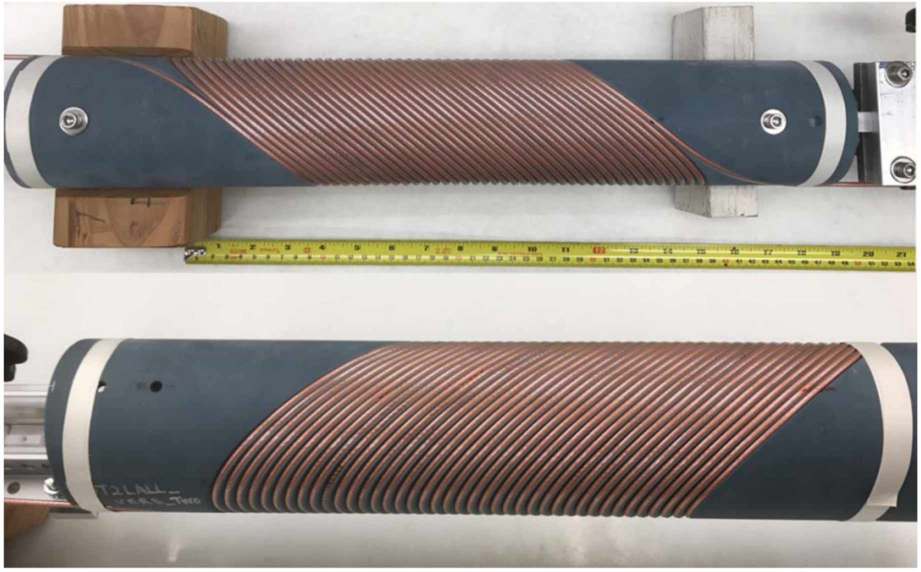

Figure 2.15 Two layers of CORC® cables embedded in the grooves of the 3D-printed mandrel at LBNL. Image from [63].

grooves of a 3D-printed mandrel with alternating the direction between the wounded layers, as shown in Figure 2.15. Recently, it was demonstrated that a CCT magnet made with REBCO CORC® wires generated a dipole field of 2.91 T at a temperature of 4.2 K [63,66]. Similarly, the performance of STAR® wires based on REBCO tapes in the CCT dipole magnet was investigated. It was reported that the dipole field of the three-turns dipole magnet reached 0.79 T [67].

### Nuclear magnetic resonance and magnetic resonance imagery magnets

In addition to the fusion magnet and acceleration magnet, Nuclear Magnetic Resonance (NMR)/Magnetic Resonance Imagery (MRI) magnets made with HTS conductors or REBCO magnet inserts are under development to increase imaging resolution and reduce cooling costs. The Francis Bitter Magnet Laboratory led a project to develop an LTS/HTS NMR hybrid magnet with a REBCO insert capable of generating a total magnetic field of 30.53 T [68].

## 2.5 Quench Protection

Several protection schemes have been studied to mitigate the risk of a thermal runaway to ensure the safe operation of HTS devices. Implementing a conventional quench detection system as in LTS devices is challenging in the case of REBCO conductors because of their low NZPV. Voltage-based quench detection techniques rely on measuring the generated voltage upon a quench. The voltage is proportional to the NZPV. The low propagation velocity of the quench in HTS conductors generates a low voltage in a noisy environment, which can delay the quench detection and the activation of the protection system. The first step of this technique is defining a voltage threshold ($V_d$). When the latter is reached, the discharge circuit is activated, the applied current is driven to zero, and the stored electromagnetic energy is extracted as heat [69]. The critical parameter in this approach is the duration that separates the detection time and the activation of the quench protection system. The peak temperature of the hot spot has to be limited when the current is driven to zero. If the detection is delayed, the temperature continues to rise rapidly and can lead to permanent damage to the REBCO conductor. Figure 2.16 shows the timeline of the voltage-based detection operation.

Other non-voltage quench detection approaches have been investigated to improve the detection time and limit the localized temperature rise. These techniques were magnetic, acoustic, and optical rather than voltage measurements. As a part of the magnetic approaches, the implementation of Hall sensors was proposed to detect the generated unbalanced magnetic field caused by current redistribution after the nucleation of a normal zone. This approach was tested experimentally to detect quenching in CORC® cables [70, 71].

In the context of acoustic approaches, the mechanical perturbation in superconducting magnets causes acoustic emissions. Several studies were interested in detecting these emissions as a quench initiation signal. The method of acoustic thermometry was explored as a non-destructive way to detect quench. The latter have demonstrated good selectivity, despite the noisy environment of HTS magnets [72–74].

Furthermore, optical fibers were recently explored to detect temperature and strain vairations when a quench is initiated, and then locate the quenched zone. In this method, optical fibers can be installed around the conductor or embedded in its structure. Sensors based on Rayleigh scattering and Fiber Bragg gratings (FBGs) could detect normal zones with different spatial resolutions [75–77]. For the rest of this chapter, we focus on modifying the architecture of REBCO conductors and on the potential of this method to avoid the risk of a thermal runaway.

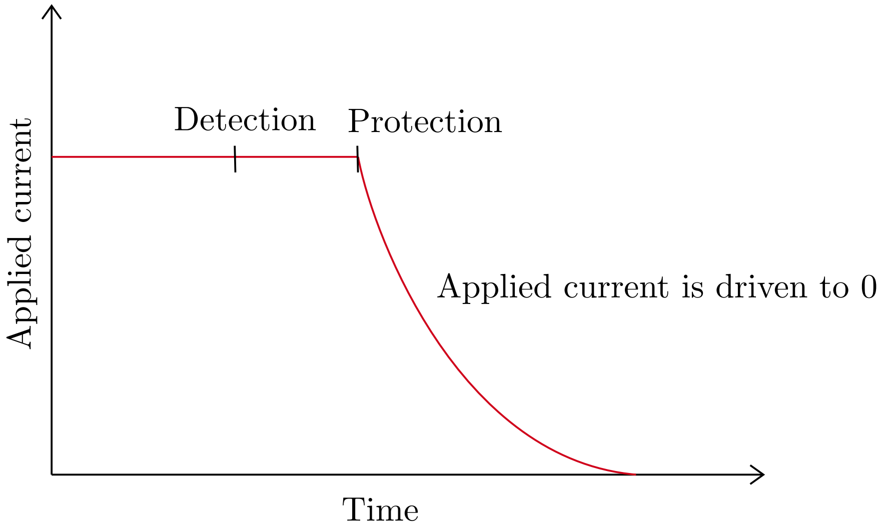

Figure 2.16 Typical voltage detection timeline. When the voltage threshold is detected, quench protection is initiated by driving the applied current to zero.

## 2.6 Current flow diverter

### 2.6.1 NZPV acceleration

The low NZPV poses a challenge to ensuring the safe operation of HTS devices [74]. If the quench propagates faster (with a higher NZPV for instance), in coil and magnet applications, the generated voltage increases more quickly, and the quench can be detected faster, preventing a thermal runaway [78]. Optimally, the NZPV of REBCO tapes should be accelerated to the same order of magnitude with that of low-temperature superconductors (hundreds of meters per second), where conventional quench detection schemes are effective. That is why, researchers aimed to modify the conventional architecture of REBCO tapes to increase the NZPV. The first approach to increase the NZPV relied on the thermal properties of the substrate. The relatively low thermal conductivity of Hastelloy amplifies the localization of the generated heat upon a quench. Sapphire is characterized by a higher thermal conductivity than Hastelloy in liquid nitrogen. Experimental studies conducted on REBCO tapes with a sapphire substrate showed that the NZPV increased [79]. However, sapphire has a lower heat capacity than Hastelloy, which reduces the overall thermal stability of the REBCO tape. Furthermore, using sapphire increases the production cost of REBCO tapes. Therefore, manufacturing REBCO tapes with thick sapphire substrate is not a promising solution for large-scale HTS applications [80–82].

In the same context of NZPV enhancement, a second strategy was initiated by Levin et al. [83]. His numerical studies showed that the NZPV can be improved by increasing the interfacial resistance between the superconducting film and the metallic stabilizer by more than two orders of magnitude. This phenomenon can be explained by the dependence of the NZPV on the Current Transfer Length (CTL). The CTL is defined as the length of the current path between two conductors separated by a resistive interface. In the case of a REBCO tape, the two conductors are the REBCO film and the metallic stabilizer. When a quench is initiated, the superconducting film becomes resistive, which deviates the current flow in the metallic layer. Increasing the interfacial resistance ($R_i$) at the REBCO/stabilizer interface extends the current path between both layers and thus the region in which heat is generated in the resistive interface. The reported $R_i$ value for commercial REBCO tapes ranges from 0.01 to 0.1 $\mu\Omega.\text{cm}^2$. This theoretical study demonstrated that for a value of $R_i$= 0.05 $\mu\Omega.\text{cm}^2$, the CTL is negligible compared to the thermal diffusion length. In this regime, the thermal diffusivity takes over on the current transfer, which means that the NZPV is constant for a low $R_i$ value. The $R_i$ value must be higher than 0.1 $\mu\Omega.\text{cm}^2$ to obtain a CTL much higher than the thermal diffusion length and enhance the NZPV. Experimental investigations performed by C. Lacroix et al. [84] demonstrated that the NZPV is improved by two orders of magnitude when the $R_i$ value is increased by three orders of magnitude. This architecture, in which $R_i$ is uniform and high along the width of REBCO tape between the REBCO layer and the silver layer, is called the uniform architecture.

The value of $R_i$ was increased by exposing the REBCO surface to ambient air, which promotes the creation of a thin resistive layer at the surface of the REBCO layer due to exposure to humidity and carbon dioxide [38, 85]. The existence of this thin resistive layer (6 nm thick) was confirmed by X-ray photoelectron spectrometry (XPS) analysis performed on REBCO tapes where their top silver layer was chemically etched to expose the surface of the REBCO layer [86]. However, poor interfacial resistivity between the REBCO layer and the silver layer increases Joule heating when applying high currents. The $R_i$ value should be lower than 100 $\mu\Omega.\text{cm}^2$ to prevent heating in the current injection regions [38]. Therefore, the main drawback of the uniform architecture is the unacceptably Joule heating that occurs with such high interfacial resistance in the current injection regions. That is why, this solution is not a potential candidate when applying high currents to REBCO tapes.

### 2.6.2 Current flow diverter (CFD) architectures

Following the numerical and experimental results that demonstrated the NZPV acceleration by increasing the interfacial resistance between the REBCO and the metallic stabilizer (silver layer in the case of REBCO tapes), a novel concept was proposed to solve the problem of heat generated in the current contacts of REBCO tapes. This concept was called the Current Flow Diverter (CFD) [10]. It consists of varying $R_i$ at the REBCO/silver interface along the width of REBCO tapes. The overall interfacial resistance ($R_i^*$) of the whole REBCO/silver interface contains a fraction of high interfacial resistance, called "CFD layer", and a fraction of the low intrinsic interfacial resistance $R_i$. The current distribution upon a quench between the REBCO layer and the stabilizer differs between the uniform architecture and the CFD architecture. The path the current takes upon a quench is represented by black arrows in Figure 2.17. It can be seen that in the uniform architecture, the current lines are parallel along the width of the tape in both the superconducting layer (black layer) and the stabilizer layer (orange layer). In the CFD architecture, the current lines bypass the CFD layer (blue layer) when it is transferred to the stabilizer, resulting in a larger CTL and higher NZPV.

Increasing the width of the CFD layer increases the CTL between the superconducting layer and the stabilizer. The coverage fraction $f$ is the ratio between the width of the CFD layer and the total width of the tape. It was demonstrated that the $R_i^*$ of CFD REBCO tapes depends on $f$ [87]:

$$R_i^* = \frac{R_i}{(1-f)}\,. \tag{2.7}$$

Typical values of $R_i$ in commercial REBCO tapes, named regular REBCO tapes in this thesis, are around 0.1 $\mu\Omega$.cm$^2$ or less [84]. For CFD tapes fabricated with a coverage fraction of 0.9, the typical value of $R_i^*$ is around 1 $\mu\Omega$.cm$^2$. If $f$ decreases to 0.75, $R_i^*$ is reduced to 0.4 $\mu\Omega.cm^2$. The NZPV is accelerated for high values of $R_i^*$. As a result, the NZPV enhancement of CFD REBCO tapes depends on $f$.

Figure 2.18 shows the calculated NZPV as a function of $I$ for a regular REBCO tape ($f = 0$), a CFD REBCO tape with a low coverage fraction ($f = 0.75$), and a CFD REBCO tape with a high coverage fraction ($f = 0.9$). The NZPV acceleration factor increases from 4 to 7 when $f$ increases from 0.75 to 0.9. The calculations were performed by the Finite element method.

Modifying the regular architecture of REBCO tapes can be achieved in many ways. Figure 2.19 shows four CFD architectures implemented by modifying commercial REBCO tapes. Figure 2.20 reveals the 3D temperature maps obtained from numerical simulations of a regular REBCO tape and three CFD REBCO tapes during a quench propagation initiated at 77 K in self-field.

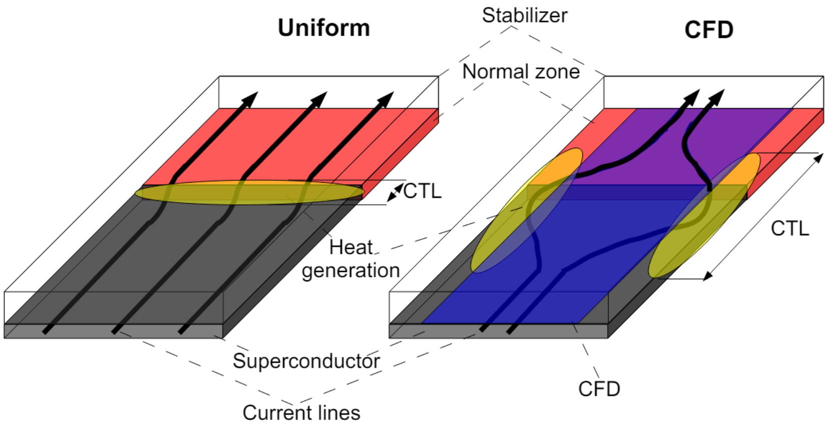

Figure 2.17 Schematic drawing of the current lines during the appearance of a normal zone in the case of i) a uniform architecture (left) and ii) a CFD architecture (right). Image from [10].

### CFD-I and CFD-II architectures

The architecture CFD-I consists in keeping the interfacial resistance between the metallic shunt and the superconductor low on the edges of the tape and high in its center. The current is forced to flow through the edges of the tape, where the interfacial resistance is low, when current transfer occurs. This redirection of the current leads to an increase in the CTL as mentioned above. Heat dissipation occurs on the edges of the tape, unlike in the uniform architecture, where heat is generated along the whole width of the tape (as shown in Figure 2.20(b). The curvature of the heat propagation front along the width of the tape is more pronounced in the case of the CFD-I architecture because of the non-uniform heat propagation. Heat propagates more quickly along the edges of the tape and more slowly in the middle, inducing a more curved front [10, 86].

The architecture CFD-II was proposed in the past, in which the interfacial resistance is kept low along a thin line in the middle of the tape. When there is a quench, the current transfers from the superconducting layer to the metallic layer, through this central line with low interfacial resistance.

### b-CFD architecture

b-CFD refers to buffer-layer-current-flow-diverter. In this architecture, a metallic layer must surround the REBCO tape, and there is no modification of the interfacial resistance between the stabilizer and the REBCO layer. However, this metallic layer should be thin on top of

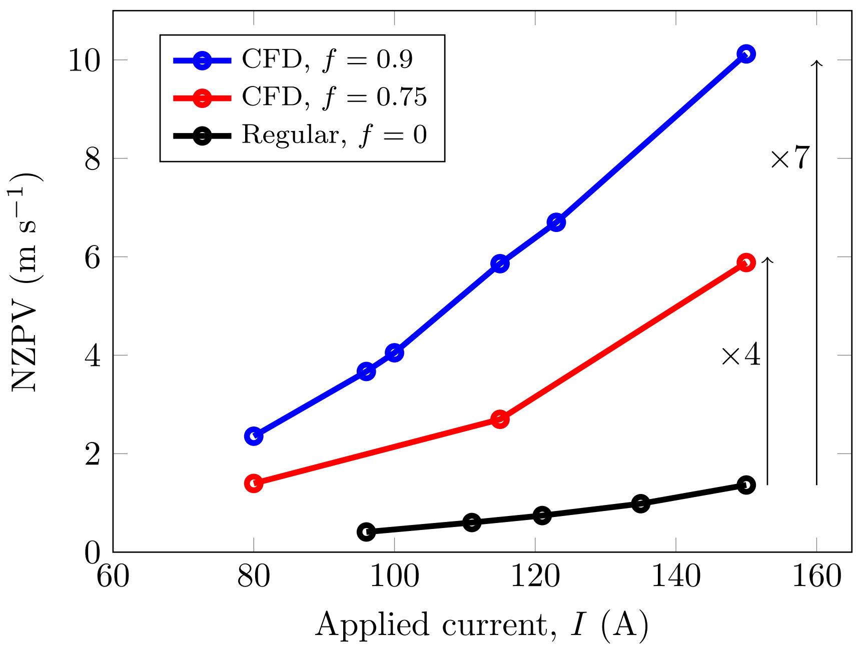

Figure 2.18 Results obtained from numerical simulations of the NZPV as a function of the applied current $I$ for a regular REBCO tape ($f = 0$), a CFD REBCO tape with a low coverage fraction ($f = 0.75$), and a CFD REBCO tape with a high coverage fraction ($f = 0.9$).

the superconducting film and thick on the bottom of the substrate. This geometry forces the current to flow from the top stabilizer to the side metallic layers of the tape surrounding the buffer layers to reach the bottom stabilizer. In Figure 2.20(c), the heat is concentrated along the edges of the tape, making the heat propagation front more curved with sharp edges. Experimental investigations and numerical analysis of the b-CFD architecture were conducted in [88]. It was demonstrated that the b-CFD effect is valid for a low thickness of the top stabilizer. There was no useful improvement for the NZPV when the thickness of the top stabilizer was larger than 1 $\mu$m. However, when the thickness of the top silver layer was between 20 nm and 100 nm, the NZPV was considerably enhanced. Furthermore, the thickness of the bottom stabilizer can be significant in this architecture, which is expected to be useful in magnets to provide additional thermal mass.

### b-CFD-II architecture

This architecture resulted from combining two basic CFD architectures together. The CFD-II and the b-CFD of Figure 2.19 concepts were merged to create the b-CFD-II. In the center of the REBCO/top stabilizer, the interfacial resistance is kept low and high in the remaining

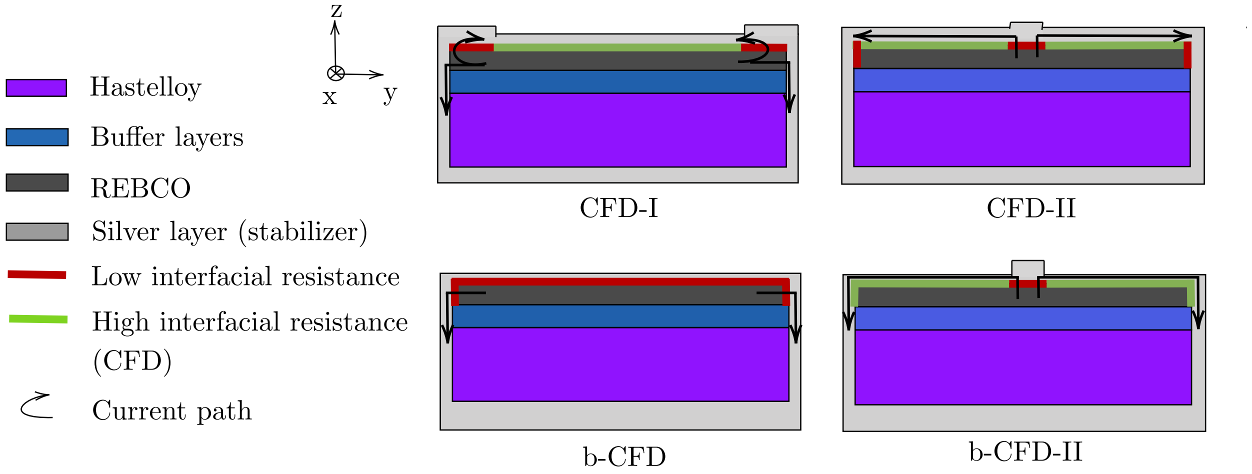

Figure 2.19 CFD architectures integrated into REBCO tapes. Upon a quench, the current (black arrows) is forced to pass through the regions with the lowest interfacial resistance to reach the stabilizer layer.

area. The thickness of the top stabilizer layer is kept thin, except for the low-resistive interfacial line. A thick metal layer is deposited on the substrate side, as in the b-CFD architecture. When a normal zone is created, the current is forced to flow from the center of the tape to the bottom stabilizer, creating a current concentration on the tape centerline. The heat generation is concentrated along the centerline with low interfacial resistivity and propagates towards the edges of the tape, as shown in Figure 2.20(d). The CTL of the b-CFD-II architecture is the highest compared to other CFD architectures. The implementation of this architecture and its impact on the NZPV was evaluated experimentally and numerically in [89]. This architecture can easily increase the NZPV by one order of magnitude compared to the regular REBCO tapes.

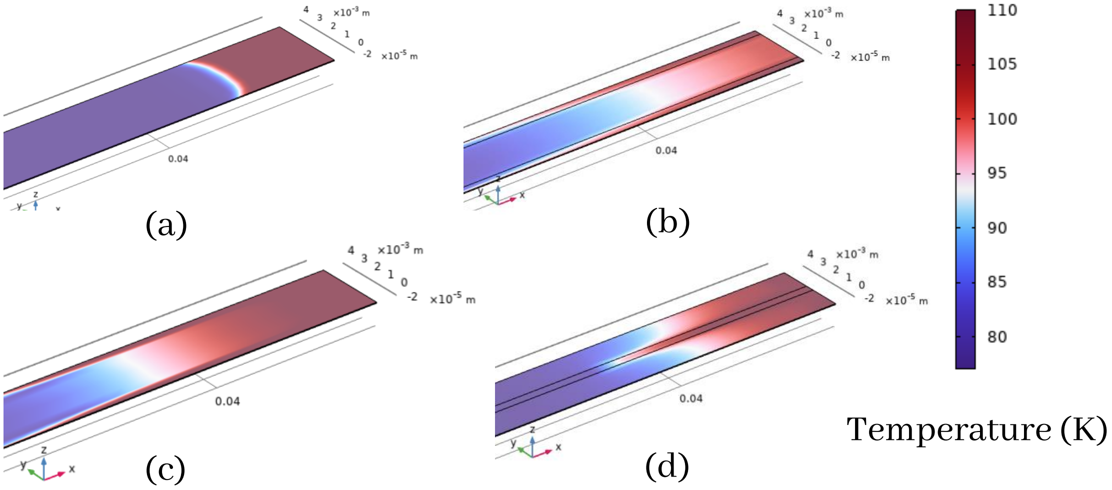

Figure 2.20 3D temperature maps obtained from numerical simulations of REBCO tapes during a normal zone propagation from right to left at 77 K incorporating (a) regular (commercial) architecture, (b) CFD-I architecture, (c) b-CFD architecture, and (d) CFD-II architecture.

# CHAPTER 3 METHODOLOGY

This chapter presents the methodology employed in this thesis to obtain experimental and numerical results discussed in the results chapters. The methodology is subdivided into four sections. The first section describes the microfabrication techniques used to modify the architecture of REBCO conductors. The second section presents the structural characterization techniques employed to perform microstructural observations and elemental analysis. The third section describes the electrical techniques applied to measure several parameters related to REBCO conductors. Finally, the final section of this chapter reports a brief description of the numerical tools used in this thesis.

## 3.1 Microfabrication techniques

### 3.1.1 Chemical etching

The chemical etching is one of the current fabrication steps of the CFD architecture. The silver stabilizer is removed by wet etching to expose the superconducting layer to humidity. In this process, a mixture of hydroxide ammonia ($NH_4OH$) and hydrogen peroxide ($H_2O_2$) diluted in water ($H_2O$) is used as the etching solution with a volume ratio of 1:1:4. The silver reacts with ammonia ions to form a silver diamine complex $[Ag(NH_3)_2]^+$. The etching equation is the following:

$$2\mathrm{Ag} + 4\mathrm{NH_3} + \mathrm{H_2O_2} = 2[\mathrm{Ag(NH_3)_2}]^+ + 2\mathrm{OH}^- \,. \tag{3.1}$$

The etching rate can be increased by increasing the peroxide concentration in the solution. The thickness of the silver layer is between 1 and 3 $\mu$m. A mask is applied to protect the patterns of silver where a low interfacial resistance is needed. The used mask can be an adhesive tape or ink as a liquid mask. The volume ratio of 1:1:4 for $H_2O_2$:$NH_4OH$: $H_2O$ ensures that the etching process does not damage the mask. A high concentration of peroxide can damage the liquid mask (ink). Etching is performed at room temperature. It takes 15 minutes to etch the top silver layer of a one-meter-long REBCO tape.

Figure 3.1 shows an example of a THEVA REBCO tape where a fraction of the top silver layer was etched to expose the REBCO layer.

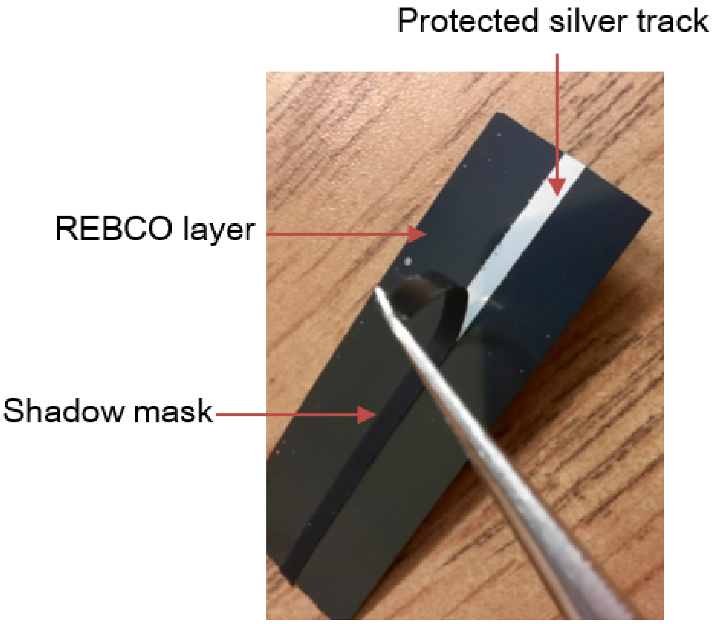

Figure 3.1 THEVA REBCO tape where the top silver layer in the middle of the tape was protected with a mask (adhesive tape os this case), and the remaining area was chemically etched.

### 3.1.2 Magnetron sputtering

In the original fabrication method of the CFD architecture, a thin layer of silver was deposited by sputtering after the chemical etching step described above. Magnetron sputtering is a Physical Vapor Deposition (PVD) technique. In this process, a silver target is bombarded by gaseous ions activated by the presence of plasma, which results in the ejection of the silver atoms from the target. The sputtered atoms cross the distance between the target and the substrate to reach the surface of the substrate. Plasma can be generated by applying a direct current (DC) or Radio Frequency (RF) excitation. A magnetron cathode is used to generate a magnetic field. The magnetic field lines around the magnetron confine the plasma, which increases the density of the plasma close to the substrate. The magnetron operates at low pressure (between 1 and 2 mTorr), which reduces collisions between the sputtered atoms.

The sputtering system used in this thesis is a homemade system installed in the clean room of Polytechnique Montreal. The deposition chamber is connected to a vacuum system to provide low pressure. The value of the pressure is measured by an ionic gauge. A silver target with a diameter of 10.16 cm (4 inches) is used as the source. A rotary sample holder is installed inside the deposition chamber to provide thickness uniformity. The distance between the target and the sample substrate holder is 12.7 cm (5 inches). A DC generator

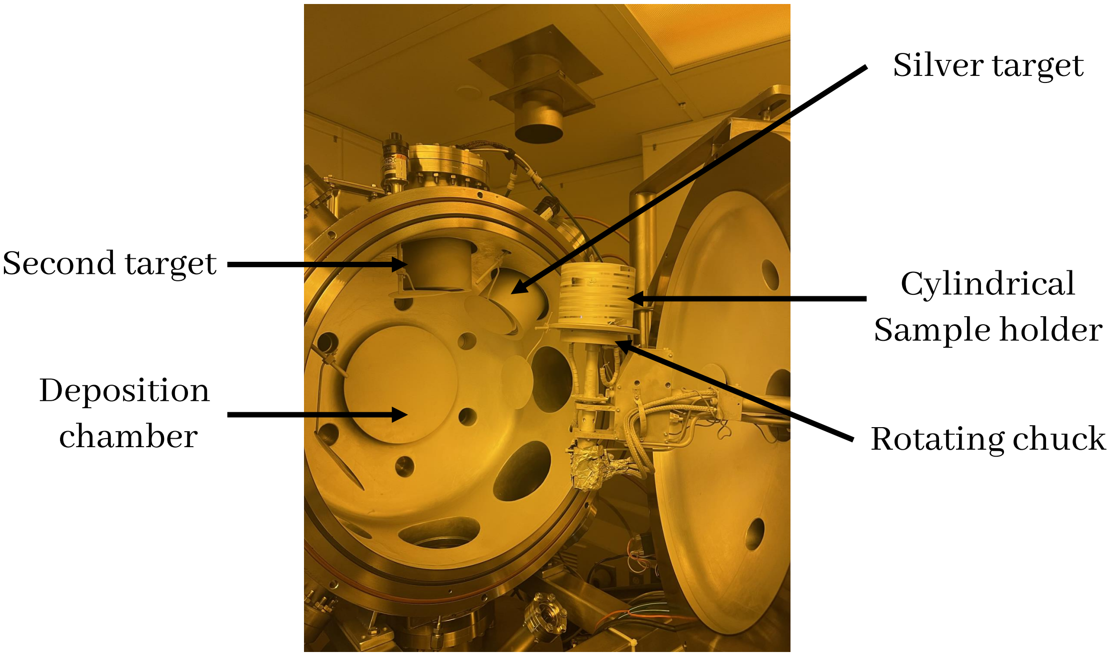

Figure 3.2 The deposition chamber of the magnetron sputtering system.

is used as the excitation source. Silver deposition occurs at a power of 300 watts, a plasma pressure of 10 mTorr, an argon gas flow rate of 15 sccm, which leads to a deposition rate of 4 nm/s. Deposition with an RF source is also possible in this system. However, DC deposition is simpler than RF deposition because there is no reflected power to control. The inside chamber of the sputtering system is presented in Figure 3.2. For short samples, REBCO tapes are fixed on top of a flat disk connected to the rotating chuck. For meter-scale samples, the REBCO tape is wound around a cylindrical sample holder, inserted inside the deposition chamber, and connected to the rotating chuck at 45° with respect to the silver target. The cylindrical sample holder can handle a maximum length of five meters of 4 mm wide REBCO tape.

### 3.1.3 Copper electrodeposition

A copper coating is usually deposited on the silver layer of REBCO tapes to add a stabilizer quench-protecting layer (especially in magnet applications), and to enhance current contacts. The existence of a copper layer enables direct soldering of current leads on the copper stabilizer of REBCO tapes. Soldering on the thin silver stabilizer is indeed risky due to a high probability of critical current degradation [90]. In this work, local or total copper layer deposition was performed using electrodeposition. The electrolyte is prepared using reagent

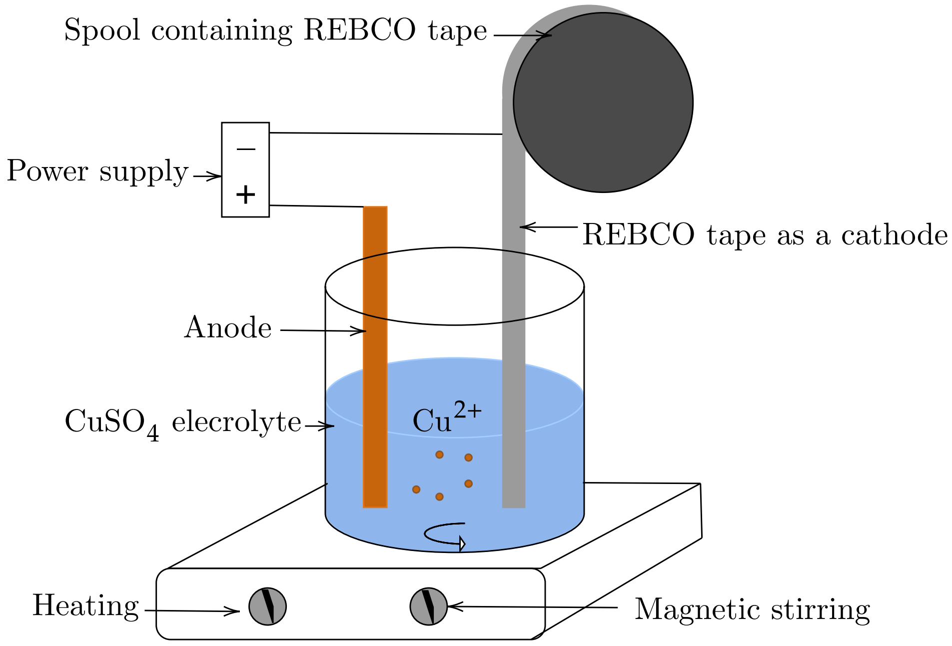

Figure 3.3 The procedure used to electrodeposit copper layers on the REBCO tape endings to serve as current contacts.

grade copper(II) sulfate pentahydrate ($CuSO_45H_2O$). The concentration of this solution is 250 g/L, which is close to the saturation concentration. Thus, dissolving the powder is a time-consuming process that requires stirring to accelerate it. The pH of the solution is acidic and it is adjusted by adding 1 wt% of sulfuric acid ($H_2SO_4$), which enhances the conductivity of the deposited copper layers. The anode is a copper rod. The cathode is the REBCO tape, as shown in Figure 3.3. The solid copper from the anode is oxidized due to the application of a DC current. Following the oxidation reaction, $Cu^{2+}$ ions are reduced to solid copper at the cathode.

To avoid a spongy deposition of the copper layer, the current density must be kept under 50 mA/cm$^2$. In our case, the current density is fixed at 30 mA/cm$^2$ for all our copper depositions. The temperature of the solution is heated between 40 °C and 50 °C. The deposition time is calculated using the following formula:

$$\omega = \frac{M_{\mathrm{Cu}} I \Delta t}{A d_{\mathrm{Cu}} \chi_e \mathcal{F}}\,, \tag{3.2}$$

where $\omega$ is the desired thickness of the copper layer, $M_{\mathrm{Cu}}$ is the molar mass of copper, $d_{\mathrm{Cu}}$ is the volume density of copper, $\Delta t$ stands for the deposition time, $\chi_e$ is the ion charge, $\mathcal{F}$ is the Faraday constant and $A$ is the immersed area in the electrolyte.

### 3.1.4 Oxygen annealing

In the previous chapter, we discussed the importance of oxygen content in REBCO conductors to confer their superconducting properties. Therefore, any annealing REBCO tapes at high temperatures exceeding 200°C must occur in an oxygen atmosphere to avoid critical current degradation [91]. In this thesis, an oxygen annealing was performed after the CFD fabrication process to improve the structural properties of the silver deposited by inkjet printing.

To perform this annealing operation, two setups were used. For long samples (length exceeding 15 cm), a compact vacuum chamber furnace is used and it is presented in Figure 3.4. This furnace contains a quartz tube chamber. The temperature can be controlled through a programmable digital temperature controller. Programmable segments are provided to set the desired temperature profile. The maximal value of the temperature is 1100 °C. Nickel Chromium Aluminum Alloy (Ni-Cr-Al) resistance wires are used as heating elements. The furnace is connected to a turbo pump to create a vacuum. Oxygen gas flow is inserted inside the chamber via a valve. A quartz thermal block is placed at the entrance of the chamber to enhance vacuum efficiency. A digital pressure gauge is installed with the system to measure the pressure of the chamber. To perform annealing, long REBCO tapes are installed around a cylindrical specimen made from Pyrex and pre-cleaned with isopropanol.

For short samples, a second homemade setup is used and it is presented in Figure 3.5. This setup consists of a metallic tube in which we insert the sample to oxygenate. The latter is connected to an oxygen tank. Oxygen flows from the tank through guiding tubes. A Proportional Integral Derivative (PID) regulator is implemented in the Labview software to control the time evolution of the temperature profile. The temperature is measured by a thermocouple installed inside the furnace next to the sample holder. An alternating current (AC) of 120 V is applied to a couple of wires connected to the furnace to provide heating. A mechanical pump is connected to the sample holder to create the vacuum prior to opening the oxygen valve.

For both setups, the ramp-up rate of the temperature is set to 10 °C/min. Slow cooling is controlled digitally and occurs naturally at a rate of -1 °C/min. The maximal dwell duration is one hour.

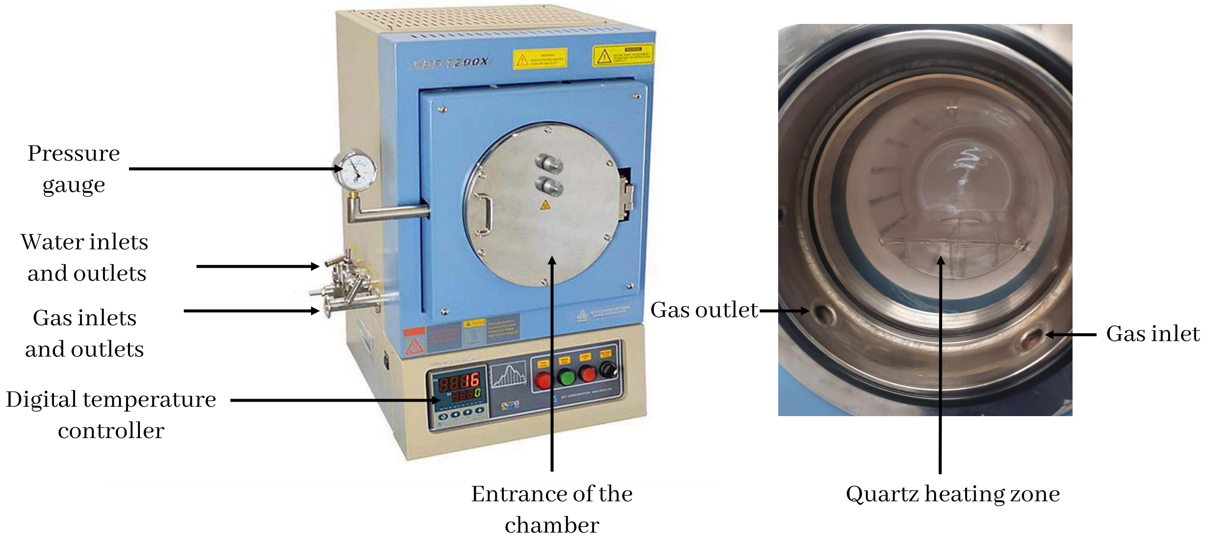

Figure 3.4 Vacuum chamber furnace with heatable quartz chamber used to oxygenate meter-scale REBCO tapes.

### 3.1.5 Drop-on-demand inkjet printing

Drop-on-Demand (DoD) Ink Jet Printing (IJP) is a high-resolution pattern deposition technique that can be used to create conductive patterns on flexible substrates without the need to use masking and/or chemical etching.

Piezoelectric DoD IJP relies on applying a voltage waveform to the piezoelectric transducer to expel ink droplets from the nozzle. The voltage pulse generates a mechanical actuation of the piezoelectric material, which separates the ink into droplets. The expansion of the piezoelectric material creates the required pressure to eject the droplets from the nozzle. The applied voltage pulse controls the velocity and the volume of the ejected droplets. Depending on the interaction of the ink with the surface of the substrate, the single droplets spread on the surface of the substrate and overlap to form a continuous track. The drop spacing, which is the distance between the center of two subsequent droplets, the ink density and velocity, and the substrate roughness and surface energy affect the continuity of the printed track.

Preliminary tests were performed using a Dimatix inkjet printer (DMP-2831) shown in Figure 3.6. The printer contains a 16-jet cartridge that simultaneously contains the ink, acts as a printing head, and moves along the $x$-direction during the printing. This machine has

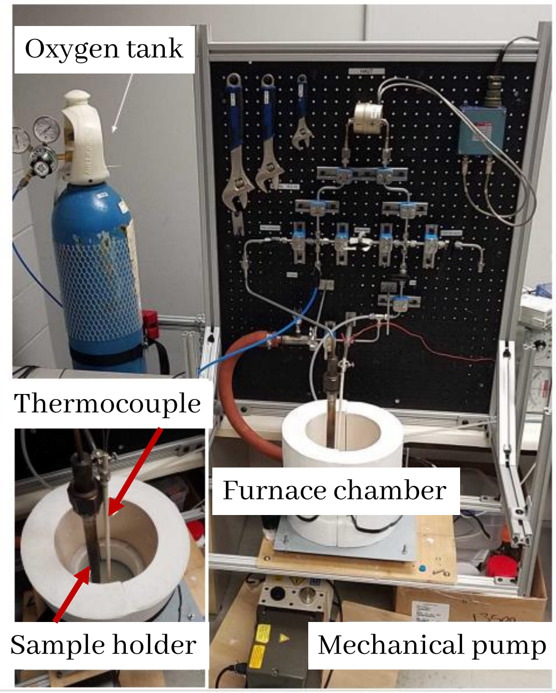

Figure 3.5 Experimental setup of the homemade furnace used to oxygenate lab-scale REBCO tapes (length varying from 1 cm to 15 cm).

a printable area of 200 mm × 300 mm called platen. The DMP-2831 is equipped with a software that enables the adjustment of parameters such as drop spacing, waveform voltage, platen temperature, and cartridge position.

First, we tested four different conductive inks to investigate the effect of the chemical components of the ink on the superconducting properties of the tape. Three inks were purchased from Novacentrix and one ink from MG Chemicals. The inks were chosen following their binder, which controls how good the adhesion on ceramic substrates is. Table 3.1 presents the characteristics of the inks and the measurement of the critical currents of HTS tapes after the ink deposition.

A thin layer of ink was applied after exposing the REBCO surface on top of commercial SuperPower (SP) tapes. Samples were annealed at 400 °C for one hour. The temperature was increased at a rate of 10 °C/min. The dwell duration was one hour. Cooling occurred naturally at a rate of -1 °C/min.

The average critical current of commercial SP tapes used in these tests at 77 K and in self-field is 147 A±8. The average critical current of commercial SP tapes used in these tests at 77 K and in self-field is 147 A±8. The measurement of the critical current shown

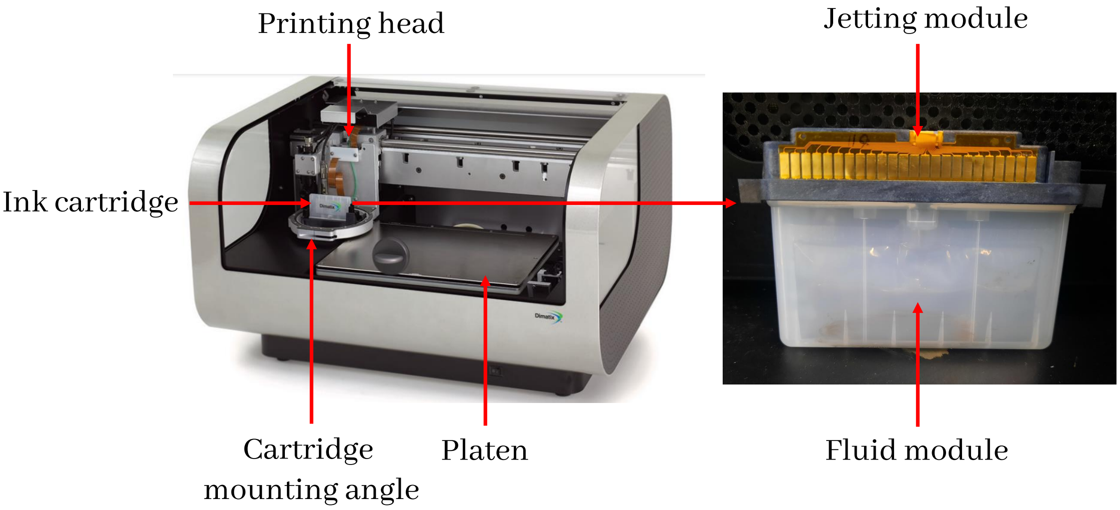

Figure 3.6 Dimatix DMP2831 inkjet printer (on the left). Image from [92]. Dimatix 16-jet cartridge (on the right).

in Table 3.1 revealed that there was a total critical current degradation upon using the Novacentrix JS-211 conductive ink and preservation of the superconducting properties with the other inks. Following these results, we assumed that this degradation is probably due to the fluorine content in the binder of the Novacentrix JS-211 ink. Furthermore, the MG Chemicals 842AR-P silver ink had to be excluded because its viscosity was not suitable for this IJP setup. Therefore, the Novacentrix JS-A291 conductive ink was the only suitable ink for printing patterns on the REBCO surface, as it had no fluorine in its binder and its viscosity was low enough.

Table 3.1 Effect of commercial conductive inks on the critical current of a SuperPower REBCO tape.

| Tested inks | Novacentrix JS-A291 | Novacentrix JS-211 | MG Chemicals 842AR-P |
|---|---|---|---|
| Binder | Polyurethane | Fluoropolymer | Acrylic adhesive |
| Viscosity (cP) | 8-12 | 8-12 | 1060 |
| Adhesion | 5B | 5B | 5B |
| $I_c$ 77 K and in self-field (A) | 145 | 0 | 151 |

## 3.2 Structural characterization techniques

### 3.2.1 Focused ion beam

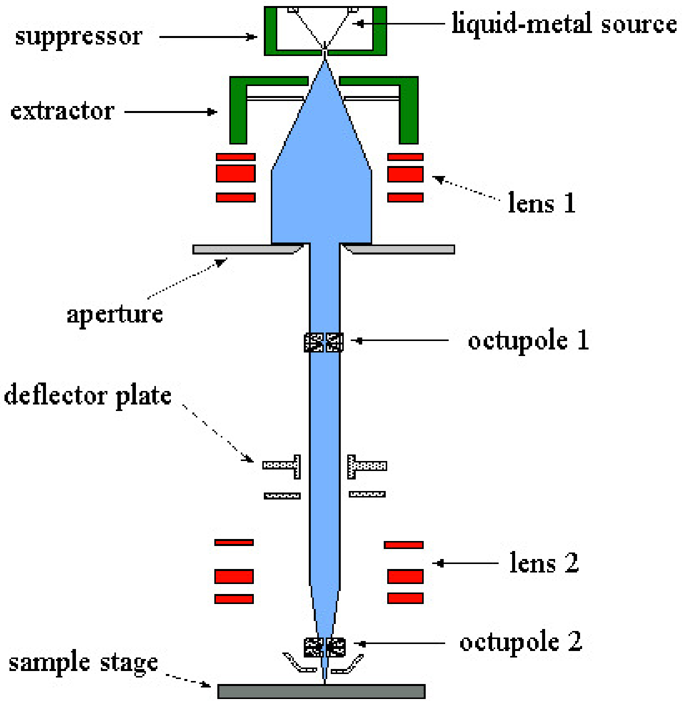

Figure 3.7 Schematic of a Focused Ion Beam (FIB) system. Image from [93].

Focused Ion Beam (FIB) is a multifunctional technique that can be used for the fabrication of certain patterns, for cross-sectional imaging, and for the removal or deposition of materials. The FIB instrument is equipped with an ion column, a Liquid Metal Ion Source (LMIS), and a tungsten (W) needle. Figure 3.7 illustrates a common schematic of the FIB system. When an electric field is applied to the LMIS, metal ions are generated. Gallium is commonly used as a metal source because of its high mass and low melting temperature ($T_m$ = 29.80 °C). The gallium ions ($Ga^{2+}$) are accelerated in the ion column to an energy varying from 1 to 30 keV. Electrostatic lenses are installed inside the ion column to focus the ion beam. The imaging resolution increases when the diameter of the beam is decreased. Subsequently, the focused beam is deflected using beam deflection coils. A 4 mm × 4 mm section of the sample is mounted in the sample holder using double-sided adhesive carbon tape. The sample holder is then inserted in a vacuum chamber connected to the ion column.

The interaction of the beam and the surface of the sample results in different processes depending on the beam current. At low beam currents, secondary electrons (SE) are emitted from the sample due to the ion beam scattering. The latter is used to produce images. When the beam current is increased, the ion-matter interaction induces the removal of matter from the surface of the sample. This feature allows the creation of 3D patterns by high-resolution milling into the sample.

Furthermore, the deposition of certain coatings is available in the FIB setup. The LMIS is connected to the tungsten needle mentioned above. A flow of the precursor gas in the chamber of the FIB system promotes the chemical vapor deposition of tungsten. Tungsten coating is used as a protective layer against undesired sputtering and charge build-up for insulating materials during scanning electron microscopy. In this work, the FIB cross-section cuts were created using a Hitachi FIB-2000A.

### 3.2.2 Scanning electron microscopy

Scanning Electron Microscopy (SEM) is a high-resolution imaging technique. The principle of imaging is similar to FIB (see Figure 3.8. However, a focused beam of electrons is used to scan the substrate instead of an ion beam. The SEM instrument is equipped with an electron gun that generates electrons. The beam of electrons is accelerated and focused using magnetic lenses. In the case of an electron beam, magnetic lenses are used instead of electrostatic ones because electrons are light particles. The imaging operation occurs in a vacuum chamber. The interaction of the electron beam and the matter produces different signals: secondary electrons (SE), backscattered electrons (BSE), characteristic X-rays, Auger electrons, and light (cathodoluminescence). Commonly, SE and BSE detectors are installed within the SEM instrumentation for imaging. SE imaging provides information about the morphology and the topology of the observed sample. BSE imaging displays the contrast in the composition. Additional detectors can be installed to obtain different data. The SEM images presented in this work were acquired using JEOL JSM-7600TFE field emission scanning electron microscope [93].

### 3.2.3 Energy dispersive spectroscopy

In the section describing the SEM instrument, we mentioned that an electron beam-matter interaction results in the emission of X-rays. The detection of the emitted X-rays enables qualitative and quantitative analysis of the scattered samples. Atoms of the samples are ionized when they are bombarded by electrons. This ionization leads to hole generation in the inner shells of the atom. Electrons from the outer shell transit to the inner shells to fill these vacancies. This process releases radiation energy. Each shell-to-shell transition has a specific X-ray line. The first inner shell (n = 1) is named by the letter K. The following shells

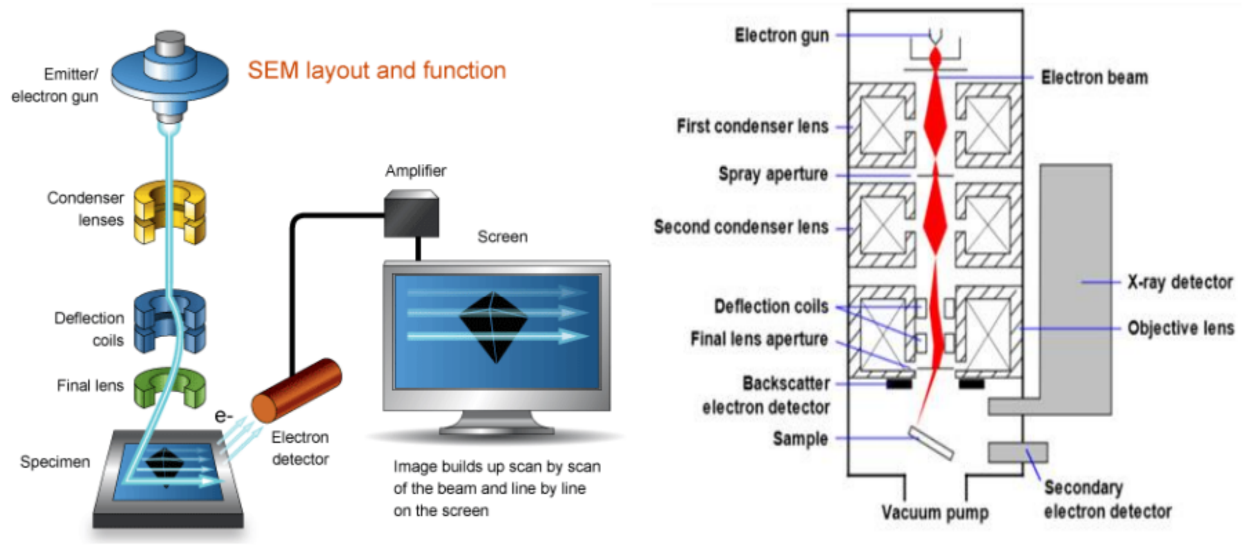

Figure 3.8 Schematic of the layout of a scanning electron microscope system (SEM). Image from [93].

are named L (n = 2) and M (n = 3) etc. A Greek letter specifies the size of the transition. For example, $L_\alpha$ corresponds to a transition from the M-shell to the L-shell. $K_\beta$ stands for a transition from the M-shell to the K-shell, etc.

An Energy Dispersive Spectroscopy (EDS) detector can be installed on the SEM or Transmission Electron Microscopy (TEM). It is composed of a collimator that collects the generated X-rays, an electron trap to prevent electrons from reaching the detector, and a semiconductor crystal. The SEM instrument used in this research work is equipped with Oxford Instruments' EDS detector.

## 3.3 Electrical measurements

### 3.3.1 Critical current and NZPV measurements

To determine the critical current ($I_c$) of REBCO tapes, a homemade setup was developed in the Laboratory of Superconductivity and Magnetism (LSM) of Polytechnique Montreal, which enables voltage measurements as a function of an applied pulsed current. This setup includes mainly two supercapacitors with a capacitance of 83 Farads each, a DC power supply, a shunt resistance of 500 $\mu\Omega$, and a current amplifier controlled by the Labview software.

First, the supercapacitors must be charged with the power supply. For the current injection in a sample, the supercapacitors are discharged through the current amplifier, which

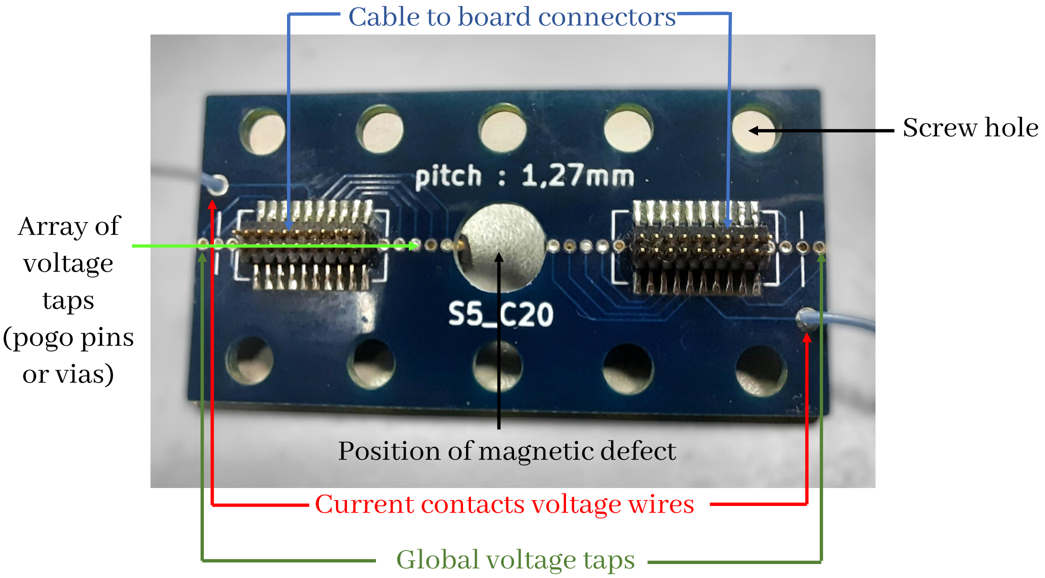

Figure 3.9 Custom printed circuit board used to measure the NZPV of REBCO tapes.

contains MOSFET transistors connected in parallel and 16 canals connected to four relays. A maximum current amplitude of 120 A can be applied through each canal, meaning that the maximal applied current delivered by the amplifier is 1960 A. The waveform of the current pulse and its duration can be modified in the Labview software. We use square current pulses with a ramp-up rate of 975 A/ms. The pulse duration can be varied from 1 to 1000 ms with some restrictions at high current values. The use of current pulses instead of DC current allows performing non-destructive quench measurements of REBCO tapes even in high currents because it limits the amount of energy injected in the sample during the experiment.

To perform the critical current measurements, the REBCO tape is fixed on a sample holder and connected to two rectangular copper blocks for current injection. A custom-made Printed Circuit Board (PCB) with an array of pogo pins or vias acting as voltage taps, is installed on top of the sample for voltage measurements. An example of a PCB that has been used during measurements is presented in Figure 3.9. The connections between the PCB, the REBCO tape, the current contacts, and the components of the electric circuit are presented in Figure 3.10.

The data is recorded through a rerouting PCB into the Labview software. Two different modes can be adapted when performing the measurements depending on the used PCB, whether it contains 40 or 80 pogo pins. Several PCBs are available at the LSM, with different lengths ranging from 2 to 74 cm and different pogo pin arrays, to perform measurements at

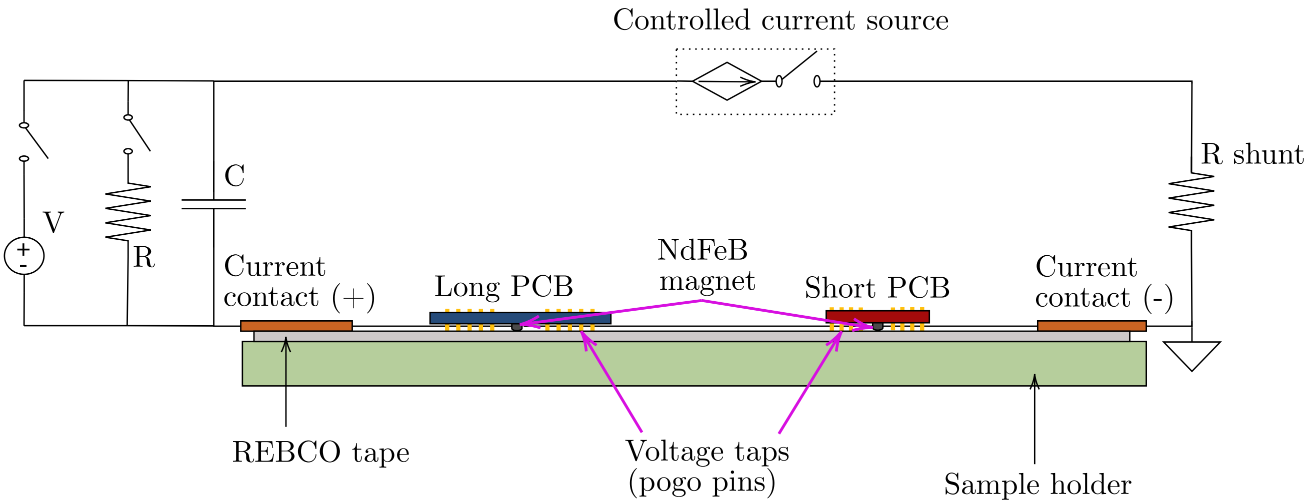

Figure 3.10 Schematic of the electric circuit that connects the pulsed current source to the capacitor (C), the shunt resistance, the copper current contacts, the PCB, and the REBCO tape.

different spatial resolutions, depending on the needs and the dimensions of the samples. The $I_c$ and the $n$-factor are determined by fitting the experimental data of the voltage ($V$) as a function of the applied current into a power law:

$$E = E_c \left( \frac{I}{I_c} \right)^n , \tag{3.3}$$

where $E = V/L$, $E_c$ is the electric field criterion of 1 $\mu$V/cm, and $L$ is the length of the measured sample. Thus, the $E$-$I$ curve of the measured REBCO tape is obtained after performing this measurement. An example of an $E$-$I$ curve of a commercial SuperPower REBCO tape is plotted in Figure 3.11. Following the data processing, an $I_c$ of 119 A and an $n$-factor of 25 were obtained.

For NZPV measurements, a local reduction of the critical current, which we shall call ”defect” in this thesis, is artificially created in the middle of the sample to induce quench propagation. In the literature, heaters have been used to create local defects [94,95]. Mechanical defects can also be created by bending or cutting the tape to induce a normal zone [96]. In this setup, we use NdFeB magnets to create a local reduction in the critical current of the REBCO tape. The

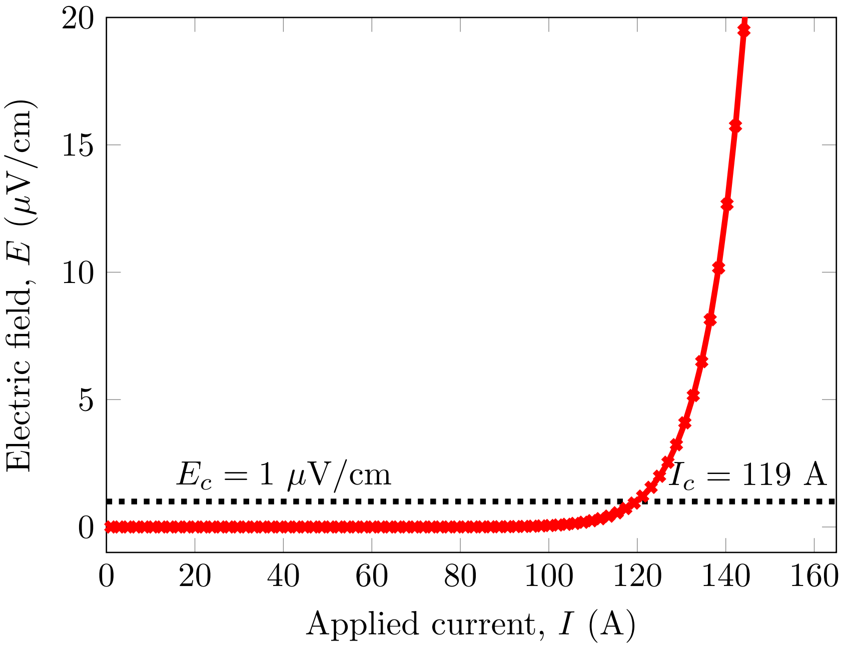

Figure 3.11 $E$-$I$ curve obtained from measuring the voltage as a function of current pulses of SP REBCO tape. The dotted black line represents the $E_c$ value. The $I_c$ and the $n$-factor are determined from a linear fit of the $E$-$I$ data on a logarithmic scale. In this case, the obtained $I_c$ was 119 A and the $n$-factor was 25.

local critical current reduction depends on the size of the magnet and the distance between the magnet and the tape. The advantage of using magnets is that it is a non-destructive method and the critical current of the defect can be monitored. When the current is injected in the tape, the defective zone generates a normal zone that propagates symmetrically on the left and on the right of the magnet location. Different amplitudes of current pulses are applied to the sample to obtain the variation of the NZPV as a function of the applied current. The propagation of the quench generates an electrical potential difference between the pogo pins. The generated voltage across the pogo pins is measured as a function of time during the whole pulse duration.

Figure 3.12 reveals the quench resistance ($R_i$, $i$ =1...5) measured by five pairs of pogo pins adjacent to the magnet location as a function of the pulse duration for an applied current of 93 A for 16 ms. The dotted black line refers to a resistance criterion ($R_c$) used to determine the NZPV. The value of the NZPV is calculated by dividing the distance between the pogo pins (pitch) and their time ($\Delta t$) between two points equal to a voltage or a resistance criterion as shown in the following equation:

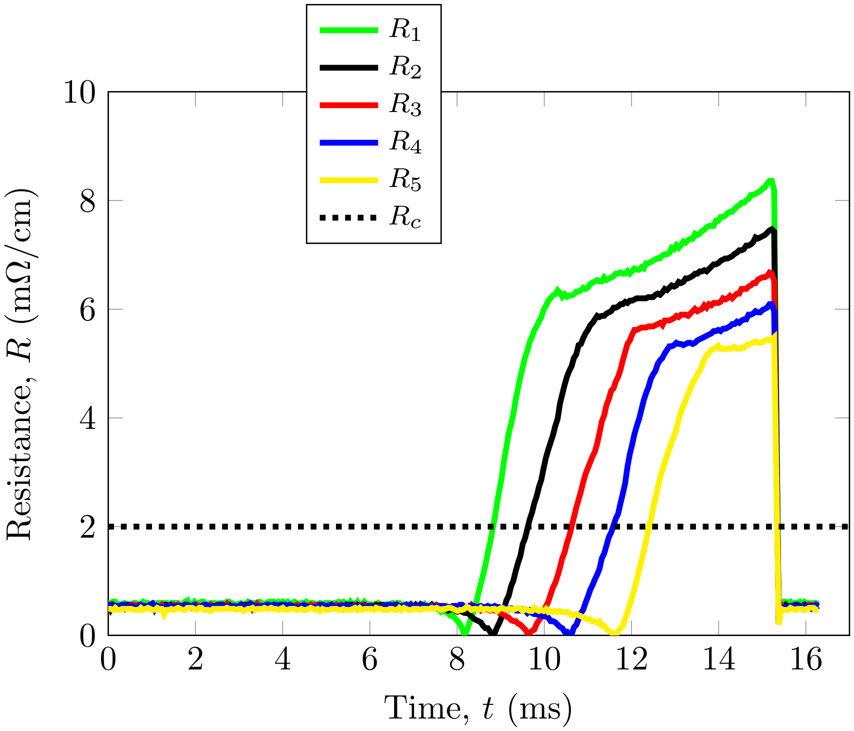

Figure 3.12 Resistance results obtained from NZPV measurement on a SP REBCO tape. $R_i$ ($i = 1,2...5$) corresponds to the measured voltage divided by the applied current at each point in time during the pulse. The dotted black line corresponds to the resistance criterion $R_c = 2$ mΩ/cm.

$$\text{NZPV(m/s)} = \frac{\text{pitch (m)}}{\Delta t \text{ (s)}} \,. \tag{3.4}$$

### 3.3.2 Resistance versus temperature measurements

The measurement of the electrical resistance ($R$) of REBCO tape as a function of the temperature provides experimental data used to determine the $T_c$ value of the measured sample. The experiment consists of a four-probe resistance measurement performed in a liquid nitrogen bath.

Figure 3.13 shows a REBCO tape installed in the sample holder with four probes connected on top of the sample. A Keithley 6221 DC current source is connected to probes 1 and 4 to inject a current into the tape. A Keithley 2182A nanovoltmeter is connected to probes 2 and 3 to record the voltage continuously. A Lakeshore 331 cryogenic temperature controller is connected to a PT1000 temperature sensor to measure and record the temperature. The

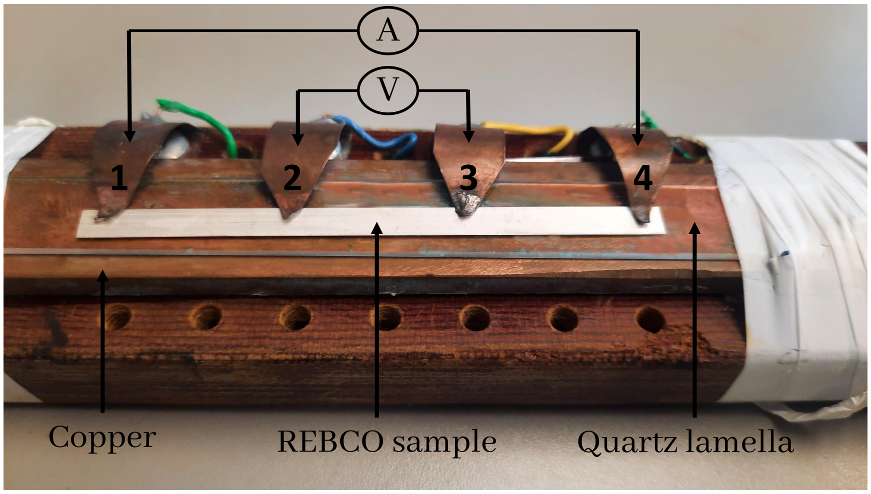

Figure 3.13 Four-probe measurement setup of HTS tape resistance as a function of temperature (77 K to room temperature).

sample is installed on a quartz lamella placed on top of a copper bar to equalize the temperature fluctuation across the sample. The delta method is used for the applied current [97]. The value of the applied current is periodically alternated between -100 mA and 100 mA during the experiment. The experiment lasts until the total natural evaporation of the liquid nitrogen and then until the temperature of the sample is at room temperature. The sample holder is inserted in a styrofoam enclosure to slow down the evaporation of liquid nitrogen and the temperature variation between 77 K and 285 K.

Figure 3.14 illustrates the temperature dependence of the resistance of a commercial SP REBCO tape. The blue circles are the experimental data obtained using the setup presented in Figure 3.13. The $T_c$ of the measured sample is 93 K. When $T < T_c$, the measured resistance of the sample is almost zero. A sharp transition of $R$ takes place around $T = T_c$. Focusing on the region where the resistance starts rising sharply, the value of $T_c$ is defined as the temperature at which the resistance becomes no longer zero.

## 3.4 FEM modeling

In this thesis, we applied the Finite Element Modeling (FEM) approach to study the nonlinear electrothermal behavior of REBCO tapes. FEM modeling takes into account the geometrical layout of REBCO tapes allowing, solving the current density and the temperature over their different layers. The COMSOL Multiphysics 5.6 software was used to perform the numerical simulations of REBCO tapes. The thermal and electrical physics of REBCO

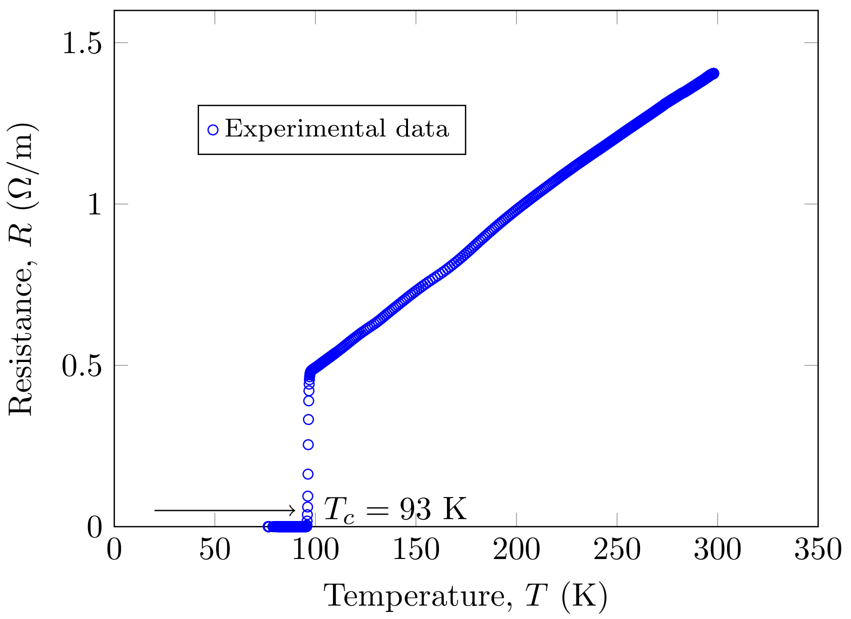

Figure 3.14 Temperature ($T$) dependence of the resistance ($R$) of a SP REBCO tape.

conductors are coupled through the Joule Heating interface implemented in COMSOL Multiphysics. Further details of FEM modeling are presented in the results chapters.

## 3.5 Article coherence with research objectives

This thesis comprises 3 papers whose coherence with the thesis is explained below.

**Article 1** - The first article addresses an important part of the main objective of this thesis and represents a direct realization of the first objective, which concerns the fabrication of long-length REBCO conductors with CFD architecture. In this article, we present results concerning the NZPV of meter-scale CFD REBCO tapes with a current flow diverter architecture, and we describe their manufacturing approach.

**Article 2** - The second article describes an alternative route to fabricate REBCO tapes with the CFD architecture without the need for any masking or chemical etching, which promptly addresses the second objective of this thesis regarding the development of an alternative low-cost manufacturing process for the CFD architecture.

**Article 3** - The third article focuses on the development of high-current REBCO cables with the CFD architecture, which represents a significant part of the third objective of this research work, which consists in evaluating the performance and the feasibility of the CFD architecture in a cable layout based on CFD REBCO conductors.

# CHAPTER 4 ARTICLE 1 - METER-SCALE REBCO TAPES WITH A CURRENT FLOW DIVERTER ARCHITECTURE

*Authors: Haïfa Ben Saâd, Delano Horn-Bourque, Simon-Mathieu Bergeron Hartman, Hamza Errabie, Christian Lacroix, and Frédéric Sirois*

This article was submitted to the journal IEEE Transactions on Applied Superconductivity on June 3rd, 2024

## 4.1 Abstract

The current flow diverter architecture (CFD) allows increasing the normal zone propagation velocity (NZPV) of rare-earth barium copper oxide (REBCO) tapes. A continuous reel-to-reel CFD fabrication process has been developed to produce high-quality long CFD REBCO tapes. Using this reel-to-reel process, meter-scale CFD REBCO tapes, precisely 74 to 100 cm long tapes, were produced. Standard scratch tests showed that the adhesion strengths of a silver layer of a regular commercial tape and an annealed CFD tape are similar while being slightly lower in the case of a non-annealed CFD tape. Experimental measurements revealed an increase in the NZPV by a factor of 6 to 22 with respect to regular tapes (depending on the CFD architecture), which is comparable to previous results obtained on short-length CFD tapes (12 cm). A detailed analysis combining optical microscopy and numerical simulations revealed that the reel-to-reel CFD fabrication minimizes geometrical imperfections, which results in a good NZPV uniformity over long lengths. This demonstration of the effectiveness of the CFD concept in long-length CFD tapes represents an important step toward the potential development of a safe and more reliable protection scheme in high-field magnets and other high-current-carrying REBCO-based devices.

## 4.2 Introduction

Second-generation (2G) High-Temperature Superconductors (HTS) Coated Conductors (CCs), also called REBCO tapes, where REBCO stands for Rare-Earth Barium Copper Oxides, have emerged as promising candidates to fabricate superconducting magnets that generate strong static magnetic fields above 20 T [98]. Additionally, their very high critical current density, high thermal stability, and mechanical properties open up several other possible applications such as fault current limiters, compact motors and generators, and magnetic energy storage [6, 99–102].

However, the expansion rate of the normal zone upon a quench, also called normal zone propagation velocity (NZPV), is low in REBCO tapes (order of cm/s), which represents a challenge for the safe operation of superconducting devices, such as high-field magnets. Furthermore, commercial REBCO tapes are known to have a non-uniform critical current ($I_c$) along their length (approximately ±20% of variation with respect to its average). This combination of inhomogeneous $I_c$ and low NZPV significantly increases the risk that a hot spot reaches a very high temperature before the appearance of a voltage that can be detected by a protection system, which makes superconducting devices prone to irreversible damages in case of a quench [9, 69, 78, 103, 104].

One way envisioned to enhance quench protection systems in superconducting devices based on REBCO tapes is to increase the NZPV of the tapes [69, 80]. This is possible with the Current Flow Diverter (CFD) concept, which refers to the deviation of the current path between the superconducting layer and the metallic stabilizer to circumvent a quenched region of the REBCO layer. The CFD can be implemented by integrating a localized high electrical resistance between the REBCO layer and the stabilizer or by using the buffer layers (see [10, 86, 88, 89, 105] for details). So far, the CFD concept has been proved experimentally on short REBCO tapes having a maximum length of 12 cm. To investigate the performance of the CFD concept for rapid quench detection in high-field devices, it is required to manufacture long-length CFD-REBCO tapes, which we shall call simply CFD tapes further on.

This paper presents results on meter-scale CFD tapes, which we shall call "long" samples, fabricated by a reel-to-reel process. To compare the quality of the tapes processed with our reel-to-reel setup, additional long CFD tapes were fabricated with the manual technique used previously [86]. A total of three long CFD tapes were fabricated, one with the reel-to-reel process and two with the manual technique. The adhesion strength of the silver layer on the CFD layer was investigated using scratch tests. NZPV measurements on the long CFD tapes were performed and are reported. Finally, a 3-D electro-thermal model based on the finite element method (FEM) was used to quantify the impact of geometrical imperfections of the CFD layer on the uniformity of the NZPV along the length.

## 4.3 Experimental procedure

### 4.3.1 Reel-to-Reel CFD fabrication process

An automated reel-to-reel system was implemented to produce long CFD tapes. The system allows the integration of the CFD in commercial REBCO tapes with high precision over meters of length of REBCO tapes, guaranteeing a high and uniform NZPV. The fabrica-

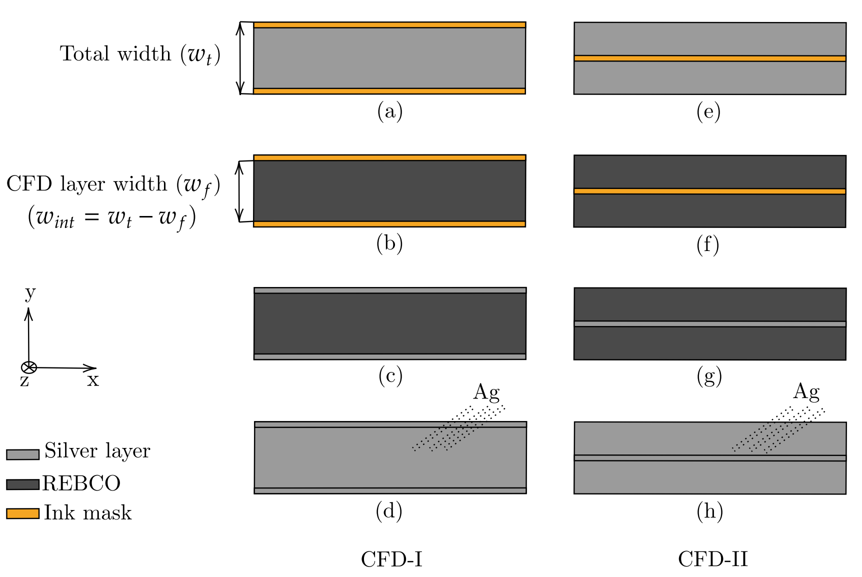

Figure 4.1 Schematic representation of the fabrication steps required to obtain the CFD-I and CFD-II architectures (top view of the tape): (a),(e) application of a mask; (b),(f) chemical etching of silver; (c),(g) removal of the mask; (d),(h) deposition of silver by sputtering. The total width ($w_t$) of the tape is indicated in (a). The CFD layer width ($w_f$) is indicated in (b). The difference between $w_t$ and $w_f$, corresponding to $w_{int}$ (yellow part), is the portion of the width where the interfacial resistance between the REBCO layer and the silver layer is low.

tion process is composed of four steps: 1) masking, 2) chemical etching, 3) mask removal, and 4) silver deposition, as presented in Figure 4.1. Two CFD architectures can be fabricated: the CFD-I architecture (Figure 4.1(a), (b), (c) and (d)) and the CFD-II architecture (Figure 4.1(e), (f), (g), and (h)).

The masking step (Figure 4.1(a) and (e)) involves applying a thin ink coating on the silver where a low interfacial resistance is required between the REBCO layer and the silver layer. Figure 4.2 shows the reel-to-reel setup used to deposit the mask on the silver layer. A commercial REBCO tape is wound on the source spool. The target spool is positioned at the same height as the source spool. A guide is installed between both spools to align the tape as it is transferred from the source to the target spool. DC stepper motors are attached to both spools and controlled by a software, which allows setting the rotation speed of the spools. An ink dispenser with a small nozzle is placed on top of the guide. One or several ink lines can be deposited on the REBCO tape. In the case of the CFD-I architecture, the ink mask is applied on both edges of the tape, as shown in Figure 4.1(a). For the CFD-II architecture, the ink mask is applied in the middle of the tape, as shown in Figure 4.1(e).

The masking speed can be varied depending on the needs and was set to 11 cm/min for the fabrication of the long CFD tapes presented in this work.

Figure 4.3 shows the chemical etching reel-to-reel setup. In addition to the source and target spools, it contains five small spools to guide the tape in a bath containing the etching chemicals, and then in a bath containing deionized water. The chemical etching of silver is done using an aqueous solution of peroxide ($H_2O_2$), ammonium hydroxide ($NH_4OH$), and water with a 1:1:4 dilution ratio. Once the etching process is completed, the etching bath is replaced with an ultrasonic bath containing an isopropanol solution to remove the ink mask. Following all these steps, the tape is dried with compressed air and installed on a cylindrical sample holder made of aluminum. This aluminum cylinder is then inserted in a magnetron sputtering chamber for the final silver deposition, as shown in Figure 4.4.

### 4.3.2 Characteristics of CFD tape samples

In this work, REBCO tapes from three different manufacturers were used, namely SuperPower Inc. (SP), THEVA Dünnschichttechnik GmbH, and Superconductor Technologies Inc. (STI).

The SP tapes comprised a 4 mm wide Hastelloy substrate (C-276$^{\text{TM}}$), a stack of buffer layers, and a GdBaCuO layer grown by metalorganic chemical vapor deposition. A thin surrounding layer of silver completes the tape architecture [34]. The THEVA tapes comprised a 12 mm wide Hastelloy substrate (C-276$^{\text{TM}}$) on which a first MgO buffer layer was deposited for the texturization, and a second MgO buffer layer was deposited prior to the growth of the GdBaCuO layer. After the growth of the GdBaCuO layer, a silver coating surrounding the whole tape was deposited [30]. The layering of STI tapes consisted of a 4 mm wide Hastelloy substrate (C-276$^{\text{TM}}$) with a stack of buffer layers of different thin films composed of $CeO_2/[Y+Zr]_2O_3/MgO$ grown on the substrate. A GdBaCuO layer was grown by a reactive co-evaporation by cyclic deposition and reaction deposition technique (RCE-CDR). Then, a metallic silver stabilizer was deposited on the GdBaCuO layer only (no silver on the bottom of the substrate) [45].

A one-meter-long SP tape was modified using the automated reel-to-reel CFD fabrication process to obtain the CFD-II architecture (see Figure 4.5(c)). To demonstrate the benefits of the automated reel-to-reel system on the NZPV uniformity, two additional CFD samples, one THEVA sample, and one STI sample were fabricated using the manual technique described in [86] (see Figure 4.5(a) and (b)). The dimensions and critical current of the SP, THEVA and STI samples after the integration of the CFD are presented in Tab. 4.1.

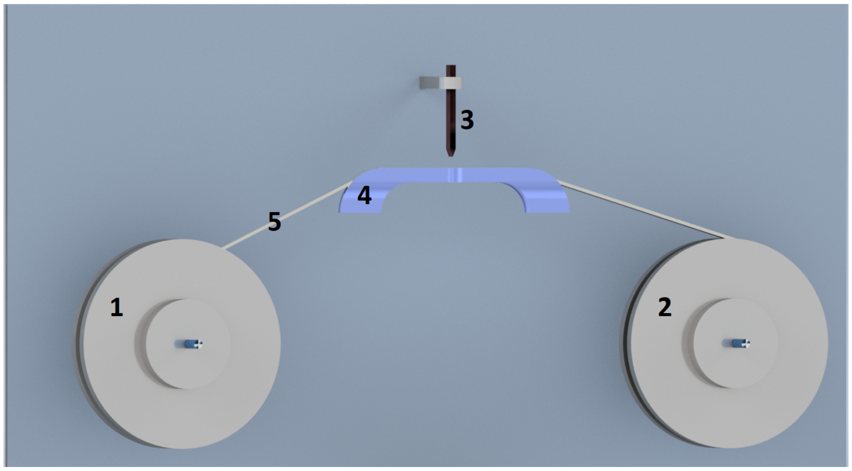

Figure 4.2 Automated reel-to-reel masking system: 1) source spool, 2) target spool, 3) ink dispenser, 4) guide, and 5) REBCO tape.

Table 4.1 Key dimensions and critical current of REBCO tapes from three manufacturers after the integration of the CFD.

| **Manufacturer** | **SP** | **THEVA** | **STI** |
|---|---|---|---|
| Substrate thickness ($\mu$m) | 50 | 97 | 50 |
| Buffer layers thickness ($\mu$m) | 0.2 | 3.1 | 0.58-0.78 |
| REBCO layer thickness ($\mu$m) | 1.6 | 3.1 | 0.8 |
| Total silver thickness ($\mu$m) | 1.3 surrounding | 2 surrounding | 2 on top |
| Width (mm) | 4 | 12 | 4 |
| Length (cm) | 100 | 74 | 74 |
| Critical current at 77 K (A) | 145 | 756 | 94 |

### 4.3.3 Samples characterization

In order to evaluate the adhesion strength of the silver layer, scratch tests at room temperature were performed using an NST$^3$ Nano scratch tester from Anton Paar [106]. A 10 $\mu$m radius diamond tip was used, the length of the scan was fixed to 1 mm, and the applied load was increased from 0.1 to 119.2 mN at a speed of 2 mm/min. The setup was equipped with a software that records microscopic observations, full panoramic images, the scratch depth, and the applied normal force as a function of the scan position, which provides data about the critical loads. More details about the scratch test interpretations are available in [107].

The scratches were further analyzed using a JOEL7600TFE scanning electron microscope (SEM) [108] equipped with an energy-dispersive detector (EDS) to identify the chemical composition of the observed debris. The acceleration voltage used was 5 kV, and the working

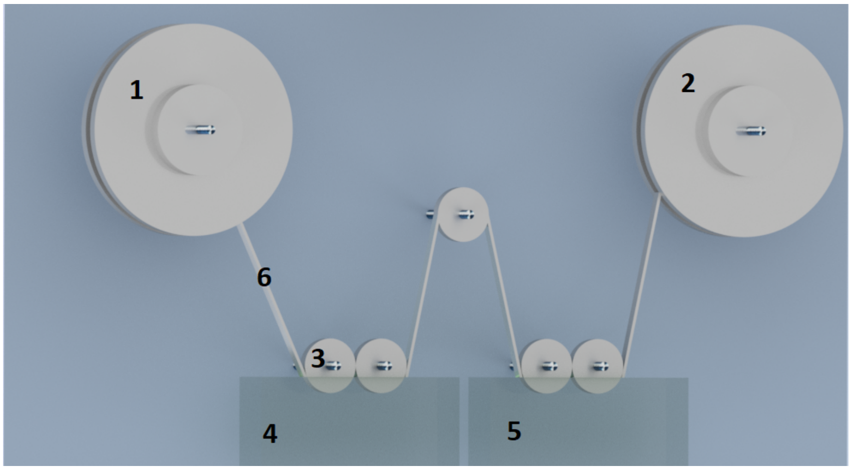

Figure 4.3 Automated reel-to-reel silver etching system: 1) source spool, 2) target spool, 3) guiding spool, 4) chemical etching bath, 5) rinsing bath, and 6) REBCO tape.

distance was approximately 15 mm. The EDS data were recorded and analyzed using the AZtec software provided by Oxford Instruments.

### 4.3.4 NZPV measurements

A homemade setup was used to measure the NZPV. This setup includes a pulsed current source that generates current pulses of constant amplitude. All electrical measurements were carried out in a liquid nitrogen bath at ambient pressure. A small NdFeB permanent magnet was used to create a local defect to initiate the quench. Upon quench initiation, the normal zone expanded on both sides of the tape with respect to the magnet position. Custom PCB-based supports with pogo pins were used to measure the voltage that rises when the normal zone propagates along the length of the tape. The NZPV was calculated by dividing the distance between two adjacent voltage probes by the corresponding time period needed to achieve a given electric field criterion. Local NZPV measurements were performed on different portions of the sample. Further details about this measurement setup can be found in [86, 89].

## 4.4 Results

### 4.4.1 Adhesion strength of the CFD layer

In a commercial fabrication process, an oxygen annealing treatment of the REBCO tape is performed after the silver deposition, whereas in the fabrication process of CFD REBCO

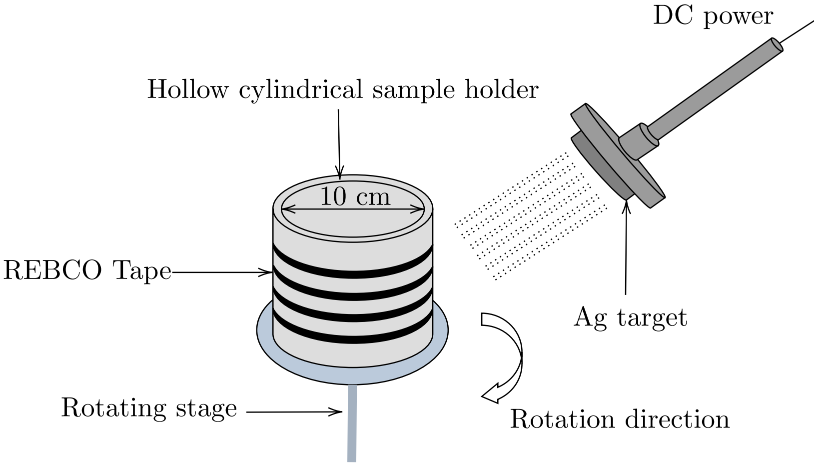

Figure 4.4 Schematic representation of a custom-made sample holder installed in the process chamber of a magnetron sputtering system for silver deposition on a meter-scale CFD tape.

tapes, the silver layer on top of the CFD layer is deposited after annealing. One can therefore wonder if this new silver layer has a sufficient adherence to the REBCO layer. The effects of annealing on the adhesion strength of the silver layer on the REBCO layer were investigated using nanoscratch testing. Scratch tests were performed on three different samples. The first sample was a regular (i.e. unmodified) SuperPower (SP-R) tape. Note that commercial SuperPower REBCO tapes are annealed in oxygen at a temperature ranging from 400 to 500°C [109–111]. The second one was a SP CFD sample (SP-N) not annealed after the silver deposition. The third sample (SP-A) was identical to SP-N except that it was annealed at 300°C in an oxygen atmosphere for one hour after the silver deposition. The thickness of the silver layer on the REBCO layer (1 $\mu$m) was the same for all three samples.

Figure 4.6 presents a microscopic panoramic image of a scratch test made on sample SP-A. Five critical loads can be defined from this image: $Lc_1$ stands for the first point at which the scratch starts to leave observable traces, $Lc_2$ is the point at which the scratch becomes continuous, $Lc_3$ refers to the first observable defect in the scratch, where defects correspond to single dark areas in the track, $Lc_4$ is defined by the beginning of multiple defects along the scratch, and $Lc_5$ stands for the appearance of secondary scratch marks (bright lines) within the main scratch.

Table 4.2 gives the values of the five critical loads for SP-R, SP-N, and SP-A. Figure 4.7 presents graphically the critical loads given in Table 4.2. The critical loads $Lc_2$ and $Lc_4$ are

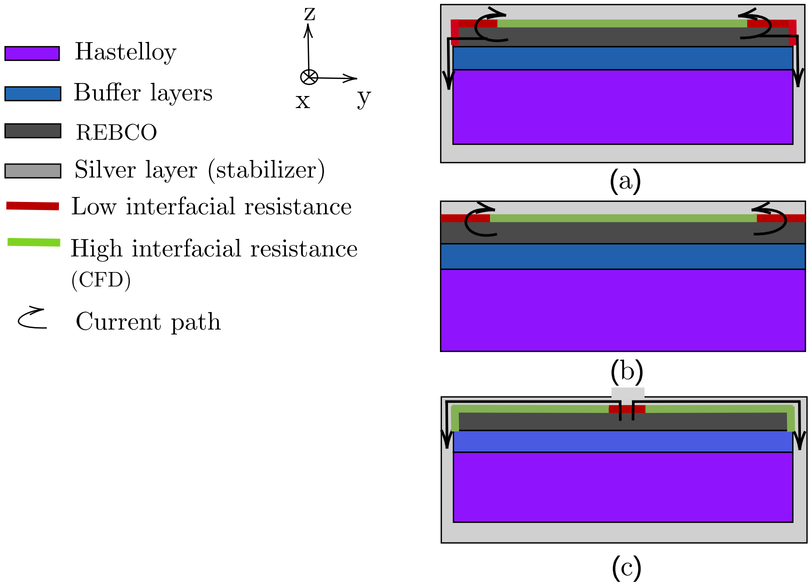

Figure 4.5 Cross-section of the CFD-I architecture implemented in commercial REBCO tapes from (a) THEVA [30] and (b) STI [45]. (c) Cross-section of the CFD-II architecture implemented in a commercial REBCO tape from SP [34]. Upon a quench, the current (black arrows) is forced to pass through the regions with the lowest interfacial resistance to reach the stabilizer layer.

similar for all three samples while $Lc_1$, $Lc_3$ and $Lc_5$ are slightly lower in the case of sample SP-N (approximately 10 to 25% lower). This means that the first observed dark areas and the secondary scratches in the tracks appear at lower loads in sample SP-N compared to samples SP-R and SP-A.

The results suggest that annealing CFD tapes at 300°C slightly improves the adhesion of the silver layer on the REBCO layer. However, this difference in the critical loads with and without annealing is probably not significant in practical applications, considering that the weakest point in REBCO tape is the interface between the REBCO layer and the buffer layers and not the interface between the silver and the REBCO layer [112].

In addition to the critical loads, the measurement of the scratch depth indicates how deep the scratch penetrates the coating. The remaining depth is an indication of the material's resistance to scratching. At the end of the scratch test, all samples showed similar scratch depths, in the 1.5–1.7 $\mu$m range, as shown in Figure 4.8, exceeding the thickness of the top silver layer (1 $\mu$m).

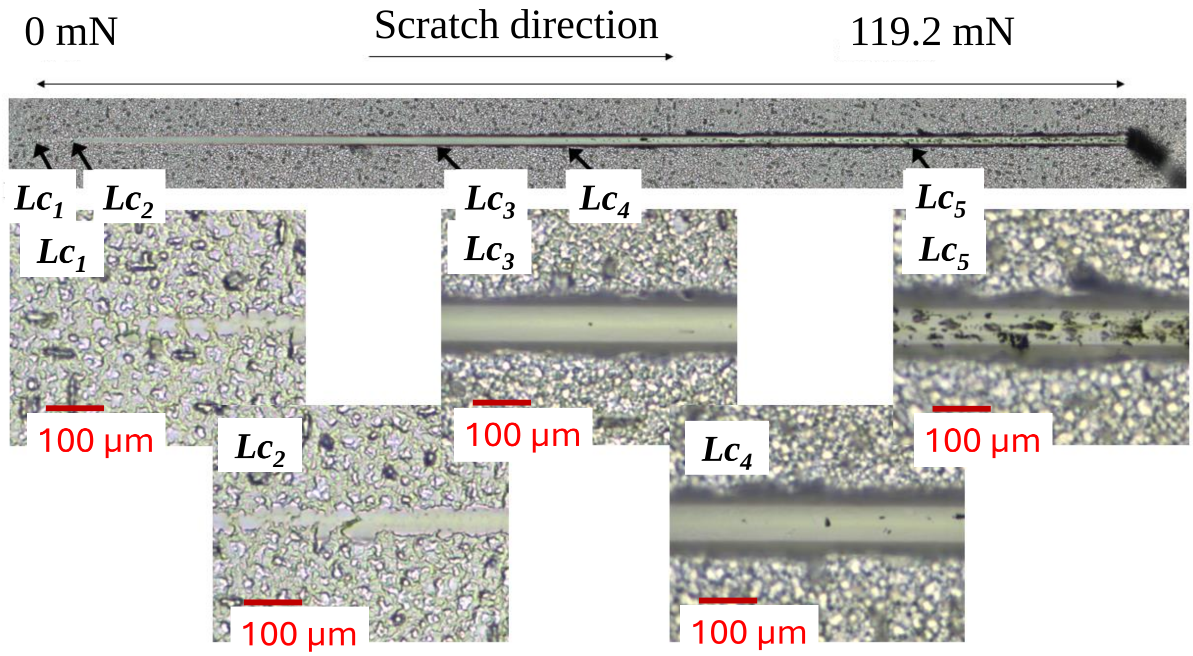

Figure 4.6 Top: Example of a panoramic image of sample SP-A scratched surface. Bottom: Zoom on the corresponding five critical loads from the panoramic image.

To investigate more deeply the nature of the dark areas created during the scratch tests, SEM imaging and EDS mapping were performed. SEM images of wear tracks in SP-R, SP-N, and SP-A samples when the applied load was close to $Lc_5$ are shown in Figure 4.9(a), 4.9(b) and 4.9(c) respectively. For all samples, EDS mapping images indicate that the dark areas observed in Figure 4.6 are characterized by an absence of silver and a presence of copper and oxygen, indicating that the REBCO layer was partially exposed at the end of the scratch. The presence of barium, gadolinium, and yttrium was also detected in low concentrations in all three samples (not shown in Figure 4.9). EDS mapping of the first detected dark areas,

Table 4.2 Values of the critical loads measured by scratch tests for the regular SuperPower tape (SP-R), the non-annealed CFD tape (SP-N), and the annealed CFD tape (SP-A).

| **Critical load (mN)** | **SP-R** | **SP-N** | **SP-A** |
|---|---|---|---|
| $Lc_1$ | 1.2 ± 0.1 | 0.1 | 0.46 ± 0.08 |
| $Lc_2$ | 5.2 ± 0.4 | 3.4 ± 0.3 | 3.1 ± 0.3 |
| $Lc_3$ | 45 ± 2 | 33.9 ± 0.1 | 46 ± 3 |
| $Lc_4$ | 57 ± 1 | 55 ± 2 | 58 ± 1 |
| $Lc_5$ | 80.7 ± 0.9 | 72.9 ± 0.8 | 87 ± 2 |

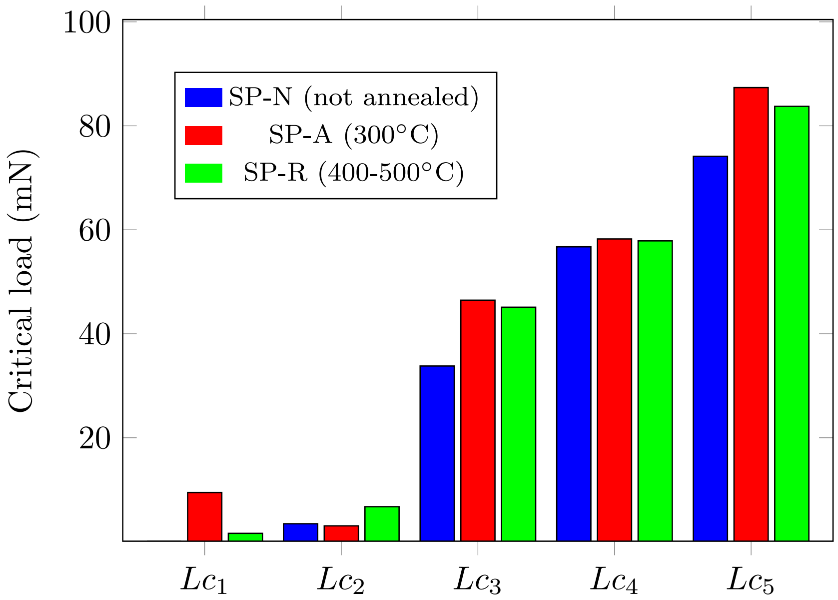

Figure 4.7 Histogram of the critical loads for the regular SuperPower tape (SP-R), non-annealed CFD tape (SP-N), and the annealed CFD tape (SP-A).

corresponding to the critical load $Lc_3$, also indicates that copper and oxygen are present in the dark areas suggesting that part of the REBCO layer was exposed for critical load $Lc_3$.

### 4.4.2 NZPV measurements on long CFD tapes

CFD tapes were manufactured using commercial REBCO tapes from three different manufacturers: SuperPower (SP), THEVA, and STI, as mentioned earlier (see Tab. 4.1). One sample of each kind was produced, for a total of three samples. The CFD-II architecture was implemented using the SP tape, and the CFD-I architecture was used for the THEVA and STI tapes (see Figure 4.5).

The measured average critical current and $n$-factor of the SP, THEVA and STI CFD samples were 141.5 A with $n = 25$, 756 A with $n = 26$, and 94 A with $n = 19$, respectively. These values are similar to those of unmodified REBCO tapes from the same manufacturers, indicating that no degradation of the critical current occurred after the CFD fabrication process.

Figure 4.10 presents the NZPV measurements as a function of the applied current at six different locations along the SP CFD sample, which was fabricated with the reel-to-reel setup. The distance $d$ in the legend corresponds to the distance between the magnet used to

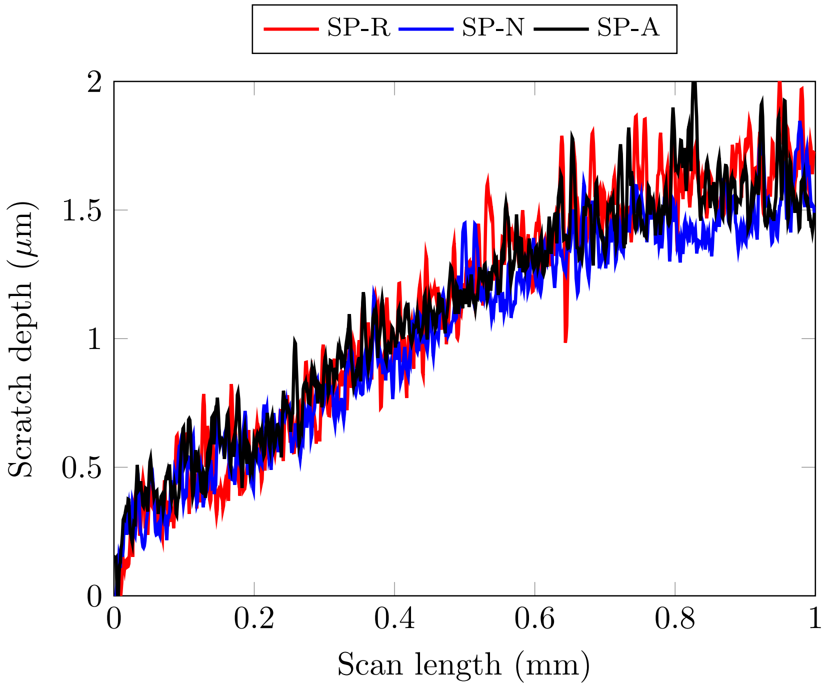

Figure 4.8 Scratch depth as a function of the scan length for the regular SuperPower tape (SP-R), the non-annealed CFD tape (SP-N), and the annealed CFD tape (SP-A).

initiate the quench and one of the current terminals. The solid line in Figure 4.10 indicates the average NZPV value as a function of the applied current. The standard deviation (SD) of the NZPV measured at six different locations is also shown (shaded gray area). The Relative Standard Deviation (RSD) ranged between 6.5% and 9.5% depending on the applied current, indicating that the NZPV is relatively uniform along the length of the tape. For comparison, the NZPV of a SP regular tape is also shown. It is observed that the NZPV is enhanced by a factor of 22. The gain factor is high because the thickness of the top silver layer was only 300 nm, which amplifies the CFD effect.

The NZPV of the two CFD tapes fabricated with the manual technique, namely the THEVA and STI CFD samples, was also measured. Figure 4.11 presents the measured NZPV versus the applied current for a 74 cm long THEVA CFD tape (red triangles) and is in agreement with previous experimental results performed on 12 cm long THEVA CFD tapes (blue squares). The NZPV of a THEVA regular tape is also shown (black diamonds). It is observed that, for the THEVA CFD tapes, the NZPV is enhanced by approximately a factor of seven. No statistical data are presented for the 74 cm long THEVA CFD tape because the NZPV was measured at only one location.

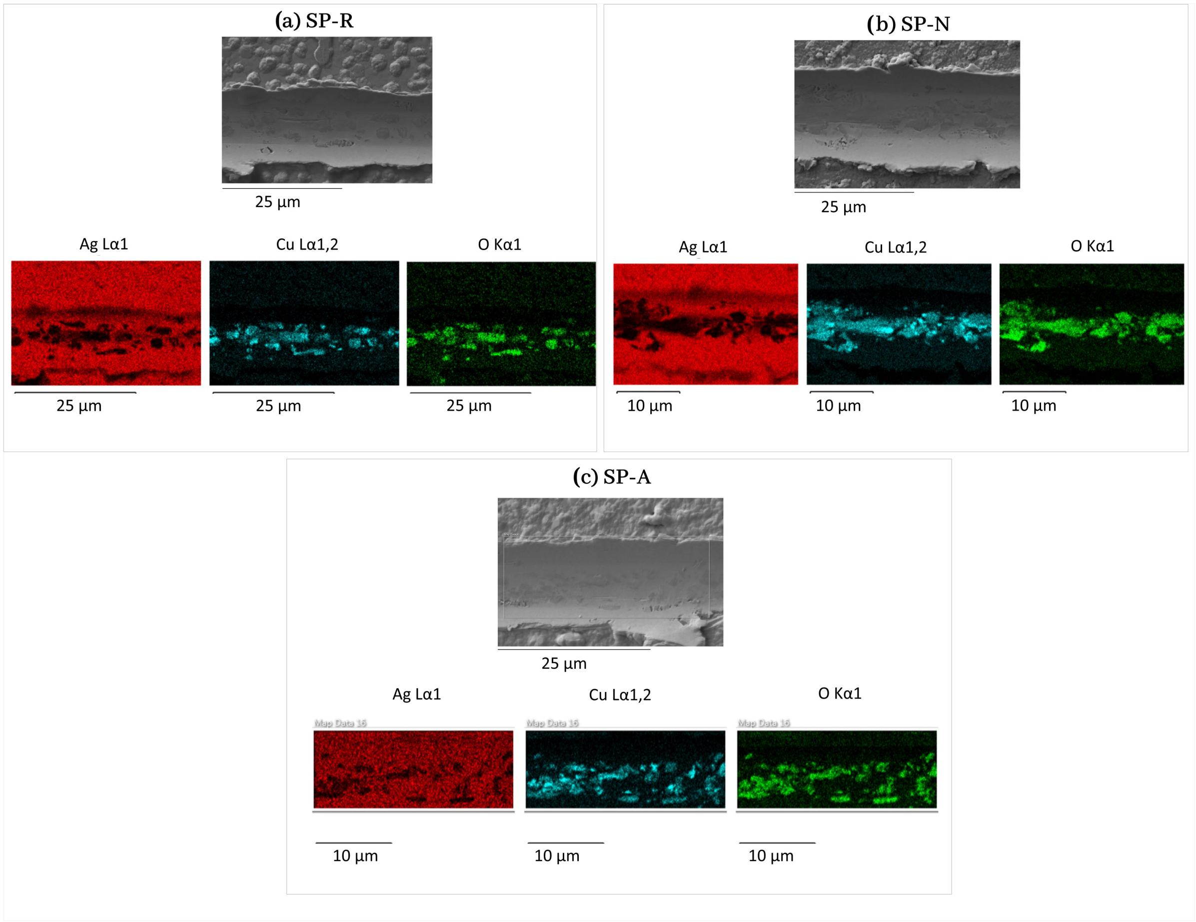

Figure 4.9 Scanning electron micrographs and EDS mappings of the wear tracks at the end of the scratch (around critical load $L_{c5}$) for (a) SP-R, (b) SP-N, and (c) SP-A.

Figure 4.12 presents the NZPV values versus the applied current for a 74 cm long STI CFD tape fabricated with the manual technique. The NZPV was measured at two different locations: $d$ = 5 cm (blue squares), and $d$ = 71 cm (red triangles). The solid black line is the average NZPV value as a function of the applied current. Values between 0.6 and 3 m/s were obtained for a transport current ranging from 70 to 110 A. Also, the NZPV depends on the location of the measurement ($d$ = 5 cm vs. $d$ = 71 cm). The standard deviation is represented by the shaded grey area in Figure 4.12. The corresponding relative standard deviation (RSD) with respect to the average NZPV value is between 5% and 18.7%. For comparison, the NZPV of a 12 cm long STI regular tape is between 0.05 and 0.41 m/s for a transport current ranging from 60 to 107 A. Here, this corresponds to an enhancement factor of 6 to 7 of the NZPV due to the CFD architecture.

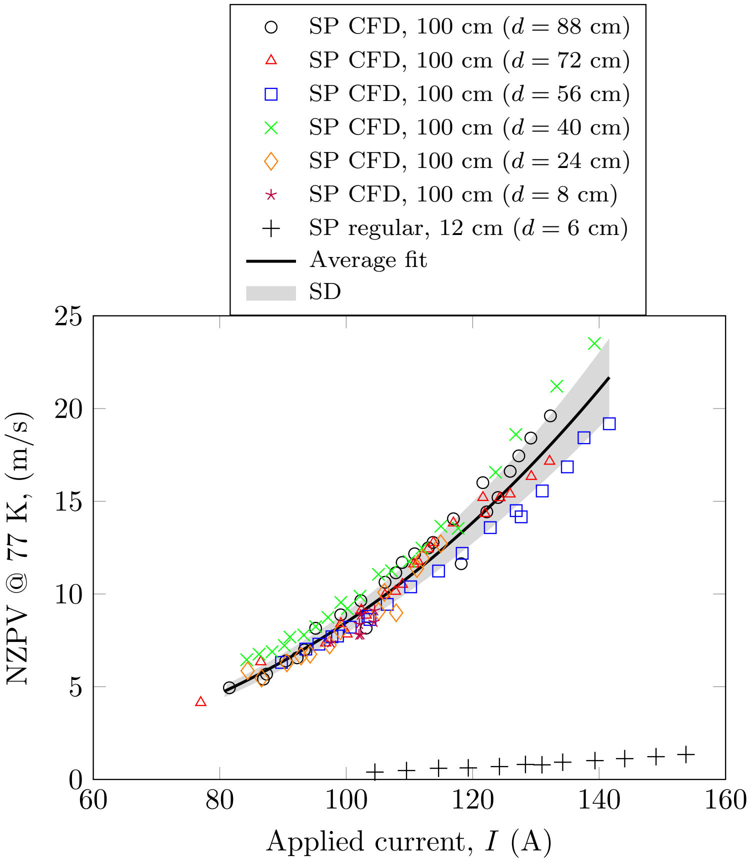

Figure 4.10 NZPV values versus applied current measured at six different locations on a 100 cm long SP CFD tape. The distance $d$ corresponds to the length between one of the current terminals and the quench initiation zone. The solid black line is the average NZPV value as a function of the applied current. The shaded grey area corresponds to the standard deviation (SD).

### 4.4.3 Geometrical imperfections in the CFD layer and their impact on the NZPV

Geometrical imperfections can be introduced during the fabrication of long-length CFD tapes, for instance, if a slight tape misalignment occurs. Such misalignment of the tape is more likely to occur during the manual CFD fabrication technique. Typical resulting imperfections are illustrated in Figure 4.13, namely a lateral displacement of the CFD layer (Figure 4.13(b)) and a variation in the width of the CFD layer (Figure 4.13(c)). For instance, as will be discussed later, a misalignment of the mask occurred during the manual fabrication technique of the STI CFD tape, which induced variations in the width of the CFD layer up to 0.5 mm (the width varied between 3 and 3.5 mm).

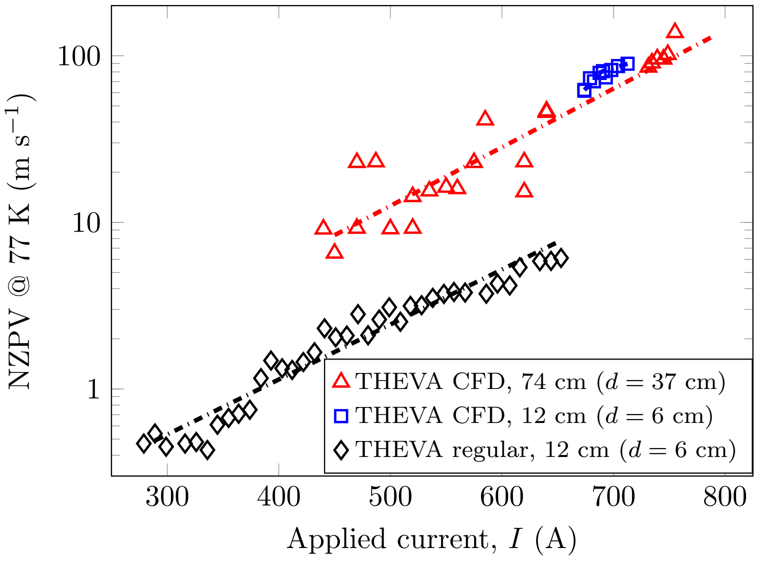

Figure 4.11 Measured NZPV values versus the applied current for a 74 cm long THEVA CFD tape (red triangles: $d = 37$ cm), a 12 cm long THEVA CFD tape (blue squares: $d = 6$ cm), and a THEVA regular tape (black diamonds $d = 6$ cm). The THEVA CFD tapes were fabricated using the manual fabrication technique. Dashed-dotted lines are guides to the eye.

A 3D electro-thermal model based on the finite element method (FEM) was used to simulate the quench behavior of CFD tapes with geometrical imperfections in the CFD layer. More precisely, the NZPV was calculated for the two types of imperfections mentioned above: i) misalignment of the position of the CFD layer relative to the centerline of the tape ($\ell \neq 0$) and ii) a variation in the coverage fraction $f$ of the CFD layer. The FEM model was based on the Joule Heating module of the COMSOL 5.6 software package, where, the heat equation and the current continuity equation are coupled through the Joule losses.

A power-law model using the electrical conductivity ($\sigma_{sc}$) was used to represent the nonlinear $E$-$J$ characteristics of the REBCO layer. The superconducting-to-normal transition was modeled assuming two conductivities in parallel, *i.e.* $\sigma_{sc}$ and $\sigma_n$, where $\sigma_n$ is the conductivity of the REBCO layer in the normal state. Thus, the conductivity of the REBCO layer ($\sigma_{REBCO}$) was expressed as follows:

$$\sigma_{REBCO}(T) = \sigma_{sc}(T) + \sigma_n(T), \tag{4.1}$$

$$\sigma_{sc}(T) = \frac{J_c(T)}{E_0}\left(\frac{||\vec{E}||}{E_0}\right)^{\frac{1-n(T)}{n(T)}}, \tag{4.2}$$

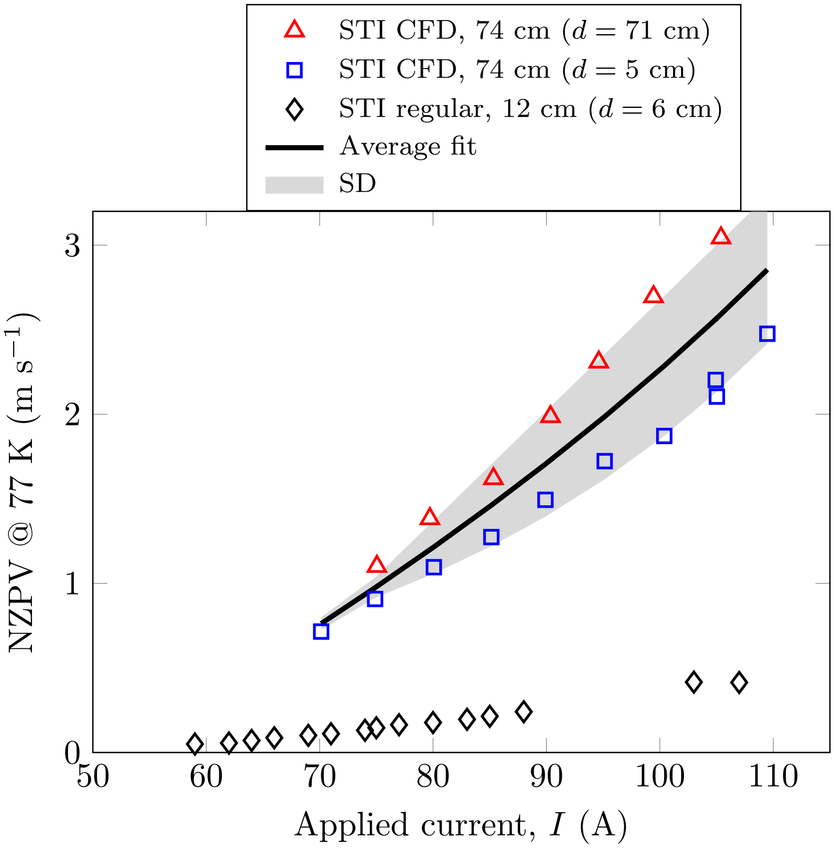

Figure 4.12 Measured NZPV values versus applied current for a 74 cm long STI CFD tape fabricated with the manual fabrication technique (red triangles: $d = 71$ cm, and blue squares: $d = 5$ cm) and a 12 cm long STI regular tape (black diamonds). The solid black line corresponds to the average NZPV value of the STI CFD tape as a function of the applied current. The shaded gray area corresponds to the Standard Deviation (SD).

$$J_c = \begin{cases} J_{c0}\left(\frac{T_c - T}{T_c - T_0}\right) & \text{for } T < T_c, \\ 0 & \text{for } \; T \geq T_c, \end{cases} \tag{4.3}$$

$$n(T) = \begin{cases} (n_0 - 10)\left(\frac{T_c - T}{T_c - T_0}\right) + 10 & \text{for } T < T_c, \\ 10 & \text{for } T \geq T_c, \end{cases} \tag{4.4}$$

where $J_{c0}$ stands for the critical current density at the operating temperature $T_0$, here the liquid nitrogen temperature (77 K), $||\vec{E}||$ represents the norm of the electric field, $E_0$ is the electric field criterion ($10^{-4}$ V/m), $T_c$ is the critical temperature and $n_0$ is the power-law index at 77 K, which was equal to 20. To initiate a local transition to the normal state, a localized heat pulse was applied at one end of the tape. More details about this model are

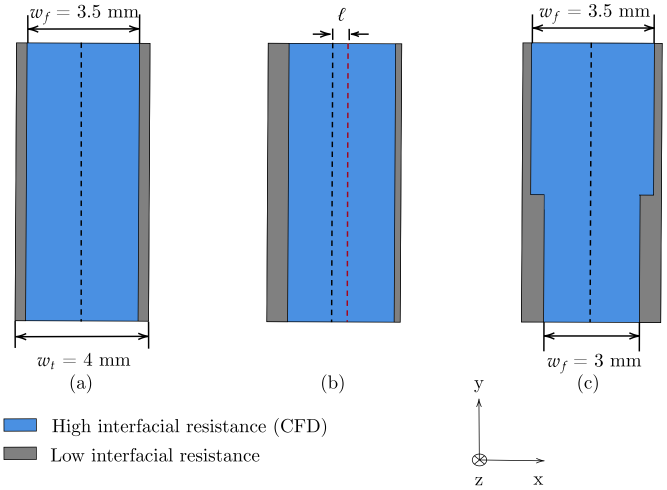

Figure 4.13 Top-view graphical representations of the typical imperfections that can arise in a CFD tape, where $w_t$ is the total width of the tape, $w_f$ is the width of the CFD layer, $f = \frac{w_f}{w_t}$ is the CFD coverage fraction and $\ell$ is the distance between the centerline of the tape and the centerline of the CFD layer. The black and red dashed lines correspond to the center line of the tape and of the CFD layer respectively. (a) Perfect CFD tape in which the CFD is perfectly centered and the width of the CFD is uniform along the length of the tape. (b) The centerline of the CFD layer with respect to that of the tape is shifted ($\ell \neq 0$). (c) Variation of the width of the CFD layer along the length.

available in [86].

The quench propagation of a STI CFD tape was simulated for different coverage fractions $f$ and lateral positions $\ell$ of the CFD layer. First, the CFD coverage fraction $f$ was varied from 0.69 to 0.98, meaning that $w_f$ was varied from 2.75 to 3.9 mm. An applied current of 84 A was used. According to the simulation results presented in Figure 4.14 (red triangles), the NZPV becomes approximately three times larger as $f$ increases, in agreement with previous works [86].

These simulation results can be compared with experimental values. Visual inspection showed that the width of the CFD layer in the STI CFD sample varied between 3 mm up to 3.5 mm, which corresponds to $f = 0.75$ up to 0.875. In Figure 4.14, the experimental NZPV values obtained for $f = 0.75$ and 0.875 are indicated (black "+"). A good agreement is found with the simulation results. This suggests that the variation in the CFD width due to the manual fabrication process explains the difference in NZPV observed in the STI CFD sample.

To investigate the effect of the lateral displacement of the CFD layer on the NZPV for the STI CFD sample, the CFD width was fixed to 3 mm ($f = 0.75$). The lateral displacement

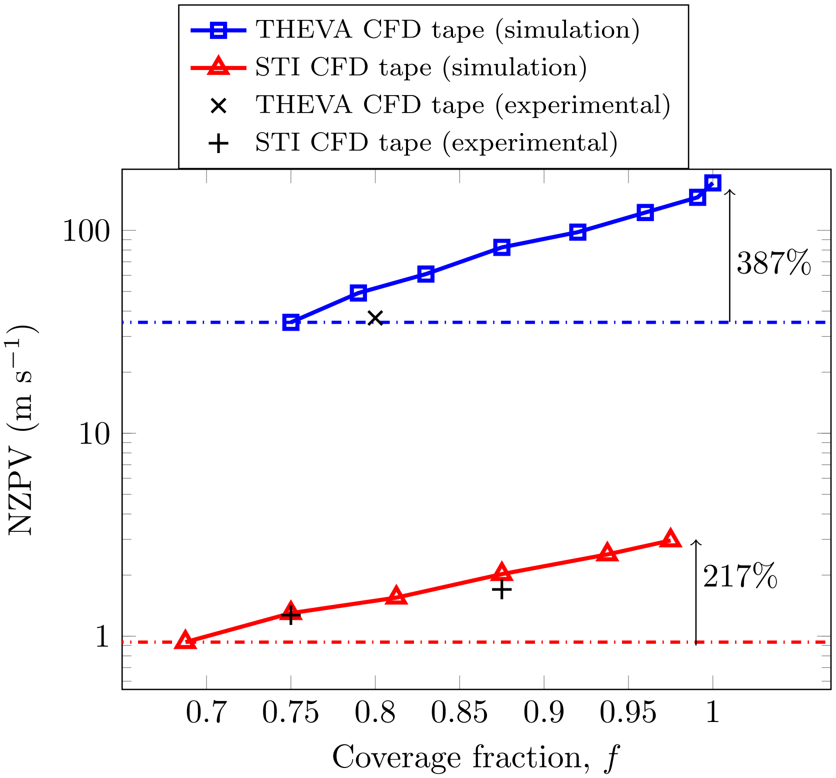

Figure 4.14 Simulated NZPV values as a function of the CFD layer coverage fraction ($f = w_f/w_t$) for a THEVA CFD tape (blue squares) and a STI CFD tape (red triangles) for a current of 600 A ($0.79I_c$) and 84 A ($0.89I_c$) respectively. Some experimental NZPV values obtained with the THEVA CFD sample (black "x") and the STI CFD sample (black "+") are also shown.

of the CFD layer from the centerline of the tape $\ell$ was varied from 0 to 0.49 mm. According to Figure 4.15 (red triangles), the NZPV decreases from 1.39 m/s to 1.14 m/s (11%) for a mismatch $\ell = 0.5$ mm. This variation in the NZPV can be considered rather small, for such a large lateral misalignment of the CFD layer, indicating that this parameter is not critical to ensure a uniform NZPV along the length of a CFD tape.

The impact of the width of the CFD layer and its lateral displacement relative to the central axis of the tape was also investigated for a wider tape. Numerical simulations were thus carried out on a 12 mm wide tape (THEVA CFD tape) in which a current of 600 A was applied. It was found that when $f$ is varied from 0.75 to 0.99, it increases the NZPV by approximately a factor of 5 (blue squares in Figure 4.14). For comparison, the black "x" corresponds to the experimental NZPV of the CFD THEVA sample at 600 A, indicating that the model overestimates the NZPV for the CFD THEVA tape. In the simulations

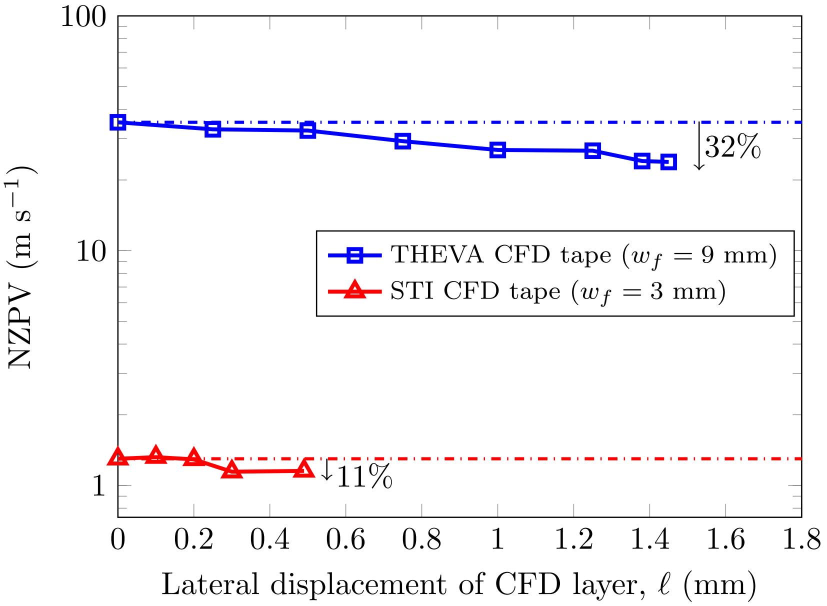

Figure 4.15 Simulated NZPV values as a function of the CFD layer displacement ($\ell$) from the centerline of the tape. The width of the CFD layer was 9 mm for the THEVA CFD tape (blue squares) and 3 mm for the STI CFD tape (red triangles) corresponding to a coverage fraction $f = 0.75$. The applied currents were 600 A (0.79 $I_c$) and 84 A (0.89 $I_c$) for the THEVA CFD and the STI CFD samples, respectively.

where $\ell$ was varied from 0 to 1.45 mm, the CFD width was fixed to 9 mm ($f = 75\%$). As seen in Figure 4.15, it was found that the NZPV is decreased by 32% for a mismatch $\ell = 1.45$ mm, *i.e.* 22%/mm, which corresponds to the same NZPV variation as for the STI CFD sample.

Following these results, we can conclude that the NZPV is much more sensitive to variations in the CFD width than to lateral displacements relative to the central axis of the tape. This is an interesting result considering that in the automated reel-to-reel machine, it is easier to control the width than the lateral adjustment of the mask.

## 4.5 Performance of the reel-to-reel CFD fabrication method

Microscopic images were taken with a digital microscope camera at six locations on the one-meter-long SP CFD tape to verify the existence of geometrical imperfections in the CFD layer. An example of an image taken at $d = 72$ cm is shown in Figure 4.16. The light gray stripe in the middle of the tape represents the silver region with low interfacial resistance between the REBCO layer and the silver layer. The dark gray stripes above and below the

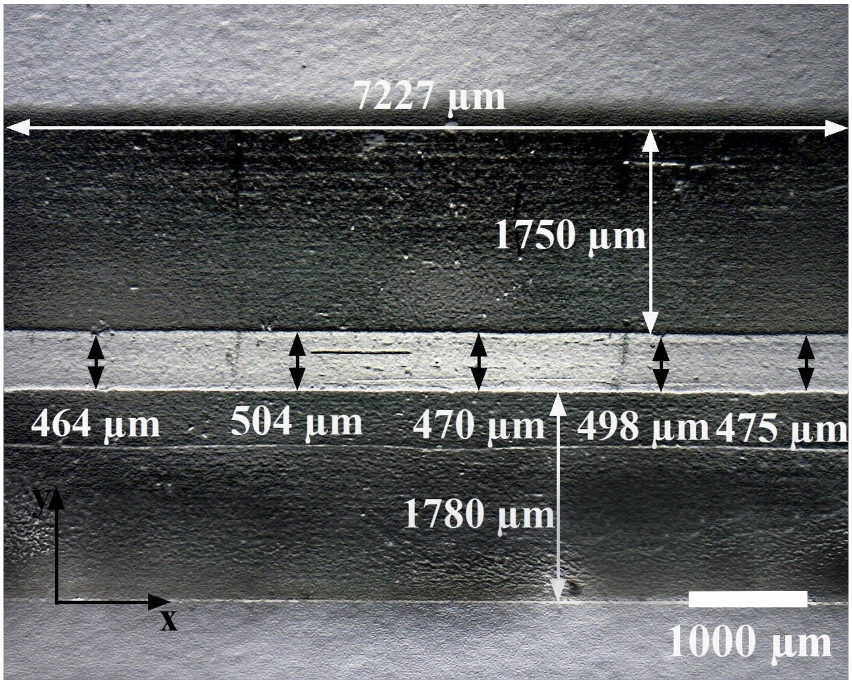

Figure 4.16 Microscopic image of the SP CFD tape taken at $d = 72$ cm. The light gray stripe represents the area with low interfacial resistance between the REBCO layer and the silver layer. Its width, indicated by black arrows, varies between 464 $\mu$m and 504 $\mu$m (thus 484 $\mu$m $\pm$ 20 $\mu$m). The displacement of the light gray stripe from the centerline of the tape was $\ell \approx 1780 - 1750 = 30$ $\mu$m.

light gray stripe correspond to the silver regions with a high interfacial resistance between the REBCO layer and the silver layer. The width of the light gray stripe ($w_{int}$) was measured using the software ImageJ [113]. The width varies between 464 $\mu$m and 504 $\mu$m, which corresponds to a coverage fraction of the CFD between 0.875 and 0.885. Considering that the manual technique induces a variation up to 0.5 mm in the width of the CFD layer, the automated reel-to-reel setup allows reducing the variation in the coverage fraction of the CFD by one order of magnitude. Furthermore, we observe that the displacement of the light gray stripe from the centerline of the tape was $\ell = 30$ $\mu$m.

Numerical simulations were conducted to evaluate the impact of these geometrical imperfections on the NZPV of the SP CFD sample. For an applied current of 118 A and a coverage fraction varying between 0.875 and 0.885, NZPV values of 10.14 m/s and 10.57 m/s were obtained, respectively. This corresponds to a variation of 4.2% in the NZPV. According to Figure 4.10, the relative standard deviation of the NZPV for 118 A is 7.1%. This suggests that the origin of those variations comes from an origin other than the geometrical imperfections of the CFD layer, unlike the case of the STI CFD tape. It is possible that variations in the silver thickness or experimental errors in the NZPV measurement could explain these variations. Regarding the lateral displacement of the CFD layer, such a small displacement affects the NZPV uniformity along the length of the tape in a negligible way.

These results indicate that the reel-to-reel fabrication system allows precise control of the geometry of the CFD layer and a uniform NZPV along the length of the tape compared to the manual fabrication technique.

## 4.6 Conclusion

This paper addressed the fabrication of meter-scale current flow diverter (CFD) REBCO tapes to increase the normal zone propagation velocity (NZPV). An automated reel-to-reel system was developed to fabricate high-performance long CFD tapes and avoid manual manipulation of REBCO tapes. A one-meter-long CFD tape was fabricated using the reel-to-reel system and characterized. The NZPV was found to be increased by a factor of 22 in comparison to a regular tape. Furthermore, very good uniformity of the NZPV along the length of the CFD tape samples was achieved, with variations of less than 10%. Numerical simulations suggest that geometrical imperfections in the CFD layer are not responsible for these variations.

Furthermore, the adhesion of the silver layer on CFD tapes was investigated using the scratch test method. No significant difference was found in the adhesion strength at the REBCO/silver interface between a regular commercial REBCO tape and an annealed CFD REBCO tape. In the case of a non-annealed CFD REBCO tape, the adhesion strength was found to be slightly weaker. Therefore, we conclude that there is no major issue with integrating the CFD architecture along several meters of REBCO tape. This result represents an important step towards the integration of CFD tapes in applications such as cables and coils. In particular, it is expected that CFD tapes in REBCO-based magnets will facilitate quench detection and ultimately prevent damage upon a quench.

## 4.7 Acknowledgments

The authors would like to acknowledge the Natural Sciences and Engineering Research Council of Canada (NSERC), CMC Microsystems, and Mitacs for their financial support in this project.

# CHAPTER 5 ARTICLE 2 - MANUFACTURING THE CURRENT FLOW DIVERTER ARCHITECTURE IN REBCO TAPES USING SILVER INKJET PRINTING

*Authors: Haïfa Ben Saâd, Christian Lacroix, Mariia Zhuldybina, and Frédéric Sirois*

This article was submitted to the journal Superconductor Science and Technology on July 1st, 2024

## 5.1 Abstract

A low normal zone propagation velocity (NZPV) combined with critical current inhomogeneities favor the nucleation of destructive hot spots in rare-earth barium copper oxide (REBCO) tapes. Increasing the NZPV using the current flow diverter (CFD) concept is a promising solution to mitigate the risk of developing hot spots. The fabrication method of CFD REBCO tapes implies several steps consisting in masking, silver etching, mask removal, and silver deposition, which takes time and remains a barrier to the implementation of a low-cost industrial production of long-length CFD REBCO tapes. This work presents a cost-effective and maskless CFD fabrication approach that relies on inkjet printing (IJP) of silver patterns directly on top of the REBCO layer to create a non-uniform interfacial resistance between the silver and the REBCO surface along the width of the tape. The parameters of IJP and oxygen annealing were optimized to obtain highly conductive silver patterns deposited on the surface of the REBCO layer. CFD REBCO tapes were successfully fabricated using commercial REBCO tapes and the proposed method without degrading the superconducting properties. Experimental measurements revealed an increase of the NZPV by a factor of 6-7 compared to commercial REBCO tapes.

## 5.2 Introduction

Rare-earth barium copper oxide (REBCO) coated conductors (CCs) are promising for high-field applications, such as fusion magnets [59], particle accelerators [114], and nuclear magnetic resonance imaging [68], due to their high critical temperature ($T_c$), high critical current density ($J_c$), and excellent mechanical properties [46,58,115]. However, one of the challenges faced by the applied superconductivity community is quench detection and protection of REBCO-based magnets. Traditionally, quench detection in low-temperature superconductor (LTS) magnets relies on measuring the voltage at both ends or in different sections of the magnet coil. However, in high-temperature superconductor (HTS) magnets, the quench produces a very small voltage that increases so slowly that it may damage the coil before being detected by the quench detection system [69]. To circumvent this problem, several novel quench detection techniques have been proposed, based on either thermometry [74], magnetic hall sensors arrays [71], optical fibers [116] or radio frequency waves [117].

In a superconducting wire, the velocity at which a hot spot expands is called the normal zone propagation velocity (NZPV). In REBCO tapes, the NZPV at 77 K and in self-field is approximately 2 to 40 cm/s. This low NZPV, coupled with critical current inhomogeneities along the length, increases the risk of developing destructive hot spots. A possible solution is to increase the NZPV with the current flow diverter (CFD) concept [10]. The CFD concept consists in modifying the architecture of REBCO tapes by patterning a high interfacial resistance between the REBCO layer and the silver layer to increase the NZPV. As a consequence, this increases the rising rate of the voltage at the ends of the tape in the same proportions and implies that a larger portion of the magnet is quenched [69, 118].

Over the years, several fabrication processes have been proposed to integrate the CFD architecture in REBCO tapes. The original approach consists in removing partially the silver layer on top of the REBCO layer using chemical etching. Silver is then redeposited on the REBCO layer using a physical method such as sputtering. One important drawback of this process is the loss of silver during the etching process [78]. Although several recycling methods can be used to recover the silver from the etching solution, exploring alternative approaches remains relevant to lower the cost and promote the industrialization of the CFD architecture [119].

An alternative technique that has been explored consisted in deliberately reducing the thickness of the silver layer to create the so-called b-CFD architecture [120]. In this work, a process based on the sulfurization of the upper part of the silver layer was used, thus creating $Ag_2S$, in order to reduce the thickness of the pure silver layer while avoiding the corrosion of the REBCO layer with sulfur and a degradation of the critical current. However, further work to ensure the quality of the contacts for current injection with this approach is required.

Another technique consisted in the deposition of a thin oxide layer at the REBCO/silver interface to create a high interfacial resistance [121]. A cerium oxide layer ($Ce_xO$) was deposited on top of the oxygenated REBCO layer before silver deposition. An additional annealing in an oxygen atmosphere was performed to reduce the interfacial resistance created by the $Ce_xO$ layer. However, it was observed that the critical current of the REBCO tape was degraded during the oxygen annealing due to a change in the stoichiometry of the REBCO layer, where barium atoms were forced to diffuse out of the REBCO layer through the cracks of the $Ce_xO$ layer.

A different approach consisted in using the inkjet printing of a yttrium oxide ($Y_2O_3$) layer on top of a pre-oxygenated REBCO layer, followed by a silver deposition and an additional annealing in an oxygen atmosphere [122]. Electrical characterization revealed the successful implementation of the CFD architecture, but the overall interfacial resistance was in the range of 100 $\mu\Omega.\text{cm}^2$, which is too high for practical applications. Furthermore, the complexity of this approach makes it unattractive for an industrial production.

In the most recent approach to create the CFD architecture, a locally controlled diffusion reaction between evaporated indium and the silver layer was used to form a stable intermetallic compound (IMC) throughout the whole thickness of the silver layer down to the REBCO/silver interface [123]. This Ag-In IMC at the interface acted as a CFD layer, leading to an increase of the NZPV. While this approach is rather simple to implement in a fabrication process, it is likely to add an extra cost to REBCO tapes production considering that indium is an expensive metal. Furthermore, more investigations on the effects of this Ag-In IMC interlayer in REBCO tapes remain to be done, especially regarding current injection.

In this work, we explore a different approach to create the CFD architecture, which consists in the direct writing of silver patterns on the REBCO surface using inkjet printing (IJP), which is now possible thanks to the commercial availability of conductive inks formulated with metallic silver [124, 125]. An oxygen annealing treatment is performed to reduce the interfacial resistance between the IJP silver and the REBCO layer. Afterwards, a silver layer is deposited using sputtering to cover the whole REBCO layer. This approach has the advantage that it requires no chemical etching or masking steps. In addition, it does not introduce additional species in the REBCO tape.

The first section of the paper describes the experimental methodology used to create the silver patterns with IJP. The second section discusses the structural and electrical properties of the silver printed patterns. The last section presents the fabrication and electrical characterization of IJP CFD tapes.

## 5.3 Experimental procedure

### 5.3.1 REBCO tape samples

Samples used in this work are commercial REBCO tapes obtained from THEVA Dünnschichttechnik GmbH, Superconductor Technologies Inc. (STI), and SuperPower Inc. (SP). The THEVA tapes consisted in a 12 mm wide and 100 $\mu$m thick Hastelloy substrate (C-276$^{\text{TM}}$) on which a 3.1 $\mu$m thick buffer layers stack was deposited. A 3.1 $\mu$m thick GdBaCuO layer was grown on top of the buffer layer [30]. The GdBaCuO layer of these THEVA tapes was not annealed in an oxygen atmosphere, and not coated with a silver layer. These tapes were used to perform preliminary IJP testing. The layered structure of commercial STI tapes consisted of a 50 $\mu$m thick Hastelloy (C-276$^{\text{TM}}$) substrate, a 0.58-0.78 $\mu$m thick buffer layers stack, and a 1 $\mu$m thick GdBaCuO layer. Finally, there was a 2 $\mu$m thick silver layer on top of the GdBaCuO layer only (no silver on the substrate side) [121]. Commercial SP tapes comprised a 50 $\mu$m thick Hastelloy (C-276$^{\text{TM}}$) substrate, a 0.2 $\mu$m thick buffer layers stack, and a 1.6 $\mu$m thick Zr-doped GdBaCuO layer. The whole architecture was surrounded with a total of 2 $\mu$m of silver (1 $\mu$m on both sides) [34]. Both the STI and SP tapes were 4 mm wide. The critical current of the tapes at 77 K and in self-field was 100 A to 110 A for the STI tapes, and 140 A to 150 A for the SP tapes.

For clarity purposes, the unmodified commercial STI and SP samples will be called “regular” tapes, while the modified tapes that include the CFD architecture fabricated using inkjet printing will be called “IJP CFD” tapes.

### 5.3.2 Inkjet printing

A Dimatix inkjet printer (DMP-2831) was used to deposit conductive silver patterns on the outer surface of the REBCO layer. The 16-jet Dimatix materials cartridge, designed for high-resolution and non-contact jetting, contained 16 nozzles. During printing, the samples were fixed on a vacuum plate whose temperature was adjusted to 70 °C.

The Novacentrix JS-A291 ink was chosen considering its good adhesion on the REBCO layer and viscosity. Silver lines having a width of 0.5-1 mm and a thickness of 3.8 $\mu$m were printed. Critical current measurements revealed no degradation in the critical current of the samples after printing the silver lines with this ink.

### 5.3.3 Microstructure characterization

A Dektak 150 surface profiler was used to determine the average thickness of the printed lines for different oxygen annealing temperatures. The microstructural properties of the printed patterns were also investigated using a scanning electron microscope (SEM) equipped with a field emission gun (FEG SEM; JOEL7600TFE). For that matter, a stair-step cut was created in 4 mm × 4 mm sample pieces using a focused ion beam instrument (Hitachi FIB-2000A). Then, the samples were cleaned and mounted on a sample holder using carbon tape. The acceleration voltage was 10 kV and the working distance was 10.7 mm. Samples were tilted to an angle of approximately 30 ° to face the secondary electron detector. Finally, a chemical

(a) $D$ = 15 $\mu$m (b) $D$ = 17 $\mu$m (c) $D$ = 20 $\mu$m

Figure 5.1 Images of printed silver lines on REBCO tapes for a drop spacing of (a) $D = 15$ $\mu$m, (b) $D = 17$ $\mu$m, and (c) $D = 20$ $\mu$m.

composition analysis was performed using energy dispersive spectroscopy (EDS) [108, 126].

### 5.3.4 Electrical characterization

A four-point method was used to determine the room-temperature resistivity of the printed patterns vs. annealing temperature. The same method was used to obtain the resistance of IJP CFD REBCO tapes from 77 to 285 K [121].

The critical current $I_c$ ($E_c = 1$ $\mu$V/cm) and the NZPV of IJP CFD REBCO tapes were measured in a liquid nitrogen bath at ambient pressure and in self-field. A pulsed current source was used to generate square current pulses lasting a few milliseconds. Up to 40 pogo pins placed every 1.27 mm were used to measure the voltage across the length of the sample. For the NZPV measurements, an NdFeB magnet was used to reduce locally the critical current to create a normal zone. More details about the measurement setup are available in [78].

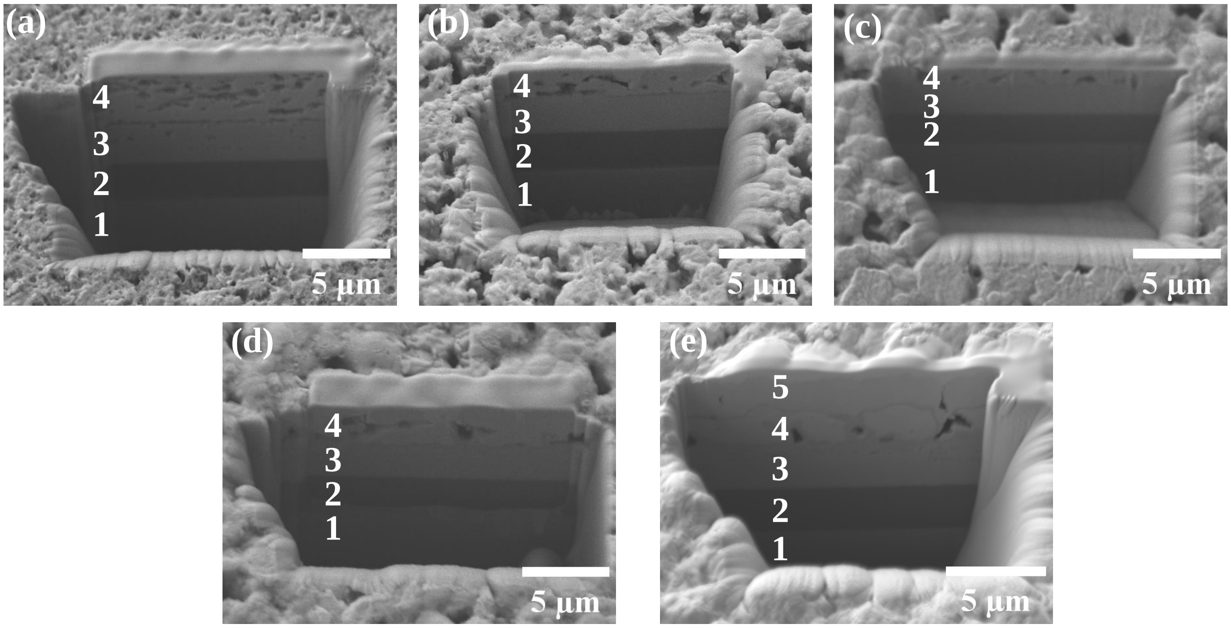

Figure 5.2 Cross-sectional views of Ag printed lines on THEVA tapes cured at 100 °C for 45 minutes: (a) before oxygen annealing, (b) after a one-hour oxygen annealing at 300 °C, (c) after a one-hour oxygen annealing at 400 °C, (d) after a one-hour oxygen annealing at 500 °C and (e) after a one-hour oxygen annealing at 400 °C and followed by the deposition by sputtering of a one-micron thick silver layer. The numbers refer to the different layers of the REBCO tape, namely 1) the substrate, 2) the buffer layers, 3) the REBCO layer, 4) the printed silver, and 5) the sputtered silver.

## 5.4 Inkjet printed silver lines on REBCO surface

### 5.4.1 Fabrication details

To obtain uniform silver lines, several tests were carried out using the Dimatix 2831 IJP system to set the optimal spacing $D$ between the drops and the pulse voltage, which controls the resolution of the printed patterns. The pulse voltage is the voltage amplitude applied to the piezoelectric part in the printhead to generate the required pressure for ejecting ink droplets on the substrate, thus controlling the size and the velocity of the ink droplets. The tests consisted in printing 1 mm wide lines on THEVA samples without a top silver layer. Figure 5.1 presents images of the silver lines for $D = 15$, 17 and 20 $\mu$m. Uniform continuous silver patterns were only obtained with $D = 15$ $\mu$m, while for $D = 17$ $\mu$m and 20 $\mu$m, the printed tracks were divided into separate lines. Also, different values of the pulse voltage were tested and it was found that the optimal pulse voltage was 16 V.

To ensure a good adhesion of the printed silver ink on the REBCO surface, samples were cured at 100 °C for 45 minutes in an ambient atmosphere. This step was followed by an oxygen annealing at temperatures between 300 °C and 500 °C to decrease the interfacial resistance between the printed silver and the REBCO layer [127]. After annealing, the adhesion of silver on the REBCO surface was verified using adhesive tape peel tests. No silver particles were found on the tape, indicating that the adhesion of silver on REBCO was good.

### 5.4.2 Microstructural characterization

Figure 5.2 presents the cross-sectional views of five printed silver lines on the surface of the REBCO layer of THEVA tapes after curing at 100 °C for 45 minutes: (a) before oxygen annealing, (b) after a one-hour oxygen annealing at 300 °C, (c) after a one-hour oxygen annealing at 400 °C, (d) after a one-hour oxygen annealing at 500 °C and (e) after a one-hour oxygen annealing at 400 °C followed by the deposition by sputtering of a one-micron thick silver layer. In Figure 5.2(a), the silver deposited by inkjet printing presents multiple voids (black areas in the Ag layer), which was confirmed by EDS mapping (not shown). Furthermore, a thin interspace is present between the REBCO layer and the printed silver, which suggests a poor adhesion of the silver to the REBCO surface. In Figure 5.2(b)-(d), following annealing in an oxygen atmosphere, a progressive agglomeration of the silver particles is observed. The size of the grains becomes larger, and the pore density is reduced, as the annealing temperature increases from 300 to 500 °C. Furthermore, no interspace at the printed silver/REBCO interface is visible after oxygen annealing at 300 °C or above. In Figure 5.2(e), while no voids are present in the sputtered silver layer, confirming its good quality, voids are still present in the silver deposited by IJP.

Figure 5.3 displays the thickness profiles of a 1 mm wide silver line before and after annealing at 300 °C for one hour in an oxygen atmosphere. It reveals that the line has shrunk after the heat treatment, which can be attributed to the coalescence of silver nanoparticles during annealing, as observed in Figure 5.2(b)-(d). The average thicknesses of a silver line before and after annealing at 300 °C, 400 °C, and 500 °C are presented in Figure 5.4, where we observe that it decreases as the annealing temperature increases.

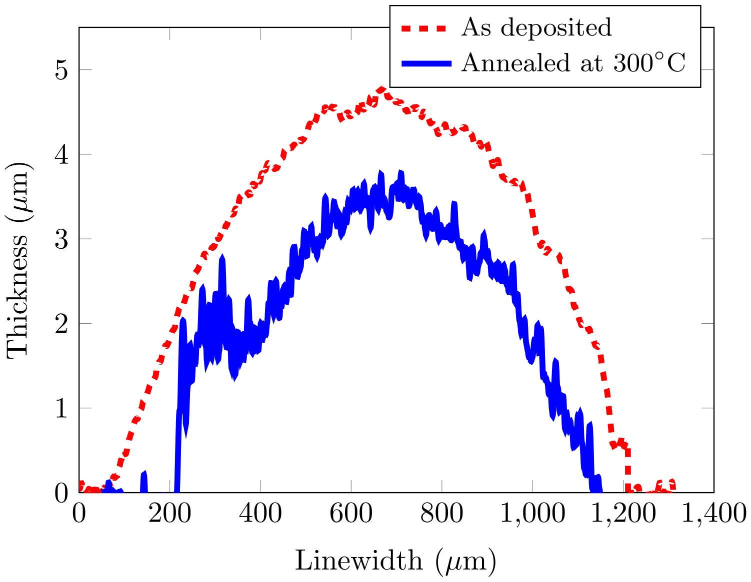

Figure 5.3 Thickness profiles of printed silver lines before (dashed red line) and after a one-hour annealing at 300 °C in an oxygen atmosphere (solid blue line).

### 5.4.3 Electrical resistivity

Figure 5.4 presents the variation of the silver resistivity vs. annealing temperature. The measurements of the electrical resistivity were performed at room temperature to study the impact of the microstructure evolution of the printed lines with the annealing on the electrical properties, specifically the impact of the porosity on the transport of electrical charge. Before annealing, the resistivity of the silver line is 20.3 $\mu\Omega$.cm, and drops to 1.9 $\mu\Omega$.cm after annealing at a temperature of 500 °C, which is of the same order of magnitude as the resistivity of pure silver (1.6 $\mu\Omega$.cm). This drop in the resistivity can be explained by the evaporation of organic components and by an increase in the mass density of silver (reduction in the void volume). The decrease in the electrical resistivity of inkjet-printed silver patterns and the coalescence of silver nanoparticles after employing heat treatment has also been reported in previous studies [128, 129].

## 5.5 Inkjet printing of CFD tapes

### 5.5.1 Fabrication details

To fabricate inkjet printing (IJP) CFD tapes, commercial STI and SP samples were used. The fabrication steps of the IJP CFD tapes are described in Figure 5.5. Firstly, the sil-

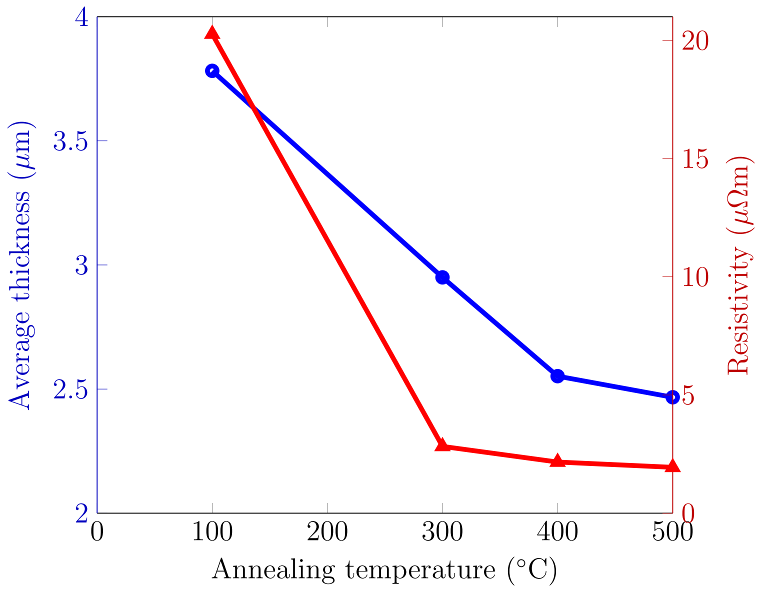

Figure 5.4 Average thickness (blue) and measured resistivity (red) of printed silver lines vs. annealing temperature.

ver layer on the REBCO layer was removed using chemical etching with a solution of $NH_4OH$:$H_2O_2$:$H_2O$;1:1:4. Then, a 3.8 $\mu$m thick and 0.5 mm wide silver line was printed locally on the REBCO surface. The CFD coverage fraction $f$, which is 1 minus the ratio between the width of the printed line and the total width of the tape, was thus 0.875. The sample was then annealed in an oxygen atmosphere at 400 °C for one hour. This heat treatment decreased the contact resistance between the silver line created by IJP and the REBCO layer, although the exact value could not be measured. Finally, a 2 $\mu$m thick layer of silver, covering the whole surface of the STI and SP IJP CFD samples, was deposited by sputtering. The resulting architectures of the IJP CFD tapes are shown in Figure 5.5.

### 5.5.2 Critical current and temperature dependence of the resistance

The critical current of the IJP CFD tapes was measured in liquid nitrogen at ambient pressure (77 K) and in self-field. Figure 5.6 shows the $E$-$I$ curves for both IJP CFD samples. The values for the critical currents are 96 A for the STI IJP CFD sample and 141 A for the SP IJP CFD sample, while the $n$-factors are 22 and 26, respectively. The temperature dependence of the electrical resistance of the samples for an applied current of 100 mA was also measured and is shown in Figure 5.7. The critical temperatures are 94 K and 92 K for the STI IJP CFD and the SP IJP CFD samples, respectively, which are the same as that of the regular

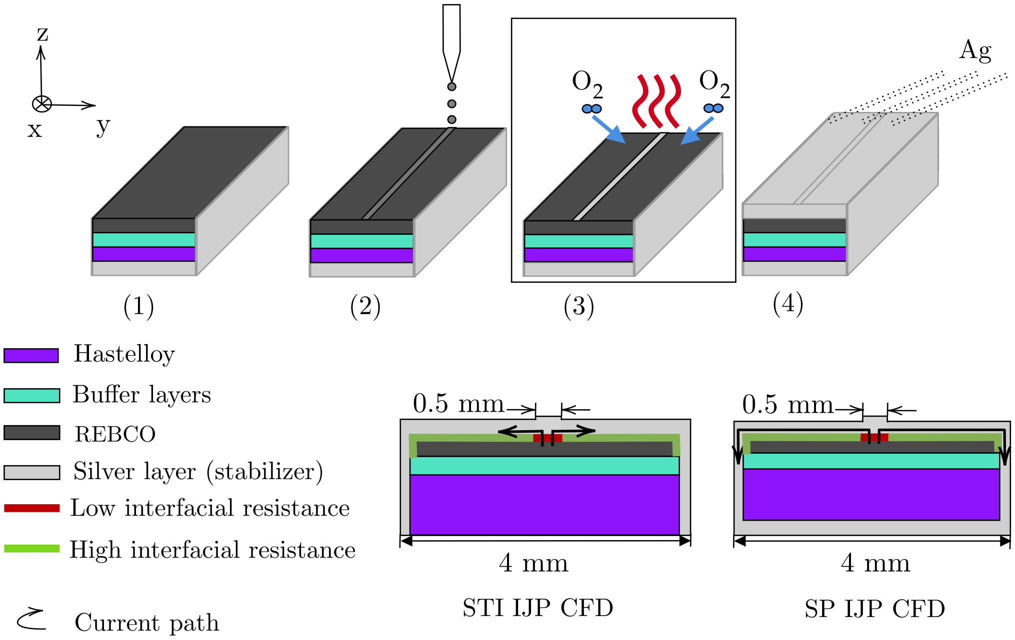

Figure 5.5 Top figures: CFD fabrication steps using IJP: (1) etching of the silver layer on top of the REBCO layer, (2) IJP of a silver line, (3) oxygen annealing, and (4) deposition of silver by sputtering. Bottom figures: the two CFD geometries fabricated by IJP are shown.

(*i.e.* unmodified) REBCO tapes. Note that the SP IJP CFD sample has a greater amount of silver, which explains the lower resistance obtained above the critical temperature.

### 5.5.3 Normal zone propagation velocity

The NZPV of both the STI and SP IJP CFD samples were measured in self-field and at 77 K and are presented in Figures 5.8 and 5.9, respectively.

For the STI IJP CFD sample, the NZPV was increased by a factor of 6-7 compared to the STI regular sample.

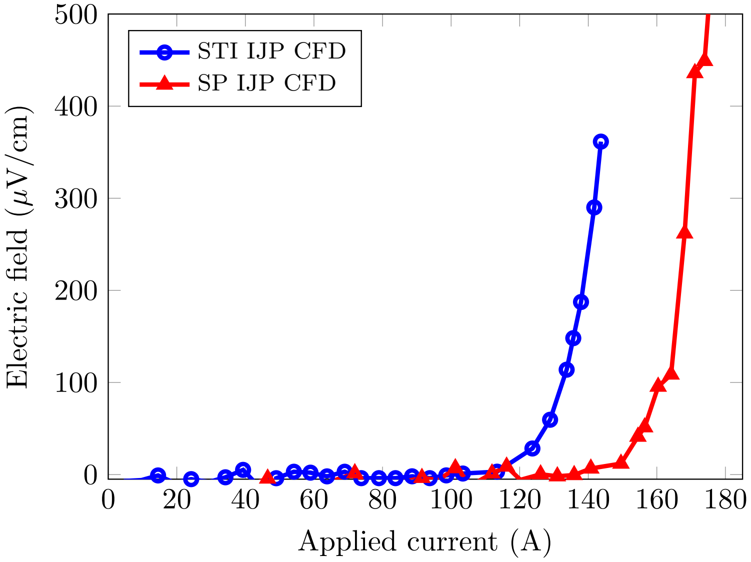

Figure 5.6 *E*-*I* curves of the STI IJP CFD sample (blue circles) and the SP IJP CFD sample (red triangles) measured at 77 K and in self-field.

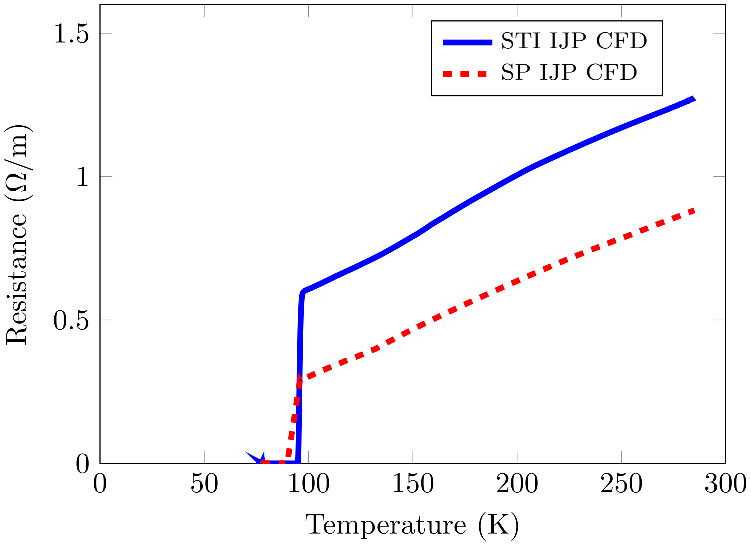

Figure 5.7 Resistance vs. temperature curves of the STI IJP CFD sample (solid blue line) and SP IJP CFD sample (dashed red line).

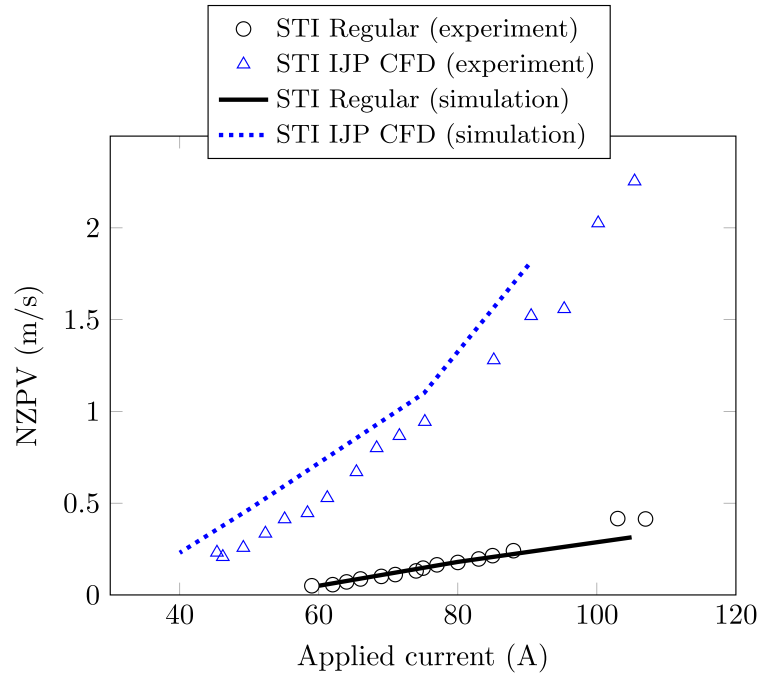

Figure 5.8 Measured NZPV values vs. the applied current for a STI regular sample (black circles) and a STI IJP CFD sample (blue triangles). The solid black line corresponds to the simulated NZPV for a STI regular sample, while the dotted blue line is the simulated NZPV for a STI IJP CFD sample.

For the SP IJP CFD sample, the NZPV was increased by a factor of 3-4 compared to the SP regular sample. However, the SP regular sample had a total silver thickness of 2 $\mu$m while the SP IJP CFD sample had a 3 $\mu$m thick silver layer, which explains why the gain is only a factor of 3-4. Typically, for the same amount of stabilizer, the CFD architecture enhances the NZPV by a factor of approximately 7.

### 5.5.4 Numerical Model

The NZPV of IJP CFD samples and regular samples were calculated using 3D finite element simulations based on the Electric Currents and Heat Transfer in Solids modules available in the COMSOL Multiphysics 5.5 software (see [10] for further details about the model). In this model, the thermal and electrical equations are interconnected through the Joule losses term. Adiabatic conditions were assumed (no heat exchange between the tape and the environment). The geometries of the samples, as depicted in Figure 5.5, were implemented in the model. To increase the computational efficiency, the number of elements was reduced by taking advantage of the symmetries in the problem. Due to their small thickness, the stack

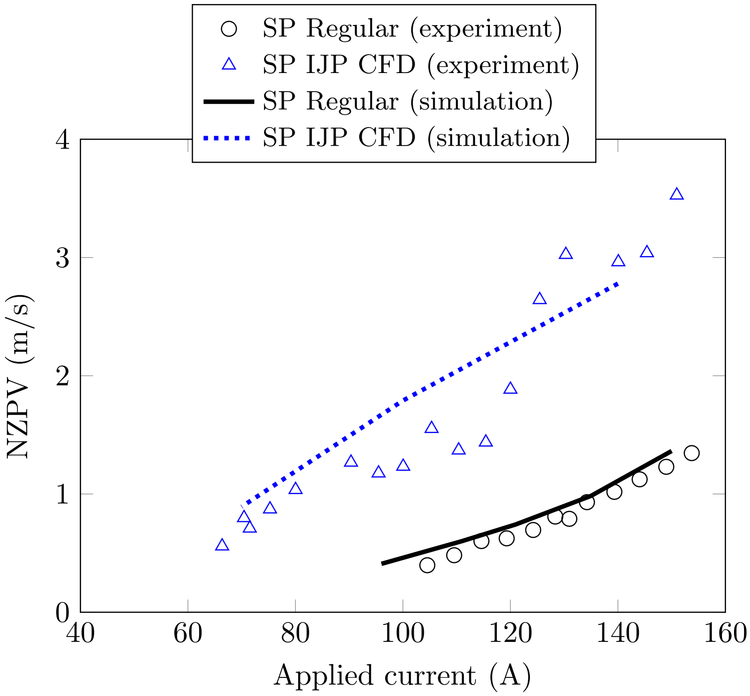

Figure 5.9 Measured NZPV values vs. the applied current for a SP regular sample (black circles) and a SP IJP CFD sample (blue triangles). The solid black line corresponds to the simulated NZPV for a SP regular sample, while the dotted blue line is the simulated NZPV for a SP IJP CFD sample.

of buffer layers and the resistive interface between the REBCO layer and the silver layer were reduced to thin-shell elements.

The electrical conductivity of the REBCO layer was expressed as two conductances in parallel, where one conductance corresponds to the normal state of REBCO ($\sigma_n$) and the second to the superconducting state of REBCO ($\sigma_{sc}$), modeled by a power-law, which is expressed as

$$\sigma_{sc}(T) = \frac{J_c(T)}{E_c}\left(\frac{||\vec{E}||}{E_c}\right)^{\frac{1-n(T)}{n(T)}}, \tag{5.1}$$

$$J_c(T) = \begin{cases} J_{c0}\left(\frac{T_c-T}{T_c-T_0}\right) & \text{for } T < T_c, \\ 0 & \text{for } \; T \geq T_c, \end{cases} \tag{5.2}$$

$$n(T) = \begin{cases} (n_0-10)\left(\frac{T_c-T}{T_c-T_0}\right)+10 & \text{for } T < T_c, \\ 10 & \text{for } T \geq T_c, \end{cases} \tag{5.3}$$

where $||\vec{E}||$ is the norm of the electric field, $E_c$ is the electric field criterion ($10^{-4}$ V/m), $J_{c0}$ is the critical current density at $T_0$, $n_0$ is the power-law index at $T_0$, $T_c$ is the critical temperature and $T_0$ is the operating temperature (77 K).

The temperature dependence of the electrical resistivity of silver was deduced from Figure 5.7. It was assumed that the electrical resistivity was the same for the printed silver and the sputtered silver. An interfacial resistance between the printed silver layer and the REBCO layer of $R_i^* = 1$ $\mu\Omega$.cm$^2$ was assumed, which is generally the case for CFD samples [86]. The remaining material properties were available in the literature [10].

As observed in Figure 5.8 and Figure 5.9, the model provided good predictions of the NZPV for both regular samples (STI and SP). While the simulation results are in good agreement with the experimental NPZV values for the SP IJP CFD sample, the model slightly overestimates the NZPV of the STI IJP CFD sample (by $\approx$ 16 %). The reasons for this discrepancy remain unclear for the moment but it is possible that the quality of the interface between the printed silver and the REBCO layer is slightly different between the STI IJP CFD tape and the SP IJP CFD tape.

## 5.6 Conclusion

In this work, it was demonstrated that the CFD architecture can be implemented by depositing a narrow line of silver directly on the REBCO surface of a commercial tape. Starting from an oxygenated REBCO tape where silver has been etched chemically, the silver line was deposited using IJP, which was followed by an oxygen annealing and by the deposition by sputtering of a silver layer on the whole REBCO layer. It was shown that this CFD fabrication method was compatible with REBCO tapes from two different tape manufacturers, STI and SuperPower. No degradation of the critical current was observed in the IJP CFD tapes in comparison with regular (unmodified) REBCO tapes. Furthermore, the measured NZPV of the IJP CFD samples was several times higher than that of the regular samples, confirming the presence of the CFD effect.

Ultimately, this CFD fabrication process could be integrated in the traditional fabrication process of REBCO tapes used by manufacturers. Indeed, the silver inkjet printing step could be easily inserted between the growth of the REBCO layer and the oxygenation step. In contrary to the original CFD fabrication method, no chemical etching and masking/demasking steps would be required, thus greatly simplifying the CFD fabrication process. Further optimization of the printing process should be done to improve the quality of the silver lines. Also, further work might be required to optimize the oxygenation of a REBCO layer in the case where its surface is only partially covered by silver.

## 5.7 Acknowledgement

This project has received funding from the Canadian National Sciences and Engineering Research Council (NSERC), CMC Microsystems, and Mitacs.

# CHAPTER 6 ARTICLE 3 - DEVELOPMENT AND PERFORMANCE OF HIGH-TEMPERATURE SUPERCONDUCTING CORC® CABLES WITH CFD REBCO TAPES

*Authors: Haïfa Ben Saâd, Christian Lacroix, Delano Horn-Bourque, Emelie Nilsson, Jean-François Rouquette, Danko van der Laan, Jeremy Weiss, Kyle Radcliff, and Frédéric Sirois*

This article was submitted to the journal Superconductor Science and Technology on August 14th, 2024

## 6.1 Abstract

Increasing the normal zone propagation velocity (NZPV) in superconducting cables based on rare earth barium copper oxide (REBCO) tapes is expected to cause a paradigm shift by enabling the development of faster and more reliable quench detection systems to mitigate the development of destructive hot spots. Furthermore, a higher NZPV is beneficial in terms of fault current limitation capabilities by accelerating the homogenization of the quench in superconducting power devices. One way envisioned to increase the NZPV of cables based on REBCO tapes is the current flow diverter (CFD) concept. A Conductor on Round Core (CORC®) cable made with CFD REBCO tapes, called CFD CORC® cable, and a CORC® cable made with regular REBCO tapes, were fabricated and tested. The critical current of the CFD and regular CORC® cables were obtained at temperatures ranging from 67 to 77 K in self-field. Measurements showed that the NZPV was increased by a factor of 4.5 in the case of the CFD CORC® cable. Furthermore, the results suggest that the NZPV depends only on the applied current, similar to what has been observed previously on single REBCO tapes. These results demonstrate the successful integration of CFD REBCO tapes in CORC® cables, which represents an important step towards the implementation of the CFD concept for increasing the reliability and protection of high-current superconducting devices based on REBCO tapes.

## 6.2 Introduction

Rare earth barium copper oxide (REBCO) coated conductors (CCs) offer unprecedented performance regarding the operating temperature, current density, and applied magnetic field. For instance, these materials exhibit excellent superconducting properties above the boiling temperature of liquid nitrogen or in a magnetic field that exceeds 20 T (upper critical magnetic field of more than 100 T at 4.2 K) [18, 130, 131]. Recently, high-field magnets based on single REBCO tapes achieved a record DC magnetic field of 45.5 T, making this class of material a promising candidate for fusion and accelerator magnets [3].

In the last decade, the fusion and particle accelerator communities, such as the U.S. Magnet Development Program (MDP) [132], the European EuCARD-2 collaboration [133, 134] and the collaboration between Commonwealth Fusion Systems (CFS) and the Massachusetts Institute of Technology (MIT) [59,135], have led several projects to develop high-field magnets manufactured from REBCO tapes and cables. These magnets require high operating currents that exceed 10 kA and low magnet inductance [46,55,136,137]. Furthermore, superconducting cables assembled from REBCO tapes have gained interest in power transmission, enabling high transmission capacity in a compact size and in some cases, fault current limitation capability [138]. REBCO cables are currently being installed and tested in the electric networks of electric navy ships [139], railway applications [140] and electric aircraft systems [4, 141], to help decarbonize transportation.

Over the years, several cabling assemblies have been proposed, including Roebel cables [47], Twisted-Stacked Tapes Cables (TSTC) [142], Symmetric Tape Round (STAR) wires [143], VIPER cables [144], and Conductors on Round Core (CORC®) cables [145]. In particular, CORC® cables have gained interest due to their round cross-section, mechanical flexibility, high current carrying capacity (up to 500 A/mm$^2$ at 4.2 K and in a magnetic field of 20 T), and thermal stability [146, 147].

An interesting feature of CORC® cables is that no interlayer insulation separates the REBCO tapes, which allows for current sharing between the tapes when a normal zone nucleates. This current redistribution in CORC® cables may provide a signal that could help detect the quench and activate a protection system to prevent a thermal runaway. Different quench detection approaches, such as optical fibers [76, 116], hall probe-based technique [71], and active acoustic thermometry [74], were tested on CORC® cables. However, the efficacy of these methods for the safe operation of superconducting devices has yet to be demonstrated [70].

Until now, quench detection experiments have been conducted on CORC® cables made from regular (commercial) REBCO tapes. Regular REBCO tapes are known to have a low normal zone propagation velocity (NZPV), as well as a local critical current ($I_c$) variation along their length [148, 149]. The combination of these two factors can produce local hot spots, that are difficult to detect, exposing CORC® cables to possible irreversible damage.

It has been demonstrated that the current flow diverter (CFD) concept can drastically increase the NZPV in REBCO tapes. This concept is based on the modification of the architecture of regular REBCO tapes by inserting a non-uniform interfacial resistance ($R_i$) between the REBCO layer and the silver stabilizer. When a normal zone nucleates, this arrangement forces the current to take the path with the lowest resistance when it transfers from the REBCO layer to the silver layer. The deviation of the current path increases the current transfer length (CTL) between the REBCO and the silver layers, leading to an increase in the NZPV [10]. This was demonstrated experimentally on centimeter-scale REBCO tapes [78], as well as on meter-scale REBCO tapes [150].

In this paper, the performance of several CFD REBCO tapes assembled in the form of a CORC® cable, called CFD CORC® cable, is investigated. The performance of the CFD CORC® cable is compared with that of a regular CORC® cable fabricated using regular REBCO tapes. The first section includes the fabrication details of the CFD and regular CORC® cables used in this paper, along with a description of the critical current and NZPV measurements setup. The second section describes the critical current measurements performed on these CORC® cables at temperatures ranging from to 67 to 77.3 K. The final section presents NZPV measurements of the CORC® cables.

## 6.3 Experimental approach

### 6.3.1 REBCO tapes parameters

Commercial REBCO tapes purchased from SuperPower Inc. (SP) were used to fabricate two CORC® cables: a first CORC® cable made with CFD REBCO tapes and a second CORC® cable made with regular REBCO tapes, which, for the rest of the paper, will be called CFD CORC® cable and "regular" CORC® cable, respectively. Regular SP REBCO tapes, as shown in Figure 6.1(a), contained a 50 $\mu$m thick Hastelloy substrate on which was grown a stack of buffer (oxides) layers having a thickness of 0.58 to 0.78 $\mu$m. On the buffer layers, a 1.6 $\mu$m thick REBCO layer was deposited by metal-organic chemical vapor deposition [34]. Finally, a silver stabilizer layer surrounding the 4 mm wide REBCO tape was deposited (the total thickness of silver was 2.5 $\mu$m). In the CFD architecture, a patterned high interfacial resistance (CFD layer) was inserted in the middle of the tape between the REBCO and the silver layer (see Figure 6.1(b)). The width of the CFD layer was 3.2 mm, which corresponds to a coverage fraction $f$ of 0.8 ($f$ is the ratio between the total width of the tape and the width of the CFD layer) [10].

To fabricate the CFD CORC® cable, six one-meter-long CFD tapes were first manufactured using a custom reel-to-reel machine. Further details about the reel-to-reel CFD fabrication

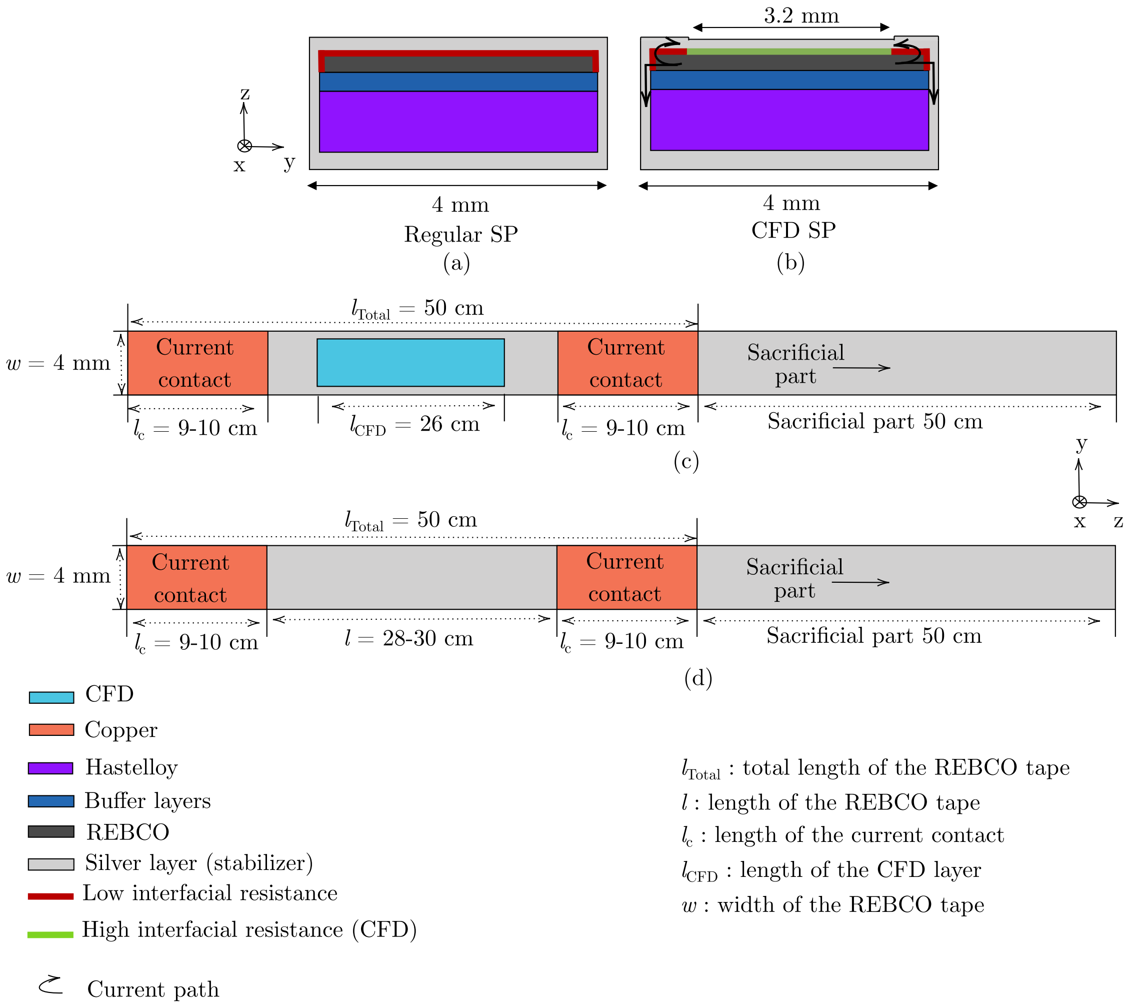

Figure 6.1 Geometry of the fabricated tapes to be integrated in CORC® cables: (a) cross-sectional view of the regular architecture, (b) cross-sectional view of the CFD architecture, (c) top view of the CFD SP tape, and (d) top view of the regular SP tape.

process are available in [150]. Figure 6.1(c) illustrates the top view of the geometry of the CFD REBCO tapes. Each tape comprised four different sections over its length. The first and the third sections (orange rectangles) of the tape were dedicated to the CORC® cable terminals. In these sections, 10 $\mu$m of copper was electrodeposited locally over a length of $l_c = 9$-10 cm on each side of the tape to facilitate the indium soldering of the CORC® cable terminals without destroying the silver layer. Indeed, soldering with indium on a thin silver layer creates an intermetallic compound indium-silver (In-Ag) on top of the REBCO layer [123,151]. In the worst case, the silver layer can be completely consumed, and the solder may react with the REBCO layer, leading to a degradation of the critical current. The CFD layer was integrated into the section between the copper contact terminals over a length of

$l_{CFD}$ = 26 cm (cyan rectangle). The fourth section acted as a 50 cm long sacrificial part used to attach the tape to the CORC® cable winding machine.

Six one-meter-long regular SP tapes were also prepared to manufacture a 30 cm long regular CORC® cable. Figure 6.1(d) illustrates the top view of the geometry of the regular REBCO tapes used to fabricate the regular CORC® cable. Similarly to the tapes used in the CFD CORC® cable, the regular REBCO tapes contained four sections: the second and the fourth sections of the REBCO tape remained unmodified (grey rectangles), and the first and third sections (orange rectangles) were copper-coated parts for current terminals. Table 6.1 gives the main parameters of the CFD and regular REBCO tapes employed to fabricate the CFD and regular CORC® cables, respectively.

### 6.3.2 CORC®cable parameters

Before the fabrication of the CORC® cables, bending tests were performed on the CFD and regular REBCO tapes to determine the minimum former diameter on which both CFD and regular tapes could be wound without degradation of their critical current [147]. Figure 6.2 shows the critical current retention as a function of the former diameter for CFD REBCO tapes (red triangles) and regular REBCO tapes (blue circles). Results showed that the critical current was reduced by 25% for the CFD tape, and by 32% for the regular tape, when the tapes were bent around a diameter of 6 mm. Therefore, a copper former of 6.35 mm OD, on which two layers of thermoplastic (heat shrink) were added to electrically insulate the REBCO tapes from the former, resulting in an overall bending diameter of 6.9 mm, was used to fabricate the CORC® cables.

The CFD and regular CORC® cables contained two layers of REBCO tapes. In one layer, three REBCO tapes were twisted, with the REBCO surface facing the insulated copper former, with a winding angle ($\beta$) of 37.7° for the outer layer. Figure 6.3 shows an example of the fabricated CORC® cables. Both ends of the CORC® cables were inserted in copper tubes with an ID of 9.4 mm and an OD of 12.7 mm. The copper tubes were then filled with indium solder to ensure a good electrical contact between the tapes and the copper tube. The terminal length was 4 cm for the CFD CORC® cable and 3 cm for the regular CORC® cable. The parameters of both cables are presented in Table 6.2. A schematic representative of a CORC® cable is presented in Fig 6.4.

Table 6.1 Main parameters of the CFD and regular REBCO tapes.

| Parameters | CFD tape | Regular tape |
|---|---|---|
| Width (mm) | 4 | 4 |
| Top silver layer thickness ($\mu$m) | 1 | 1 |
| Bottom silver layer thickness ($\mu$m) | 1.5 | 1.5 |
| $I_c$ at 77 K, self field (A) | $120 \pm 4$ | $123 \pm 3$ |
| $n$ at 77 K, self field | $22 \pm 2$ | $21 \pm 2$ |
| Thickness of the tape $e$ ($\mu$m) | 55 | 55 |
| CFD coverage fraction $f$ | 0.8 | 0 |

Table 6.2 Main parameters of the CFD and regular CORC®cables.

| Parameters | CFD CORC® | Regular CORC® |
|---|---|---|
| Total cable length (cm) | 30 | 30 |
| Number of layers | 2 | 2 |
| Number of tapes per layer | 3 | 3 |
| Terminals length (cm) | 4 | 3 |
| Terminals diameter (mm) | 12.7 (OD), 9.4 (ID) | 12.7 (OD), 9.4 (ID) |
| Copper former diameter (mm) | 6.9 | 6.9 |
| Copper former radius $R$ (mm) | 3.45 | 3.45 |
| Twist pitch of the outer layer $t$ (mm) | 17 | 17 |
| Winding angle of outer layer $\beta$ (°) | 37.7 | 37.7 |
| Former-tape insulation | Thermoplastic | Thermoplastic |

### 6.3.3 Critical current and NZPV measurements

Figure 6.5 displays a picture of the sample holder and voltage measurement system used in this work. The sample was connected to the power supply with copper cables screwed in copper blocks fixed to the CORC® cable terminations. Cylindrical grooves were made in the copper blocks to match the shape of the CORC® cable terminations. Each cable termination was securely screwed between the two copper blocks to ensure a balanced current injection. The sample and copper blocks were installed on a wooden support but not anchored to avoid damage due to thermomechanical constraints during cooling. During measurements, the entire assembly was immersed in a liquid nitrogen bath.

For the electrical measurements, a pulsed current source was used to inject square pulse currents of various amplitudes in the cables. The $I_c$ was determined by measuring the total voltage over the entire cable and by using an electric field criterion ($E_c$) of 1 $\mu$V/m. The total voltage was measured from two voltage taps soldered inside the CORC® cable terminals, with a tap dedicated to each terminal.

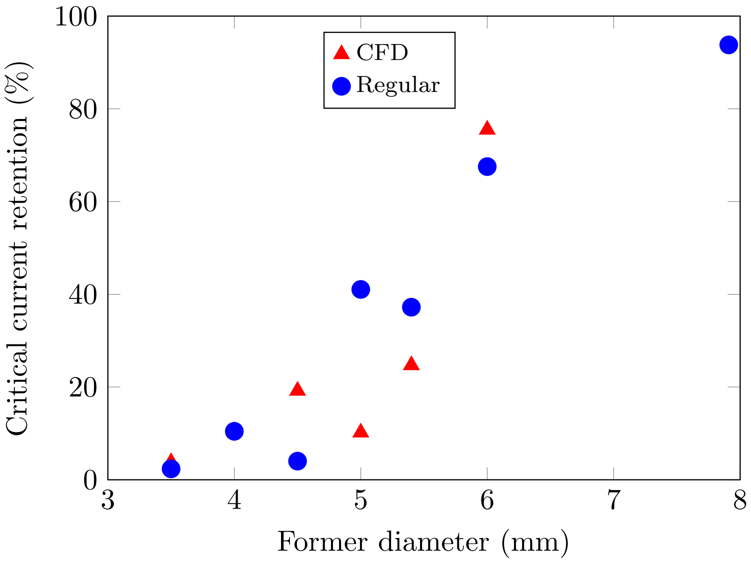

Figure 6.2 Critical current retention of CFD REBCO tapes (red triangle) and regular REBCO tapes (blue circles), after being bent at an angle of approximately 45° on copper formers with various diameters.

A 16 cm long printed circuit board (PCB) with pogo pins soldered at every 5.9 mm, used as voltage taps, was used to measure the NZPV. The distance between each pogo pin was based on the twist pitch of the cables, which ensured that each pogo pin was positioned in the middle of each tape on the outer layer, as shown in Figure 6.4 (top). Pogo pins thus measured the potential difference ($V_{i,l}$, $i = 10$, 9 and 8 in Figure 6.4) between two adjacent tapes on the outer layer. The measured voltages were recorded by a multi-channel data acquisition card (DAQ). To initiate a quench, cylindrical NdFeB magnets were inserted in the wooden support to decrease locally the critical current of the CORC® cable over a length of 8 mm (see Figure 6.5(d)).

To perform temperature dependent measurements, the CORC® cable and its sample holder were installed in a closed cryostat containing liquid nitrogen, and in which the pressure was reduced with a vacuum pump to reduce the boiling point of the liquid nitrogen and decrease its temperature. This method enabled us to perform measurements at any temperature between 65 and 77 K. Within the cryostat, PT100 sensors were employed to monitor the temperature. A capacitive level sensor was used to measure the liquid nitrogen level during measurements, to make sure the sample remained in liquid nitrogen during the entire experiment.

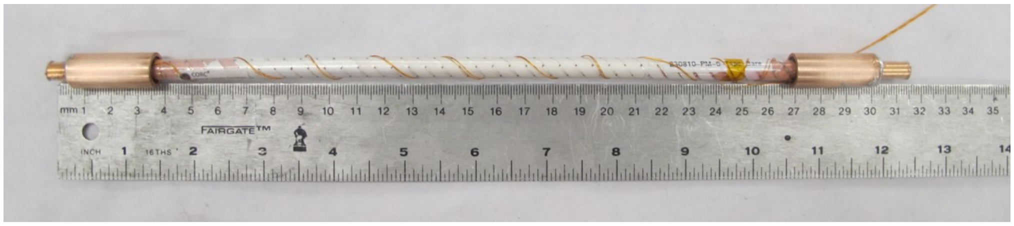

Figure 6.3 CORC® cable containing two layers. Three REBCO tapes were twisted in each layer facing the copper former.

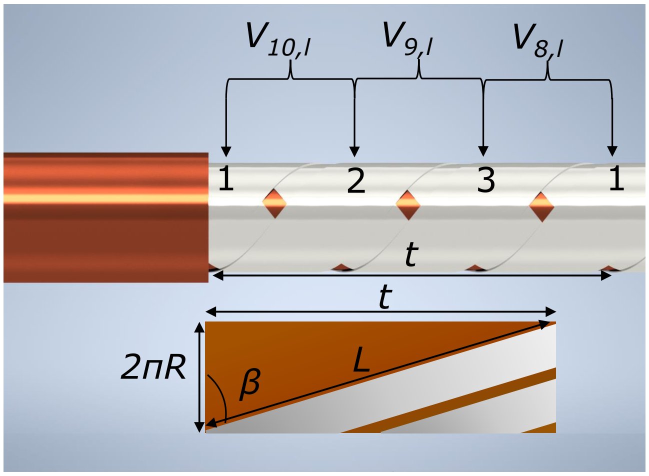

Figure 6.4 Top figure: schematic of the position of the voltage taps ($V_{i,l}, i = 10, 9, 8, l =$ left) on the outer layer of the CORC® cable. Bottom figure: schematic of REBCO tapes in a CORC® cable in a rectangular plane showing the length $L$ of a straight piece of REBCO tape along a full twist pitch $t$, and the twist angle of the outer layer $\beta$.

## 6.4 Critical current measurements

Before the fabrication of the CORC® cables, the critical currents of the CFD and regular REBCO tapes dedicated to the cables were measured in liquid nitrogen at ambient pressure (77 K) and in self-field. Figure 6.6 presents measurements of the $E$-$I$ characteristics of three CFD tapes and two regular tapes prepared for the CORC® cables fabrication. The average value of the critical currents of the CFD tapes was $120 \pm 4$ A at an electric field criterion of 1 $\mu$V/cm, while the $n$-factor was $22 \pm 2$. For the regular tapes, the average critical current was $123 \pm 3$ A, while the $n$-factor was $21 \pm 3$.

Considering the average critical current of a single tape at 77 K in self-field, the nominal

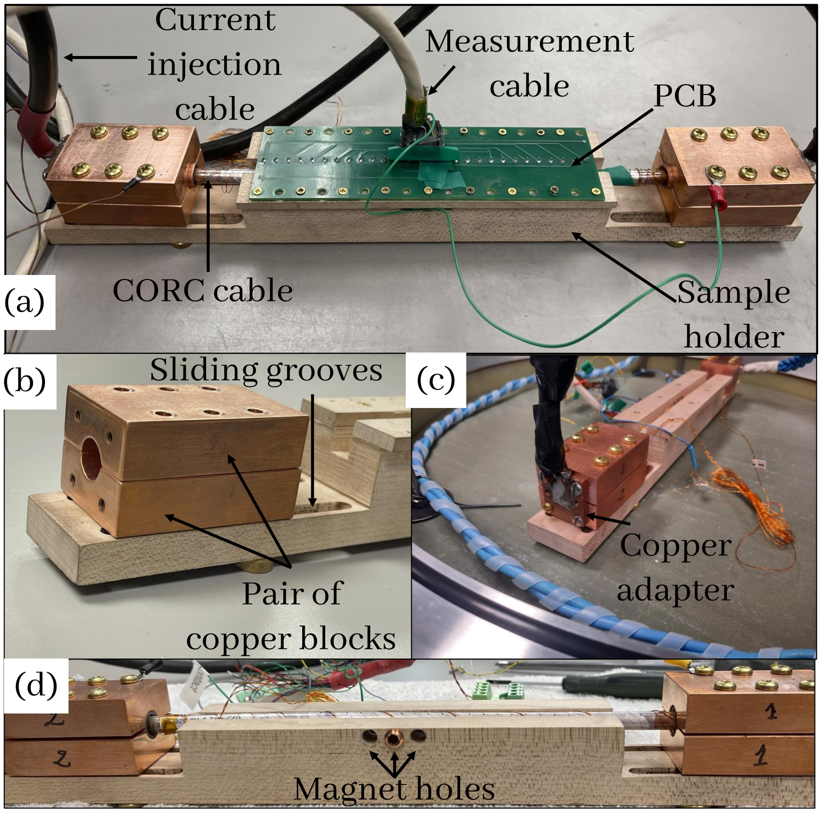

Figure 6.5 Sample holder and voltage measurement system used to obtain the critical current and the NZPV. The PCB has pogo pins on the hidden side that are used as electrodes for the voltage taps. (a) Example of a CORC® cable installed in the sample holder. (b) Copper blocks between which the CORC® cable terminals were clamped to ensure a good current injection. (c) Rectangular copper adapter that connects the current injection cable to the copper blocks. (d) Holes were created in the sample holder to insert NdFeB magnets during NZPV measurements.

critical current of the CORC® cables was determined by multiplying the average tape $I_c$ by the number of tapes (6), giving a nominal $I_c$ of 720 A for the CFD CORC® cable, and 738 A for the regular CORC® cable.

Before performing critical current experiments on the CORC® cables, the room temperature resistance was measured using the voltage taps inserted in the terminals. Values of 52 mΩ for the CFD CORC® cable and 44 mΩ for the regular CORC® cable were obtained.

The $E$-$I$ curve of the CFD CORC® cable was first measured at 77 K (black triangles in Figure 6.7). At low currents, a voltage originating from the current transfer from the cable terminals to the superconductor can be observed. Using the baseline method [38], this contribution can be subtracted from the experimental data to obtain the electric field of the superconductor alone. A power law function was used to fit the experimental data at low

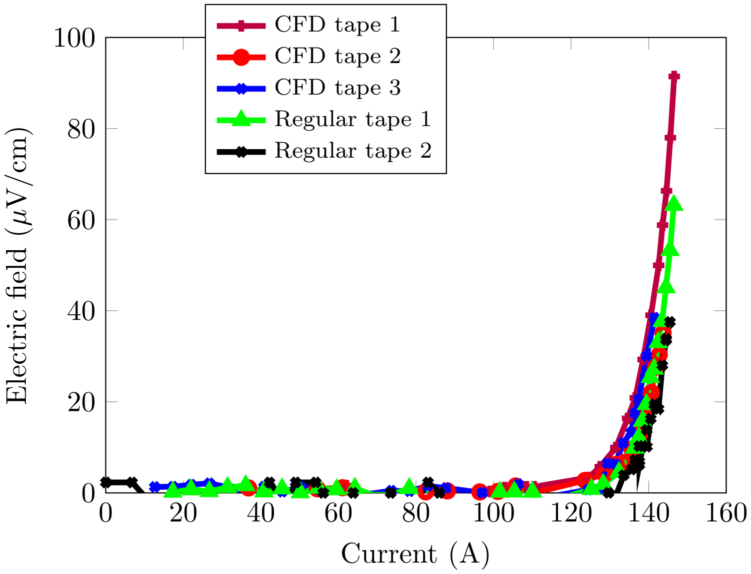

Figure 6.6 $E$-$I$ curves of three CFD REBCO tapes and two regular REBCO tapes used to fabricate both CORC® cables. The measurements were performed at 77 K and in self-field before integrating the tapes into the cables.

currents. The electric field in the superconductor $E_s$ is thus given by:

$$E_s = E - E_c \left( \frac{I}{I_{c,r}} \right)^{n_r} , \tag{6.1}$$

where $E_c = 1$ $\mu$V/cm , $I_{c,r}$ and $n_r$ (the index $r$ refers to the resistive current transfer voltage) are variables that were adjusted for the fit (red dashed line in Figure 6.7). Values of 150 A and 1.9 were found respectively for $I_{c,r}$ and $n_r$.

Once the current transfer voltage is removed, the resulting data correspond to the blues squares in Figure 6.7. These data were then fitted with a power law function (blue line). Using an electric field criterion of 1 $\mu$V/cm, a critical current of $581 \pm 4$ A and an $n$-factor of $26 \pm 4$ were found. We note that the critical current is 19% lower than the nominal critical current of 720 A estimated earlier. The difference between the nominal $I_c$ and the measured $I_c$ is probably due to a reduction in the critical current due to the magnetic field produced by the tapes on each other, or to the $I_c$ degradation due to the strain induced in the tapes when bending them around the former [152].

For the regular CORC® cable, the critical current was measured at 76 K using the measurement setup described in [153]. A critical current of 629 A was found. A calibrated sample was used to determine a conversion factor between 76 K and 77 K. A conversion factor of

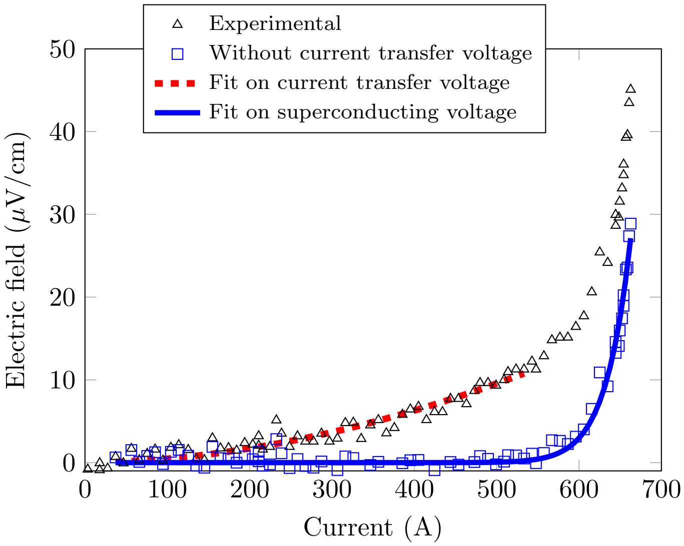

Figure 6.7 *E*-*I* curve of the CFD CORC® cable at 77 K and in self-field. The black triangles correspond to the measured electric field. The dashed red line is a fit of the current transfer voltage at low currents. Blue squares correspond to the remaining electric field after removing the current transfer voltage from the terminals over the whole range of current according to eq. (6.1). The solid blue line is a fit of the electric field of the superconductor alone using a power law model. Using a criterion of $E_c = 1$ μV/ cm, a $I_c$ of $581 \pm 4$ A and a *n*-factor of $26 \pm 4$ were found.

1.15 was found, resulting in a $I_c$ of 546 A for the regular CORC® cable at 77 K, which is 26% lower than the nominal critical current of 738 A.

The critical current of the CFD CORC® cable was measured at different temperatures. Figure 6.8 depicts the *E*-*I* curves obtained at 67.2 K, 71.3 K and 77.3 K. Experimental data of the *E*-*I* curves are presented in Figure 6.8(a), while Figure 6.8(b) shows the resulting *E*-*I* characteristics after subtracting the current transfer voltage. The solid lines represent curve fittings with a power law model.

Figure 6.9 presents the variation of the critical current ($E_c = 1$ μV/ cm) vs. the temperature for the CFD CORC® cable. The critical current increases from $540 \pm 5$ A to $1031 \pm 7$ A when the temperature decreases from 77.3 to 67.2 K. The temperature dependence of the critical current is linear, which is consistent with previous measurements performed on single tapes and CORC® cables at low temperatures (40-77 K) [152]. The *n*-factor was found to remain approximately constant ($\approx 33 \pm 4$) for this temperature range. We note that this *n*-factor is much higher than that of single REBCO tapes ($\approx 22 \pm 2$). Although the reason behind this sharp transition is not clear, previous measurements performed on CORC® cables between 40 and 77 K reported a high *n*-factor, up to 50 [55, 152].

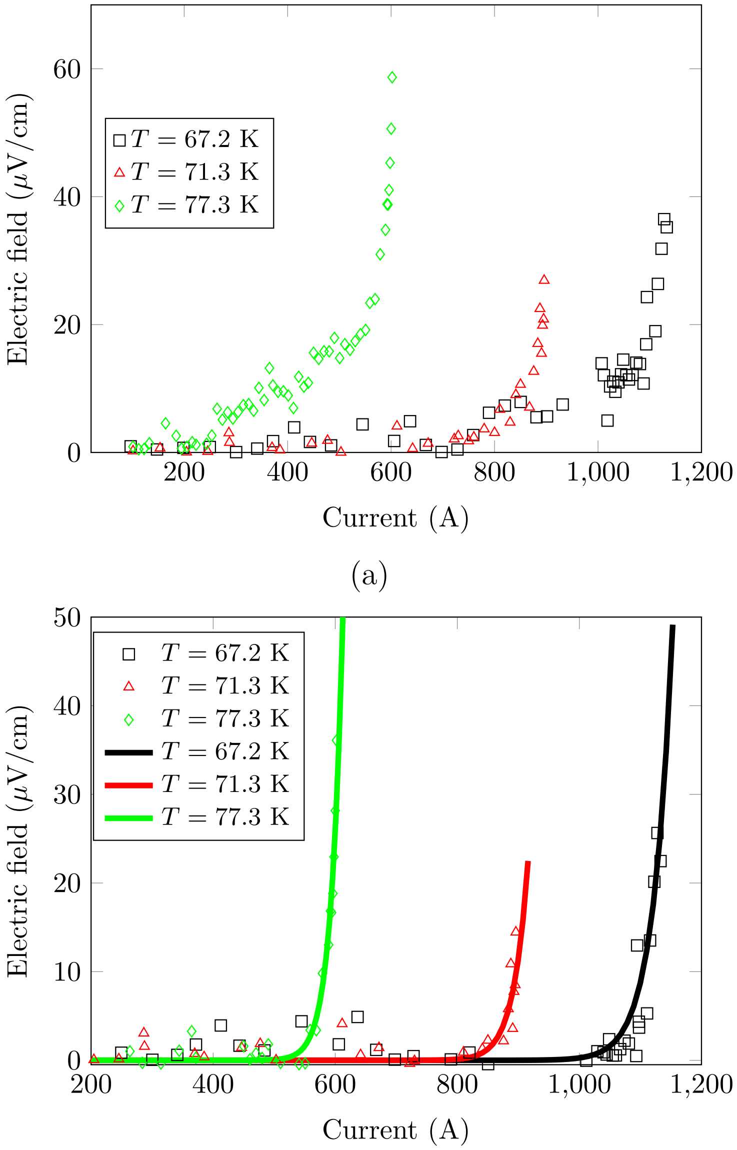

(a)

(b)

Figure 6.8 (a) *E*-*I* curves of a CFD CORC® cable as measured at temperatures $T$ of 67.2 K, 71.3 K, and 77.3 K. (b) Same *E*-*I* data without the current transfer voltage, at temperatures $T$ of 67.2 K, 71.3 K, and 77.3 K. The solid lines are a curve fitting based on a power law model.

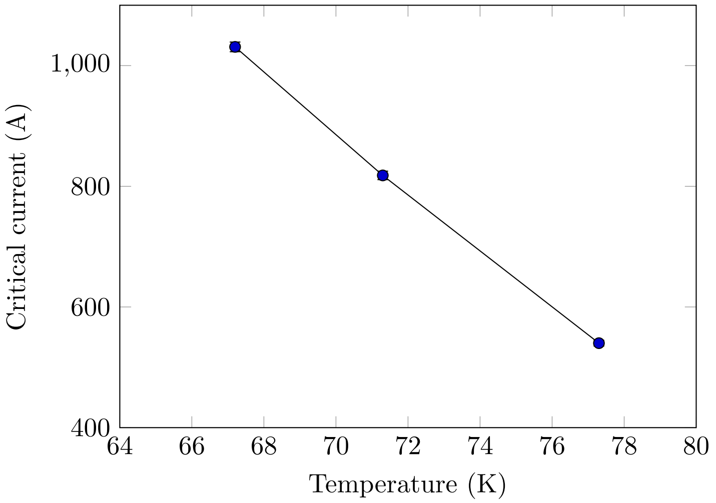

Figure 6.9 Temperature dependence of the critical current of the CFD CORC® cable (blue circles).

Note that the $I_c$ of the CFD CORC® cable at 77.3 K was slightly lower than that obtained in the initial measurement at 77 K (shown in Figure 6.7) (540 A vs. 581 A). Local measurements indicated that the voltage appeared in one of the terminals, suggesting that a degradation occurred in this terminal. It is suspected that this degradation is probably related to a bad current transfer due to the short length of the terminals. The use of longer terminals could probably solve this issue.

Unfortunately, the temperature dependence of the critical current of the regular CORC® cable could not be determined experimentally because the sample was degraded during NZPV measurements (see below). However, it is reasonable to assume that its critical current will depend on the temperature in a similar manner than the CFD CORC® cable, which would give a critical current of 1044 A at 67.2 K.

## 6.5 Normal zone propagation velocity measurements

As described in section 6.3.3, the NZPV was measured using voltage taps placed every 5.9 mm. Figure 6.10 presents the measured voltage that rises upon a quench in the regular CORC® cable for an applied current of 590 A. Each $V_{i,l}(i = 1, 2, 3)$ (solid lines) represents the potential difference between the voltage taps placed on the left side of the quenched zone, while $V_{i,r}(i = 1, 2, 3)$ (dashed lines) stands for the potential difference between the taps on the right side of the quenched zone. We observe that the generated voltage upon a quench is symmetric relative to the defect, indicating that the normal zone propagates similarly in

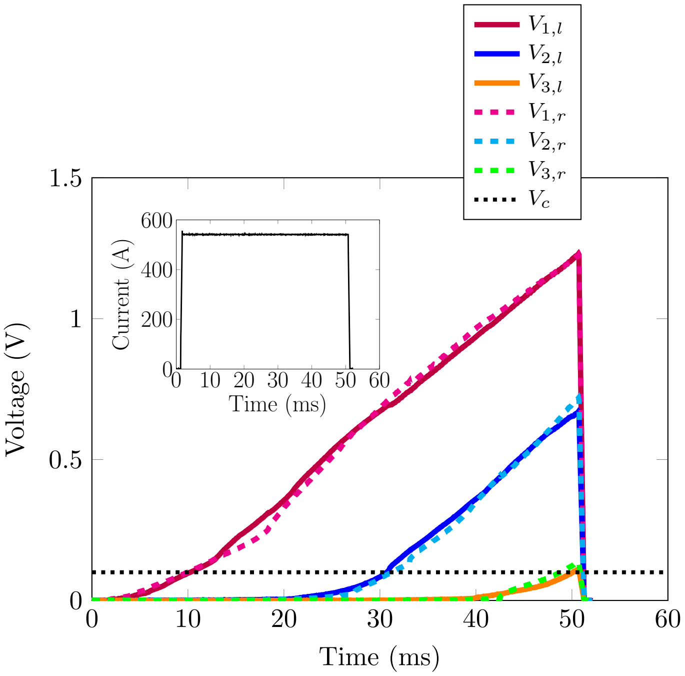

Figure 6.10 Measured voltage vs. time during the propagation of the normal zone in the regular CORC® cable. Solid lines represent the voltage measured in the voltage taps ($V_{i,l}$ ($i = 1, 2, 3$)) placed on the left side of the quench initiation zone. Dashed lines represent the voltages measured in the taps ($V_{i,r}$ ($i = 1, 2, 3$)) placed on the right of the quench initiation zone. The dotted black line is the voltage criterion ($V_c$) used to calculate the NZPV. Inset: applied current vs. time (590 A lasting 49 ms).

both directions. The voltage is highest at the probes that are the closest to the defect zone, and decreases as we move away from the defect. When the cable is superconducting, the interpretation of the local voltages in CORC® cables is not obvious because of the current sharing between the tapes. However, when all REBCO tapes are quenched, the entire current flows in the stabilizer layers and the current distribution in the CORC® cable becomes homogeneous, allowing us to measure the NZPV [154, 155]. Thus, the NZPV was calculated in the conventional way, that is, by dividing the distance between two successive voltage taps by the time required to reach $V_c = 0.1$ V at both taps.

The NZPV of the CFD CORC® cable and of the regular CORC® cable was first obtained at 77 K and in self-field. Figure 6.11 presents the NZPV obtained from the propagation of the normal zone for both CORC® cables. Similar to the quench behavior of a single REBCO tape, the NZPV increases with the applied current. Furthermore, the NZPV of the CFD CORC® cable is higher by a factor of 4.5 compared to the NZPV of a regular CORC® cable.

It is interesting to compare the behavior of CORC® cables with that of single REBCO tapes.

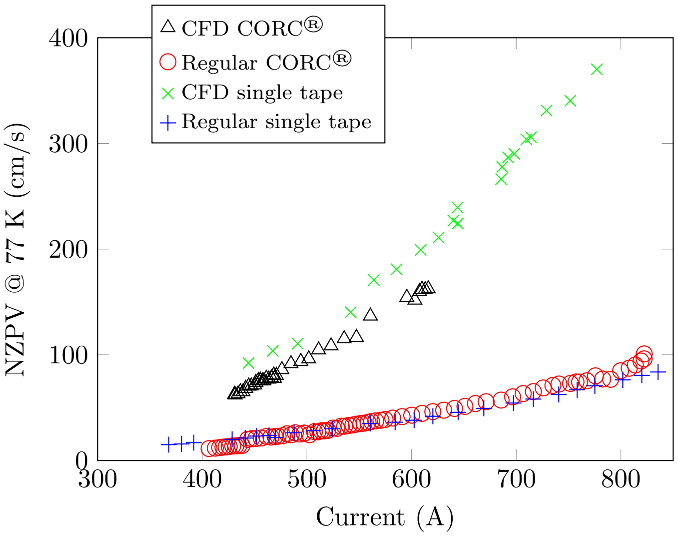

Figure 6.11 NZPV obtained at 77 K in self-field versus applied current for the CFD CORC® cable (black triangles), and the regular CORC® cable (red circles). The NZPV of a CFD tape (green x) and a regular tape (blue +) divided by the length ratio $p$ are also shown. For comparison, the applied current applied on the single tapes was multiplied by a factor of six, *i.e.* the number of tapes in the CORC® cables.

To make a fair comparison, the NZPV of the single REBCO tapes was divided by the ratio ($p$) between the initial length of the straight REBCO tape ($L$) and the twist pitch ($t$). This adjustment thus takes into account the helicoidal arrangement of the tapes in the cable. Fig 6.4 (bottom) presents a two-dimensional projection of the geometry of a CORC® cable in a rectangular plane. This projection was used to calculate $p$ between the length of a straight REBCO tape and wounded tape in the CORC® cable as follows [156]:

$$p = \frac{L}{t} = \frac{1}{sin(\beta)}\,, \tag{6.2}$$

$$t = 2\pi\tan(\beta)(R+e)\,, \tag{6.3}$$

where $t$ is the twist pitch of the outer layer, $\beta$ is the winding angle of the outer layer, $R$ is the radius of the former, $L$ is the initial length of the straight REBCO tape over a full twist pitch, which was equal to 27 mm in our case, and $e$ is the thickness of the tape. The $p$ value for our CORC® cables was 1.6.

Furthermore, the current applied on the single tapes was multiplied by six, to consider that the CORC® cables contain a total of 6 tapes. In Figure 6.11, we observe that the NZPV

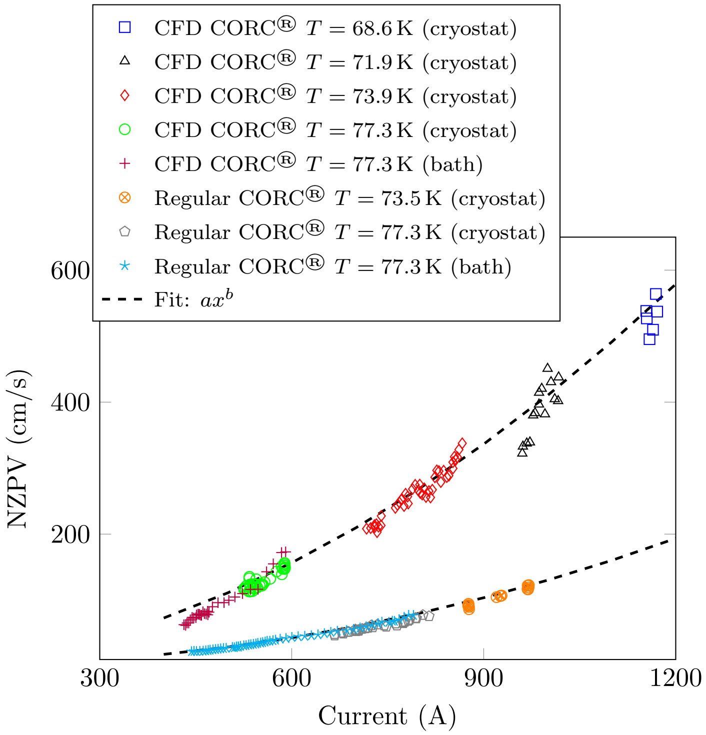

Figure 6.12 Experimental NZPV obtained at temperatures ranging from 68 K to 77 K in self-field vs. the applied current. Dashed lines are power law functions in the form of $y = ax^b$ fitted to the experimental data. Values of $a = 9.10^{-4}$ and $b = 1.89$ were found for the CFD CORC® cable, while values of $a = 4.10^{-5}$ and $b = 2.17$ were found for the regular CORC® cable.

values for a given architecture (regular or CFD) all follow the same curve. We conclude that the geometrical arrangement of the tapes in the configuration of a CORC® cable does not affect the NZPV gain factor that we observe on individual CFD tapes.

The temperature dependence of the NZPV was measured at temperatures ranging from 68.6 K to 77.3 K (see Figure 6.12). NZPV measurements performed in the cryostat were first made at 77.3 K to make sure that we obtained the same results as those obtained in a liquid nitrogen bath.

The dependence of the NZPV on the applied current could be well fitted with a power law function as follows:

$$\mathrm{NZPV}_{\mathrm{CFD}}(I) = 9.10^{-4}\, I^{1.89}\,, \tag{6.4}$$

$$\mathrm{NZPV}_{\mathrm{regular}}(I) = 4.10^{-5}\, I^{2.17}\,. \tag{6.5}$$

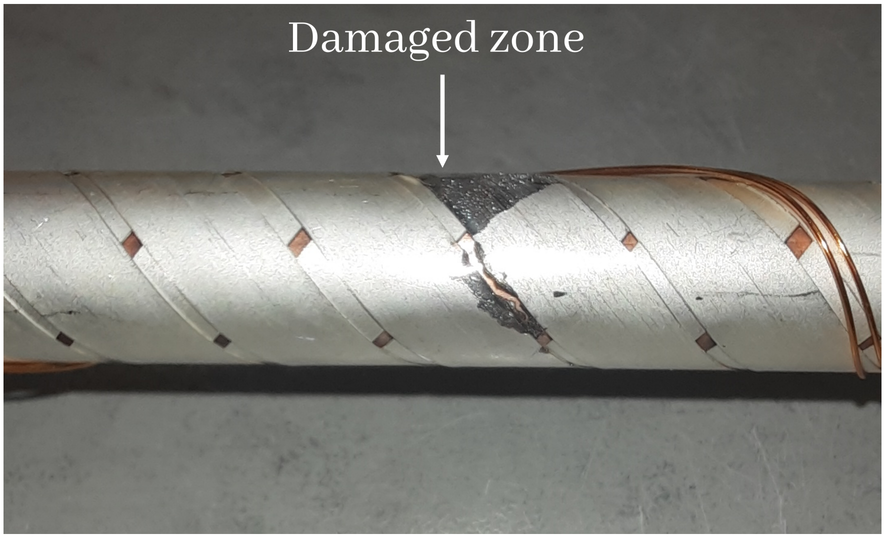

Figure 6.13 Damaged zone at the defect location in the regular CORC® cable. The damage occurred during NZPV measurements.

These results suggest that the NZPV primarily depends on the applied current rather than the temperature. This is consistent with previous results found for single REBCO tapes [8, 157].

Unfortunately, the regular CORC® cable was degraded after measuring the NZPV at 73.5 K (see Figure 6.13). The degradation occurred at the magnet location. Indeed, because of the slow NZPV, longer pulses had to be used to obtain reliable values. This increased the temperature at the defect location to much higher values than in the case of the CFD CORC® cable.

## 6.6 Conclusion

A CFD CORC® cable has been successfully manufactured by assembling six CFD REBCO tapes (two layers, three tapes per layer). The performance of the CFD CORC® cable was compared with a regular CORC® cable manufactured using six regular REBCO tapes. The critical current of the CFD CORC® cable at 77.3 K was 581 A, slightly higher than the critical current of the regular CORC® cable (546 A). A critical current of 1031 A was obtained at 67.2 K for the CFD CORC® cable.

Measurements showed that the NZPV of the CFD CORC® cable is 4.5 times higher than that of the regular CORC® cable. Furthermore, it was shown that the quench behaviors of the CFD and regular CORC® cables are similar to the behavior of single CFD and regular REBCO tapes, considering a helical longitudinal quench propagation along the tape. Also, the results suggest that the NZPV of CORC® cables depends only on the applied current and not the temperature, in agreement with previous results on the NZPV of single REBCO tapes. No degradation in the superconducting properties of the CFD CORC® cable was observed during the quench experiments. On the other hand, the regular CORC® cable was burnt at the defect location.

Finally, the successful incorporation of the CFD architecture in CORC® cables was achieved. The gain factor of the NZPV could be further improved by adjusting adequately the CFD tape architecture. These results are promising for the realization of superconducting power transmission cables with fault current limitation capabilities. The results are also promising in the context of magnets, since the different quench dynamics of CFD CORC® cables could help to improve eventually the response time of quench detection systems.

## 6.7 Acknowledgement

This project has received funding from the Canadian National Sciences and Engineering Research Council (NSERC), Mitacs, and CMC Microsystems. Part of the work was also supported by the U.S. Department of Energy, Office of High Energy Physics under contract number DE-SC140009, and ARPA-E under contract number DE-AR0001459. This work has also been supported by La direction Générale de l’Aviation civile (DGAC).

# CHAPTER 7 CFD REBCO COIL AND QUENCH PROTECTION

## 7.1 Introduction

It was demonstrated in **article 1** and **article 3** of this thesis, that implementing the CFD architecture in REBCO tapes led to an enhancement of the NZPV in long-length REBCO tapes and in an arrangement of CORC cables assembled from CFD REBCO tapes.

This chapter discusses the incorporation of the CFD architecture in a small-scale coil and explores its potential to improve quench protection in HTS magnet applications. More precisely, this work aims to increase the developed voltage upon a quench by increasing the NZPV of HTS coils using the CFD REBCO tapes. Indeed, the quench voltage is proportional to the NZPV. Increasing the quench voltage may improve the response time of quench detection systems, which could limit the rise of the hot spot temperature if the quench is detected early enough [69].

To test the performance of the CFD architecture in a coil, we conducted a comparative study of the quench behavior of i) a racetrack coil made from a CFD REBCO tape with one and a half turns, and ii) a coil fabricated from a regular (commercial) REBCO tape. Racetrack coils based on REBCO tapes were fabricated and tested in previous works for superconducting motors [158–160], and for magnet applications [161, 162].

Firstly, the NZPV and the quench voltage ($V_q(t)$) were measured for different applied currents at 77 K and in self-field. Secondly, numerical simulations using the power law model were carried out in COMSOL Multiphysics as an attempt to recreate the experimental results and extract the hot spot temperature. Thirdly, a second numerical model was developed to simulate the temporal profile of the quench voltage across REBCO tapes more accurately. This model, called the “piecewise model”, uses a new mathematical expression to model the $E$-$J$ characteristics of REBCO tapes. In the final section, the validity of the piecewise model was evaluated by comparing the experimental data of $V_q(t)$ obtained for the regular coil with the numerical data obtained using the piecewise model.

## 7.2 Experimental procedure

### 7.2.1 Samples preparation and description

In this experiment, two 1.5-turn coils were fabricated using REBCO tapes manufactured by SuperPower (SP) [34]. Details about the architecture of the REBCO tapes used in this

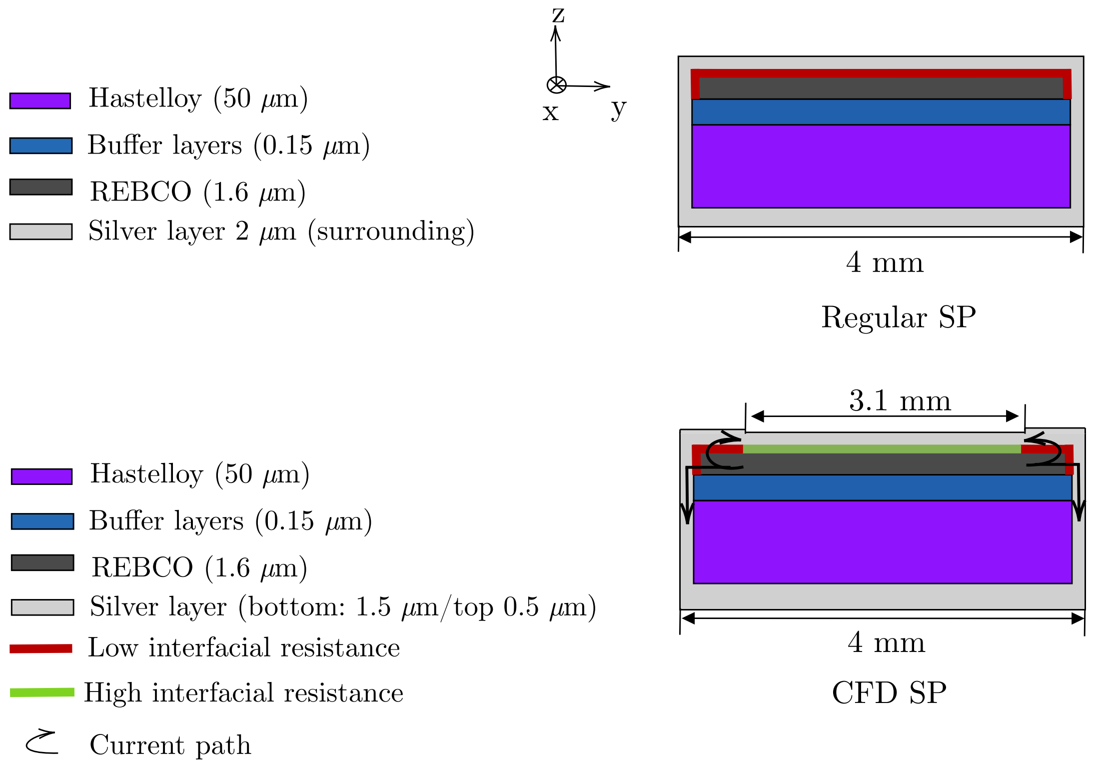

Figure 7.1 Cross-section of a commercial regular SP tape (top figure) [34], and cross-section of a CFD SP tape (bottom figure). Upon a quench, the current (black arrows) is forced to pass through the regions that have the lowest interfacial resistance to reach the stabilizer (*i.e.* silver) layer.

experiment are shown in Figure. 7.1. The first coil was manufactured using a regular (*i.e.* unmodified) SP tape. The second one was fabricated using a CFD SP tape. Both tapes had a total length of 50 cm, a width of 4 mm, a 50 $\mu$m thick Hastelloy substrate, a 1.6 $\mu$m thick REBCO layer, a 0.15 $\mu$m thick buffer layers stack, and a 2 $\mu$m thick surrounding silver layer. The key dimensions of the REBCO tapes are shown in Table. 7.1. The CFD fabrication process included an etching step of the top silver layer of the CFD tape. Then, silver was deposited by sputtering on both the HTS and the substrate side, keeping a total thickness of 2 $\mu$m surrounding silver with a thicker stabilizer (1.5 $\mu$m) for the bottom layer.

### 7.2.2 Coil fabrication and experimental setup

In this chapter, we refer to the coil fabricated from a regular SP tape as the regular coil, and the one fabricated from the CFD SP tape as the CFD coil. The regular tape and CFD tape

Table 7.1 Key dimensions of the regular SP tape, the CFD SP tape, the regular coil, and the CFD coil.

| REBCO tape dimensions | | |
|---|---|---|
| Parameters | Regular tape | CFD tape |
| Manufacturer | SuperPower | SuperPower |
| Width (mm) | 4 | 4 |
| Top silver layer thickness ($\mu$m) | 1 | 0.5 |
| Bottom silver layer thickness ($\mu$m) | 1 | 1.5 |
| $I_c$ at 77 K and in self-field (A) | 159±1 | 159±1 |
| CFD coverage fraction | 0 | 0.77 |
| Racetrack coil dimensions | | |
| Total tape length (cm) | 50 | |
| Number of turns | 1.5 | |
| Length of the straight section (mm) | 110 | |
| Outer diameter (mm) | 70 | |
| Turn to turn insulation | Kapton tape | |

were wound on a racetrack coil support with an outer diameter of 70 mm and a straight line section of 110 mm as shown in Figure 7.2. The coil support was made of wood. Both coils consisted of one and a half turns isolated by a Kapton tape. The key dimensions of the coils and the coil support are shown in Table. 7.1.

Figure. 7.2 and Figure. 7.3 respectively show the dimensions of the racetrack coil and the coil support with the PCB installed on top of the straight section. Copper blocks were attached to both ends of the coil and were used as current terminals. A PCB-based support with pogo pins was installed on the straight section of the racetrack to measure the critical current, the quench voltage across the coil, and the NZPV. A pair of voltage taps were installed on each copper block to measure the voltage between each current terminal and the PCB. A NdFeB permanent magnet was placed in the middle of the PCB to create a local critical current reduction that acts as a defect. Current pulses with constant amplitudes were injected in the coil, triggering a quench at the defect location. The voltage that rises when a normal zone propagates was measured by the PCB and the data was collected on a PC using a LabVIEW program. The NZPV was determined by the ratio between the distance separating two voltage taps and the time required to reach a given voltage criterion. The setup was immersed in a liquid nitrogen bath to perform the measurements at 77 K and in self-field.

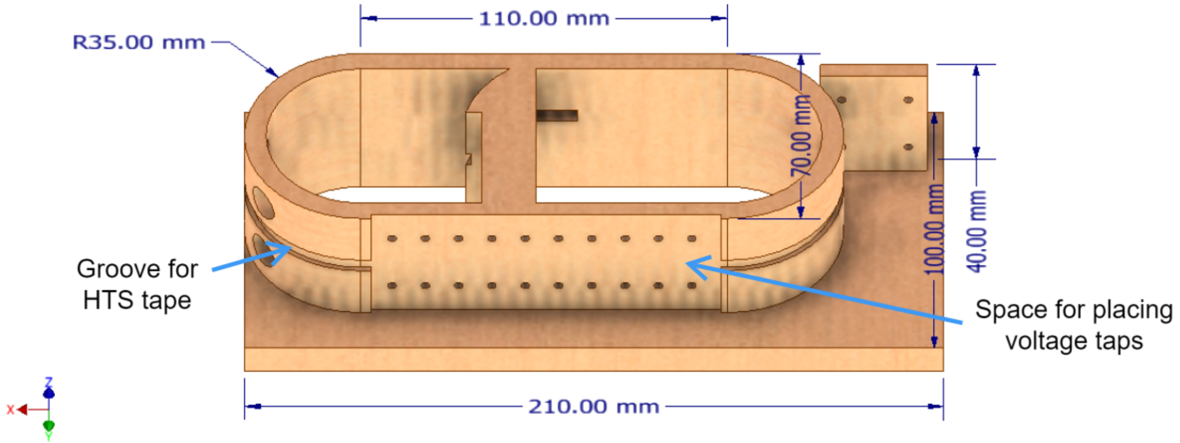

Figure 7.2 Schematic of the racetrack coil support.

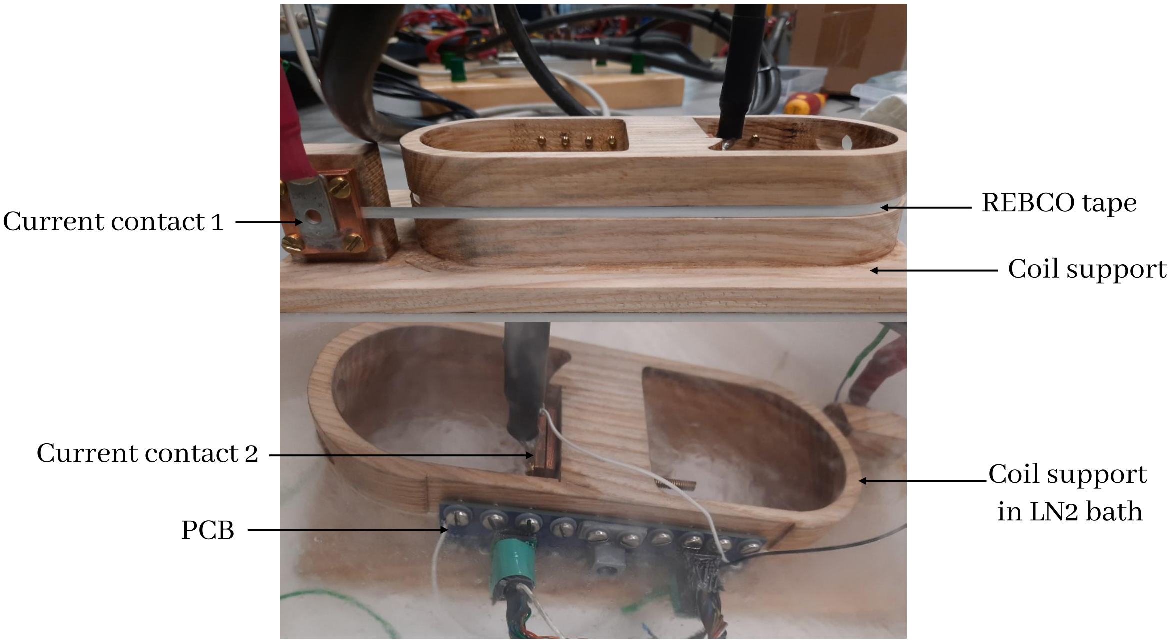

Figure 7.3 Final racetrack coil with the REBCO sample, before (top), and after (bottom) immersion in a liquid nitrogen bath. The PCB comprises voltage taps used to measure the critical current, the quench voltage, and the NZPV.

### 7.2.3 Finite element model based on a power law resistivity model

A 3D Finite Element (FE) electrothermal model based on a power law resistivity model was developed in the COMSOL 5.6 software package. In this model, the current continuity and the heat transfer equations were coupled by solving simultaneously in a time-dependent study, the electric current and heat transfer in solids modules of COMSOL. The geometry of the regular SP tape and the CFD SP tape implemented in the model were identical to the ones tested experimentally. The buffer layers and the resistive layer at the superconducting/silver interface were reduced to 2D boundaries to reduce the computational time. The experimental values of the applied current vs. time were added to the model as a floating potential at one extremity of the tape. The second extremity was grounded. The electrical conductivity data of silver were obtained from measurements of the tape resistance as a function of the temperature. Only the straight parts of the regular coil and the CFD coil were taken into account in this model.

To recreate the defect created by the permanent magnet in the experiment, a local reduction of the critical current density ($J_c$) was added to the model to act as a quench initiation zone.

The nonlinear conductivity ($\sigma_{PL}$) of the REBCO layer was implemented using the power law model. The superconducting-to-normal transition was implemented as two conductivities in parallel, *i.e.* $\sigma_{PL}$ and $\sigma_n$, where $\sigma_n$ is the conductivity of the REBCO layer in the normal state. A residual conductivity ($\sigma_{max} = 10^{17}$ S/m) was added to the expression of $\sigma_{REBCO}$ to avoid numerical problems when the current is around 0 A [10]. Thus, the conductivity of the REBCO layer ($\sigma_{REBCO}$) can be expressed as follows:

$$\sigma_{REBCO}(T) = (\sigma_{PL}(T) + \sigma_n(T)) + \sigma_{max}\,, \tag{7.1}$$

$$\sigma_{PL}(T) = \frac{J_c(T)}{E_c}\left(\frac{||\mathbf{E}||}{E_c}\right)^{\frac{1-n(T)}{n(T)}}\,, \tag{7.2}$$

$$J_c(T) = \begin{cases} J_{c0}\left(\frac{T_c - T}{T_c - T_0}\right) & \text{for } T < T_c\,, \\ 0 & \text{for } T \geq T_c\,, \end{cases} \tag{7.3}$$

$$n(T) = \begin{cases} (n_0 - 1)\left(\frac{T_c - T}{T_c - T_0}\right)^{1/4} + 1 & \text{for } T < T_c, \\ 1 & \text{for } T \geq T_c\,, \end{cases} \tag{7.4}$$

where $E_c$ is the electric field criterion (1 $\mu$V/cm), $J_{c0}$ represents the critical current density at the operating temperature $T_0$, here the liquid nitrogen temperature (77 K), $||\mathbf{E}||$ represents the norm of the electric field, $T_c$ is the critical temperature and $n_0$ is the power law index determined from experimental $V$-$I$ curves. The normal state conductivity $\sigma_n$ has the following dependence on the temperature [163]:

$$\sigma_n(T) = \frac{10^6}{100 + 0.47(T - T_c)} \,. \tag{7.5}$$

## 7.3 Critical current and NZPV measurements

The critical current ($I_c$) of the regular and CFD test coils was measured at 77 K and in self-field after each coil fabrication. The $I_c$ was 159±1 A for both coils (at an electric field criterion of 1 $\mu$V/cm), with a $n$-factor of 27±1. The fact that the critical current was the same for the regular coil and the CFD coil indicates that there was no degradation of the superconducting properties after the CFD tape fabrication and its winding in a coil geometry.

The results of the NZPV measurements at different applied currents for the regular and CFD coils are presented in Figure. 7.4. The symbols correspond to the experimental values, and the solid lines correspond to the simulation results with the power law model.

In the simulations, the value of the interfacial resistance ($R_i$) between the superconductor and the stabilizer layer was adjusted to 0.1 $\mu\Omega$.cm$^2$ instead of 1 $\mu\Omega$.cm$^2$ for a better agreement with the experimental results [84]. For instance, with $I = 135$ A, the numerical value of the NZPV for the regular coil was 1.11 m/s when $R_i = 1$ $\mu\Omega$.cm$^2$, while it was 0.98 m/s when $R_i = 0.1$ $\mu\Omega$.cm$^2$, which was closer to the experimental NZPV value (0.94 m/s). The critical current at the defect location was decreased by 47% due to the presence of the permanent magnet. This reduction was taken into account in the simulations.

The reported values show that for the same range of current, the NZPV of the CFD coil is 3 to 4 times higher than that of the regular coil. For example, when the applied current is 154 A, the value of the NZPV of the regular coil reaches 1.34 m/s, while it reaches 5.42 m/s in the case of the CFD coil. As a matter of fact, the NZPV of the CFD coil depends on the ratio between the width of the CFD layer and the total width of the tape, namely the coverage fraction ($f$) [86]. We expect a lift factor of 3 to 4 for the NZPV when the coverage fraction of the CFD tape is around 0.75-0.77.

## 7.4 Quench voltage measurements

The developed voltage upon a quench ($V_q(t)$) of the regular coil and the CFD coil was measured for different applied currents. Figure 7.5a, Figure 7.5b, Figure 7.5c, and Figure 7.5d present the experimental data of $V_q(t)$ of the regular coil (red dashed line) and the CFD coil

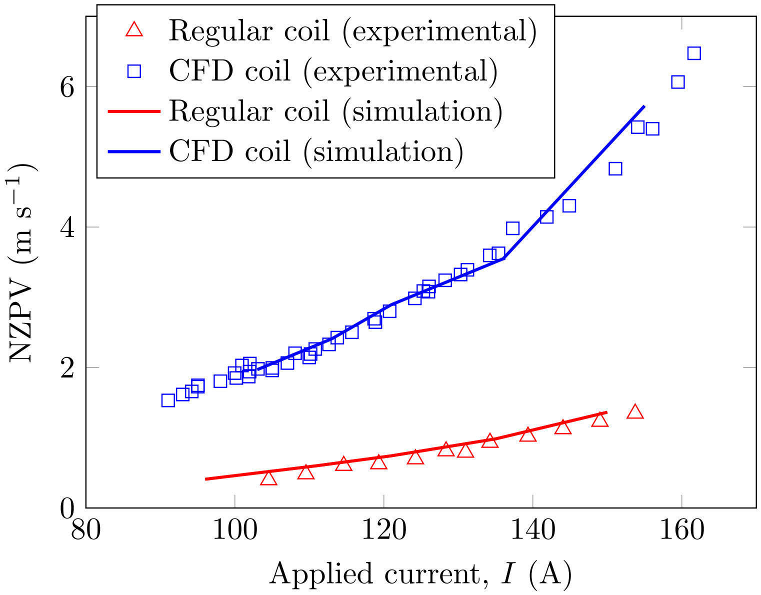

Figure 7.4 Measured NZPV values vs. the applied current for i) a regular coil (red triangles), and ii) a CFD coil (blue squares) at 77 K and in self-field. Solid lines were calculated by finite elements using the power law model for REBCO resistivity.

(blue dashed line) for an applied current of 96 A (*i.e.* 0.60 $I_c$), 120 A (*i.e.* 0.75 $I_c$), 135 A (*i.e.* 0.85 $I_c$), and 154 A (*i.e.* 0.97 $I_c$) respectively, along with the numerical simulation results (solid lines). No measurements were performed at an applied current of 96 A for the CFD coil (the applied current was 100 A, which was not the same amplitude). In the numerical model, the critical current of the defect region was fixed at 85 A. This value refers to the $I_c$ degradation caused by the permanent magnet in the experiment.

The developed quench voltage in the CFD coil is higher compared to that of the regular coil for all applied currents. For example, at $t = 13.2$ ms, and for $I = 120$ A, $V_q$ of the regular coil reaches 2.7 V, while it reaches 8.9 V for the CFD coil. At $t = 6.3$ ms, and for $I = 154$ A, the obtained $V_q$ is 2.8 V for the regular coil and 11.5 V for the CFD coil.

The value of $V_q(t)$ of the CFD coil is approximately 3 to 4 times higher than that of the regular coil after quenching. The quench voltage is proportional to the length of the normal zone ($L_{NZ}$) [164]. The NZPV measurements showed that the ratio between the NZPV of the CFD coil and of the regular coil is ranging between 3 and 4. As a result, the ratio between the quench voltage of the CFD coil and the regular coil should be equal to the NZPV ratio, which is confirmed by the measurements shown in Figure 7.5.

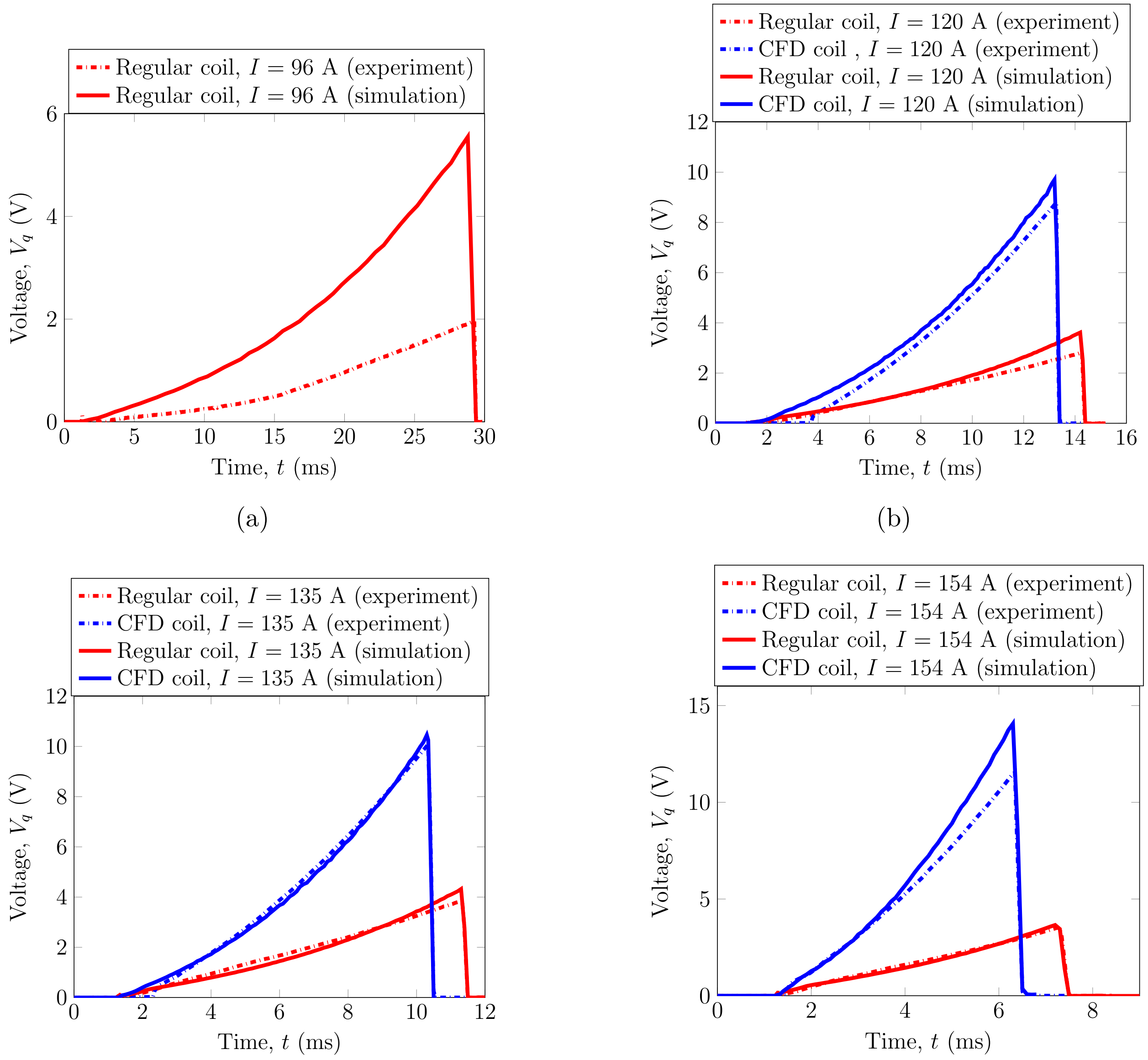

(a)

(b)

(c)

(d)

Figure 7.5 Measured quench voltages $V_q$ vs. time for i) a regular coil (red lines), and ii) a CFD coil (blue lines) for different applied currents: (a) $I = 96$ A, (b) $I = 120$ A, (c) $I = 135$ A, and (d) $I = 154$ A. Dashed lines correspond to experimental results and solid lines were calculated by finite elements using the power law numerical model for REBCO resistivity.

The numerical values of the quench voltages are slightly different than the experimental values. This discrepancy can be explained by the fact that the power law model does not accurately estimate the developed voltage upon a quench. Another explanation is that the critical current of the defect location can vary with respect to the position of the permanent magnet on the REBCO tape between the measurements. In our simulation, the degradation rate was kept at 47%. However, this should not affect much the NZPV.

The variation of the quench voltage vs. the hot spot temperature of both architectures (regular and CFD) was extracted from the numerical simulations for an applied current of 154 A. Results are presented in Figure. 7.6. As expected in the case of the CFD architecture, the developed quench voltage is increased by a factor of 4 when the hot spot temperature is less than room temperature.

To increase the gain factor in the quench voltage, the NZPV must be increased. The value of the coverage fraction was increased in the same simulation discussed above from 0.77 to 0.9. The applied current remained the same (154 A). According to the simulation results, the NZPV in the case of the CFD architecture is increased by a factor of 6. We obtain an NZPV of 8.01 m/s for the CFD tape and 1.34 m/s for the regular tape. As expected, the quench voltage is increased by a factor of 6 in the case of the CFD architecture before reaching room temperature. Thus the relationship between the quench voltage and the NZPV after the quench can be expressed by a simple proportionality law:

$$\frac{\mathrm{NZPV}_{\mathrm{CFD}}(T)}{\mathrm{NZPV}_{\mathrm{regular}}(T)} = \frac{V_{q\ \mathrm{CFD}}(T)}{V_{q\ \mathrm{regular}}(T)}\,, \tag{7.6}$$

where $\mathrm{NZPV}_{\mathrm{CFD}}(T)$ and $\mathrm{NZPV}_{\mathrm{regular}}(T)$ are the NZPV values of the CFD coil and the regular coil respectively, and $V_{q\ \mathrm{CFD}}(T)$ and $V_{q\ \mathrm{regular}}(T)$ are the quench voltages across the CFD coil and the regular coil respectively. This relationship is valid once the hot spot temperature is higher than $T_c$ (after quench, the pre-quench regime is not considered).

### 7.5 Finite element model based on a piecewise resistivity model

The range of operation of superconducting applications based on REBCO tapes or REBCO coils is around the critical current value. Mathematically, the power law model is commonly implemented to describe the non-linear ($E$-$J$) characteristics [165]. As mentioned above, in the power law model, $\sigma_{REBCO}$ is expressed as two conductivities in parallel, *i.e.* $\sigma_{PL}$ and $\sigma_n$, to model the superconducting-to-normal transition, and to ensure a gradual decrease of $\sigma_{REBCO}$ during the transition from the superconducting state to the normal state.

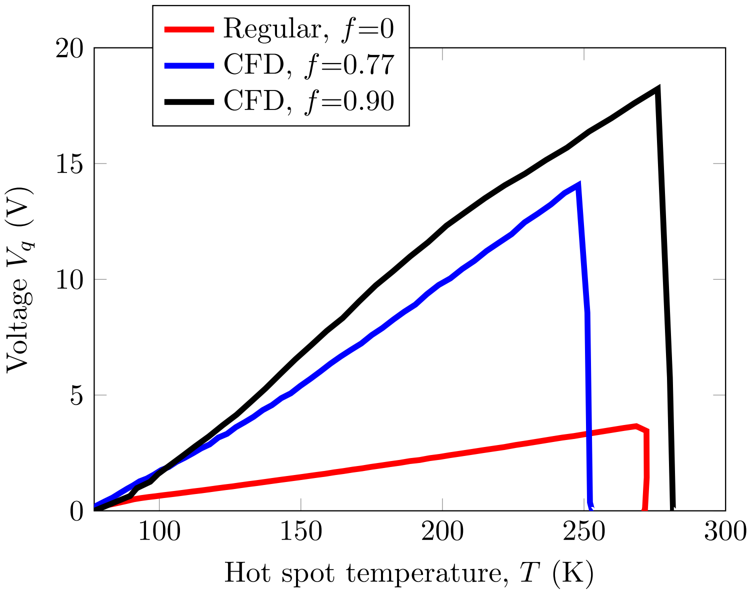

Figure 7.6 Numerical results of $V_q$ vs. the hot spot temperature for i) the regular (uniform) architecture ($f = 0$), ii) the CFD architecture with $f = 0.77$, and iii) the CFD architecture with $f = 0.90$. The quench voltage of the CFD architecture is 4 to 6 times higher than the quench voltage of the regular architecture.

Using this model, the simulated quench voltage was slightly different than the experimental data shown in Figures 7.5a, 7.5b, 7.5c and 7.5d. The regular tape quenches more rapidly compared to reality. We assumed that the power law model overestimates the quench voltage and temperature, especially for low values of the applied current. The deviation of the electrothermal response of REBCO tapes from the power law was reported in previous works [167–169].

In previous works, different models were developed to improve the accuracy of the simulated quench behavior of REBCO tapes, such as the piecewise power law model [166], the overcritical current model [170, 171], and the eta-beta model [167].

In this work, a piecewise model was developed based on subdividing $\sigma_{REBCO}(E)$ in three regimes with different mathematical expressions, representing the flux creep state, the flux flow state, and the normal state. The idea is similar to the piecewise power law model proposed in [166]. However, the originality of this model is that the flux flow state is not expressed by a power law function.

Figure 7.7 presents the schematic of the log-log plot of $E$ vs. $J$ for a fixed temperature. In the piecewise power law model [166], $E(J)$ is composed of three regions with three power laws

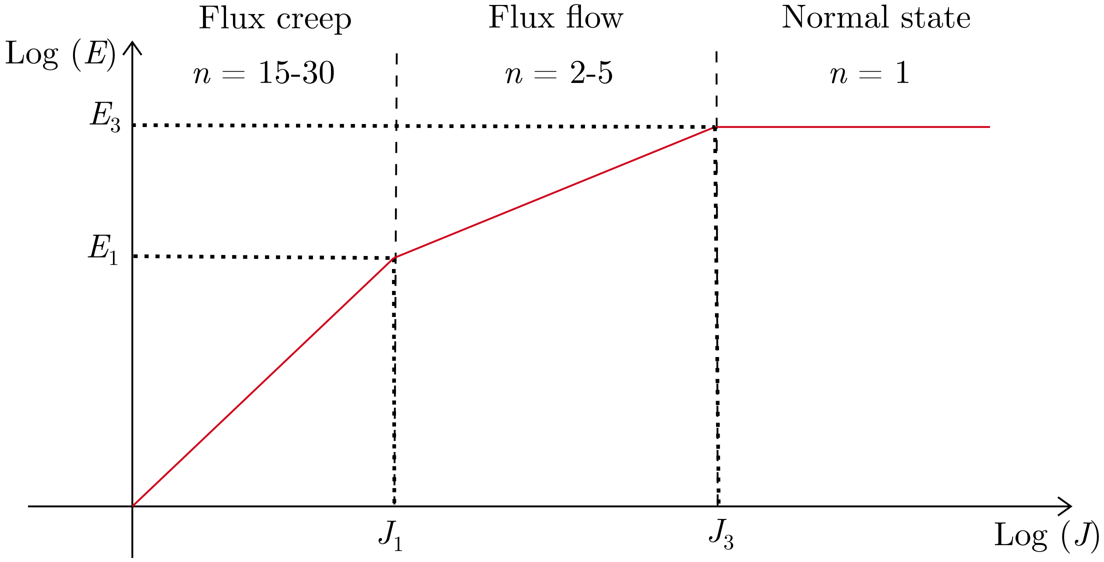

Figure 7.7 Schematic of the log-log plot of the $E$-$J$ characteristics of a REBCO tape for a fixed temperature. In the piecewise power law model [165, 166], the $E(J)$ curve is composed of three regions with three power laws. The point defined by $E_1(T)$ and $J_1(T)$ represents the transition from the flux creep state to the flux flow state and the point defined by $E_3(T)$ and $J_3(T)$ represents the transition from the flux flow state to the normal stale.

(three different $n$-factors). The point defined by $E_1(T)$ and $J_1(T)$ represents the transition from the flux creep state to the flux flow state, and the point defined by $E_3(T)$ and $J_3(T)$ represents the transition from the flux flow state to the normal stale.

In the new model proposed here, the power law represents the flux creep state. The flux flow state is represented by a quadratic continuous Bézier curve defined by three control points in each of the curves $\sigma_{REBCO}(E,T)$ and $\rho_{REBCO}(J,T)$, as shown in Figure 7.8a and Figure 7.8b respectively. The start points $A$ and $A'$ are defined by the coordinates $(\sigma_1(T), E_1(T))$ and $(\rho_1(T), J_1(T))$; the middle control points $B$ and $B'$ are defined by the coordinates $(\sigma_2(T), E_2(T))$ and $(\rho_2(T), J_2(T))$; the endpoints $C$ and $C'$ defined by the coordinates $(\sigma_3(T), E_3(T))$ and $(\rho_3(T), J_3(T))$. The curve starts at the first points $A$ and $A'$, ends at the third point $C$ and $C'$, and its curvature is influenced by the position of the two control points $B$ and $B'$.

Figure 7.8c and Figure 7.8d show respectively, the piecewise and power law conductivity $\sigma_{REBCO}(E,T)$, and resistivity $\rho_{REBCO}(J,T)$ at a temperature ranging from 77 to 83 K.

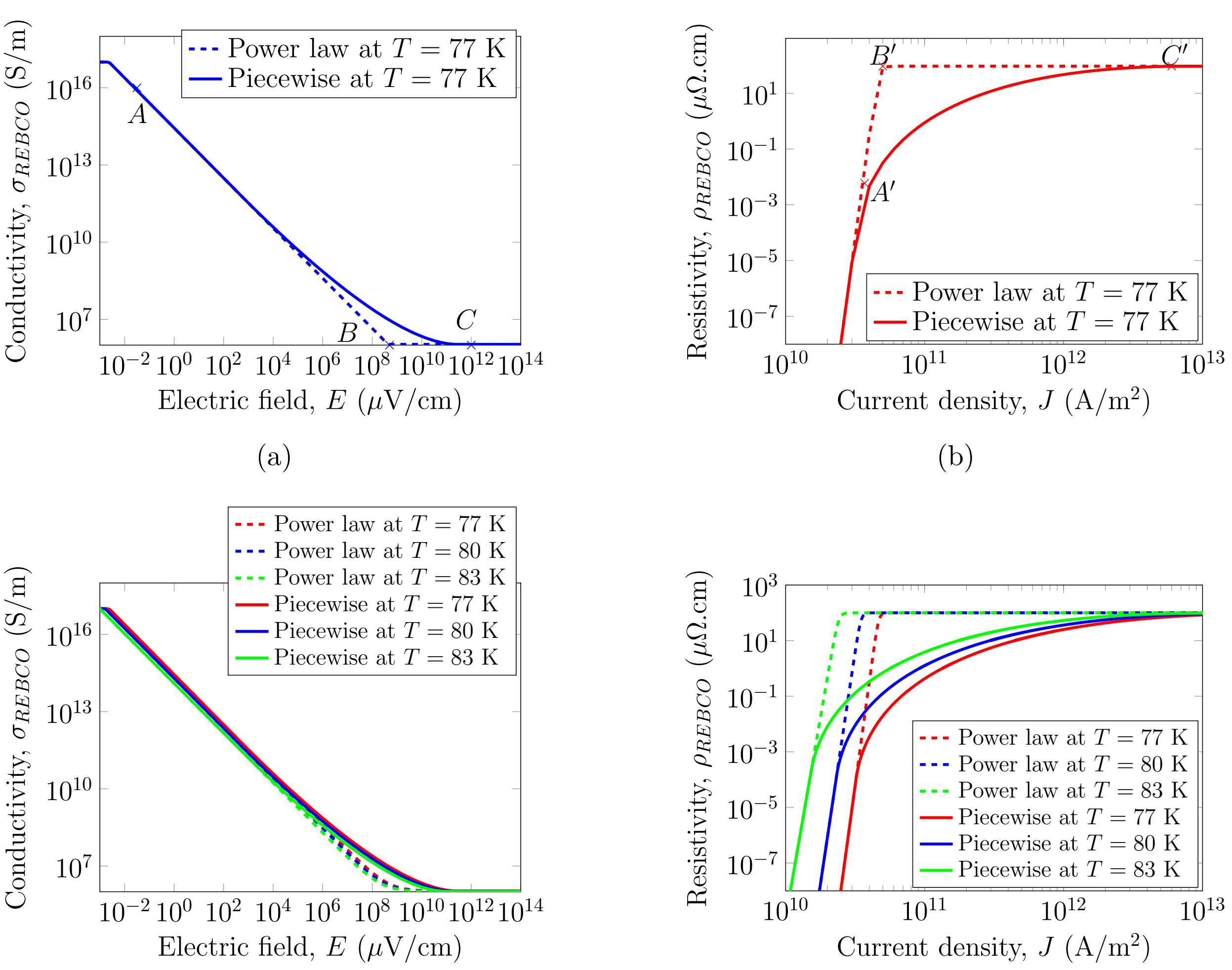

(a)

(b)

(c)

(d)

Figure 7.8 Left: REBCO layer conductivity $\sigma_{REBCO}(E)$ obtained with the new piecewise model (solid line) and with the power law model (dashed line) at a temperature of: (a) $T = 77$ K, and (c) $T = 77 - 83$ K. Right: REBCO layer resistivity $\rho_{REBCO}(J)$ obtained with the new piecewise model (solid line) and with the power law model (dashed line) at a temperature of: (a) $T = 77$ K, and (d) $T = 77{-}83$ K. The points $A$ and $A'$ are the intersection of the power law and the flux flow regimes. The points $B$ and $B'$ are the intersection of the power law regime and the normal state. The points $C$ and $C'$ are the intersection of the flux flow regime and the normal state.

Regardless of the operating temperature, the curves obtained using the Bézier function are continuous and do not overlap. The superconducting-to-normal transition of the curves obtained using the piecewise model is softened compared to those obtained using the power law model.

The mathematical expressions of the current densities $J_1(T)$, $J_2(T)$, and $J_3(T)$ are determined from the log-log plot of the $E$-$J$ characteristics as follows:

$$J_1(T) = J_c(T) 10^{\left(\frac{d}{n(T)}\right)}\,, \tag{7.7}$$

$$J_2(T) = J_1(T) \left(\frac{\rho_n(T)}{\rho_1(T)}\right)^{\left(\frac{1}{n(T)-1}\right)}\,, \tag{7.8}$$

$$J_3(T) = J_1(T) \left(\frac{\rho_n(T)}{\rho_1(T)}\right)^{\left(\frac{1}{n_{FF}}\right)}\,, \tag{7.9}$$

$$\rho_1(T) = \frac{E_c}{J_c(T)} \left|\frac{J_1(T)}{J_c(T)}\right|^{(n(T)-1)}\,, \tag{7.10}$$

where $d$ is an inflection point defining the beginning of the flux flow state, $n_{FF}$ is the exponent of the idealized flux flow state, $\rho_1(T)$ is the power law resistivity at $J_1(T)$, and $\rho_n(T)$ is the normal state resistivity. The mathematical expressions of $\sigma_1(T)$, $\sigma_2(T)$, $\sigma_3(T)$, $E_1(T)$, $E_2(T)$, and $E_3(T)$ are expressed as follows:

$$\sigma_1(T) = \frac{1}{\rho_1(T)}\,, \quad (7.11) \qquad \sigma_2(T) = \frac{1}{\rho_n(T)}\,, \quad (7.12) \qquad \sigma_3(T) = \frac{1}{\rho_n(T)}\,, \quad (7.13)$$

$$E_1(T) = \frac{J_1(T)}{\sigma_1(T)}\,, \quad (7.14) \qquad E_2(T) = \frac{J_2(T)}{\sigma_n(T)}\,, \quad (7.15) \qquad E_3(T) = \frac{J_3(T)}{\sigma_n(T)}\,. \quad (7.16)$$

In the general formula of the Bézier curve, the control points are named $P_0$, $P_1$, and $P_2$. The quadratic Bézier curve is expressed by a parametric equation $B(u)$ vs. the parameter $u$ as follows [172]:

$$B(u) = (1-u)^2 P_0 + 2(1-u)uP_1 + u^2 P_2\,, \qquad 0 \geq u \geq 1\,, \tag{7.17}$$

where the parameter $u$ varies between 0 at the starting point of the curve, and 1 at the ending point of the curve. The $x$ and the $y$ coordinates of the Bézier curve are given by the parametric equations:

$$P_0 = (x_0, y_0), P_1 = (x_1, y_1), P_2 = (x_2, y_2)\,. \tag{7.18}$$

$$x(u) = (1-u)^2 x_0 + 2(1-u)ux_1 + u^2 x_2\,, \qquad 0 \geq u \geq 1\,, \tag{7.19}$$

, where $x(u)$ represents the decimal logarithm (base 10) of the electric field ($\log_{10}(E(T))$), and $x_0$, $x_1$, and $x_2$, are the decimal logarithmic values of the electric field of the three control points $\log_{10}(E_1(T))$, $\log_{10}(E_2(T))$, and $\log_{10}(E_3(T))$, respectively. Three intermediate variables $a_1$, $b_1$, and $c_1$ represent the coefficients derived from equation (7.19) and are expressed as follows:

$$a_1 = \log_{10}(E_1(T)) - 2\log_{10}(E_2(T)) + \log_{10}(E_3(T))\,, \tag{7.20}$$

$$b_1 = \log_{10}(E_1(T)) - \log_{10}(E_2(T))\,, \tag{7.21}$$

$$c_1 = \log_{10}(E(T)) - \log_{10}(E_1(T))\,. \tag{7.22}$$

By solving equation (7.19), the Bézier parameter $u$ is obtained and expressed as follows:

$$u = \frac{b_1 + \sqrt{b_1^2 + a_1 c_1}}{a_1}\,. \tag{7.23}$$

The $y$ coordinates $y_0$, $y_1$, and $y_2$ of the Bézier curve are the decimal logarithmic values of the conductivity at the three control points, *i.e.* $\log_{10}(\sigma_1)$, $\log_{10}(\sigma_2)$, and $\log_{10}(\sigma_3)$. Thus, $\log_{10}(\sigma(u))$ is determined as follows:

$$\log_{10}(\sigma(u)) = (1-u)^2 y_0 + 2(1-u)uy_1 + u^2 y_2\,, \qquad 0 \geq u \geq 1\,. \tag{7.24}$$

The conductivity in the flux flow state ($\sigma_{FF}(E,T)$) is determined at a given electric field and a given temperature using the Bézier curve. The formula used to determine $\sigma_{FF}(E,T)$ is as follows:

$$\sigma_{FF}(u) = 10^{(1-u)^2 y_0 + 2(1-u)uy_1 + u^2 y_2}\,, \qquad 0 \geq u \geq 1\,. \tag{7.25}$$

The conductivity of the REBCO layer, $\sigma_{REBCO}$, is modeled by a piecewise function, containing three mathematical expressions corresponding to $\sigma_{PL}(E,T)$ for the flux creep state, $\sigma_{FF}(E,T)$ for the flux flow state, and $\sigma_n(T)$ for the normal state, and is written as follows:

$$\sigma_{REBCO}(E,T) = \begin{cases} \sigma_{PL}(E,T) & \text{for } E < E_1(T)\,, \\ \sigma_{FF}(E,T) & \text{for } \; E_1(T) \geq E < E_3(T)\,, \\ \sigma_n(T) & \text{for } \; E \geq E_3(T)\,. \end{cases} \tag{7.26}$$

## 7.6 Comparison of the piecewise model with the power law model

For the purpose of comparison, the piecewise model was implemented in COMSOL Multiphysics 5.6 to compute the developed quench voltage of the regular and CFD REBCO tapes described above. The finite element model is similar to that of the power law model implemented in section (7.2.3), with the difference in the expression of the conductivity of the REBCO layer. The results of the simulations are compared with those obtained using the power law model and with the experimental data of $V_q(t)$ for applied currents of 96 A ($0.60I_c$), 120 A ($0.75I_c$), 135 A ($0.85I_c$) and 154 A ($0.96I_c$).

In the piecewise model, $d$ was set to 2.5, and $n_{FF}$ takes a value between 2 and 5 in physical models [165]. In this work, simulations with the piecewise model were conducted for $n_{FF} = 2$ and for $n_{FF} = 3$, to evaluate the influence of the flux flow exponent on the developed quench voltage. Increasing $n_{FF}$ from 2 to 3, results in decreasing the value of $J_3(T)$ and $E_3(T)$. This reduction leads to a sharper transition from the flux flow state to the normal state, as shown in the resistivity curve presented in Figure 7.9.

### 7.6.1 Impact of the piecewise resistivity model in a regular architecture

Figure 7.10a, Figure 7.10b, Figure 7.10c, and Figure 7.10d present the experimental results of $V_q$ vs. time of the regular coil, the simulated results obtained using the piecewise model with $n_{FF} = 2$ and $n_{FF} = 3$, and the simulated results obtained using the power law model, for an applied current of 96 A ($0.6I_c$), 120 A ($0.75I_c$), 135 A ($0.85I_c$) and 154 A ($0.96I_c$), respectively.

For all applied currents, the power law model overestimates the value of $V_q(t)$ compared to the experimental results of the regular coil. The discrepancy between the experimental results (dashed red) and the simulation results of the power law model (solid red) is high when $I = 96$ A, and it decreases as the applied current increases to $I = 154$ A.

Using the piecewise model with $n_{FF} = 2$, the simulation results (solid blue) of $V_q(t)$ are in better agreement with the experimental results than the power law model for $I = 96$ A,

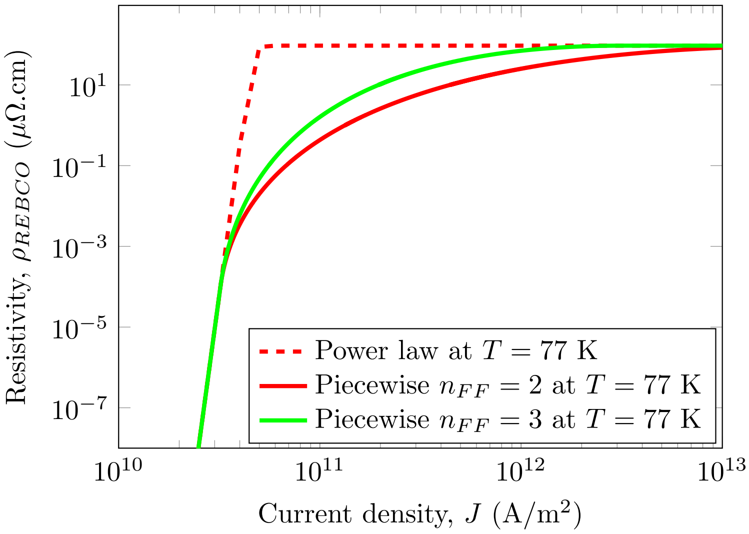

Figure 7.9 Resistivity of the REBCO layer $\rho_{REBCO}(J)$ obtained with the piecewise model with $n_{FF} = 2$ (solid red line), with the piecewise model with $n_{FF} = 3$ (solid green line), and with the power law model (dashed line) at $T$ =77 K.

$I = 120$ A, and $I = 135$ A, especially for the peak values of $V_q$. For $I = 154$ A, the piecewise model with $n_{FF} = 2$ underestimates the measured $V_q(t)$. The beginning of the quench is delayed compared to the experiment results for all applied current if we consider the simulation results obtained using the piecewise model with $n_{FF} = 2$. A possible explanation for the quench delay is that the transition from the flux flow state to the normal state predicted by the piecewise model with $n_{FF} = 2$ is smoother than the transition predicted by the power law model, but too smooth compared to the reality.

To validate this assumption, simulations were conducted using the piecewise model with $n_{FF} = 3$, which results in decreasing the value of $E_3(T)$ and $J_3(T)$. The transition from the flux flow state to the normal state occurs at lower values of the electric field and current density compared to the piecewise model with $n_{FF} = 2$. The simulation results of $V_q(t)$ obtained using the piecewise model with $n_{FF} = 3$ for an applied current of 96 A, 120 A, 135 A, and 154 A are presented respectively in Figures 7.10a to 7.10d (solid green).

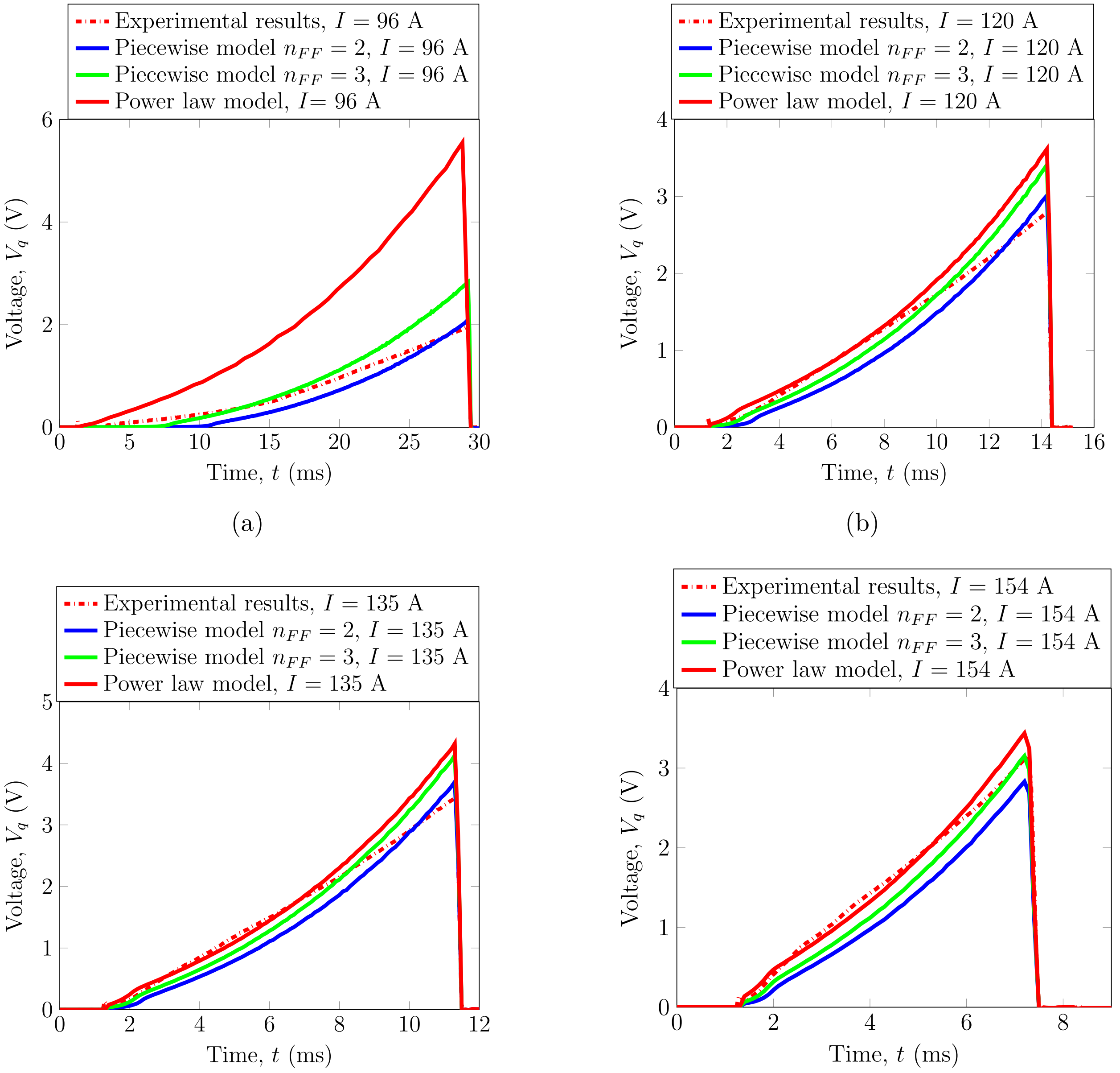

(a) (b)

(c) (d)

Figure 7.10 Quench voltages $V_q$ vs. time of a regular REBCO coil at different applied currents: (a) $I = 96$ A, (b) $I = 120$ A, (c) $I = 135$ A, and (d) $I = 154$ A. Dashed lines correspond to experimental results, solid blue and green lines were calculated with the piecewise model with $n_{FF} = 2$, and $n_{FF} = 3$, respectively, and red lines were calculated with the power law model.

For all applied currents, the values of $V_q(t)$ of the piecewise model with $n_{FF} = 3$ are lower than those obtained with the power law model and higher than those obtained with the piecewise model with $n_{FF} = 2$. The tape quenches slower than in the case of the power low model and faster than in the case of the piecewise model with $n_{FF} = 2$. The simulation results of the peak value of $V_q(t)$ were lower than the experimental data. The peak value of $V_q(t)$ was overestimated in the case of $I = 96$ A, $I = 120$ A, and $I = 135$ A and well reproduced in the case of $I = 154$ A, using the piecewise model with $n_{FF} = 2$.

### 7.6.2 hot spot temperature comparison of the regular architecture

Figures 7.11a to 7.11d present the numerical temporal profile of the temperature of the hot spot of the regular tape obtained using the power law model, the piecewise model with $n_{FF} = 2$, and the piecewise model with $n_{FF} = 3$, for applied currents of 96 A, 120 A, 135 A, and 154 A, respectively. Similar to the temporal profile of the quench voltage across the regular tape, the discrepancy between the simulation results of the power law model and the piecewise model is large for $I = 96$ A and tends to be similar when the applied current is increased to $I = 154$ A. The simulated temperature of the hot spot rises faster in the case of the power law model (red line), resulting in a faster quench and a higher hot spot temperature. In the case of the simulation results of the piecewise model, increasing $n_{FF}$ from 2 to 3 triggers an earlier quench, especially for low applied currents ($I \leq 0.85 I_c$). For an applied current of 154 A, the quench occurs at the same time with all models.

If we consider the simulations performed with an applied close to the critical current, softening the resistivity curve of REBCO tapes using the piecewise model seems to have little impact on the variation of the hot spot temperature over time. However, when the applied current is only 60% of the critical current, the quench occurs slowly in the case of the piecewise model, resulting in a considerable discrepancy in the obtained temperature of the hot spot.

### 7.6.3 Quench voltage comparison of the CFD architecture

Figures 7.12a to 7.12c show the experimental and simulation results of the quench voltage vs. time of the CFD architecture for $I = 120$ A, $I = 135$ A, and $I = 154$ A, respectively. The numerical results were obtained using the power law model (solid blue line) and the piecewise model (solid yellow line) with $n_{FF} = 3$.

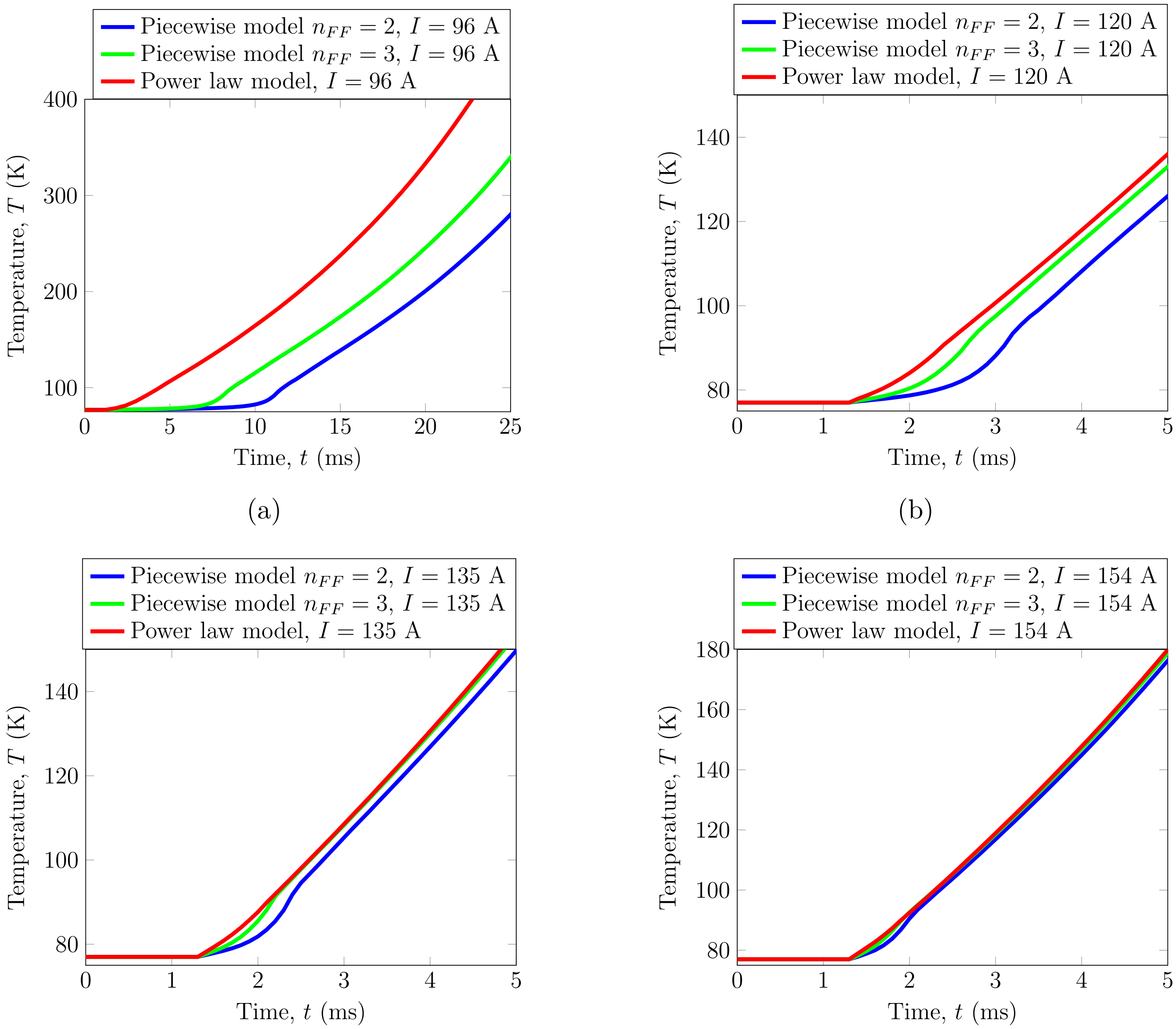

(a) (b)

(c) (d)

Figure 7.11 Simulation results of the temperature of the hot spot vs. time of a regular tape for an applied current of: (a) $I = 96$ A, (b) $I = 120$ A, c) $I = 135$ A, and (d) $I = 154$ A. Solid blue and green lines were calculated using the piecewise model with $n_{FF} = 2$, and $n_{FF} = 3$, respectively. Solid red lines were calculated using the power law model.

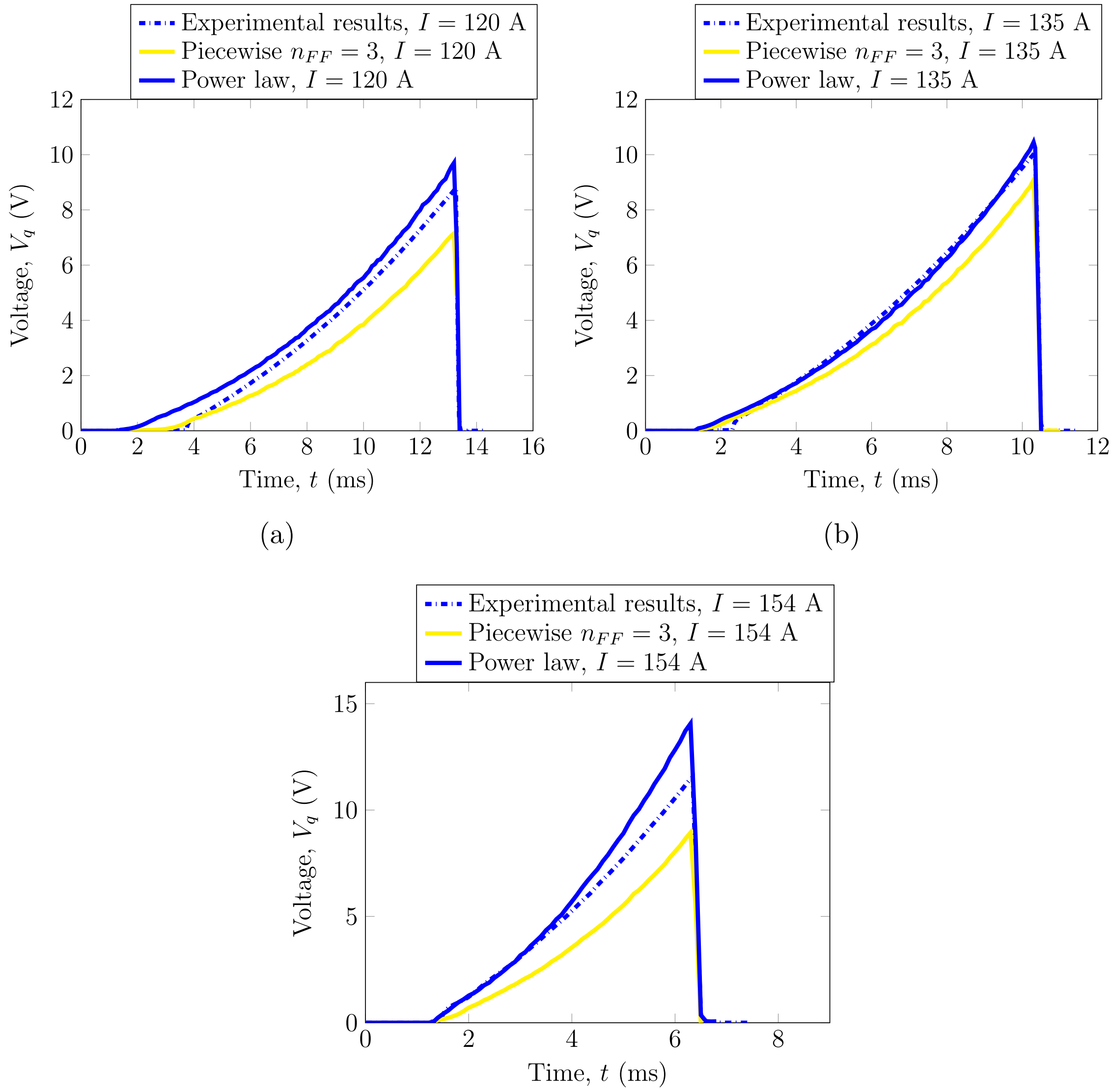

(a)

(b)

(c)

Figure 7.12 Quench voltage $V_q$ values vs. time for different applied currents;: (a) $I = 120$ A (b) $I = 135$ A, and (c) $I = 154$ A, for a CFD REBCO tape. Dashed lines correspond to experimental results, solid yellow lines were calculated using the piecewise model with $n_{FF} = 3$, and blue lines were calculated using the power law model.

Unlike with the regular architecture, the piecewise model failed to predict the quench voltage vs. time in the CFD tape. The numerical results of $V_q(t)$ obtained with the piecewise model were lower than the experimental data and lower than the power law model. These results depict that to model accurately the quench dynamics of the CFD architecture, the electrothermal piecewise model is probably not sufficient.

## 7.7 Discussion and conclusion

In this chapter, we demonstrated that implementing the CFD architecture in the layout of a small-scale REBCO coil does not prompt any discordance with the benefits of the CFD concept. An improvement ratio of 3-4 of the NZPV was obtained for the CFD coil. This NZPV acceleration resulted in an increase of the developed voltage upon a quench for the CFD coil by a factor of 3-4, meaning that the gain factor of the NZPV resulting from using the CFD architecture produced the same gain factor in the generated voltage upon a quench. Increasing the quench voltage across REBCO tapes can be efficient in improving the sensitivity of quench detection methods based on voltage measurements.

Furthermore, we demonstrated that the power law model is inadequate to predict the distinctive quench behavior of regular REBCO tapes for an applied current lower than the critical current. The measured voltage across the regular coil was overestimated using the power law model. Thus, the variation of the hot spot temperature over time obtained using the power law model does not represent the accurate temperature variation for low applied currents ($I \leq 0.85 I_c$).

To further explore this issue, we developed a piecewise resistivity model, assumed to be more faithful to the physics, to accurately predict the voltage and temperature across REBCO tapes during a quench. The piecewise model has demonstrated that it is capable of predicting the developed voltage across regular REBCO tapes better than the power law model for currents lower than the critical current. The nucleation of the quench is delayed for $I \leq 0.85 I_c$ resulting in a lower hot spot peak temperature.

However, the numerical quench behavior estimated with the piecewise model depends on the value of flux flow exponent $n_{FF}$. Changing the value of $n_{FF}$ in the piecewise model modifies the temporal profile of the quench voltage. The shape of the Bézier curve in the flux flow state is influenced by the triplet control points $J_1$, $J_2$, and $J_3$ and the triplet $E_1$, $E_2$, and $E_3$. These control points depend on the value of $d$ and $n_{FF}$. To determine the accurate value of $d$ and $n_{FF}$, experimental measurements of the wide range $E$-$J$ characteristics at different temperatures and for different applied currents would be required.

The simulation results presented in this chapter thus confirmed that the piecewise model has the potential of reproducing the quench voltage of regular REBCO tapes over time better than the power law model for low applied currents. This model however failed to accurately predict the voltage temporal profile of CFD REBCO tapes. Further calibration of the model should help in predicting accurately the quench behavior of the CFD architecture.

# CHAPTER 8 POTENTIAL OF THE CFD CONCEPT IN IMPROVING QUENCH DETECTION

## 8.1 Introduction

In this work, it was demonstrated that the CFD architecture accelerates the NZPV of REBCO single tapes, high-current cables, and coils based on CFD REBCO tapes. Improving the NZPV is a promising approach to enhance the quench protection of superconducting devices based on REBCO tapes. Conventional voltage-based detection techniques rely on measuring the developed voltage upon a quench [69]. In chapter 7, it was shown that increasing the NZPV of REBCO tapes results in increasing the quench voltage.

The voltage is the line integral of the electric field between two adjacent voltage taps. The temperature profile over time depends on the electric field profile. When the NZPV is low, the hot spot temperature gets to a high peak over a short period. If the NZPV is enhanced, a low peak temperature profile is developed over a long time. However, both cases generate the same voltage. That's why it is more difficult to detect a quench using conventional voltage detection schemes before a thermal runaway when the NZPV is low. Using the CFD architecture, the quench voltage is increased, which has the potential to accelerate the detection of the quench before a thermal runaway.

In this chapter, the performance of the CFD concept in improving conventional voltage-based detection techniques is evaluated. First, a voltage-based quench detection experiment was performed on a regular REBCO tape and a CFD REBCO tape at an operating temperature of 77 K and in self-field. In the second section of this chapter, numerical simulations of voltage quench detection experiments were conducted to validate the efficacy of the CFD concept in improving voltage-based detection techniques and to predict the maximum temperature of the hot spot.

## 8.2 Experimental approach

### 8.2.1 Investigated samples

The samples used in this experiment were two SuperPower (SP) samples. The first sample was a regular REBCO tape, named regular tape, and the second sample was a CFD REBCO tape, named CFD tape. Both samples were 4 mm wide, 10 cm long, and comprised a 50 $\mu$m thick Hastelloy (C276$^{\mathrm{TM}}$) substrate, a 1.6 $\mu$m thick GdBaCuO layer, a 0.2 $\mu$m thick

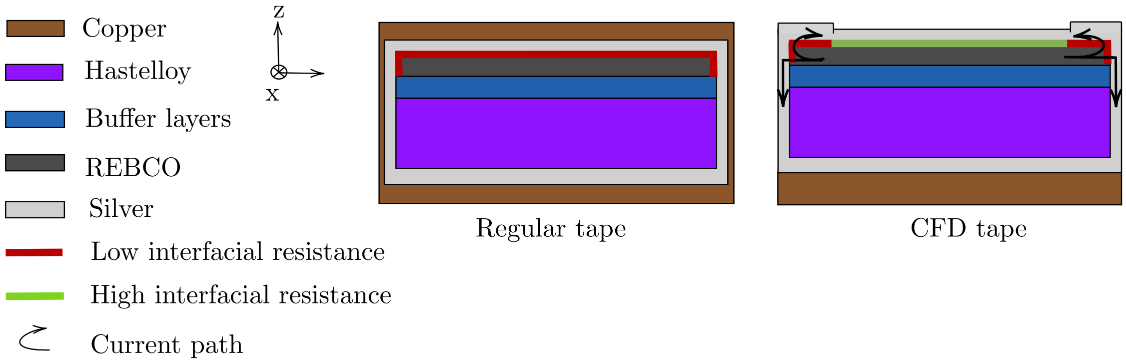

Figure 8.1 Cross-section of the regular tape architecture (left figure) and the CFD tape (right figure). Upon a quench, the current (black arrows) is forced to pass through the regions with the lowest interfacial resistance to reach the stabilizer layer.

buffer layer, and a 2.5 $\mu$m silver layer surrounding the whole tape. To reduce the risk of degradation of the samples during the quench detection tests, a 5 $\mu$m thick copper layer was electrodeposited on both samples to increase their thermal stability. Figure 8.1 shows the architecture of the regular tape and the CFD tape used in the quench detection experiment. For the regular REBCO tape, a 2.5 $\mu$m thick copper layer was deposited on the substrate side and another 2.5 $\mu$m thick copper layer was deposited on the REBCO layer side. For the CFD tape, the copper layer was only deposited on the substrate side after the CFD fabrication. Upon a quench, part of the current will flow in the bottom stabilizer because it is thicker, which helps increasing the NZPV more than just using the CFD layer alone.

The critical current of the regular and the CFD tapes at 77 K and in self-field was measured and determined at an electric field criterion of 1 $\mu$V/cm after copper electrodeposition, and it was 131 A with an $n$-factor of 27 for the regular tape, and 133 A with an $n$-factor of 26 for the CFD tape. The room temperature resistance was 3.7 m$\Omega$/cm for the regular tape and 4.5 m$\Omega$/cm for the CFD tape.

Before performing the quench detection experiment, the NZPV of the regular and the CFD tapes were measured by inducing a quench using an NdFeB magnet, so we could evaluate the NZPV gain factor. The critical current of the defect location was reduced by 50% for both tapes. The same defect was used to initiate the quench during the voltage detection experiments.

### 8.2.2 Quench detection experiment

The quench detection experiment relied on i) measuring the generated voltage upon a quench of the regular tape and the CFD tape, ii) setting a voltage threshold ($V_d$), and iii) driving the applied current to zero once the threshold is reached.

To protect the REBCO tapes from a thermal runaway, the applied current must be driven to zero before reaching the operational temperature limit and degrading the critical current of the tested tapes. The current source generated pulses of current and was controlled by a LabVIEW program. This program was modified to perform the quench detection measurements. In the LabVIEW program, a voltage threshold was defined. To avoid background noise and improve the sensitivity of the detection, the program compares the average value of five successive voltage measurements across the tape to the chosen value threshold $V_d$. Once this average value reaches $V_d$, the program triggers an exponential decrease of the applied current at the detection time $t_d$ as follows:

$$I(t) = \begin{cases} I_0 & \text{for } V < V_d, \\ I_0 \exp\left(\frac{-t}{\tau}\right) & \text{for } \; V \geq V_d, \end{cases} \tag{8.1}$$

where $I_0$ stands for the applied current and $\tau$ is the discharge time constant. The discharge duration ($\Delta t$) is equal to $5\tau$. Both parameters $\tau$ and $\Delta t$ are pre-determined in the LabVIEW program to emulate the physical voltage detection circuit presented in Figure. 8.2. Equation (8.1) imitates the discharge of the stored energy of a REBCO coil zone in a dump resistor ($R_d$) [69, 164, 173, 174].

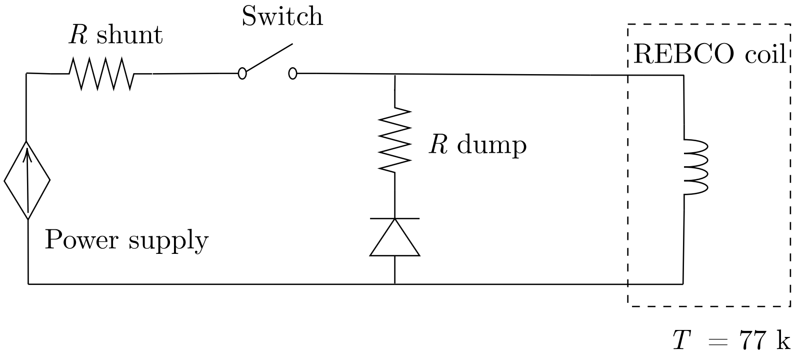

Figure 8.2 Circuit representing the detect-and-dump active quench protection of a REBCO coil with a normal zone ($r_q$).

## 8.3 NZPV measurements

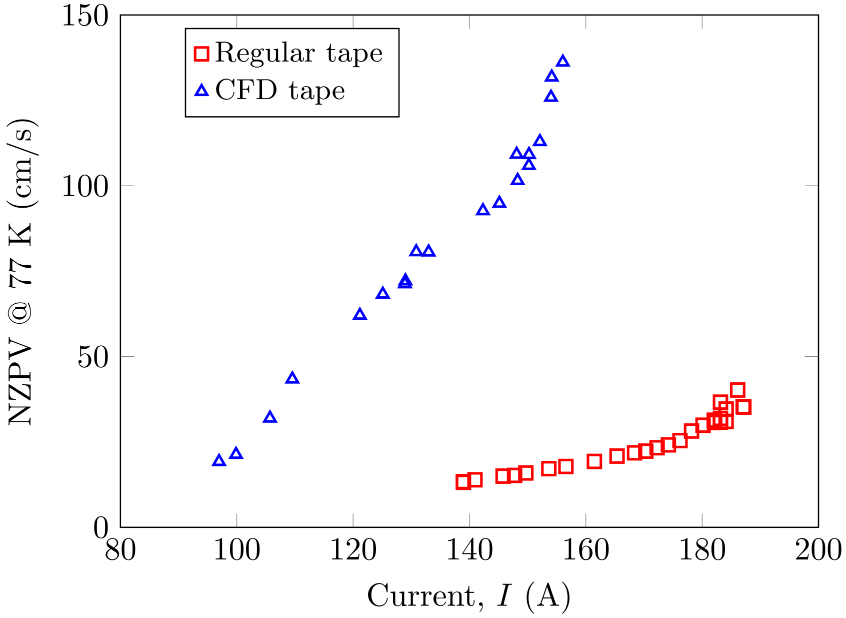

Figure 8.3 Measured NZPV values versus applied current for i) a regular tape (red squares), and ii) a CFD tape (blue triangles).

Figure 8.3 shows the measured NZPV values for the regular tape and the CFD tape as a function of the applied current at 77 K and in self-field. The NZPV results revealed an increase of the NZPV by a factor of 6-7 for the CFD tape, which demonstrates that adding a layer of copper in the template of the CFD tape did not diminish the benefits of the CFD architecture, which is consistent with previous results [87].

## 8.4 Quench detection measurements

Quench detection measurements were performed for $V_d = 5$ mV, $V_d = 10$ mV, and $V_d = 20$ mV at 77 K. The current discharge duration $\Delta t$ was set to 55 ms for all the tests. The applied current ($I_0$) was increased from 105 A when $V_d = 5$ mV, to 112 A when $V_d = 10$ mV, and to 121 A when $V_d = 20$ mV.

Figure 8.4a, Figure 8.4c and Figure 8.4e show the temporal profile of the applied current for $V_d = 5$ mV, $V_d = 10$ mV and $V_d = 20$ mV, respectively, and Figure 8.4b, Figure 8.4d and Figure 8.4f present their corresponding temporal profile of the voltage respectively, for the regular tape (in red) and the CFD tape (in blue).

Table 8.1 Results of quench detection tests performed on the regular and the CFD tapes.

| $V_d$ (mV) | $t_{d,1}$ (ms) | $V_{max,1}$ (mV) | $t_{d,2}$ (ms) | $V_{max,2}$ (mV) | Time gained (ms) |
|---|---|---|---|---|---|
| 5 | 9.7 | 7.5 | 6 | 89.9 | 3.7 |
| 10 | 9.9 | 14.5 | 5.1 | 110.1 | 4.8 |
| 20 | 10.7 | 27.6 | 3.6 | 151.5 | 7.1 |

For all values of $V_d$, the discharge is triggered faster in the case of the CFD tape. Due to the accelerated NZPV, the voltage generated upon the quench of the CFD tape rises faster than that of the regular tape, which means that the measured voltage reaches $V_d$ earlier in the case of the CFD tape. The voltage curves show that the voltage generated by the CFD tape is higher than that generated by the regular tape. Table 8.1 illustrates the detection time $t_{d,1}$ of the regular tape and $t_{d,2}$ of the CFD tape, the maximum reached voltage during the discharge $V_{max,1}$ of the regular tape, and $V_{max,2}$ of the CFD tape and the time margin gained, which is the time difference between $t_{d,1}$ and $t_{d,2}$ for $V_d = 5$ mV, $V_d = 10$ mV and $V_d = 20$ mV.

For $V_d = 5$ mV, the detection of the voltage threshold happens 3.7 ms faster for the CFD tape. Increasing the voltage threshold to 10 mV and then 20 mV, resulted in increasing the time gain to 4.8 ms and 7.1 ms, respectively.

Although the discharge starts faster in the case of the CFD tape, the maximal voltage reached during the current discharge is higher than for the regular tape. For example, when $V_d$ was set to 20 mV, the discharge started 7.1 ms faster in the case of the CFD tape and the voltage generated by the CFD tape reached a maximum value of 151.5 mV, while the voltage generated by the regular tape reached a maximum value of 27.6 mV. This can be attributed to the high NZPV of the CFD tape. Indeed, the resistive normal zone across the CFD tape created during the current discharge is larger than in the case of the regular tape.

In all experiments, the voltage drops to zero before the applied current reaches zero. For $V_d = 5$ mV, the voltage of the regular tape and the CFD tape reaches zero at 20 ms. When $V_d$ is increased to 10 mV, the voltage generated by the CFD tape reaches zero at 21 ms, while the voltage generated by the regular tape attains zero at 28 ms. When $V_d$ is 20 mV, the voltage generated by the CFD tape takes more time to attain zero as it disappears at 48 ms, unlike the voltage generated by the regular tape, which attains zero at 23 ms.

The disappearance of the quench voltage during the discharge indicates the resorption of the created normal zone and the recovery of the superconducting state. During the discharge, the normal zone of the CFD tape is 6 to 7 times larger than the normal zone of the regular tape, and consequently, the developed voltage during the current discharge is proportional

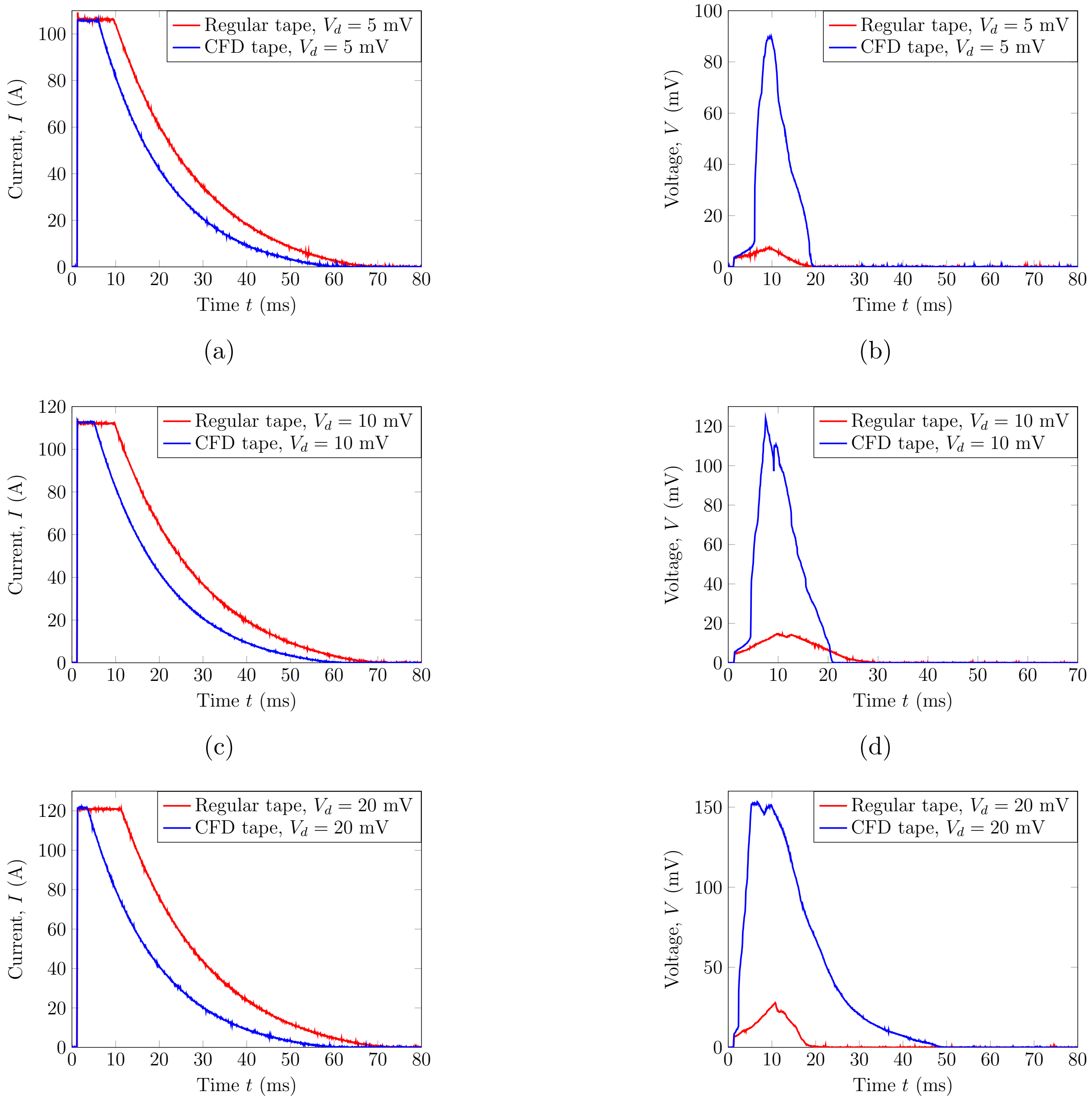

(a)

(b)

(c)

(d)

(e)

(f)

Figure 8.4 Temporal profile of the applied current and the corresponding temporal voltage profile during the quench detection experiment for the regular tape (blue) and the CFD tape (red) for a voltage threshold of: (a)-(b) $V_d = 5$ mV, (c)-(d) $V_d = 10$ mV, and (e)-(f) $V_d = 20$ mV. Once $V_d$ is reached, the current is driven exponentially to zero in 55 ms.

to the size of the normal zone. Regardless of the applied current, the CFD tapes generate higher voltage after the quench detection, which is easier to detect faster.

The experimental measurements show that incorporating the CFD architecture ensures an earlier quench detection. However, to validate the gain of the CFD effect, an evolution of the temperature rise is required to support the experimental work performed in this section.

## 8.5 Quench detection simulation

To further investigate the effect of the CFD concept in enhancing the quench protection of REBCO tapes, finite element simulations were performed to extract the maximum hot spot temperature ($T$) during the current discharge. The simulations were carried out using the 3D FEM piecewise model and power law model implemented in COMSOL Multiphysics 5.6. The input parameters of the geometry of REBCO tapes and the critical current were those of the quench detection experiment described in the previous sections. The measured temporal profile of the applied current for $V_d = 5$, 10, and 20 mV, was implemented as an input for the simulated applied current. For the piecewise model, $d$ was set to 2.5, and $n_{FF}$ was set to 3.

### 8.5.1 Quench detection simulation of the regular REBCO tape

First, numerical simulations were performed for the regular REBCO tape. The voltage curves obtained from the experiment (solid red), from simulations with the piecewise model (dotted red), and from simulations with the power law model (dashed blue) for $V_d = 5$, 10 and 20 mV are presented in Figure 8.5a, Figure 8.5c, and Figure 8.5e, respectively. The evolution of the temperature of the hot spot during the current discharge obtained with the piecewise model and with the power law model for $V_d = 5$, 10 and 20 mV is presented in Figure 8.5b, Figure 8.5d, and Figure 8.5f, respectively. For all values of $V_d$, the numerical evolution of the voltage across the regular tape during the current discharge is well represented with the piecewise model, and overestimated with the power law model. Thus, the maximum hot spot temperature achieved in the simulations with the power law model is 3 to 4 K higher than the value obtained using the piecewise model. The numerical results of the hot spot temperature reveal that the quench detection occurred in the pre-quench regime for all detection values of $V_d$.

### 8.5.2 Quench detection simulation of the CFD REBCO tape

Finite element simulations of the CFD REBCO tape were performed using the piecewise model and the power law model. The voltage curves obtained by numerical simulations with

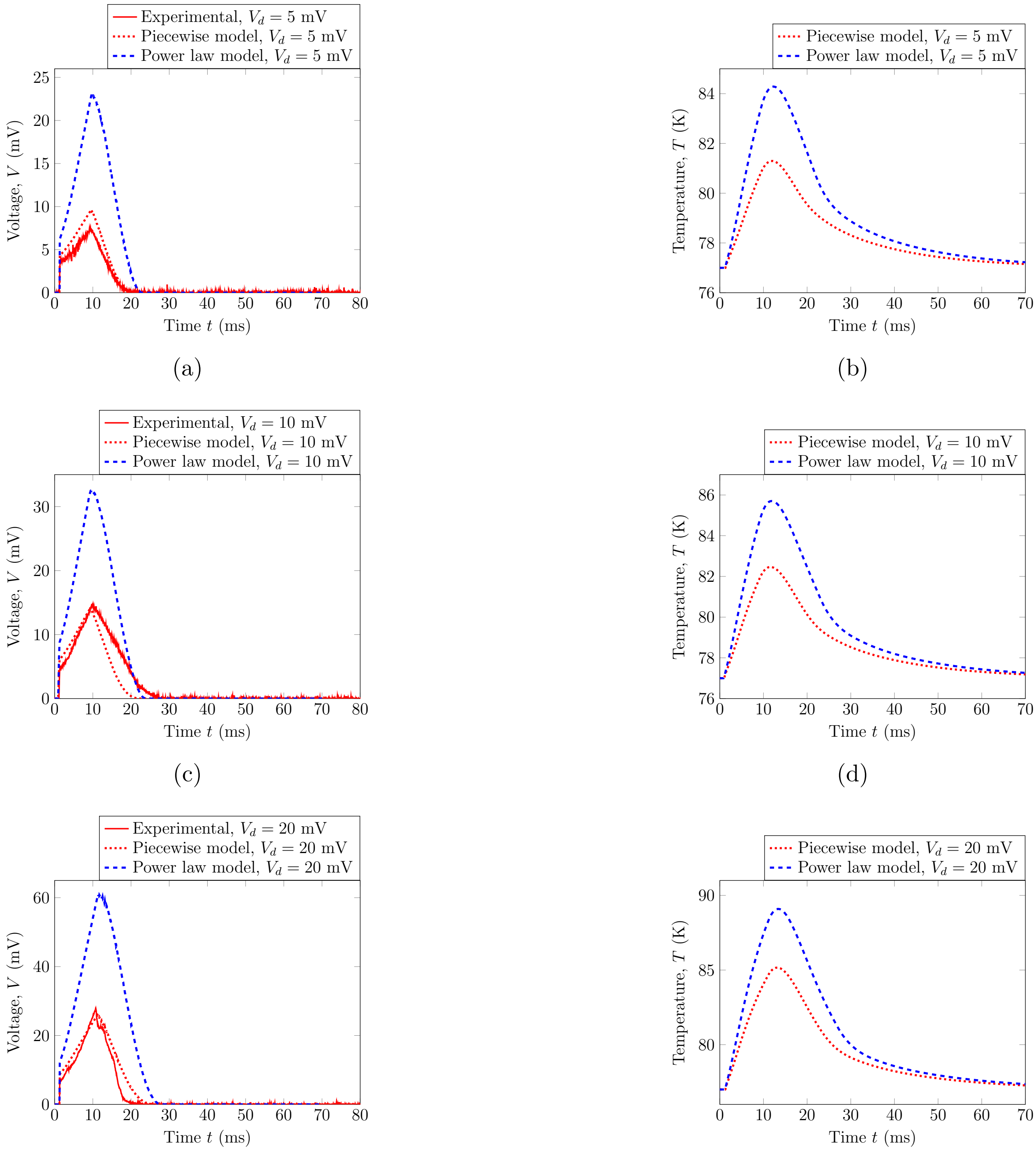

(a) (b)

(c) (d)

(e) (f)

Figure 8.5 Measured and simulated voltage curves obtained with the piecewise model (dotted red) and with the power law model (dashed blue) for the regular tape, along with their corresponding simulated hot spot temperature profiles at a voltage threshold $V_d$ of: (a)-(b) $V_d = 5$ mV, (c)-(d) $V_d = 10$ mV, and (e)-(f) $V_d = 20$ mV.

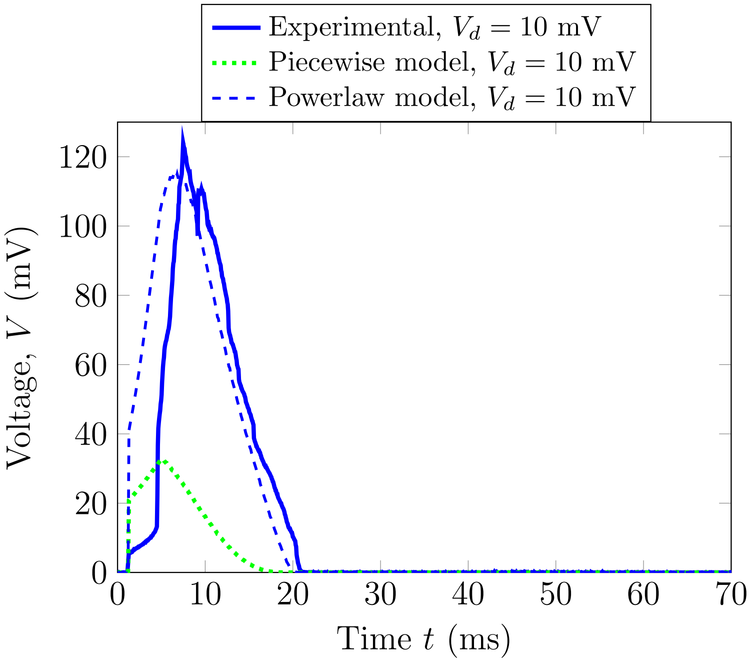

Figure 8.6 Measured and simulated voltage curves obtained with the piecewise model (dotted green) and with the power law model (dashed blue) for the CFD tape at a voltage threshold $V_d$ of 10 mV.

the piecewise model (dotted green), with the power law model (dashed blue), and the voltage measurements (solid blue) during the current discharge of the CFD tape for $V_d = 10$ mV are presented in Figure 8.6.

The piecewise model underestimates the maximum value of the voltage across the CFD tape during the current discharge. When using the power law model, the voltage across the CFD tape reaches a maximum value in the same order of magnitude as the peak measured voltage during the current discharge. However, a sharp rise in the voltage during the beginning of the quench is observed in the voltage curves obtained with the piecewise model and the power law model compared to the experimental voltage measurements. The same discrepancy between the simulation results and the experimental results was obtained for $V_d = 5$ mV and $V_d = 20$ mV (not shown here).

Unlike with the regular REBCO tape, all simulations failed to estimate correctly the developed voltage across the CFD tape during the discharge of the applied current. These results suggest that the simulated temporal profile of the hot spot temperature obtained with the piecewise model and with the power law mode of the CFD tape are not accurate. That's why we chose to not present them in this thesis to not base our conclusion on inaccurate results.

Many aspects of the model were addressed to improve its accuracy, such as the thickness of the deposited copper layer and the critical current of the defect. However, these aspects seem to have little impact on the voltage rise during the beginning of the quench. Another attempt is currently being studied in another PhD project, and it consists in using a magnetothermal piecewise model to simulate the quench behavior of CFD REBCO tapes.

## 8.6 Conclusion

In this chapter, an exploratory basic voltage detection experiment was conducted on a regular REBCO tape and on a CFD REBCO tape to evaluate the benefits of the CFD architecture in improving quench detection. The measured NZPV was 6 to 7 times higher in the case of the CFD tape.

Different voltage thresholds were applied during the experiment. Measurements of the voltage across the regular tape and the CFD tape during the current discharge demonstrated that the current discharge is triggered faster in the case of the CFD tape because of its relatively high NZPV. Increasing $V_d$ from 5 mV to 20 mV increased the detection time margin gain from 3.7 ms to 7.1 ms.

Finite element simulations were performed to estimate the temperature of the hot spot during the voltage detection experiment. In the case of the regular tape, the experimental results of the quench detection experiment could be well reproduced by simulations with the piecewise model. However, the power law model failed to reproduce the measured temporal profile of the voltage accurately. These results further suggest that the power law model is not suitable for estimating the quench behavior of REBCO tapes in the pre-quench regime and that the piecewise model has the potential to be more accurate to represent the electrothermal response of REBCO tapes in the pre-quench regime.

Unfortunately, the experimental results of the CFD tapes could not be reproduced either with the power law model or the piecewise model. This discrepancy can be related to different limitations of the models, such as assuming a uniform current density along the width and the length of the REBCO layer or considering an electrothermal model rather than a magnetothermal model for stimulating the quench. Although the electrothermal response of the regular REBCO tape seems to be predictable using an electrothermal piecewise model, further work has to be done to model accurately the quench behavior of the CFD tapes during the pre-quench regime.

# CHAPTER 9 GENERAL DISCUSSION

## 9.1 Synthesis of research objectives

This chapter presents an interpretation of the results obtained in the previous chapters in the context of the research question and research objectives presented in the introduction of this thesis. The relations between the key findings in each chapter and the objectives of the thesis are discussed below.

### 9.1.1 Objective 1: fabrication of long-length REBCO tapes with CFD architecture

The work presented in chapter 4 (article 1) consists in the fabrication and investigation of meter-scale REBCO tapes with a CFD architecture, which represents a valid realization of the first objective of this thesis. Following the results presented in the article, the challenge of integrating the CFD architecture in meter-scale REBCO tapes was achieved by upgrading the CFD fabrication method to an automated reel-to-reel process. Although meter-scale CFD REBCO tapes could be fabricated using the conventional handmade method, too many geometrical imperfections are generated in the CFD layer. The simulation results showed that these imperfections can affect the NZPV uniformity over long lengths, which diminishes the benefits of the CFD architecture. Furthermore, numerical simulations and visual inspections conducted in the article demonstrated that the automated reel-to-reel CFD fabrication process enabled precise control of the geometry of the CFD layer, which guarantees a uniform NZPV over the length of meter-scale REBCO tapes. It was also demonstrated that depositing a silver layer on top of the CFD layer of REBCO tapes without performing annealing did not raise major issues in the adhesion strength between the REBCO layer and the silver layer. However, performing subsequent annealing at low temperatures (300 °C) further improved the adhesion of the silver layer on top of the CFD layer.

### 9.1.2 Objective 2: development of an alternative low-cost manufacturing process of the CFD architecture

The findings presented in chapter 5 (article 2) addressed the second objective of this thesis. In parallel with upgrading the CFD fabrication process into an automated method, an alternative approach was studied in the view of reducing the production cost of long-length CFD REBCO tapes and minimizing the complexity of their manufacturing line. In the article, inkjet printing (IJP) of silver lines on top of the surface of the REBCO layer followed by an oxygen annealing, demonstrated its potential as an alternative route to integrate the CFD architecture in REBCO tapes without the need to use chemical etching or masking. The printing parameters were optimized to print uniform conductive silver tracks on the rough surface of the superconducting layer. Results showed that the conductivity of the printed silver patterns was in the same order of magnitude as the conductivity of pure silver after annealing in an oxygen atmosphere for one hour at a temperature of 500 °C. The NZPV measurements conducted in the article showed that CFD REBCO tapes fabricated with the IJP method possessed an NZPV 3 to 6 times higher than the NZPV of regular REBCO tapes. These findings confirmed the feasibility of producing the CFD architecture with the IJP method without the need to apply masking and chemical etching steps, which promotes a less complex manufacturing process, suitable for the industrial production of REBCO tapes.

### 9.1.3 Objective 3: evaluate the performance and the feasibility of the CFD architecture in a cable/small-scale coil layout based on CFD REBCO tapes

In chapter 6 (article 3) and chapter 7, we validated the efficacy of the CFD architecture in a test demonstrator coil and a CORC® cable, which suggests that the benefits of the CFD concept are independent of the geometrical layout of REBCO tapes.

Due to the low availability of CFD REBCO tapes, they have never been tested in a cable or coil layout. In the article, a CORC® cable assembled from meter-scale REBCO tapes was fabricated for the first time. Measurements of the critical current of the CFD CORC® cable performed in the article demonstrated that the superconducting properties of the cable were not degraded. Then, the CFD performance was experimentally validated by measuring and comparing the NZPV of a CFD CORC® cable and a regular CORC® cable at temperatures between 67 K and 77 K. A gain factor of 4.5 was obtained in the case of the CFD CORC® cable, which suggests that the benefits of the CFD architecture measured on REBCO tapes are still there when the tapes are arranged in a cable configuration such as CORC® cables. Furthermore, the temperature-dependent measurements of the NZPV of the CFD and regular CORC® cables demonstrated that the NZPV depends primarily on the applied current rather than the operational temperature, similar to single REBCO tapes.

In chapter 7, the CFD architecture was successfully implemented in a minimalistic coil layout. NZPV and quench voltage measurements of the fabricated CFD test coil and of a regular coil are presented. These results highlighted the fact that the NZPV is increased by a factor of 3-4 in the case of the CFD coil with respect to the regular coil. The same gain factors were observed for quench voltage in the CFD coil.

### 9.1.4 Objective 4: investigate the potential of the CFD concept in improving quench protection systems of REBCO tapes

In chapter 8, a preliminary voltage detection experiment was performed on a CFD REBCO tape and a regular REBCO tape containing a 5 $\mu$m thick copper stabilizer in their architecture, in order to compare the quench voltage in both tapes during the detection and discharge of the current. The results obtained during this experiment showed that the detection of the chosen voltage threshold was reached faster in the case of the CFD REBCO tape.

Finite element (FE) simulations also reported in chapter 8 indicated that the quench detection was achieved in the pre-quench regime for the regular REBCO tape, *i.e.* the temperature of the hot spot was less than the critical temperature. The FE simulations obtained for the CFD tapes did not represent accurately the measured voltage curves, thus, the evolution of the temperature of the hot spot in the CFD tape during a current discharge could not be estimated with a sufficient confidence to be reported in this thesis.

Nevertheless, the main finding in chapter 8 is a first confirmation that the CFD architecture accelerates the reach of the quench detection voltage threshold and the initiation of the current discharge, which is promising for improving quench detection schemes in magnets or other DC applications.

Sophisticated and computationally demanding numerical simulation tools were needed in this research to accurately predict the electrothermal behavior of REBCO tapes during a quench. The power law model was used in this thesis to estimate the NZPV of regular and CFD REBCO tapes. However, the power law model was not accurate in the pre-quench regime, leading to a discrepancy between the experimental and simulation results of the developed quench voltage. In chapter 7, we developed a piecewise resistivity model to improve the prediction of the electrothermal response of REBCO tapes, especially in the pre-quench regimes, where the use of a power law model does not provide good results. This model consists in a piecewise conductivity function that allows a gradual transition between the superconducting state and the normal state. In the flux flow state, a Bézier curve connects the power law conductivity to the normal state conductivity of REBCO. Simulations using the piecewise model were conducted in chapter 7 and chapter 8 to reproduce the quench voltages measured in a regular REBCO tape and in a coil made with the same tape. The experimental results were well reproduced in both chapters with the piecewise model for the regular REBCO architecture, which was not the case for CFD tapes and coils. Further work on the model is required to reproduce the electrothermal behavior of REBCO tapes with the CFD architecture.

### 9.1.5 Main objective: find a fabrication process for implementing the CFD architecture in long lengths and quantify their performance in quench situations

This thesis demonstrated various steps of a reel-to-reel method for manufacturing REBCO tapes with the CFD architecture, which would be compatible with the industrial fabrication process. Meter-scale REBCO tapes with the CFD architecture were successfully fabricated and assembled in different geometrical layouts. Furthermore, this thesis has allowed for further exploration of a second route to produce long-length CFD REBCO tapes with less cost and complexity. The first approach allowed us to produce meter-scale CFD tapes, which paved the way for evaluating the performance of the CFD architecture in a cable arrangement. Although this method demonstrated good NZPV uniformity over the length of REBCO tapes, it may be even better to avoid the step of chemical etching when producing hundreds of meters of CFD tapes. The silver loss during the etching step is time-consuming and remains costly. This metal can be recovered elsewhere in the process (see Annexe B). However, this step can be completely removed by applying the second fabrication route, which adds only a single new step to the conventional fabrication process of commercial REBCO tapes.

# CHAPTER 10 CONCLUSION

## 10.1 Summary of accomplished work

The CFD concept increases the NZPV of REBCO tapes, which seems propitious to enhance quench detection and protection of in various applications of REBCO tapes, in particular in high-field magnets. Previously, the efficacy of the CFD concept has only been proved on short lab-scale samples, because the manufacturing process was not compatible with the production of long samples, and thus even less compatible with mass production. The main objective of this research project was therefore to upgrade the CFD manufacturing method in order to achieve a process that meets the industrial standards of REBCO tape manufacturers.

Developing an automated reel-to-reel CFD fabrication process was the first achievement of this thesis, which allowed us to produce meter-scale CFD REBCO tapes and examine the uniformity of the accelerated NZPV over long lengths. We also explored an alternative CFD fabrication approach that does not require a mask and/or chemical etching. This approach consisted in printing silver lines on top of the REBCO surface using Ink Jet Printing (IJP) method followed by an oxygen annealing process to generate a non-uniform interfacial resistance between the REBCO layer and the stabilizer layer over the width of REBCO tapes.

We then integrated the CFD REBCO tapes produced into different geometrical arrangements of HTS cables. In particular, a Conductor on Round Core (CORC®) cable with the CFD architecture was fabricated and tested at different operational temperatures. Additionally, a minimalistic 1.5 turn test coil was fabricated using a 50 cm long CFD REBCO tape. The NZPV of both the CFD CORC® cable and the CFD coil was 3 to 5 times higher than the NZPV of the regular CORC® cable and regular coil.

Finally, the benefits of the CFD architecture in accelerating quench detection of hot spots were studied by performing a voltage-based quench detection experiment on both the CFD and the regular tapes. We showed that during the nucleation of the normal zone, the REBCO tape with the CFD architecture reached the voltage threshold faster than the regular tape, which triggers a faster discharge of the applied current in the case of the CFD REBCO tape.

The possibility of fabricating long-length CFD REBCO tapes, achieved in this thesis, opened up new routes to explore the benefits of the CFD architecture in high-current cables, coils, and other superconducting devices. Furthermore, the availability of an alternative approach to fabricating the CFD architecture is promising for commercializing this architecture. During a quench, accelerating the detection of the voltage threshold by using the CFD architecture can potentially reduce the risk of a thermal runaway by accelerating the activation of the protection system of HTS devices.

## 10.2 Limitations

During this research work, a maximum length of five meters of CFD tapes could be produced in a single batch, because of the limits of the equipment used to deposit the silver layer by sputtering. In addition, the developed automated reel-to-reel fabrication process includes steps of masking and chemical etching over long lengths, which remain costly for an industrial production line. We proposed an IJP CFD fabrication process as an alternative to avoid the steps of chemical etching and masking by printing directly conductive silver patterns on top of the surface of the REBCO layer followed by an oxygen annealing. Due to the non-existence of commercial non-oxygenated REBCO tapes without a silver layer during this project, we did not have access to this kind of tapes and this process was only tested on oxygenated REBCO tapes, whose silver layer has been completely removed by chemical etching. The concept of oxygenating REBCO tapes with only a fraction of silver on top of the superconducting layer could not be tested to achieve a complete proof-of-concept of this alternative CFD fabrication method. Although the feasibility of the CFD effect with the IJP process was validated through NZPV measurements, the porosity in the printed silver lines did not disappear even after annealing in an oxygen atmosphere for one hour at a temperature of 500 °C.

Finally, in the framework of numerical simulation tools of quench, we proposed the piecewise model as a substitute for the power law model to model the resistivity of HTS materials. The simulation results obtained with the piecewise model were in good agreement with the experimental measurements in the case of regular REBCO tapes. However, the availability of experimental data for the temperature dependence of the $E$-$J$ characteristics of REBCO tapes during the transition from the superconducting state to the normal state are still limited. Thus, the piecewise model was developed based on theoretical considerations and the limited experimental data reported in previous works. Meanwhile, Ito model the flux flow regime, the conductivity was represented by Bézier curves in a logarithmic space. The control points of the Bézier curves in the model will require further calibration with new experimental data such as the value of the flux flow exponent $n_{FF}$.

## 10.3 Suggestions for future Research

Further research work may be employed to build on the outcomes of this thesis. First, tens of meters of CFD REBCO tapes could be fabricated if a reel-to-reel silver deposition system were available, allowing us to explore the efficacy of the CFD architecture in large-scale devices. In addition, exploring the feasibility of oxygenating REBCO layers with only a partial layer of silver is required to fully test the IJP fabrication approach reported in this thesis. Other printing parameters, conductive inks, or even local deposition methods could be tested to improve the quality of the deposited patterns. For instance, if one aims at enhancing the interfacial resistance between the printed patterns and the REBCO layer and reducing the porosity of the silver layer, an analysis of the morphology and the roughness of the surface of the REBCO layer and the effect of the surface free energy and wettability on the bonding strength between the REBCO layer and the printed ink is required, which would help to determine the suitable ink binder and viscosity. Additionally, determining the diameter of silver nanoparticles would be essential to determine the maximum annealing temperature to apply on the printed lines without reaching the melting temperature of nanoparticles. Then, this approach could be transposed into a reel-to-reel local deposition system of conductive patterns on top of the REBCO layer to fabricate long-length CFD tapes without the need to apply chemical etching.

In addition, this thesis focused on studying the CFD concept in a CORC® cable arrangement and a minimalistic insulated coil structure. It would be interesting to investigate the benefits of the CFD architecture in other geometrical layouts of REBCO tapes such as HTS non-insulated coils, HTS twisted stacked-tape cable conductors, and other cables structures in which the current-sharing within REBCO tapes may have an impact on the quench dynamics.

Regarding to the potential of the CFD architecture to improve quench detection systems, other non-voltage quench detection techniques could be tested, such as optical or magnetic approaches, to evaluate the effectiveness of this concept in enhancing the sensitivity of these methods. Furthermore, other quench detection experiments could be performed at lower temperatures and under a magnetic field to encompass all the operational range of high-field applications.

Finally, in terms of numerical simulation tools, further experimental studies of the conductivity of REBCO conductors are planned to be performed in the future, in order to calibrate certain parameters in the piecewise model and increase the accuracy of the simulations of the quench protection of the electrothermal behavior of REBCO tapes with the CFD architecture.

# REFERENCES

[1] J. L. MacManus-Driscoll and S. C. Wimbush, “Processing and application of high-temperature superconducting coated conductors,” *Nature Reviews Materials*, vol. 6, no. 7, pp. 587–604, 2021.

[2] J. G. Bednorz and K. A. Müller, “Possible high T c superconductivity in the Ba- La-Cu- O system,” *Zeitschrift für Physik B Condensed Matter*, vol. 64, no. 2, pp. 189–193, 1986.

[3] S. Hahn *et al.*, “45.5-tesla direct-current magnetic field generated with a high-temperature superconducting magnet,” *Nature*, vol. 570, no. 7762, pp. 496–499, 2019.

[4] E. Nilsson *et al.*, “Performance of the 500 kW superconducting DC and AC links of the ASCEND demonstrator at Airbus,” *IEEE Transactions on Applied Superconductivity*, 2023.

[5] P. T. Pascal *et al.*, “Superconducting fault current limiter for ship grid simulation and demonstration,” *IEEE Transactions on Applied Superconductivity*, vol. 27, no. 4, pp. 1–5, 2017.

[6] A. Bergen *et al.*, “Design and in-field testing of the world’s first ReBCO rotor for a 3.6 MW wind generator,” *Superconductor science and technology*, vol. 32, no. 12, p. 125006, 2019.

[7] V. S. Vyatkin *et al.*, “Design of practical superconducting DC power cable with REBCO coated conductors,” *IEEE Transactions on Applied Superconductivity*, vol. 25, no. 4, pp. 1–7, 2015.

[8] M. Bonura and C. Senatore, “Temperature and field dependence of the quench propagation velocity in industrial REBCO coated conductors,” *IEEE Transactions on Applied Superconductivity*, vol. 27, no. 4, pp. 1–5, 2016.

[9] A. Zampa *et al.*, “Influence of local inhomogeneities in the REBCO layer on the mechanism of quench onset in 2G HTS tapes,” *IEEE Transactions on Applied Superconductivity*, vol. 32, no. 3, p. 6600807, 2022.

[10] C. Lacroix and F. Sirois, “Concept of a current flow diverter for accelerating the normal zone propagation velocity in 2G HTS coated conductors,” *Superconductor Science and Technology*, vol. 27, no. 3, p. 035003, 2014.

[11] H. K. Onnes, “Further experiments with liquid helium,” in *Proceedings of the KNAW*, vol. 13, 1911, pp. 1910–1911.

[12] H. Maeda and Y. Yanagisawa, “Recent developments in high-temperature superconducting magnet technology,” *IEEE Transactions on applied superconductivity*, vol. 24, no. 3, pp. 1–12, 2013.

[13] C. Yao and Y. Ma, “Superconducting materials: Challenges and opportunities for large-scale applications,” *Iscience*, vol. 24, no. 6, 2021.

[14] H. Hosono *et al.*, “Recent advances in iron-based superconductors toward applications,” *Materials today*, vol. 21, no. 3, pp. 278–302, 2018.

[15] C. Eom *et al.*, “High critical current density and enhanced irreversibility field in superconducting MgB2 thin films,” *Nature*, vol. 411, no. 6837, pp. 558–560, 2001.

[16] D.-X. Wang *et al.*, “Development of metal-organic deposition-derived second-generation high-temperature superconductor tapes and artificial flux pinning,” *Advances in Manufacturing*, pp. 1–18, 2023.

[17] C. Rey and A. Malozemoff, “Fundamentals of superconductivity,” in *Superconductors in the Power Grid.* Elsevier, 2015, pp. 29–73.

[18] D. Larbalestier *et al.*, “High-T c superconducting materials for electric power applications,” *Nature*, vol. 414, no. 6861, pp. 368–377, 2001.

[19] A. A. Abrikosov, “Nobel Lecture: Type-II superconductors and the vortex lattice,” *Reviews of modern physics*, vol. 76, no. 3, p. 975, 2004.

[20] W. T. B. de Sousa, “Transient simulations of superconducting fault current limiters,” *Diss. Ph. D. dissertation, Dept. Elect. Eng, Federal University of Rio de Janeiro, Brazil*, 2015.

[21] S. Foltyn *et al.*, “Materials science challenges for high-temperature superconducting wire,” *Nature materials*, vol. 6, no. 9, pp. 631–642, 2007.

[22] T. Kiss *et al.*, “Critical current properties in HTS tapes,” *Physica C: Superconductivity*, vol. 392, pp. 1053–1062, 2003.

[23] J. Duron *et al.*, “Computer modeling of YBCO fault current limiter strips lines in over-critical regime with temperature dependent parameters,” *IEEE transactions on applied superconductivity*, vol. 17, no. 2, pp. 1839–1842, 2007.

[24] D. Shi, *High-temperature superconducting materials science and engineering: new concepts and technology.* Elsevier, 1995.

[25] E. Zeldov *et al.*, "Optical and electrical enhancement of flux creep in YBa 2 Cu 3 O 7-$\delta$ epitaxial films," *Physical review letters*, vol. 62, no. 26, p. 3093, 1989.

[26] E. Stilp *et al.*, "Controlling the near-surface superfluid density in underdoped YBa2Cu3O6+ x by photo-illumination," *Scientific reports*, vol. 4, no. 1, p. 6250, 2014.

[27] V. Z. Kresin and S. A. Wolf, *Fundamentals of superconductivity.* Springer Science & Business Media, 2013.

[28] J. Durrell and N. Rutter, "Importance of low-angle grain boundaries in YBa2Cu3O7- $\delta$ coated conductors," *Superconductor Science and Technology*, vol. 22, no. 1, p. 013001, 2008.

[29] Y. Iijima *et al.*, "BMO-Doped REBCO-Coated Conductors for Uniform In-Field $I\_\{c\}$ by Hot-Wall PLD Process Using IBAD Template," *IEEE Transactions on Applied Superconductivity*, vol. 27, no. 4, pp. 1–4, 2017.

[30] "THEVA Dünnschichttechnik GmbH 2022," (available at:www.theva.com).

[31] M. Dürrschnabel *et al.*, "DyBa2Cu3O7- x superconducting coated conductors with critical currents exceeding 1000 A cm- 1," *Superconductor Science and Technology*, vol. 25, no. 10, p. 105007, 2012.

[32] W. Prusseit *et al.*, "ISD process development for coated conductors," *Physica C: Superconductivity and its applications*, vol. 426, pp. 866–871, 2005.

[33] P. Gao *et al.*, "Interface Properties and Failures of REBCO Coated Conductor Tapes: Research Progress and Challenges," *Superconductivity*, p. 100068, 2023.

[34] "Superpower," (available at:www.superpower-inc.com/specification.aspx).

[35] K. Tsuchiya *et al.*, "Superconducting properties of commercial REBCO-coated conductors with artificial pinning centers," *Superconductor Science and Technology*, vol. 34, no. 10, p. 105005, 2021.

[36] G. Jiang *et al.*, "Recent development and mass production of high Je 2G-HTS tapes by using thin hastelloy substrate at shanghai superconductor technology," *Superconductor Science and Technology*, vol. 33, no. 7, p. 074005, 2020.

[37] V. Chepikov *et al.*, “Introduction of BaSnO3 and BaZrO3 artificial pinning centres into 2G HTS wires based on PLD-GdBCO films. Phase I of the industrial R&D programme at SuperOx,” *Superconductor Science and Technology*, vol. 30, no. 12, p. 124001, 2017.

[38] J. Ekin, *Experimental techniques for low-temperature measurements: cryostat design, material properties and superconductor critical-current testing.* Oxford university press, 2006.

[39] P. Cayado *et al.*, “Untangling surface oxygen exchange effects in YBa 2 Cu 3 O 6+ x thin films by electrical conductivity relaxation,” *Physical chemistry chemical physics*, vol. 19, no. 21, pp. 14 129–14 140, 2017.

[40] Z. Stekly, J. Zar *et al.*, “Stable superconducting coils,” *IEEE Transactions on Nuclear Science*, vol. 12, no. 3, pp. 367–372, 1965.

[41] L. Dresner, *Stability of superconductors.* Springer Science & Business Media, 2006.

[42] B. Maddock, G. James, and W. Norris, “Superconductive composites: heat transfer and steady-state stabilization,” *Cryogenics*, vol. 9, no. 4, pp. 261–273, 1969.

[43] M. Bonura and C. Senatore, “An equation for the quench propagation velocity valid for high field magnet use of REBCO coated conductors,” *Applied Physics Letters*, vol. 108, no. 24, 2016.

[44] ——, “Transverse thermal conductivity of REBCO coated conductors,” *IEEE Transactions on Applied Superconductivity*, vol. 25, no. 3, pp. 1–4, 2014.

[45] “Superconductor Technologies Inc. 2022,” (available at:ir.suptech.com).

[46] D. Uglietti, “A review of commercial high temperature superconducting materials for large magnets: from wires and tapes to cables and conductors,” *Superconductor Science and Technology*, vol. 32, no. 5, p. 053001, 2019.

[47] W. Goldacker *et al.*, “Roebel cables from REBCO coated conductors: a one-century-old concept for the superconductivity of the future,” *Superconductor Science and Technology*, vol. 27, no. 9, p. 093001, 2014.

[48] M. Takayasu *et al.*, “Present status and recent developments of the twisted stacked-tape cable conductor,” *IEEE transactions on applied superconductivity*, vol. 26, no. 2, pp. 25–34, 2016.

[49] D. Uglietti, R. Wesche, and P. Bruzzone, “Fabrication trials of round strands composed of coated conductor tapes,” *IEEE transactions on applied superconductivity*, vol. 23, no. 3, pp. 4 802 104–4 802 104, 2013.

[50] N. Glasson *et al.*, “Development of a 1 MVA 3-phase superconducting transformer using YBCO Roebel cable,” *IEEE transactions on Applied Superconductivity*, vol. 21, no. 3, pp. 1393–1396, 2010.

[51] M. Takayasu *et al.*, “Development of REBCO twisted stacked-tape cables for magnet application,” in *Proc. 1st Workshop Accel. Magn. HTS*, 2014, pp. 1–27.

[52] N. Yanagi *et al.*, “Stable operation characteristics and perspectives of the large-current HTS STARS conductor,” in *Journal of Physics: Conference Series*, vol. 2545, no. 1. IOP Publishing, 2023, p. 012008.

[53] D. Van Der Laan, D. McRae, and J. Weiss, “Effect of monotonic and cyclic axial tensile stress on the performance of superconducting CORC® wires,” *Superconductor Science and Technology*, vol. 32, no. 5, p. 054004, 2019.

[54] D. C. van der Laan, X. Lu, and L. F. Goodrich, “Compact GdBa2Cu3O7–$\delta$ coated conductor cables for electric power transmission and magnet applications,” *Superconductor Science and Technology*, vol. 24, no. 4, p. 042001, 2011.

[55] D. C. Van der Laan, J. D. Weiss, and D. McRae, “Status of CORC® cables and wires for use in high-field magnets and power systems a decade after their introduction,” *Superconductor Science and Technology*, vol. 32, no. 3, p. 033001, 2019.

[56] D. Castelvecchi, “How would room-temperature superconductors change science?” *Nature*, vol. 621, no. 7977, pp. 18–19, 2023.

[57] “HTS Magnets,” (available at: https://cfs.energy/technology/hts-magnets).

[58] N. Mitchell *et al.*, “Superconductors for fusion: a roadmap,” *Superconductor science and technology*, vol. 34, no. 10, p. 103001, 2021.

[59] Z. S. Hartwig *et al.*, “The SPARC toroidal field model coil program,” *IEEE Transactions on Applied Superconductivity*, 2023.

[60] H. Jin *et al.*, “Performance test of REBCO CICC sub-cables with 10 kA current under 20 T background field,” *Superconductor Science and Technology*, vol. 36, no. 12, p. 12LT01, 2023.

[61] Y. Zhai *et al.*, "Conceptual design of HTS magnets for fusion nuclear science facility," *Fusion Engineering and Design*, vol. 168, p. 112611, 2021.

[62] A. Zappatore *et al.*, "A new model for the analysis of quench in HTS cable-in-conduit conductors based on the twisted-stacked-tape cable concept for fusion applications," *Superconductor Science and Technology*, vol. 33, no. 6, p. 065004, 2020.

[63] X. Wang *et al.*, "A 1.2 T canted cos$\theta$ dipole magnet using high-temperature superconducting CORC® wires," *Superconductor Science and Technology*, vol. 32, no. 7, p. 075002, 2019.

[64] F. Borgnolutti *et al.*, "Status of the EuCARD 5.4-T REBCO dipole magnet," *IEEE Transactions on Applied Superconductivity*, vol. 26, no. 4, pp. 1–5, 2016.

[65] L. Rossi and C. Senatore, "HTS accelerator magnet and conductor development in Europe," *Instruments*, vol. 5, no. 1, p. 8, 2021.

[66] X. Wang *et al.*, "Development and performance of a 2.9 Tesla dipole magnet using high-temperature superconducting CORC® wires," *Superconductor Science and Technology*, vol. 34, no. 1, p. 015012, 2020.

[67] ——, "An initial magnet experiment using high-temperature superconducting STAR® wires," *Superconductor Science and Technology*, vol. 35, no. 12, p. 125011, 2022.

[68] D. Park *et al.*, "Design overview of the MIT 1.3-GHz LTS/HTS NMR magnet with a new REBCO insert," *IEEE Transactions on Applied Superconductivity*, vol. 31, no. 5, pp. 1–6, 2021.

[69] M. Marchevsky, "Quench detection and protection for high-temperature superconductor accelerator magnets," *Instruments*, vol. 5, no. 3, p. 27, 2021.

[70] R. Teyber *et al.*, "CORC cable terminations with integrated Hall arrays for quench detection," *Superconductor Science and Technology*, vol. 33, no. 9, p. 095009, 2020.

[71] J. Weiss *et al.*, "Quench detection using Hall sensors in high-temperature superconducting CORC®-based cable-in-conduit-conductors for fusion applications," *Superconductor Science and Technology*, vol. 33, no. 10, p. 105011, 2020.

[72] M. Marchevsky *et al.*, "Ultrasonic waveguides for quench detection in HTS magnets," *IEEE Transactions on Applied Superconductivity*, vol. 32, no. 6, pp. 1–5, 2022.

[73] M. Takayasu, "Acoustic MEMS sensor array for quench detection of CICC superconducting cables," *IEEE Transactions on Applied Superconductivity*, vol. 30, no. 4, pp. 1–5, 2020.

[74] M. Marchevsky *et al.*, "Quench detection for high-temperature superconductor conductors using acoustic thermometry," *IEEE Transactions on Applied Superconductivity*, vol. 28, no. 4, pp. 1–5, 2018.

[75] F. Scurti *et al.*, "Quench detection for high temperature superconductor magnets: a novel technique based on Rayleigh-backscattering interrogated optical fibers," *Superconductor Science and Technology*, vol. 29, no. 3, p. 03LT01, 2016.

[76] D. Van Der Laan *et al.*, "CORC® wires containing integrated optical fibers for temperature and strain monitoring and voltage wires for reliable quench detection," *Superconductor Science and Technology*, vol. 33, no. 8, p. 085010, 2020.

[77] F. Scurti and J. Schwartz, "Optical fiber distributed sensing for high temperature superconductor magnets," in *2017 25th Optical Fiber Sensors Conference (OFS)*. IEEE, 2017, pp. 1–4.

[78] C. Lacroix *et al.*, "Normal zone propagation in various REBCO tape architectures," *Superconductor Science and Technology*, vol. 35, no. 5, p. 055009, 2022.

[79] L. Antognazza *et al.*, "Comparison between the behavior of HTS thin film grown on sapphire and coated conductors for fault current limiter applications," *IEEE transactions on applied superconductivity*, vol. 19, no. 3, pp. 1960–1963, 2009.

[80] P. Tixador *et al.*, "Status of the european union project FASTGRID," *IEEE Transactions on Applied Superconductivity*, vol. 29, no. 5, p. 5603305, 2019.

[81] ——, "Some results of the EU project FASTGRID," *IEEE Transactions on Applied Superconductivity*, vol. 32, no. 4, pp. 1–6, 2022.

[82] F. Roy, "Modeling and characterization of coated conductors applied to the design of superconducting fault current limiters," EPFL, Tech. Rep., 2010.

[83] G. Levin, K. Novak, and P. Barnes, "The effects of superconductor–stabilizer interfacial resistance on the quench of a current-carrying coated conductor," *Superconductor Science and Technology*, vol. 23, no. 1, p. 014021, 2009.

[84] C. Lacroix *et al.*, “Normal zone propagation velocity in 2G HTS coated conductor with high interfacial resistance,” *IEEE transactions on applied superconductivity*, vol. 23, no. 3, pp. 4 701 605–4 701 605, 2013.

[85] S. E. Russek *et al.*, “Surface degradation of superconducting YBa2Cu3O7- $\delta$ thin films,” *Applied physics letters*, vol. 64, no. 26, pp. 3649–3651, 1994.

[86] C. Lacroix *et al.*, “High normal zone propagation velocity in second generation high-temperature superconductor coated conductors with a current flow diverter architecture,” *Superconductor Science and technology*, vol. 27, no. 5, p. 055013, 2014.

[87] C. Lacroix, F. Sirois, and J. F. Lupien, “Engineering of second generation HTS coated conductor architecture to enhance the normal zone propagation velocity in various operating conditions,” *Superconductor Science and Technology*, vol. 30, no. 6, p. 064004, 2017.

[88] J. Fournier-Lupien *et al.*, “Use of the buffer layers as a current flow diverter in 2G HTS coated conductors,” *Superconductor Science and Technology*, vol. 31, no. 12, p. 125019, 2018.

[89] J. Giguère *et al.*, “High normal zone propagation velocity in copper-stabilized 2G HTS coated conductors,” *Superconductor Science and Technology*, vol. 34, no. 4, p. 045010, 2021.

[90] P. Barusco *et al.*, “Enhanced normal zone propagation velocity in REBCO coated conductors using an intermetallic stabilizer coating,” *IEEE Transactions on Applied Superconductivity*, 2024.

[91] J. Lu *et al.*, “Oxygen out-diffusion in REBCO coated conductor due to heating,” *Superconductor Science and Technology*, vol. 34, no. 7, p. 075004, 2021.

[92] F. Dimatix, “Materials Printer & Cartridges dmp-2831 & dmc-11601/11610-datasheet,” *Datasheet http://www. dimatix. com.(accessed 2010)*, 2008.

[93] W. Zhou *et al.*, “Fundamentals of scanning electron microscopy (SEM),” *Scanning microscopy for nanotechnology: techniques and applications*, pp. 1–40, 2007.

[94] M. Daibo *et al.*, “Evaluation of the normal-zone propagation characteristics of REBCO coated conductors with laminated Cu tape,” *IEEE transactions on applied superconductivity*, vol. 21, no. 3, pp. 2428–2431, 2011.

[95] B. Chen *et al.*, “Distributed optical fiber sensor for investigation of normal zone propagation and hot spot location in REBCO cables,” *Fusion Engineering and Design*, vol. 156, p. 111569, 2020.

[96] P. Yang *et al.*, “Experimental and numerical study of quench characteristics of nonuniform REBCO-coated conductors,” *IEEE Transactions on Applied Superconductivity*, vol. 27, no. 4, pp. 1–6, 2016.

[97] L. L. M. Handbook, “6th,” *Keithley*, 2004.

[98] T. Benkel *et al.*, “REBCO tape performance under high magnetic field,” *The European Physical Journal Applied Physics*, vol. 79, no. 3, p. 30601, 2017.

[99] M. Filipenko *et al.*, “Concept design of a high power superconducting generator for future hybrid-electric aircraft,” *Superconductor Science and Technology*, vol. 33, no. 5, p. 054002, 2020.

[100] M. Búran *et al.*, “Impact of a REBCO coated conductor stabilization layer on the fault current limiting functionality,” *Superconductor Science and Technology*, vol. 32, no. 9, p. 095008, 2019.

[101] J. Ciceron *et al.*, “Test in strong background field of a modular element of a REBCO 1 MJ high energy density SMES,” *IEEE Transactions on Applied Superconductivity*, vol. 28, no. 4, p. 5701005, 2018.

[102] G. Ma *et al.*, “Experiment and simulation of REBCO conductor coils for an HTS linear synchronous motor,” *IEEE Transactions on Applied Superconductivity*, vol. 27, no. 4, p. 5201805, 2017.

[103] G. Iannone *et al.*, “Quench propagation in commercial REBCO composite tapes,” *Cryogenics*, vol. 109, p. 103116, 2020.

[104] J. Schwartz, “QUENCH IN HIGH TEMPERATURE SUPERCONDUCTOR MAGNETS,” in *WAMSDO: Workshop on Accelerator Magnet Superconductors, Design and Optimization*, 2013, p. 21.

[105] C. Lacroix, “Accelerating quench propagation in 2G HTS coated conductors by engineering the tape architecture,” in *Superconducting Fault Current Limiter: Innovation for the Electric Grids.* World Scientific, 2019, pp. 347–355.

[106] “Anton Paar,” (available at:https://www.anton-paar.com/ca-en/products/details/nano-scratch-tester-nst3/).

[107] N. X. Randall, "The current state-of-the-art in scratch testing of coated systems," *Surface and Coatings Technology*, vol. 380, p. 125092, 2019.

[108] "Scanning Electron Microscope (SEM) Products JEOL Ltd," (available at:https://www.jeol.com/products/scientific/sem/).

[109] H. Kim *et al.*, "The influence of heat-treatment and oxygenation annealing on the superconducting properties of YBCO coated conductors," *Superconductor Science and Technology*, vol. 22, no. 12, p. 125016, 2009.

[110] Y. Li *et al.*, "Texture development and superconducting properties of YBCO thick films deposited on buffered metal substrates at various deposition rates," *IEEE Transactions on Applied Superconductivity*, vol. 13, no. 2, pp. 2758–2761, 2003.

[111] V. Selvamanickam *et al.*, "MOCVD-Based YBCO-Coated Conductors," *MRS Bulletin*, vol. 29, no. 8, p. 579–582, 2004.

[112] C. Barth, G. Mondonico, and C. Senatore, "Electro-mechanical properties of REBCO coated conductors from various industrial manufacturers at 77 K, self-field and 4.2 K, 19 T," *Superconductor Science and Technology*, vol. 28, no. 4, p. 045011, 2015.

[113] T. J. Collins, "ImageJ for microscopy," *Biotechniques*, vol. 43, no. S1, pp. S25–S30, 2007.

[114] J. van Nugteren *et al.*, "Toward REBCO 20 T+ dipoles for accelerators," *IEEE Transactions on Applied Superconductivity*, vol. 28, no. 4, p. 4008509, 2018.

[115] B. Sorbom *et al.*, "ARC: A compact, high-field, fusion nuclear science facility and demonstration power plant with demountable magnets," *Fusion Engineering and Design*, vol. 100, pp. 378–405, 2015.

[116] F. Scurti *et al.*, "SMART conductor on round core (CORC®) wire via integrated optical fibers," *Superconductor Science and Technology*, vol. 34, no. 3, p. 035026, 2021.

[117] M. Marchevsky *et al.*, "Radio Frequency-Based Diagnostics for Superconducting Magnets," *IEEE Transactions on Applied Superconductivity*, vol. 33, no. 5, pp. 1–6, 2023.

[118] S. Muto *et al.*, "Quench Protection Study of a Large Scale REBCO Magnet With Additional Copper Tapes," *IEEE Transactions on Applied Superconductivity*, vol. 32, no. 6, p. 4701605, 2022.

[119] S. Syed, “Silver recovery aqueous techniques from diverse sources: Hydrometallurgy in recycling,” *Waste management*, vol. 50, pp. 234–256, 2016.

[120] P. Barusco *et al.*, “A Sulfurization method for creating the buffer-layers Current Flow Diverter architecture in REBa2Cu3O7 coated conductors,” *Superconductor Science and Technology*, 2023.

[121] J.-H. Fournier-Lupien *et al.*, “Effect of annealing on HTS tapes with a cerium oxide layer inserted between the REBaCuO and silver layers,” *Materialia*, vol. 15, p. 101029, 2021.

[122] P. Barusco *et al.*, “Chemical Solution Deposition of Insulating Yttria Nanolayers as Current Flow Diverter in Superconducting GdBa2Cu3O7- $\delta$ Coated Conductors,” *ACS omega*, vol. 7, no. 18, pp. 15 315–15 325, 2022.

[123] ——, “Enhanced normal zone propagation velocity in REBCO coated conductors using an intermetallic stabilizer coating,” *IEEE Transactions on Applied Superconductivity*, pp. 1–6, 2024.

[124] J. Perelaer, B.-J. De Gans, and U. S. Schubert, “Ink-jet printing and microwave sintering of conductive silver tracks,” *Advanced materials*, vol. 18, no. 16, pp. 2101–2104, 2006.

[125] S. Uttiya *et al.*, “Inkjet printing of conducting silver patterns on alumina and insulating ceramic-glass by saline precursors,” *Thin Solid Films*, vol. 642, pp. 370–376, 2017.

[126] “Hitachi FB-2000A FIB,” (available at:https://www.mtu.edu/acmal/shared-facilities/electron-optics/instrumentation/hitachi-fb-2000a-fib/).

[127] J. W. Ekin *et al.*, “High T c superconductor/noble-metal contacts with surface resistivities in the 10- 10 Ω cm2 range,” *Applied physics letters*, vol. 52, no. 21, pp. 1819–1821, 1988.

[128] I. J. Fernandes *et al.*, “Silver nanoparticle conductive inks: synthesis, characterization, and fabrication of inkjet-printed flexible electrodes,” *Scientific reports*, vol. 10, no. 1, p. 8878, 2020.

[129] W. Shen *et al.*, “Preparation of solid silver nanoparticles for inkjet printed flexible electronics with high conductivity,” *Nanoscale*, vol. 6, no. 3, pp. 1622–1628, 2014.

[130] Y. Zhang *et al.*, "Progress in production and performance of second generation (2G) HTS wire for practical applications," *IEEE Transactions on applied superconductivity*, vol. 24, no. 5, pp. 1–5, 2014.

[131] U. P. Trociewitz *et al.*, "35.4 T field generated using a layer-wound superconducting coil made of (RE) Ba2Cu3O7- x (RE= rare earth) coated conductor," *Applied Physics Letters*, vol. 99, no. 20, 2011.

[132] S. A. Gourlay *et al.*, "The US magnet development program plan," Lawrence Berkeley National Lab.(LBNL), Berkeley, CA (United States), Tech. Rep., 2016.

[133] G. Kirby *et al.*, "Status of the demonstrator magnets for the EuCARD-2 future magnets project," *IEEE transactions on applied superconductivity*, vol. 26, no. 3, pp. 1–7, 2016.

[134] L. Rossi *et al.*, "The EuCARD-2 future magnets European collaboration for accelerator-quality HTS magnets," *IEEE transactions on applied superconductivity*, vol. 25, no. 3, pp. 1–7, 2014.

[135] A. Creely *et al.*, "Overview of the SPARC tokamak," *Journal of Plasma Physics*, vol. 86, no. 5, p. 865860502, 2020.

[136] P. Bruzzone *et al.*, "High temperature superconductors for fusion magnets," *Nuclear Fusion*, vol. 58, no. 10, p. 103001, 2018.

[137] X. Wang, S. A. Gourlay, and S. O. Prestemon, "Dipole magnets above 20 tesla: Research needs for a path via high-temperature superconducting REBCO conductors," *Instruments*, vol. 3, no. 4, p. 62, 2019.

[138] M. Yazdani-Asrami *et al.*, "High temperature superconducting cables and their performance against short circuit faults: current development, challenges, solutions, and future trends," *Superconductor Science and Technology*, vol. 35, no. 8, p. 083002, 2022.

[139] D. Van Der Laan *et al.*, "Development of CORC® cables for helium gas cooled power transmission and fault current limiting applications," *Superconductor Science and Technology*, vol. 31, no. 8, p. 085011, 2018.

[140] A. Allais *et al.*, "SuperRail–World-First HTS Cable to be Installed on a Railway Network in France," *IEEE Transactions on Applied Superconductivity*, vol. 34, no. 3, p. 4802207, 2024.

[141] L. Ybanez *et al.*, “ASCEND: The first step towards cryogenic electric propulsion,” in *IOP Conference Series: Materials Science and Engineering*, vol. 1241, no. 1. IOP Publishing, 2022, p. 012034.

[142] M. Takayasu *et al.*, “Conductor characterization of YBCO twisted stacked-tape cables,” *IEEE transactions on applied superconductivity*, vol. 23, no. 3, pp. 4 800 104–4 800 104, 2012.

[143] S. Kar *et al.*, “Next-generation highly flexible round REBCO STAR wires with over 580 A mm- 2 at 4.2 K, 20 T for future compact magnets,” *Superconductor Science and Technology*, vol. 32, no. 10, p. 10LT01, 2019.

[144] Z. S. Hartwig *et al.*, “VIPER: an industrially scalable high-current high-temperature superconductor cable,” *Superconductor Science and Technology*, vol. 33, no. 11, p. 11LT01, 2020.

[145] D. Van der Laan *et al.*, “Record current density of 344 A mm- 2 at 4.2 K and 17 T in CORC® accelerator magnet cables,” *Superconductor Science and Technology*, vol. 29, no. 5, p. 055009, 2016.

[146] J. D. Weiss *et al.*, “Introduction of CORC® wires: highly flexible, round high-temperature superconducting wires for magnet and power transmission applications,” *Superconductor science and technology*, vol. 30, no. 1, p. 014002, 2016.

[147] “Advanced Conductor Technologies LLC,” (available at:www.advancedconductor.com/corccable/).

[148] P. Tixador *et al.*, “Impact of conductor inhomogeneity on FCL transient performance,” *IEEE transactions on applied superconductivity*, vol. 21, no. 3, pp. 1194–1197, 2010.

[149] A. Zampa *et al.*, “Current redistribution during inhomogeneous quench of 2G HTS tapes,” *Superconductor Science and Technology*, vol. 35, no. 9, p. 095003, 2022.

[150] H. Ben Saad *et al.*, “Meter-scale REBCO tapes with a current flow diverter architecture,” *Manuscript in preparation*, 2024.

[151] E. R. Canavan, H. Leidecker, and L. Panashchenko, “Conductance Degradation in HTS Coated Conductor Solder Joints,” in *IOP Conference Series: Materials Science and Engineering*, vol. 102, no. 1. IOP Publishing, 2015, p. 012032.

[152] C. Barth *et al.*, "Temperature-and field-dependent characterization of a conductor on round core cable," *Superconductor Science and Technology*, vol. 28, no. 6, p. 065007, 2015.

[153] J. D. Weiss *et al.*, "Hybrid superconducting fault current limiting CORC® wires with millisecond response time," *Superconductor Science and Technology*, vol. 32, no. 3, p. 034005, 2019.

[154] G. Willering *et al.*, "Effect of variations in terminal contact resistances on the current distribution in high-temperature superconducting cables," *Superconductor Science and Technology*, vol. 28, no. 3, p. 035001, 2015.

[155] M. Majoros *et al.*, "Stability and normal zone propagation in YBCO CORC cables," *Superconductor Science and Technology*, vol. 29, no. 4, p. 044006, 2016.

[156] D. Laan *et al.*, "High-temperature superconducting CORC wires with record-breaking axial tensile strain tolerance present a breakthrough for high-field magnets," *Supercon Sci Technol*, vol. 34, p. 10LT01, 2021.

[157] J. Van Nugteren *et al.*, "Measurement and analysis of normal zone propagation in a ReBCO coated conductor at temperatures below 50 K," *Physics procedia*, vol. 67, pp. 945–951, 2015.

[158] J. ter Harmsel *et al.*, "Magnetization loss and transport current loss in ReBCO racetrack coils carrying stationary current in time-varying magnetic field at 4.2 K," *Superconductor Science and Technology*, vol. 36, no. 1, p. 015011, 2022.

[159] Y. Jiang *et al.*, "Development of a YBCO racetrack coil for HTS machine applications," *IEEE Transactions on Applied Superconductivity*, vol. 24, no. 5, pp. 1–4, 2014.

[160] Y. Gao *et al.*, "Design, fabrication, and testing of a YBCO racetrack coil for an HTS synchronous motor with HTS flux pump," *IEEE Transactions on Applied Superconductivity*, vol. 30, no. 4, pp. 1–5, 2020.

[161] T. Nes *et al.*, "Design of a cloverleaf-racetrack dipole demonstrator magnet with dual ReBCO conductor," *IEEE transactions on applied superconductivity*, vol. 32, no. 6, pp. 1–5, 2022.

[162] K. Mizuno *et al.*, "Experimental production of a real-scale REBCO magnet aimed at its application to maglev," *IEEE Transactions on Applied Superconductivity*, vol. 27, no. 4, pp. 1–5, 2016.

[163] C.-H. Bonnard *et al.*, "Multi-scale model of resistive-type superconducting fault current limiters based on 2G HTS coated conductors," *Superconductor Science and Technology*, vol. 30, no. 1, p. 014005, 2016.

[164] Y. Iwasa, *Case studies in superconducting magnets: design and operational issues.* Springer science & business media, 2009.

[165] F. Trillaud, G. Dos Santos, and G. Goncalves Sotelo, "Essential material knowledge and recent model developments for REBCO-coated conductors in electric power systems," *Materials*, vol. 14, no. 8, p. 1892, 2021.

[166] W. Paul *et al.*, "Fault current limiter based on high temperature superconductors–different concepts, test results, simulations, applications," *Physica C: Superconductivity*, vol. 354, no. 1-4, pp. 27–33, 2001.

[167] N. Riva *et al.*, "A wide range E- J constitutive law for simulating REBCO tapes above their critical current," *Superconductor Science and Technology*, vol. 34, no. 11, p. 115014, 2021.

[168] I. Falorio, E. Young, and Y. Yang, "EJ characteristic of 2G YBCO coated conductor tapes at different temperatures," *Physics Procedia*, vol. 36, pp. 1462–1467, 2012.

[169] I. Falorio, E. A. Young, and Y. Yang, "Flux pinning distribution and EJ characteristics of 2G YBCO Tapes," in *Journal of Physics: Conference Series*, vol. 507, no. 2. IOP Publishing, 2014, p. 022004.

[170] S. Richard, F. Sirois, and C. Lacroix, "Post-processing method for extracting the resistivity of Rare-Earth Barium Copper Oxide (REBCO) coated conductors in over-critical current conditions from ultra-fast VI pulsed current measurements," *Journal of Applied Physics*, vol. 126, no. 2, 2019.

[171] N. Riva *et al.*, "Overcritical current resistivity of YBCO-coated conductors through combination of PCM and finite-element analysis," *IEEE Transactions on Applied Superconductivity*, vol. 29, no. 5, pp. 1–5, 2019.

[172] N. S. Sapidis and W. H. Frey, "Controlling the curvature of a quadratic Bézier curve," *Computer Aided Geometric Design*, vol. 9, no. 2, pp. 85–91, 1992.

[173] A. Badel *et al.*, "Modeling of 'quench'or the occurrence and propagation of dissipative zones in REBCO high temperature superconducting coils," *Superconductor Science and Technology*, vol. 32, no. 9, p. 094001, 2019.

[174] M. A. Green, "Various quench protection methods for HTS magnets," in *IOP Conference Series: Materials Science and Engineering*, vol. 755, no. 1. IOP Publishing, 2020, p. 012134.

[175] Y. Touloukian *et al.*, "Thermophysical Properties of Matter˜ Plenum," *New York*, 1970.

[176] J. Gordon *et al.*, "Lattice and electronic specific heat of YBa2Cu3O7," *Physica C: Superconductivity and its Applications*, vol. 162, pp. 484–485, 1989.

[177] J. Lu, E. Choi, and H. Zhou, "Physical properties of Hastelloy® C-276™ at cryogenic temperatures," *Journal of applied physics*, vol. 103, no. 6, 2008.

[178] S. Hagen, Z. Wang, and N. P. Ong, "Anisotropy of the thermal conductivity of YBa 2 Cu 3 O 7- y," *Physical Review B*, vol. 40, no. 13, p. 9389, 1989.

[179] L. E. Gamage *et al.*, "Recycling of Gold and Silver from Electronic Waste—A Review," *Materials Circular Economy*, vol. 5, no. 1, p. 8, 2023.

[180] F. Okamoto, "Etching solution for silver," *Patent, US3860423A*, 1973.

[181] K.-S. Chou, Y.-C. Lu, and H.-H. Lee, "Effect of alkaline ion on the mechanism and kinetics of chemical reduction of silver," *Materials Chemistry and Physics*, vol. 94, no. 2-3, pp. 429–433, 2005.

[182] S. Aktas, M. Morcali, and O. Yucel, "Silver recovery from waste radiographic films by cementation and reduction," *Canadian Metallurgical Quarterly*, vol. 49, no. 2, pp. 147–153, 2010.

[183] G. Sulka and M. Jaskuła, "Effect of sulphuric acid and copper sulphate concentrations on the morphology of silver deposit in the cementation process," *Electrochimica acta*, vol. 51, no. 27, pp. 6111–6119, 2006.

[184] O. Keleş, "An optimization study on the cementation of silver with copper in nitrate solutions by taguchi design," *Hydrometallurgy*, vol. 95, no. 3-4, pp. 333–336, 2009.

# APPENDIX A MATERIALS PROPERTIES

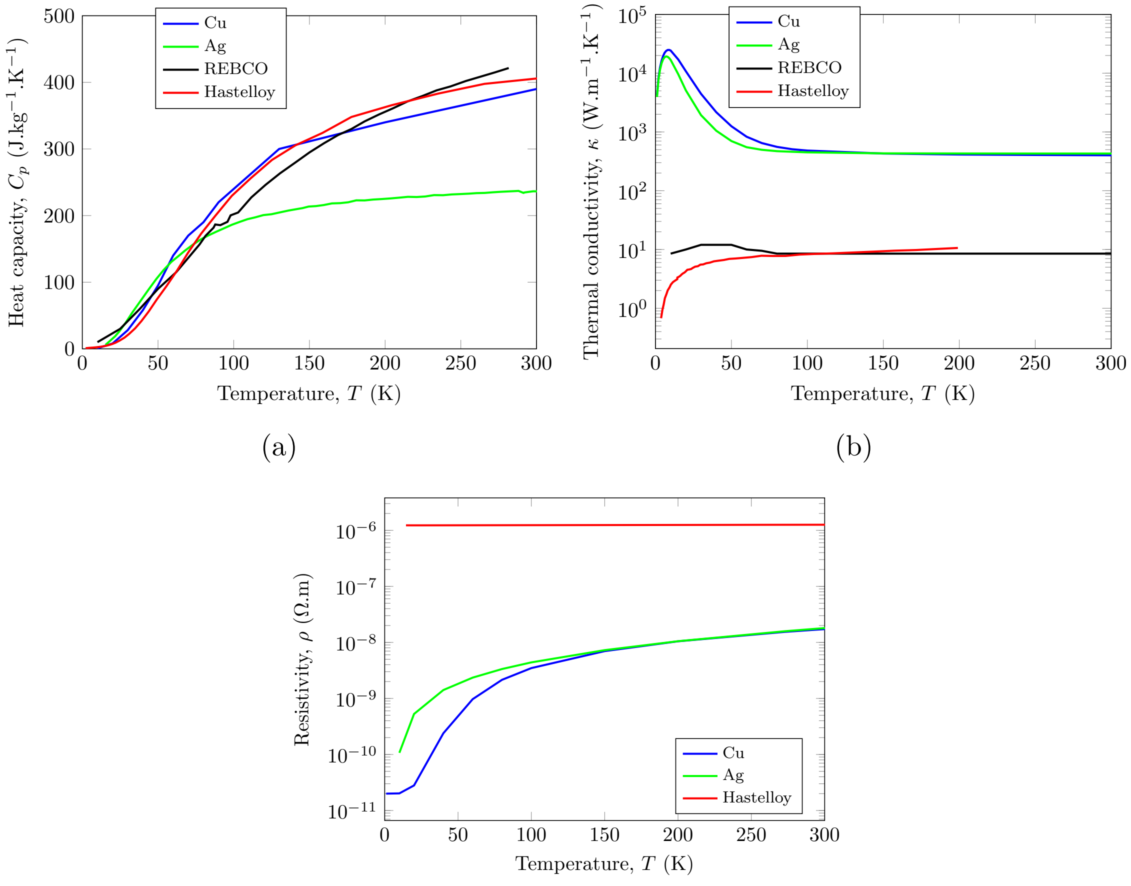

(a)

(b)

(c)

Figure A.1 Data of materials properties vs the temperature used in the simulations. (a) Heat capacity $C_p$ of copper, silver, REBCO, and hastelloy. (b) Thermal conductivity $\kappa$ of copper, silver, REBCO, and hastelloy. (c) Electrical resistivity $\rho$ of copper, silver, and hastelloy. Data from [175–178].

# APPENDIX B SILVER RECYCLING

Preliminary silver recycling experiments were performed during this work to recover the silver etched during the CFD fabrication process. Several recycling methods are applied to recover precious metals like silver from several sources [119, 179]. We tested two recovery techniques to extract the silver from the stored silver etching solution, which resulted from the CFD fabrication process. The silver etching was performed using an aqueous solution of peroxide ($H_2O_2$) and ammonium hydroxide ($NH_4OH$) with a 1:1:4 dilution ratio. Following the etching process, the eliminated silver reacts with the peroxide and ammonium hydroxide, forming a silver diamine complex. The equation of the chemical reaction is expressed as follows [180]:

$$2\mathrm{Ag} + 4\mathrm{NH_3} = 2[\mathrm{Ag(NH_3)_2}]^{+} + 2\mathrm{OH}^{-}, \tag{B.1}$$

The reduction of the $[Ag(NH_3)_2]^+$ leads to the formation of metallic silver following this reaction:

$$[\mathrm{Ag(NH_3)_2}]^{+}_{aq} + e = \mathrm{Ag(s)} + 2\mathrm{NH_3}\,, \tag{B.2}$$

Copper and dextrose represent elements that can reduce the diamine silver complex to metallic silver [119, 181]. These elements are used for silver extraction from silver-based spent materials and they provide low toxicity and low-cost recycling techniques. In this work, we tested both elements to recover silver from the etching solution.

## Dextrose reduction

To extract the silver from the etching solution using dextrose, a solution containing 10 ml of dextrose with a concentration of 90 g/L, 10 ml of sodium hydroxide (NaOH) with a concentration of 3.2 g/L, and 10 ml of the etching solution was prepared. The silver formation equation is as follows:

$$\begin{aligned}&\mathrm{CH_2OH(CHOH)_4CH}O + 2[\mathrm{Ag(NH_3)_2}]^{+}_{aq} + 3\mathrm{OH}^{-}\\ &\qquad = 2\mathrm{Ag(s)} + \mathrm{CH_2OH(CHOH)_4COO}^{-} + 4\mathrm{NH_3} + 2\mathrm{H_2O},\end{aligned} \tag{B.3}$$

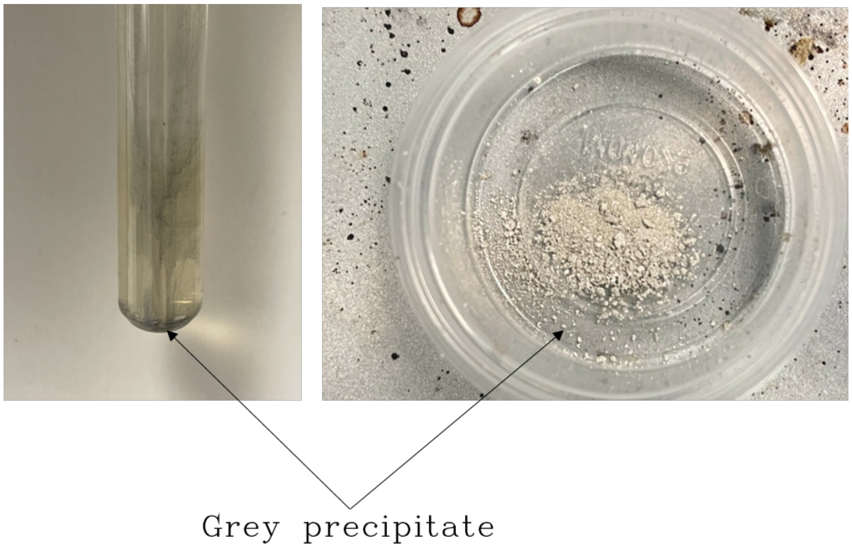

Figure B.1 Silver extraction from the etching solution using dextrose as a reducing element. The appearance of a grey precipitate in the left figure. Obtained powder after filtration in the right figure.

After 30 minutes, the solution becomes darker and a grey precipitate is formed in the solution as shown in Figure B.1. After filtration, a grey powder was extracted indicating the formation of silver powder (Figure B.1). However, the quantity of silver that exists in the etching solution was unknown. Therefore, the same test was reproduced, only this time an amount of pure silver was dissolved in the etching solution. The initial mass of the dissolved silver was 250 mg. The final mass of the recovered powder was 190 mg. This indicates that the recovery rate was 76%.

### Cementation

Cementation is a well-known hydro-metallurgical process to recover silver ions from industrial baths based on a red-ox reaction between electronegative metal and electropositive ions [119, 182]. Copper is widely applied in the cementation of silver [183, 184].

In this experience, a polished copper bar was immersed in the etching solution. The recovery reaction consists in substituting the silver ion in the silver diamine complex with the copper ion. The solution contains copper tetraamine complex ($[Cu(NH_3)_4]^{2+}$) after the substitution reaction occurs. The substitution reaction is expressed as follows:

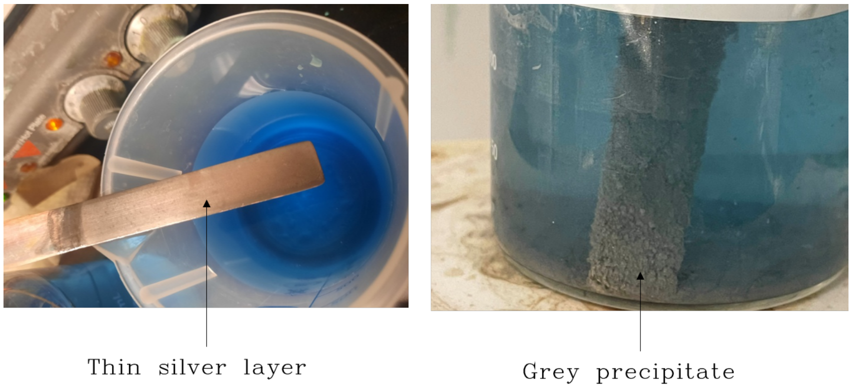

Figure B.2 Silver extraction from the etching solution using copper cementation process. A copper bar coated with a silver layer is shown in the left figure. The appearance of a grey precipitate the copper bar is shown in the right figure.

$$2[\mathrm{Ag(NH_3)_2}]^{+}_{aq} + \mathrm{Cu(s)} = 2\mathrm{Ag(s)} + [\mathrm{Cu(NH_3)_4}]^{2+}_{aq}, \tag{B.4}$$

The etching solution was heated to 50 °C and was stirred during the experiment to accelerate the cementation process. After one hour, a thin silver layer was formed on the surface of the copper bar and the color of the solution turned from transparent to pale blue as shown in Figure B.2. After 24 hours, the color of the solution turned to dark blue, indicating the formation of a tetraamine copper complex. However, the substitution reaction stopped once the copper bar was fully covered with silver. There was no formation of precipitates due to the low quantity of silver present in the etching solution. To quantify the recovery rate of this reaction, we dissolved a mass of 264 g of pure silver in 170 ml of the etching solution, and we reproduced the same cementation process. After six hours, silver precipitates were formed on the surface of the copper bar as shown in Figure B.2 (left figure). After filtration, the mass of the recovered powder was 152 mg. This means that the recovery rate of this process was 57%. This reaction had a lower efficiency because the rest of the silver was deposited as a thin layer on the copper bar.

### Conclusion

This work demonstrated that the etched silver during the CFD fabrication process could be recovered. However, further studies on the purity of the extracted precipitates need to be performed along with optimizing the experimental conditions, such as controlling the pH and the temperature of the etching solution to enhance the recovery rate. Two important drawbacks of these approaches are the left-over solutions obtained after the recycling process and the fact that they add extra steps to the CFD fabrication process. In a future project, an exploration of an environmental approach to extracting silver from the etching solution can be explored with fewer residual solutions.